

2018-09-21

# Ta-Based Nanostructured Materials for Proton Exchange Membrane Fuel Cells

Abhayawardhana, Anusha Dilhani

---

Abhayawardhana, A. D. (2018). Ta-Based Nanostructured Materials for Proton Exchange Membrane Fuel Cells (Doctoral thesis, University of Calgary, Calgary, Canada). Retrieved from <https://prism.ucalgary.ca>. doi:10.11575/PRISM/33130

<http://hdl.handle.net/1880/108778>

*Downloaded from PRISM Repository, University of Calgary*

UNIVERSITY OF CALGARY

Ta-Based Nanostructured Materials for Proton Exchange Membrane Fuel Cells

by

Anusha Dilhani Abhayawardhana

A THESIS

SUBMITTED TO THE FACULTY OF GRADUATE STUDIES

IN PARTIAL FULFILMENT OF THE REQUIREMENTS FOR THE

DEGREE OF DOCTOR OF PHILOSOPHY

GRADUATE PROGRAM IN CHEMISTRY

CALGARY, ALBERTA

SEPTEMBER, 2018

© Anusha Dilhani Abhayawardhana 2018

## Abstract

The focus of this work has been to assess the suitability of nanostructured TaO<sub>x</sub>N<sub>y</sub>, primarily as nanotubes (NTs), as a catalyst and/or catalyst support material for proton exchange membrane fuel cell (PEMFC) applications. It was found that this n-type material could be switched between an insulating state at > 0.6 V vs RHE to a conducting state at < 0.6 V in both aqueous and organic media. In the conducting state, the redox activity was proposed to be due to the Ta<sup>4+/5+</sup> reaction, along with insertion/de-insertion of solution cations. The conductivity switching behavior was correlated with electrochromism, with the NTs being yellow-orange in the oxidized state and blue-black when reduced.

TaO<sub>x</sub>N<sub>y</sub> was then tested for its activity in catalyzing hydrogen oxidation (HOR) and oxygen reduction (ORR) in acidic medium. Although TaO<sub>x</sub>N<sub>y</sub> alone is inactive towards these reactions, the presence of Pt nanoparticles (NPs) changed its behaviour. When deposited on a thin compact TaO<sub>x</sub>N<sub>y</sub> film, normal Pt electrochemistry was seen with a ~60 mV·decade<sup>-1</sup> ORR Tafel slope. When Pt NPs were deposited on TaO<sub>x</sub>N<sub>y</sub> NPs, a 105 mV·decade<sup>-1</sup> ORR Tafel slope was seen attributed to porosity or resistance of the TaO<sub>x</sub>N<sub>y</sub>.

Both the TaO<sub>x</sub>N<sub>y</sub> NTs alone and the Pt NPs/TaO<sub>x</sub>N<sub>y</sub> NTs material were found to be very resistant to corrosion under PEMFC operating conditions, evaluated through an in-house accelerated durability test. Further, due to its conductivity switching characteristics, the HOR showed better performance than the ORR, but not as good as for state-of the art Pt/Carbon. Interestingly, some hydrogen oxidation was seen even when TaO<sub>x</sub>N<sub>y</sub> is non-conducting, attributed to stabilization of the Ta<sup>4+</sup> state in H<sub>2</sub>.

TaO<sub>x</sub>N<sub>y</sub> was also anchored on colloid imprinted carbon (CIC) to improve its conductivity and durability. Although the CIC improved the conductivity, all CIC based materials failed the corrosion accelerated durability tests (ADT). The presence of TaO<sub>x</sub>N<sub>y</sub> or N-doping of CIC (N is doped during synthesis) also did not improve the corrosion resistance.

Overall, TaO<sub>x</sub>N<sub>y</sub> was shown to be a very durable material, resistant to corrosion even at very high anodic potentials. It is also a promising support material for Pt NPs for the catalysis of the HOR, but its conductivity likely needs to be improved further in order to catalyze the ORR.

## Acknowledgements

I would like to extend my heartfelt thanks and deepest appreciation to my supervisor and mentor, Dr. Viola Birss, for her unwavering support and encouragement throughout my Ph.D. years. Her patience, meticulous editing, and enthusiasm for electrochemistry were crucial to the success of this work. She has nurtured my scientific thinking and imparted an indelible effect on shaping my career.

I would also like to thank my committee members, Drs. Todd Sutherland and George Shimizu, for their assistance and helpful advice throughout the years and during my defense. Special thanks to Dr. Sutherland for allowing me to use his laboratory instruments and teaching me the first lessons in practical electrochemistry. I would also like to thank Dr. Anne Co (external examiner) and Dr. Sathish Ponnuram (internal external examiner) for agreeing to be on my defense committee and for their valuable suggestions to improve my thesis.

I am fortunate to have worked with many wonderful people throughout my academic life here at the U of C. My special thanks are extended to Drs. Simon Trudel, Tobias Fürstenhaupt, Max Anikovskiy, Hebert Molero, and Maen Husein for their assistance in various ways. I would also like to thank the many past and present members of the Birss and Thangadurai groups with whom I shared office and laboratory spaces. They made my life memorable and enjoyable and I made lasting friendships with some of them. A big thank you to Drs. Corie Horwood, Dustin Banham, Hany El-Sayed, Farisa Farouzandeh, Xiaoan Li, Bri Campbell, Scott Paulson, Jack Kan, Hebert Molero, Ehab El-Sawy, and Hameed Shabhaazi for useful discussions, insightful ideas/suggestions, collaboration, editing my thesis, and much more. Also, I would like to thank

Drs. Erwan Bertin, Javad Parnian, and Haris Ansari as well as Robert Mayall, Jachym Slaby and Annie Hoang for help in editing my thesis. I have made many other friends during my time at U of C and I would like to thank them all for their support.

Many thanks also to all of the administrative staff in the Chemistry Department office, especially Bonnie King, Janice Crawford, Sarah Boschman, Chad Dawes and others. Also, I would like to thank the support staff, especially Mark Toonen (Glass Shop), Ed Cairns and Mike Siewert (Electronics Shop), Andy Read, Darren Gisby and Todd Will (Machine Shop), Johnson Li (Instrumentation), and Magdi Khalil, Bob Stockwell and Nelson Cruz (Chemistry Stores), for their essential technical support that allowed me to complete my project.

On the personal note, to Amma (mother), thank you for teaching me the value of education, not the money. Thank you Thaththa (father) for never forcing me to be a conformist. To my sister, Thushari, thank you for staying awake when I was teaching you chemistry. Thank you Ulinda, my brother-in-law, for seeing fungi in my TEM/SEM images. To Janaka, my husband, thank you for being a true feminist although you always win.

## **Dedication**

To the General Public who bear the cost of my achievements as well as failures.

## Table of Contents

Abstract .....	ii
Acknowledgements .....	iv
Dedication.....	vi
Table of Contents.....	vii
List of Tables.....	xii
List of Figures and Illustrations .....	xiii
List of Symbols, Abbreviations and Nomenclature.....	xix
<b>Chapter 1 : Nanostructured Ta-Based Materials for Fuel Cell Applications .....</b>	<b>2</b>
<b>1.1 Relevant Background for the Project .....</b>	<b>2</b>
<b>1.2 Research Objectives.....</b>	<b>6</b>
<b>1.3 Organization of Thesis.....</b>	<b>7</b>
<b>Chapter 2 : Relevant Background Information.....</b>	<b>10</b>
<b>2.1 Fuel Cells (FCs).....</b>	<b>10</b>
<b>2.2 Basics of Proton Exchange Membrane Fuel Cells (PEMFCs).....</b>	<b>12</b>
<b>2.2.1 The PEMFC catalyst layer .....</b>	<b>14</b>
<b>2.2.2 Proton exchange membranes (polymer electrolyte membrane, PEM) .....</b>	<b>16</b>
<b>2.3 Challenges faced by PEMFCs.....</b>	<b>17</b>
<b>2.3.1 Cost</b>	<b>17</b>
<b>2.3.2 Durability.....</b>	<b>19</b>
<b>2.4 Degradation of PEMFC Catalyst Layers (CL) .....</b>	<b>20</b>
<b>2.4.1 Catalyst degradation.....</b>	<b>20</b>
<b>2.4.2 Carbon catalyst support degradation .....</b>	<b>22</b>
<b>2.4.2.1 Mechanism of carbon catalyst support degradation [Carbon oxidation reaction (COR)].....</b>	<b>24</b>
<b>2.4.2.2 Participation of Pt NPs in carbon corrosion.....</b>	<b>26</b>

<b>2.5</b>	<b>Protecting the PEMFC Catalyst Layer from Corrosion</b> .....	<b>27</b>
<b>2.5.1</b>	<b>Non-carbon PEMFC catalyst support materials</b> .....	<b>28</b>
<b>2.5.1.1</b>	<i>Metal Oxides</i> .....	<b>29</b>
<b>2.5.1.2</b>	<i>Metal Carbides</i> .....	<b>31</b>
<b>2.5.1.3</b>	<i>Metal Nitrides</i> .....	<b>31</b>
<b>2.5.2</b>	<b>Non-carbon materials as co-supports to carbon</b> .....	<b>32</b>
<b>2.5.3</b>	<b>Protecting the cathode catalyst layer from corrosion by protecting the anode</b> 34	
<b>2.6</b>	<b>Protocols for Evaluation of Catalyst Layer Degradation</b> .....	<b>34</b>
<b>2.7</b>	<b>Oxygen Reduction Reaction (ORR)</b> .....	<b>37</b>
<b>2.7.1</b>	<b>Relevant electrochemistry of the ORR</b> .....	<b>38</b>
<b>2.8</b>	<b>Hydrogen Oxidation Reaction (HOR)</b> .....	<b>40</b>
<b>2.9</b>	<b>Evaluation of Electrocatalyst Activity</b> .....	<b>44</b>
<b>2.10</b>	<b>Catalyst Layer Nanostructuring by Anodization</b> .....	<b>46</b>
<b>Chapter 3</b>	<b>: Experimental Methods</b> .....	<b>54</b>
<b>3.1</b>	<b>Preparation of Ta oxide samples</b> .....	<b>54</b>
<b>3.1.1</b>	<b>Anodization of Ta metal</b> .....	<b>54</b>
<b>3.1.1.1</b>	<i>Preparation of Ta oxide compact layers (CLs)</i> .....	<b>55</b>
<b>3.1.1.2</b>	<i>Preparation of Ta oxide nanotubes (NTs)<sup>15-16</sup></i> .....	<b>56</b>
<b>3.2</b>	<b>Preparation of Ta oxynitride (TaO<sub>x</sub>N<sub>y</sub>) samples</b> .....	<b>56</b>
<b>3.3</b>	<b>Deposition of Pt nanoparticles (NPs) on TaO<sub>x</sub>N<sub>y</sub> CLs and NTs<sup>157</sup></b> .....	<b>57</b>
<b>3.4</b>	<b>Preparation of colloid imprinted carbon (CIC) based materials</b> .....	<b>57</b>
<b>3.4.1</b>	<b>Synthesis of CIC100</b> .....	<b>57</b>
<b>3.4.2</b>	<b>Synthesis of TaO<sub>x</sub> NPs on CIC100 (TaO<sub>x</sub>N<sub>y</sub> NPs/CIC100)</b> .....	<b>59</b>
<b>3.4.3</b>	<b>Synthesis of TaO<sub>x</sub>N<sub>y</sub> NPs on CIC100 (TaO<sub>x</sub>N<sub>y</sub> NPs/N-CIC100)</b> .....	<b>60</b>
<b>3.4.4</b>	<b>Synthesis of CIC100 treated with benzyl alcohol (BnOH)</b> .....	<b>60</b>
<b>3.4.5</b>	<b>Synthesis of nitrogen-doped CIC100 (N-CIC100)</b> .....	<b>61</b>

3.4.6	Synthesis of Pt NPs on TaO <sub>x</sub> N <sub>y</sub> NPs/N-CIC100 material .....	61
3.5	Electrochemical Characterization of Samples .....	61
3.5.1	Buffer and electrolyte solution preparation .....	61
3.5.2	Instruments and general experimental methods.....	62
3.5.3	Working Electrodes (WE).....	63
3.5.3.1	<i>Working electrodes made with Ta foils or rods</i> .....	63
3.5.3.2	<i>Glassy Carbon (GC) working electrodes made with CIC100-based materials</i> .....	63
3.5.4	Corrosion Evaluation Protocols.....	66
3.5.4.1	<i>Corrosion Evaluation protocol based on CV</i> .....	66
3.5.4.2	<i>Corrosion evaluation protocol based on potentiostatic ADT</i> .....	68
3.6	Material Characterization Techniques .....	70
3.6.1	Field Emission Scanning Electron Microscopy/Energy Dispersive X-Ray Spectroscopy (FESEM/EDX) Analysis .....	70
3.6.2	Transmission Electron Microscopy/ Energy Dispersive X-Ray Spectroscopy (TEM/EDX) .....	71
3.6.3	X-Ray Photoelectron Spectroscopy (XPS).....	72
3.6.4	X-Ray Diffraction (XRD) .....	73
3.6.5	Diffuse reflectance UV-Visible Spectroscopy (DRUV-Vis) .....	74
3.6.6	Elemental Analysis (EA).....	74
3.7	Error Analysis .....	75
Chapter 4	: General Electrochemical Characteristics of TaO <sub>x</sub> N <sub>y</sub> Nanotubes.....	77
4.1	Introduction.....	77
4.2	Results and Discussion.....	79
4.2.1	<i>Morphology and composition of Ta<sub>2</sub>O<sub>5</sub> and TaO<sub>x</sub>N<sub>y</sub> nanotubes (NTs):</i> .....	79
4.2.2	Electrochemistry of TaO <sub>x</sub> N <sub>y</sub> NTs .....	89
4.2.2.1	<i>Cyclic Voltammetry (CV)</i> .....	89
4.2.2.2	<i>Electrochemical impedance spectroscopy (EIS)</i> .....	98

4.2.3	Electrochromic response .....	110
4.3	Summary.....	112
<b>Chapter 5 : Evaluation of TaO<sub>x</sub>N<sub>y</sub> nanotubes for use in PEM Fuel Cell Cathode Catalyst Layers.....115</b>		
5.1	Introduction.....	115
5.2	Results and Discussion.....	117
5.2.1	Structure, Morphology and Compositional Characterization.....	117
5.2.1.1	<i>Compact TaO<sub>x</sub>N<sub>y</sub> Layer (CL)</i> .....	117
5.2.1.2	<i>Pt nanoparticle-loaded TaO<sub>x</sub>N<sub>y</sub> Nanotubes (NTs)</i> .....	119
5.2.2	Oxygen reduction at.....	124
5.2.2.1	<i>ORR at TaO<sub>x</sub>N<sub>y</sub> compact layer coated with Pt NPs (Pt NPs/ TaO<sub>x</sub>N<sub>y</sub> CL)</i> .....	124
5.2.2.2	<i>Electrochemistry and ORR at TaO<sub>x</sub>N<sub>y</sub> NTs (~1 μm in length)</i> .....	129
5.2.2.3	<i>Electrochemistry and ORR at Pt NP decorated shorter (0.3 μm) TaO<sub>x</sub>N<sub>y</sub> NTs</i> .....	147
5.2.2.4	<i>Summary of Section 5.2.2</i> .....	149
5.2.3	Corrosion Stability of TaO <sub>x</sub> N <sub>y</sub> NTs and Pt NPs/TaO <sub>x</sub> N <sub>y</sub> NTs composite	152
5.2.3.1	<i>Corrosion resistance of 1 μm TaO<sub>x</sub>N<sub>y</sub> NTs without Pt</i> .....	154
5.2.3.2	<i>Corrosion resistance of Pt NP-loaded TaO<sub>x</sub>N<sub>y</sub> NTs</i> .....	158
5.3	Summary.....	161
<b>Chapter 6 : Electrochemistry of TaO<sub>x</sub>N<sub>y</sub> NPs (with/without Pt) mixed with Carbon Powder .....</b>		
<b>Chapter 6 : Electrochemistry of TaO<sub>x</sub>N<sub>y</sub> NPs (with/without Pt) mixed with Carbon Powder .....</b>		
6.1	Introduction.....	163
6.2	Results and Discussion.....	166
6.2.1.	Structure, Morphology and Composition of Mixtures of TaO <sub>x</sub> or TaO <sub>x</sub> N <sub>y</sub> with CIC100 Powder .....	166
6.2.2	Electrochemistry of CIC100, TaO <sub>x</sub> NPs/CIC100, TaO <sub>x</sub> N <sub>y</sub> NPs/N-CIC100, Bn-CIC100 and N-CIC100, all in the absence of Pt.....	177
6.2.2.1	<i>Cyclic Voltammetry analysis of carbon-based materials (no Pt)</i> ..	179

6.2.2.2	<i>Potentiostatic ADT analysis of carbon-based materials without Pt</i>	188
6.2.3	Structure, Morphology, and Composition of Pt NPs/TaO <sub>x</sub> N <sub>y</sub> NPs/N-CIC100 Catalysts.....	196
6.2.4	Electrochemistry of Pt NPs/TaO <sub>x</sub> N <sub>y</sub> NPs/N-CIC100 material.....	197
6.3	Summary.....	202
<b>Chapter 7 : Hydrogen Oxidation Reaction at TaO<sub>x</sub>N<sub>y</sub> Nanotubes With/Without Pt Nanoparticles.....</b>		
7.1	Introduction.....	205
7.2	Results and Discussion.....	208
7.2.1	Structure, Morphology and Compositional Characterization of TaO <sub>x</sub> N <sub>y</sub> NTs with and without Pt NPs.....	208
7.2.2	HOR at TaO <sub>x</sub> N <sub>y</sub> NTs with and without Pt NPs.....	209
7.3	Summary.....	216
<b>Chapter 8 Conclusions and Future Work .....</b>		
8.1	Conclusions.....	218
8.1.1	Physiochemical properties of TaO <sub>x</sub> N <sub>y</sub> NTs in comparison to the precursor Ta <sub>2</sub> O <sub>5</sub> NTs.....	218
8.1.2	TaO <sub>x</sub> N <sub>y</sub> NTs (with and without Pt NPs) as ORR and HOR catalysts and as catalyst support materials .....	219
8.1.3	TaO <sub>x</sub> N <sub>y</sub> mixed with carbon nanomaterials.....	221
8.2	Suggestions for Future Work.....	223
<b>References .....</b>		
<b>Appendix.....</b>		
<b>Copy right permission .....</b>		

## List of Tables

Table 2.1 Comparison of Fuel Cell Technologies <sup>27</sup> .....	12
Table 2.2 ORR in different solutions .....	37
Table 4.1 Values of circuit elements for TaO <sub>x</sub> N <sub>y</sub> NTs studied by EIS in 0.5 M H <sub>2</sub> SO <sub>4</sub> solution and employing the equivalent circuits shown in Figure 4.11 <sup>a</sup> . .....	106
<b>Table 4.2</b> Values of circuit elements for Ta oxide NTs studied by EIS in 0.5 M H <sub>2</sub> SO <sub>4</sub> solution and employing the equivalent circuit (a) shown in Figure 4.11. ....	107
Table 4.3 Values of circuit elements obtained for TaO <sub>x</sub> N <sub>y</sub> NTs by EIS in phosphate buffer solution and employing the equivalent circuits shown in Figure 4.11 <sup>a</sup> . ....	108
<b>Table 5.1</b> Cathodic ORR Tafel slopes for the data shown in Figure 5.9b and d* .....	143
Table 5.2 Summary of salient electrochemical results for the ORR of Pt NPs deposited TaO <sub>x</sub> N <sub>y</sub> CL and TaO <sub>x</sub> N <sub>y</sub> NTs (1 μm and 0.3 μm in length) .....	151
Table 6.1 Elemental analysis of the CIC100, Bn-CIC100, N-Bn-CIC100, TaO <sub>x</sub> NPs/CIC100, and TaO <sub>x</sub> N <sub>y</sub> NPs/N-CIC100 materials .....	175
Table 6.2 The full width at half maximum for the PC peaks that are seen in the Figure 6.8. ....	182
<b>Table 6.3</b> Pseudocapacitance (PC) and Double Layer (DL) charges from CVs for the carbon-based materials before and after ADT .....	184

## List of Figures and Illustrations

Figure 2.1 Classification of current FC systems, showing typical operating temperatures, fuel feeds and reactants/products, where possible. <sup>9</sup> .....	11
Figure 2.2 Schematic of a single cell within a PEMFC stack. <sup>28</sup> .....	14
Figure 2.3 (a) SEM image of MEA and (b) TEM image of the Pt/C catalyst layer along with the particle size distribution histogram. <sup>31-32</sup> .....	15
Figure 2.4 (a) Chemical structure of Nafion <sup>®</sup> and (b) cluster network model of Nafion <sup>®</sup> in a PEMFC. ....	17
Figure 2.5 Breakdown of the 2017 automotive PEM fuel cell stack cost. <sup>11</sup> .....	18
Figure 2.6 (a) CL degradation in PEMFCs. After 2259 h of operation, (b) shows SEM images of the MEA and (c) shows a TEM image of the Pt/C catalyst layer, along with the Pt NP size distribution histogram. <sup>31-32</sup> .....	21
Figure 2.7 A schematic of reverse current generation at the H <sub>2</sub> /O <sub>2</sub> front in a PEMFC during shut-down and start-up. <sup>66</sup> .....	24
Figure 2.8 Dual site ORR mechanism on Pt surfaces. ....	40
Figure 2.9 Volcano plot for Metal-Hydrogen (M-H) bond strength. <sup>123</sup> .....	41
Figure 2.10 Possible steps involved in the HOR and HER. * denotes a site on the surface where the reaction occurs.....	43
Figure 2.11 Anodization of valve metals to produce nanopores and nanotubes. <sup>148</sup> .....	49
Figure 2.12 (1) Ta oxide NTs made by anodization of Ta at 15 V vs. Pt CE in 16.4 M H <sub>2</sub> SO <sub>4</sub> + (a) 0.51 M, (b) 0.85 M, (c) 1.17 M HF for 10 min and (d) NT's length as a function of time in 16.4 M H <sub>2</sub> SO <sub>4</sub> + 0.51 M HF <sup>16</sup> , (2) Short Ta oxide NTs formed by anodization of Ta at 15 V vs. Pt CE in 16 M H <sub>2</sub> SO <sub>4</sub> + 0.6 M HF for 23.9 seconds <sup>17</sup> , (3) 2 μm long Zr oxide NTs formed by two step anodization of Zr. First step at 20 V vs. Pt CE in 1 M [(NH <sub>4</sub> ) <sub>2</sub> SO <sub>4</sub> and 4.5 % wt NH <sub>4</sub> F for 30 min and the second step at 10 V vs. Pt CE in 1 M [(NH <sub>4</sub> ) <sub>2</sub> SO <sub>4</sub> and 0.5 % wt NH <sub>4</sub> F for 5 min <sup>153</sup> , and (4) Au NPs were made on the Ta oxide dimples (formed after detaching Ta oxide NTs) by dewetting. 3-4 nm sputter Au thin film is annealed in N <sub>2</sub> environment for 30 min at 450 °C <sup>21</sup> .....	52
Figure 3.1 Anodization set-up used for preparing Ta oxide compact layers and nanotubes. ....	55
Figure 3.2 Synthesis scheme for CIC100. ....	59
Figure 3.3 Ink spreading onto the shroud of the GC electrode. <sup>165</sup> .....	65

Figure 3.4 Graphical representation showing the potential range over which the double layer (DL) and pseudocapacitance (PC) features are seen and how charges were obtained from the CVs of the carbon-based materials under study here. ....	67
Figure 3.5 (a) E vs. t program used for corrosion evaluation of catalysts and supports, based on the potentiostatic ADT. Steady-state CVs were collected before and after potential stepping, as shown in (b) and (d), respectively. (c) shows the I vs t transient for one cycle of potentiostatic stepping (1.4 V for 50 s and 0.8 V for 10 s). ....	69
Figure 3.6 Schematic diagram of the Zeiss Sigma VP SEM at the University of Calgary. <sup>168</sup> .....	70
Figure 4.1 (a) Typical current density vs. time curve obtained during Ta oxide NT preparation. The inset shows the expansion of the first few seconds of the i vs. t results, with (b) showing a comparison of the i vs. t data obtained here relative to the literature. 140 .....	80
Figure 4.2 (a) High magnification FESEM image of Ta oxide nanotubes at a ‘crack’ in the film (annealed at 450 °C for 30 min), with the inset showing the same crack, but at a lower magnification, (b) FESEM image of TaO <sub>x</sub> N <sub>y</sub> nanotubes at a ‘crack’ in the film after formation by ammonolysis of Ta oxide, with the inset showing the top view of the same film, (c) TEM image of the base of two Ta oxide nanotubes, and (d) TEM image of a few TaO <sub>x</sub> N <sub>y</sub> nanotubes, showing periodic holes in their walls.....	83
Figure 4.3 Single Ta oxide NT formed after annealing the Ta oxide nanotubes in N <sub>2</sub> at 700 °C for 7 h at a flow rate of 10 ml·min <sup>-1</sup> . Inset shows the FFT pattern of the nanoarray of Ta oxide NTs.....	85
Figure 4.4 Top-down XPS analysis of Ta <sub>2</sub> O <sub>5</sub> and TaO <sub>x</sub> N <sub>y</sub> nanotubular array (ca. 1 μm thick) on a Ta substrate, showing the (a) Ta 4f, (b) O 1s, and (c) N 1s spectra, as well as (d) depth profile XPS analysis of a 1μm film of TaO <sub>x</sub> N <sub>y</sub> NTs.....	86
Figure 4.5 Powder XRD experimental and fitting pattern for TaO <sub>x</sub> N <sub>y</sub> NTs. The PXRD data sets were refined by LeBail refinement using the General Structure Analysis System (GSAS) package with the EXPGUS interface to obtain the cell parameters of Ta (Pearson Crystal Structure code 261169), TaN <sub>0.1</sub> (Pearson Crystal Structure code 531979) and Ta <sub>3</sub> N <sub>x</sub> O <sub>y</sub> (Pearson Crystal Structure code 1409825). The background, zero-point position, cell parameters, and profile coefficients for the Pseudo-Voigt/Finger–Cox–Jephcoat (FCJ) asymmetric peak function were refined until convergence was achieved. ....	88
Figure 4.6 CVs (50 mV·s <sup>-1</sup> ) of TaO <sub>x</sub> N <sub>y</sub> NTs in (a) 0.5 M H <sub>2</sub> SO <sub>4</sub> (black ), pH 7 PB solution (red) and 0.5 M KOH (green) and those for the Ta oxide NTs in 0.5 M H <sub>2</sub> SO <sub>4</sub> (blue), pH 7 PB solution (magenta) and 0.5 M KOH (yellow). All of these CVs were collected for the same TaO <sub>x</sub> N <sub>y</sub> or Ta oxide samples. (b) and (c) are CVs obtained at 50 mV·s <sup>-1</sup> at variable cathodic switching potentials for the same TaO <sub>x</sub> N <sub>y</sub> NTs in 0.5 M H <sub>2</sub> SO <sub>4</sub> and PB solutions, respectively. (d) shows the CVs (50 mV·s <sup>-1</sup> ) obtained for the TaO <sub>x</sub> N <sub>y</sub> NTs in	

anhydrous acetonitrile using 0.1 M tetra-n-butylammonium hexafluorophosphate as the electrolyte and a Ag/Ag <sub>2</sub> O pseudo-reference electrode. ....	91
Figure 4.7 Logarithm of anodic peak current vs. logarithm of scan rate ( $\nu$ ) for TaO <sub>x</sub> N <sub>y</sub> NTs in (a) 0.5 M H <sub>2</sub> SO <sub>4</sub> and (b) pH 7 PBS. Solid lines are best fit lines. (c) and (d) show the CVs obtained at various scan rates for TaO <sub>x</sub> N <sub>y</sub> NTs in 0.5 M H <sub>2</sub> SO <sub>4</sub> and pH 7 PBS, respectively. ....	94
Figure 4.8 TaO <sub>x</sub> N <sub>y</sub> NTs as a function of anodization times of (a) 2.5 min, (b) 7.5 min, and (c) 10 min, and (d) nanodimples covered by TaO <sub>x</sub> N <sub>y</sub> compact film. ....	97
<b>Figure 4.9</b> (a) CV response of the TaO <sub>x</sub> N <sub>y</sub> NTs as a function of their length, all in deaerated 0.5 M H <sub>2</sub> SO <sub>4</sub> at 50 mV·s <sup>-1</sup> . (b) Average charge obtained from the CV redox features in (a) for the NTs and also for the case when the NTs were removed from the surface ('0 anodization time'). ....	98
Figure 4.10 (a) and (b) Nyquist plots obtained for the TaO <sub>x</sub> N <sub>y</sub> NTs at various potentials vs. the reference electrode in (a) 0.5 M H <sub>2</sub> SO <sub>4</sub> , and (b) in the PB solution, and (c) Nyquist plots for Ta <sub>2</sub> O <sub>5</sub> NTs in 0.5 M H <sub>2</sub> SO <sub>4</sub> for comparison with (a). Symbols are experimental data while solid lines are fitted data. (d) shows the comparison CV (50 mV/s) of the Ta <sub>2</sub> O <sub>5</sub> NTs and TaO <sub>x</sub> N <sub>y</sub> NTs in the potential range of 0.8-1.5 V in 0.5 M H <sub>2</sub> SO <sub>4</sub> . Insets in (a) and (b) show Nyquist plots obtained at more cathodic potentials. ....	101
Figure 4.11 (a) and (b) Bode plots obtained for the TaO <sub>x</sub> N <sub>y</sub> NTs at various applied potentials in (a) 0.5 M H <sub>2</sub> SO <sub>4</sub> and in (b) PB solution, and (c) Bode plots obtained for the Ta <sub>2</sub> O <sub>5</sub> NTs in 0.5 M H <sub>2</sub> SO <sub>4</sub> , for comparison with (a). Figures at top are for the total impedance (Z) and figures at bottom of for the phase angle. Symbols are experimental data while solid lines are fitted data. ....	102
Figure 4.12 (a), (b) and (c) show the equivalent circuits used to fit the EIS experimental data.	103
Figure 4.13 Diffuse reflectance UV-Visible analysis of Ta oxide and TaO <sub>x</sub> N <sub>y</sub> NTs, with the data obtained using a Cary 5000 double beam scanning spectrophotometer, equipped with a diffuse reflectance accessory. ....	105
Figure 4.14 Mott-Schottky (MS) plots obtained for TaO <sub>x</sub> N <sub>y</sub> NTs in 0.5 M H <sub>2</sub> SO <sub>4</sub> at various perturbation frequencies (a) and an MS plot of the same material using capacitance values from CNLS fitting (b). ....	110
Figure 5.1 (a) and (b) FESEM images of TaO <sub>x</sub> N <sub>y</sub> CL and Pt NPs/TaO <sub>x</sub> N <sub>y</sub> CL, respectively, while (c) shows the EDX spectrum of the Pt NPs/ TaO <sub>x</sub> N <sub>y</sub> CL. ....	119
Figure 5.2. Top view SEM images of TaO <sub>x</sub> N <sub>y</sub> NTs (anodized for 5 min, giving 1 $\mu$ m long nanotubes) before (a) and after (b and c) the deposition of Pt on these NTs. (d) TaO <sub>x</sub> N <sub>y</sub> NTs (anodized for 2.5 min, giving ca. 0.3 $\mu$ m long tubes), viewed from within a crack in the NT film. ....	121

Figure 5.3 (a) TEM image and (b) histogram of the Pt NPs in the Pt NPs/TaO <sub>x</sub> N <sub>y</sub> NTs composite. ....	122
Figure 5.4 EDX spectrum of Pt NPs/TaO <sub>x</sub> N <sub>y</sub> NTs composite. ....	123
Figure 5.5 (a) CVs obtained in quiescent 0.5 M H <sub>2</sub> SO <sub>4</sub> at 10 mV·s <sup>-1</sup> in N <sub>2</sub> (blue) and O <sub>2</sub> (red) saturated conditions, also showing the difference between these two CVs (green) for the Pt NPs/TaO <sub>x</sub> N <sub>y</sub> CL material. (b) shows the cathodic scan Tafel plot obtained from (a) between 0.7-0.9 V at 10 mV·s <sup>-1</sup> , while (c) shows the CVs at various scan rates (0.01, 0.05, 0.2, 0.6, and 1 V·s <sup>-1</sup> ) in O <sub>2</sub> -saturated 0.5 M H <sub>2</sub> SO <sub>4</sub> . (d) shows the ORR activity of TaO <sub>x</sub> N <sub>y</sub> CL without Pt. Note: The currents in all of the CVs have been divided by the geometrical area of the electrode. ....	127
Figure 5.6 (a and c) CVs obtained at 10 mV·s <sup>-1</sup> in 0.5 M H <sub>2</sub> SO <sub>4</sub> saturated with N <sub>2</sub> (blue) or O <sub>2</sub> (red), and the subtracted CV (red minus blue = green) for (a) TaO <sub>x</sub> N <sub>y</sub> NTs and (c) Pt NPs/ TaO <sub>x</sub> N <sub>y</sub> , with Pt NPs deposited by the incipient impregnation method. (b) CVs obtained in N <sub>2</sub> -saturated acid for TaO <sub>x</sub> N <sub>y</sub> NTs and Pt NPs/ TaO <sub>x</sub> N <sub>y</sub> NTs, as well as the subtracted CV. Inset shows double layer charging region. Pt NPs were deposited on the NTs by incipient impregnation method. (d) shows the Tafel plot for the ORR in the cathodic scan at the Pt NPs/ TaO <sub>x</sub> N <sub>y</sub> NTs [data from (c)]. Note: All currents have been divided by the geometric area of the electrode. ....	131
Figure 5.7 Cathodic peak current (at -0.3 V vs RHE) vs. scan rate and square root of scan rate for Pt NPs/TaO <sub>x</sub> N <sub>y</sub> NTs in O <sub>2</sub> -saturated 0.5 M H <sub>2</sub> SO <sub>4</sub> solution (see Figure 5.6c). ....	138
Figure 5.8 (a) RDE set up and (b) the RDE tip, with the electrode shrouded in an insulating layer. <sup>239</sup> .....	139
Figure 5.9 CVs obtained at 0.05 -1.1 V vs RHE for the Pt NPs/TaO <sub>x</sub> N <sub>y</sub> NTs at 10 mV·s <sup>-1</sup> at various RDE rotation rates in (a) N <sub>2</sub> -saturated 0.5 M H <sub>2</sub> SO <sub>4</sub> and (b) O <sub>2</sub> -saturated 0.5 M H <sub>2</sub> SO <sub>4</sub> after subtracting the data from N <sub>2</sub> -saturated electrolyte. (c) Cathodic scan Tafel plot for the ORR at the Pt NPs/TaO <sub>x</sub> N <sub>y</sub> NTs from the data in (b). (d) CVs obtained in N <sub>2</sub> and O <sub>2</sub> saturated 0.5 M H <sub>2</sub> SO <sub>4</sub> without rotation, as well as subtracted data. Note: all currents are corrected for WE geometrical area.....	141
Figure 5.10 CVs obtained for the Pt NPs/TaO <sub>x</sub> N <sub>y</sub> NTs composite over the extended potential range of -0.05 to 1.1 V vs RHE in N <sub>2</sub> -saturated and O <sub>2</sub> -saturated 0.5 M H <sub>2</sub> SO <sub>4</sub> solutions at 10 mV·s <sup>-1</sup> (a) at various rotation speeds and (b) without electrode rotation. (c) and (d) are Koutecky-Levich plots at 0.35 V and 0.8 V vs. RHE, respectively.....	146
Figure 5.11 CVs obtained at 10 mV·s <sup>-1</sup> in N <sub>2</sub> and O <sub>2</sub> saturated 0.5 M H <sub>2</sub> SO <sub>4</sub> for (a) Pt NPs/TaO <sub>x</sub> N <sub>y</sub> NTs (shorter length of 0.3 μm), where the Pt NPs were deposited on the NTs by the incipient impregnation method, and (b) the cathodic scan Tafel plot for the ORR at this material. (c) shows the CVs obtained in N <sub>2</sub> -saturated 0.5 M H <sub>2</sub> SO <sub>4</sub> for both shorter (0.3 μm) and longer (1 μm) TaO <sub>x</sub> N <sub>y</sub> NTs decorated with Pt NPs. Current is	

normalized to geometrical area of the electrode. (d) CV responses of the 20 wt % Pt/C catalyst in N<sub>2</sub> (black) and O<sub>2</sub> (red) saturated 0.5 M H<sub>2</sub>SO<sub>4</sub> at 10 mV·s<sup>-1</sup> scan rate.<sup>242</sup> ..... 148

Figure 5.14 Accelerated durability test (ADT) used for the testing of the TaO<sub>x</sub>N<sub>y</sub> NTs in 0.5 M H<sub>2</sub>SO<sub>4</sub>. (a) 2<sup>nd</sup> and 100<sup>th</sup> CVs obtained at 10 mV·s<sup>-1</sup>, (b) 66 cycles (note a break in the x axis) of potential stepping (pstep), and (c) corrosion charges obtained from the pstep experiment. The corrosion charges were calculated by taking the difference between q<sup>+</sup> and q<sup>-</sup> ..... 156

Figure 5.15 Accelerated durability test (ADT) results for Vulcan carbon (VC) in 0.5 M H<sub>2</sub>SO<sub>4</sub>. (a) Corrosion charges related to pstep experiment (18 Cycles). Corrosion charges are calculated by taking the difference between q<sup>+</sup> and q<sup>-</sup>. (b) CVs (10 mV/s) obtained for the same material before and after the pstep experiment.<sup>164</sup> ..... 158

Figure 5.16 Results of accelerated durability testing (ADT) of Pt NPs/TaO<sub>x</sub>N<sub>y</sub> NTs in 0.5 M H<sub>2</sub>SO<sub>4</sub>. (a) CVs obtained at 10 mV·s<sup>-1</sup> before and after potential stepping experiment and (b) corrosion charge as a function of step number in the ADT experiment for Pt NPs/TaO<sub>x</sub>N<sub>y</sub> NTs and TaO<sub>x</sub>N<sub>y</sub> NTs ..... 160

Figure 6.1 HRTEM images of CIC100 (a) showing part of a CIC100 particle and (b) a higher magnification image of the CIC100 particle, where the diameter of the pores can be seen clearly ..... 167

**Figure 6.2** Synthesis route for the formation of the TaO<sub>x</sub> NPs/CIC100 composite, showing the possible interactions between Ta(OEt)<sub>5</sub> and CIC100 and the formation of the TaO<sub>x</sub> NPs/CIC100 material. .... 170

**Figure 6.3** HRTEM images of N-CIC100 with (a) showing part of an N-CIC100 particle and (b) showing the high magnification image of the CIC100 particle, where the diameter of the pores can be seen clearly ..... 172

Figure 6.4 HRTEM images of the (a) TaO<sub>x</sub> NPs/CIC100 (1:3 w:w) and (b) TaO<sub>x</sub>N<sub>y</sub> NPs/N-CIC100 (1:3 w:w) powders ..... 174

Figure 6.5 PXRD pattern of Bn-CIC100 and N-CIC100, showing the graphite peak of 002 at 2θ = 25° ..... 176

Figure 6.6 PXRD data, after refinement, for the (a) TaO<sub>x</sub> NPs/CIC100 and (b) TaO<sub>x</sub>N<sub>y</sub> NPs/N-CIC100 powder samples. The PXRD data sets were refined using the LeBail refinement method, using the General Structure Analysis System (GSAS) package with an EXPGUS interface to obtain the cell parameters of (a) Ta<sub>2</sub>O<sub>5</sub> and (a), β-TaON and Ta<sub>3</sub>O<sub>x</sub>N<sub>y</sub> ..... 177

Figure 6.7 Graphical representation showing the potential range of the double layer (DL) and pseudocapacitance (PC) and how charges were obtained from the CVs of the carbon-based materials under study here. .... 178

Figure 6.8 Steady-state CVs of the materials under investigation here, before and after the potentiostatic ADT. The name of the material is shown in the respective CVs and also (a) to (e) naming is given for more clarification (a) CIC100, (b) Bn-CIC100, (c) N-CIC100, (d) TaO <sub>x</sub> NPs/CIC100 and (e) TaO <sub>x</sub> N <sub>y</sub> NPs/N-CIC100. All CVs were obtained in deaerated 0.5 M H <sub>2</sub> SO <sub>4</sub> at 10 mV·s <sup>-1</sup> and all of the currents were normalized to the carbon weight.....	181
Figure 6.9 Comparison of the (a) corrosion charge (Equation 3.1), (b) anodic charge (q <sup>+</sup> ) and (c) cathodic charge (q <sup>-</sup> ) for the materials under study here. Note: The TaO <sub>x</sub> N <sub>y</sub> NPs/N-CIC100 material is named TaON/CIC100 and TaO <sub>x</sub> NPs/CIC100 named TaO NPs/CIC100 in the legend. ....	190
Figure 6.10 Black trace is the cathodic segment immediately after ADT potentiostatic step, red trace is the 1 <sup>st</sup> full CV between 0.05 V to 1.1 V and blue is the steady state (S-S) CV for Bn-CIC100 in 0.5 M H <sub>2</sub> SO <sub>4</sub> at a scan rate of 10 mV·s <sup>-1</sup> . The ‘before corrosion’ steady state CV is given in Figure 6.8. ....	194
Figure 6.11 FESEM images of TaO <sub>x</sub> N <sub>y</sub> NPs/N-CIC100 (a) before and (b) after the potentiostatic step ADT experiments.....	195
Figure 6.12 TEM images of (a) Pt NPs/N-CIC100 and (b) Pt NPs/TaO <sub>x</sub> N <sub>y</sub> NPs/N-CIC100 composites.....	197
Figure 6.13 CVs before and after potentiostatic step ADT of (a) Pt NPs/TaO <sub>x</sub> N <sub>y</sub> NPs/N-CIC100, (b) and (c) Pt NPs/TaO <sub>x</sub> N <sub>y</sub> NPs/N-CIC100, TaO <sub>x</sub> N <sub>y</sub> NPs/N-CIC100 and N-CIC100, respectively. All CVs were obtained in 0.5 M H <sub>2</sub> SO <sub>4</sub> at 10 mV·s <sup>-1</sup> . Note: All currents and charges are normalized to the carbon weight. ....	199
Figure 6.14 Comparison of normalized corrosion charge (q <sup>+</sup> -q <sup>-</sup> , green), cathodic charge (q <sup>-</sup> , blue), and anodic charge (q <sup>+</sup> , red) for the Pt NPs/TaO <sub>x</sub> N <sub>y</sub> NPs/N-CIC100 material.....	201
Figure 7.1 CVs of (a) TaO <sub>x</sub> N <sub>y</sub> NTs and (b) Pt NPs/TaO <sub>x</sub> N <sub>y</sub> NTs composite at 50 mV·s <sup>-1</sup> obtained in quiescent 0.5 M H <sub>2</sub> SO <sub>4</sub> . The red CVs were obtained in H <sub>2</sub> -saturated acid solution and the blue CVs were in N <sub>2</sub> -saturated solution. The green CVs represent the subtraction of those two CVs. The inset of (a) shows subtracted CV of TaO <sub>x</sub> N <sub>y</sub> NTs.....	210
Figure 7.2 CVs (anodic scan only) of Pt NPs/TaO <sub>x</sub> N <sub>y</sub> NTs obtained at 10 mV·s <sup>-1</sup> in (a) N <sub>2</sub> -saturated purged 0.5 M H <sub>2</sub> SO <sub>4</sub> and (b) H <sub>2</sub> -saturated purged 0.5 M H <sub>2</sub> SO <sub>4</sub> , and (c) the relevant Koutecky-Levich plots at various potentials for the data in the (b).....	214

## List of Symbols, Abbreviations and Nomenclature

Symbol	Definition
$i_o$	Exchange current density
$\alpha$	Transfer coefficient
$\eta = E - E_{eq}$	Overpotential
F	Faraday constant
R	Universal gas constant
T	Temperature
$i_p$	Peak current
n	Stoichiometric number of electrons involved in a redox reaction
A	Geometrical surface area of the electrode
D	Diffusion coefficient
C	Concentration
v	Linear potential scan rate
$\omega$	Angular frequency of rotation
$i_K$	Kinetic current
$i_l$	Limiting current

v	Kinematic viscosity or frequency
RHE	Reversible Hydrogen Electrode
CL	Catalyst layer or Compact layer
ADT	Accelerated Durability Test
NT	Nanotubes
NP	Nanoparticles
TS	Tafel Slope
BV	Butler-Volmer
OER/ORR	Oxygen Evolution or Reduction Reaction
HER/HOR	Hydrogen Evolution or Oxidation reaction
COR	Carbon Oxidation Reaction
DL	Double layer
PC	Pseudocapacitance



## **Chapter 1 : Nanostructured Ta-Based Materials for Fuel Cell Applications**

### **1.1 Relevant Background for the Project**

Currently, one of the most critical problems confronting humanity is the environmental impact arising from greenhouse gas (GHG) emissions, escalated by accelerated industrialization and increasing vehicle use, especially in emerging economies, such as China, India, and Brazil.<sup>1-2</sup> Moving to alternative energy sources having lower or even zero GHG emissions and high fuel conversion efficiency seems to be non-negotiable for our sustainable future. However, the complete conversion of fossil fuel rich energy sources to renewable sources may not be easily achievable.

Furthermore, it is logical to design and construct an infrastructure that relies on more than one energy source. In this regard, electrochemical cells and systems play a vital role as they can be used in empowering technologies, i.e., renewable energy, energy management, conservation, conversion, storage, and pollution control/monitoring (GHG reduction). An established fuel cell technology can play a critical role in increasing the usage of available renewable energy sources, enhancing the energy conversion efficiency associated with the use of fossil fuels, as well as the efficient storage of energy, to name a few key steps that need to be taken to address the future demands of energy usage.

Fuel cells are electrochemical devices that convert chemical energy directly into electrical energy with very high efficiency.<sup>3-5</sup> A thorough discussion about the theory and types of fuel cells is presented in Chapter 2. All fuel cells have common advantages, including a relatively

high operating efficiency, zero or little emission of pollutants, no moving parts, a wide range of fuel options (from fossil fuels to high purity H<sub>2</sub>), and very rapid ‘recharging’ capability.<sup>6</sup> High temperature fuel cells (e.g., solid oxide fuel cells, which operate at 600-800°C) are used primarily in distributed stationary power generation applications, whereas the main applications of low temperature fuel cells, such as proton exchange membrane fuel cells (PEMFCs, which operate at 50-90°C), are in transportation and portable power units, and are also emerging for stationary applications.<sup>3, 5, 7</sup> Of the low temperature fuel cells (< 120 °C), PEMFCs have gained significant attention recently, despite rejection by NASA over 40 years ago for the Apollo Space Mission due to reliability problems.<sup>8</sup> In the last few decades, PEMFCs have made significant advancements and presently offer many attractive features, such as high power density (1 W·cm<sup>-2</sup> at 1.5 A·cm<sup>-2</sup>)<sup>9</sup>, fast start-up, no corrosive liquids, etc.<sup>8</sup>

In most case, FC technologies have to compete with reigning technologies, which are inferior in terms of pollution and efficiency. For example, the comparison of the energy conversion efficiency of PEMFCs with that of ubiquitous internal combustion technologies highlights the importance of moving towards FCs. The efficiency of the PEMFC is in the range of 60-80%, whereas for the heat engine, it is ca. 40%.<sup>4, 8</sup> The incumbent technologies are well developed, produced large scale and hence cost effective. Therefore, adequate acceptance is received by the end-users. Although the incentive for modern society to embrace FC technologies is more societal than economic, the economic factor cannot completely be ignored, thus forcing FC developers to attempt to lower cost and increase durability.

The European Union fuel cell program and the U.S. Department of Energy (DOE) have launched programs to address the key challenges to accelerate the market growth of FC technologies. One of the key issues has been setting targets (key performance indicators, KPI) for their durability by 2020. For PEMFCs, the DOE expects 6,000 h (ultimately 8,000 h) for transportation and 60,000 h for a 5 kW micro-combined heat and power ( $\mu$ -CHP) fuel cell energy system. Similar targets have also been set by the EU FC programme.<sup>10-11</sup> By 2017, the EU fuel cell program for PEMFCs was able to meet its target of 6000 h KPI at the research level, but on the road, efforts to achieve this are still ongoing.<sup>10</sup> The DOE stated in their 2016 annual report that the FC bus program has met its real-world targets, while other automobile sectors have lagged behind.<sup>11</sup> Further, both reports mention that stationary applications are yet to achieve these technical targets, although significant improvements have been continuously made since 2014.<sup>10-11</sup>

The failure of PEMFCs to meet their targets arises from several key contributors, such as catalyst layer and membrane degradation, performance degradation, etc. The catalyst layer degradation causes the Pt nanoparticles (Pt NPs), which are the electrocatalysts for the oxygen reduction reaction (ORR) and the hydrogen oxidation reaction (HOR), to dissolve and sinter. Furthermore, the typical support for the Pt NPs is carbon, which also undergoes corrosion (also called oxidation or electrooxidation), especially during start-up/shutdown of PEMFCs [more details about the carbon corrosion reaction (COR) can be found in Chapter 2, Section 2.4.2].<sup>10-11</sup> Therefore, there is significant interest in developing alternative catalyst supports that are more

stable than carbon. As well, there is an on-going effort to identify new ORR catalyst materials that are lower in cost and are potentially more stable than Pt NPs.

A variety of metals, oxides, nitrides, carbides, borides, mesoporous silica, conducting polymers, and conducting oxides have been considered as alternative PEMFC catalyst supports, as reported in the literature.<sup>12-14</sup> These materials can be used as a single phase support for the cathode (Section 2.5.1) or anode (Section 2.5.3), or as a co-support to carbon, normally consisting of a mixture of the new material, sometime serving as the catalyst (Section 2.3.1), and carbon (Section 2.5.2), which serves as the electronic conductor.<sup>13</sup>

This thesis is focused on investigating an alternative catalyst support based on Ta-based materials to replace the ubiquitous carbon. Also, it explores the possibility that these materials could also serve as a replacement for expensive Pt or Pt alloy catalysts in PEMFCs. Specifically, this thesis has focused on  $\text{TaO}_x\text{N}_y$  as the Ta-based material and to thus understand the physiochemical properties of  $\text{TaO}_x\text{N}_y$ , as little is published in this area. Further, another focus of this work was to determine how these properties can be modified for intended electrochemical applications.

The study of Ta-based nanostructures and determining their potential applications is one of the areas of focus in the Birss research group. Specifically, Ta oxide nanotube (NT) arrays have been formed by Ta anodization, with a good understanding having been reached of the mechanism of NT growth, especially at very short times.<sup>15-17</sup> Interference colours produced by the Ta oxide short NTs (< 500 nm) can be used for the determination of NT length.<sup>18</sup> Notably,

when the Ta oxide NTs are made longer than several microns, they become unstable and are dislodged, leaving behind a nanoarray of Ta nanodimples (NDs) on the Ta substrate.<sup>15, 19-20</sup> These NDs can be used as a model support to study the dewetting of thin metal films, resulting in a nanoarray of metal NPs.<sup>21-23</sup>

It was thus decided to explore these Ta-based nanostructures for PEMFC applications. It is well known that Ta oxide is a high band gap insulator (3.9 eV)<sup>24</sup> and therefore the use of these oxides in a PEMFC would be limited by resistance issues. Therefore, the oxides were converted to TaO<sub>x</sub>N<sub>y</sub>, known to have a low band gap (2.26 eV). The fully nitrated version of Ta oxide is even more conductive than TaO<sub>x</sub>N<sub>y</sub>, but it can undergo oxidation under PEMFC conditions, as shown by the study of other metal nitrides in PEMFC work.

## 1.2 Research Objectives

The primary goal of the thesis work has been to assess Ta oxynitride (TaO<sub>x</sub>N<sub>y</sub>) as a material for use as catalysts and/or catalyst supports for PEMFC applications, potentially replacing Pt and Pt alloys, as well as carbon, respectively. Nanostructuring of TaO<sub>x</sub>N<sub>y</sub> in the form of nanotubes (NTs) and nanoparticles (NPs) is vital because nanostructures are known to give unique behavior as well as to increase the surface area, which is essential for both catalysts and catalyst supports. The precise goals of the thesis are to:

- Synthesize nanostructured TaO<sub>x</sub>N<sub>y</sub> in the forms of compact layers, NTs of various lengths, and NPs.

- Evaluate the electrochemistry and electrocatalytic activity of synthesized TaO<sub>x</sub>N<sub>y</sub> nanostructures for both hydrogen oxidation and oxygen reduction.
- Deposit Pt NPs on the TaO<sub>x</sub>N<sub>y</sub> nanostructures and determine their electrocatalytic activity towards these reactions.
- Establish the benefits of mixing TaO<sub>x</sub>N<sub>y</sub> nanomaterials with carbon powders, specifically colloid imprinted carbons (CICs), for these same electrochemical applications.

### 1.3 Organization of Thesis

This thesis consists of eight chapters. While Chapter 1 briefly introduces the research topic and explains the specific goals of the thesis, Chapter 2 discusses the relevant background and the literature pertaining to this research topic. The experimental techniques and methods used throughout this work are presented in Chapter 3.

The thesis results and related discussion are given from Chapters 4-7. Each of the results chapters consists of a short introduction, a lengthy result and discussion section, and a detailed summary section.

Chapter 4 focuses on the synthesis and characterization of various lengths of TaO<sub>x</sub>N<sub>y</sub> NTs and the results were published in the *Journal of Physical Chemistry C*, 2015, 119, 24, 13847-13857.<sup>25</sup> The work shows that various lengths of Ta oxide NTs can be made changing the time of anodization of Ta metal in aqueous HF and H<sub>2</sub>SO<sub>4</sub> solutions, then converting the Ta oxide to TaO<sub>x</sub>N<sub>y</sub> by high temperature nitriding. It is shown that these materials can be converted from insulating to conducting (and yellow-orange to blue-black in color) at < 0.6 V vs. RHE, in both

aqueous and acetonitrile media, ascribed to the  $\text{Ta}^{4+/5+}$  redox reaction, accompanied by counter ion insertion/de-insertion.

Chapter 5 examines the electrochemical characteristics of the  $\text{TaO}_x\text{N}_y$  NTs (with and without Pt nanoparticles present), also showing their excellent electrochemical stability at high potentials (ca. 1.4 V vs. RHE). A  $\text{TaO}_x\text{N}_y$  compact layer (CL) was also examined in order to ensure that Pt NP electrochemistry, as well as oxygen reduction (ORR) activity, could be seen when these two materials were combined. It is shown that the Pt signature is not seen at the longer (one micron)  $\text{TaO}_x\text{N}_y$  NTs, even though ORR activity is observed, possibly due to inadequate conductivity.

In Chapter 6,  $\text{TaO}_x\text{N}_y$  nanoparticles were used as a co-support along with colloid imprinted carbon (CIC100, having a 100 nm pore diameter) powder for the further investigation of  $\text{TaO}_x\text{N}_y$  as a catalyst support in PEMFCs, with carbon mixed in in order to provide the additional needed conductivity. It was found that the CICs corroded in all of the samples studied, while the Pt NPs, attached primarily to the CIC, did not show evidence of corrosion. Parts of the results in this chapter were published in the *Electrochemical Society Transaction*, 2015, 69(17): 1227-1235.<sup>26</sup>

Chapter 7 discuss the  $\text{TaO}_x\text{N}_y$  NTs, without any carbon but with and without Pt NPs attached, as a hydrogen oxidation (HOR) catalyst support and catalyst, respectively. It is shown that reasonable HOR activity is obtained, but the performance is not on par with standard Pt/carbon catalysts. Interestingly, HOR current is seen even in the potential range where  $\text{TaO}_x\text{N}_y$  should be insulating attributed to the action of hydrogen gas on maintaining a certain population

of Ta<sup>4+</sup>, even at high potentials, thus introducing sufficient conductivity into the TaO<sub>x</sub>N<sub>y</sub> material.

Finally, Chapter 8 summarizes the main conclusions obtained from this thesis work, as well as suggesting some possible future research directions.

## Chapter 2 : Relevant Background Information

### 2.1 Fuel Cells (FCs)

Fuel cells are electrochemical devices that convert chemical energy directly into electrical energy with very high efficiency. They offer an attractive alternative, as incumbent technologies contribute to environmental pollution and are less efficient.<sup>3-7</sup> Fuel cells can be operated on a variety of fuels, such as H<sub>2</sub>, natural gas, methanol, etc. and because of these diverse fuel feeds, FCs are seen as a technology that can be competitive, provide energy security, sustainable and contributing to a clean economy. As mentioned in Chapter 1, the benefits of FCs are immense and include high operating efficiency, zero or little emission of pollutants, no moving parts and hence low maintenance, reliable grid support, very rapid 'recharging' capability, etc.<sup>3-7</sup>

Figure 2.1 shows a typical summary of the fuel cell systems currently commercialized or near to commercialization.<sup>9</sup> This classification is mainly based on the electrolyte type that, in turn, sets the basis for the operating temperature and the fuel type. There are 5 major types of fuel cells, as seen in Figure 2.1, and under the Proton Exchange Membrane Fuel Cells (PEMFCs) category, a sub-category of Direct Methanol Fuel Cells (DMFCs, not seen in Figure 2.1) is normally listed, where methanol (MeOH) is used as the fuel.

In Table 2.1, a comparison of these FC technologies is shown (2016), prepared by the US DOE.<sup>27</sup> It is seen that the flexible fuel choices and broad operating temperatures make FCs a suitable energy option for many sectors (commercial, residential, transportation and industrial). Nevertheless, there are still challenges remaining.

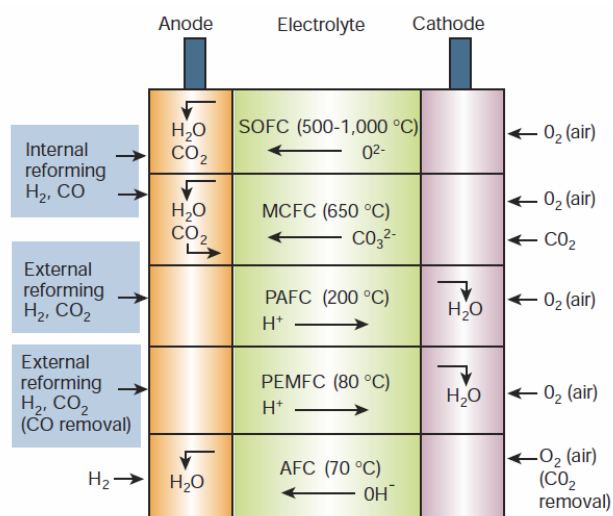


**Figure 2.1** Classification of current FC systems, showing typical operating temperatures, fuel feeds and reactants/products, where possible.<sup>9</sup>

PEMFCs have attracted attention particularly for transportation applications, which run at  $< 120$  °C and require fast start up, frequent shut-down/start-up, and low maintenance. Furthermore, PEMFCs are used for back-up power and increasingly in stationary applications. As mentioned earlier, PEMFCs can be fueled by methanol or H<sub>2</sub> and when fueled by H<sub>2</sub>, they become a major part of the broader hydrogen economy, which is to be fully implemented in the future. However, using methanol as a fuel has the advantage that liquid methanol can be incorporated into the existing fossil fuel infrastructure and thus can be adopted quite easily. Although DMFCs are a viable option to H<sub>2</sub> fuel cells, DMFCs produce a lower mass energy density (19.9 MJ·kg<sup>-1</sup>) than when H<sub>2</sub> is used (120 MJ·kg<sup>-1</sup>).<sup>6</sup>

**Table 2.1** Comparison of Fuel Cell Technologies<sup>27</sup>

Fuel Cell Type	Common Electrolyte	Operating Temperature	Typical Stack Size	Electrical Efficiency (LHV)	Applications	Advantages	Challenges
<b>Polymer Electrolyte Membrane (PEM)</b>	Perfluorosulfonic acid	<120°C	<1 kW - 100 kW	60% direct H <sub>2</sub> , 40% reformed fuel	<ul style="list-style-type: none"> <li>• Backup power</li> <li>• Portable power</li> <li>• Distributed generation</li> <li>• Transportation</li> <li>• Specialty vehicles</li> </ul>	<ul style="list-style-type: none"> <li>• Solid electrolyte reduces corrosion &amp; electrolyte management problems</li> <li>• Low temperature</li> <li>• Quick start-up and load following</li> </ul>	<ul style="list-style-type: none"> <li>• Expensive catalysts</li> <li>• Sensitive to fuel impurities</li> </ul>
<b>Alkaline (AFC)</b>	Aqueous potassium hydroxide soaked in a porous matrix, or alkaline polymer membrane	<100°C	1 - 100 kW	60%	<ul style="list-style-type: none"> <li>• Military</li> <li>• Space</li> <li>• Backup power</li> <li>• Transportation</li> </ul>	<ul style="list-style-type: none"> <li>• Wider range of stable materials allows lower cost components</li> <li>• Low temperature</li> <li>• Quick start-up</li> </ul>	<ul style="list-style-type: none"> <li>• Sensitive to CO<sub>2</sub> in fuel and air</li> <li>• Electrolyte management (aqueous)</li> <li>• Electrolyte conductivity (polymer)</li> </ul>
<b>Phosphoric Acid (PAFC)</b>	Phosphoric acid soaked in a porous matrix or imbed in a polymer membrane	150 - 200°C	5 - 400 kW, 100 kW module (liquid PAFC); <10 kW (polymer membrane)	40%	<ul style="list-style-type: none"> <li>• Distributed generation</li> </ul>	<ul style="list-style-type: none"> <li>• Suitable for CHP</li> <li>• Increased tolerance to fuel impurities</li> </ul>	<ul style="list-style-type: none"> <li>• Expensive catalysts</li> <li>• Long start-up time</li> <li>• Sulfur sensitivity</li> </ul>
<b>Molten Carbonate (MCFC)</b>	Molten lithium, sodium, and/or potassium carbonates, soaked in a porous matrix	600 - 700°C	300 kW - 3 MW, 300 kW module	50%	<ul style="list-style-type: none"> <li>• Electric utility</li> <li>• Distributed generation</li> </ul>	<ul style="list-style-type: none"> <li>• High efficiency</li> <li>• Fuel flexibility</li> <li>• Suitable for CHP</li> <li>• Hybrid/gas turbine cycle</li> </ul>	<ul style="list-style-type: none"> <li>• High temperature corrosion and breakdown of cell components</li> <li>• Long start-up time</li> <li>• Low power density</li> </ul>
<b>Solid Oxide (SOFC)</b>	Yttria stabilized zirconia	500 - 1000°C	1 kW - 2 MW	60%	<ul style="list-style-type: none"> <li>• Auxiliary power</li> <li>• Electric utility</li> <li>• Distributed generation</li> </ul>	<ul style="list-style-type: none"> <li>• High efficiency</li> <li>• Fuel flexibility</li> <li>• Solid electrolyte</li> <li>• Suitable for CHP</li> <li>• Hybrid/gas turbine cycle</li> </ul>	<ul style="list-style-type: none"> <li>• High temperature corrosion and breakdown of cell components</li> <li>• Long start-up time</li> </ul>

## 2.2 Basics of Proton Exchange Membrane Fuel Cells (PEMFCs)

PEMFCs consist of a proton exchange membrane, sometimes called polymer electrolyte membranes, sandwiched between two electrodes (catalyst layers), the anode and cathode. The full assembly is called the membrane electrode assembly (MEA). Fuel (e.g., H<sub>2</sub>) is oxidized at the anode and the released electrons travel through an external circuit to the cathode, where oxygen is reduced. Inside the fuel cell, the electronically insulating electrolyte layer transports

protons to the cathode, thus completing the electrical circuit. Further, the electrolyte layer acts as a barrier between the fuel and the oxidant and hence they normally cannot mix and react.

In the H<sub>2</sub>-fueled PEMFC, the anode reaction is the ultrafast hydrogen oxidation reaction (HOR):



and the cathode reaction is the sluggish oxygen reduction reaction (ORR):

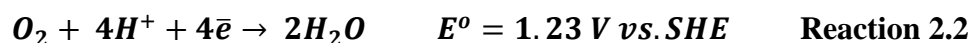
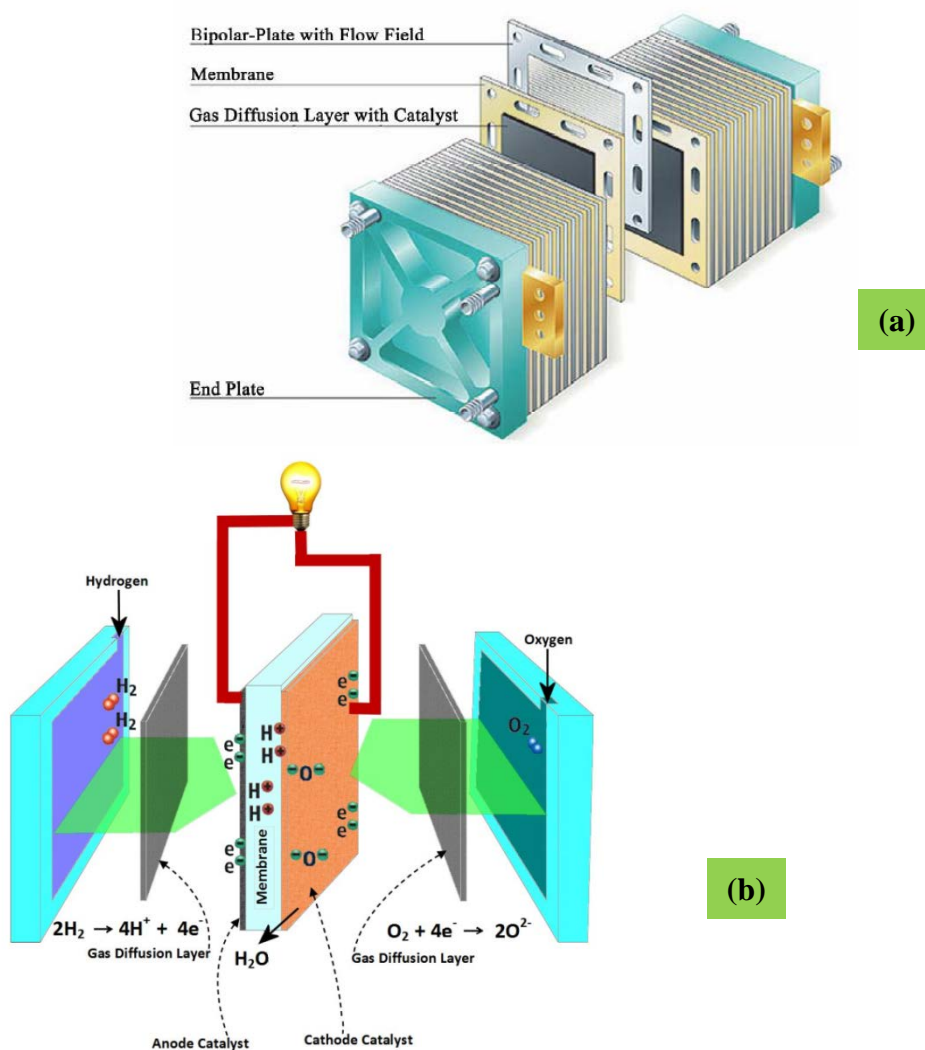


Figure 2.2a shows a PEMFC stack, which consists of a number of individual cells. The number of cells in a stack determines the power output of the stack. Part of a PEMFC schematic is displayed in Figure 2.2b, where the heart of the PEMFC is seen, consisting of the membrane, the anode and cathode catalyst layers, and the gas diffusion layers (GDL). The rest of the FC is called hardware, consisting of bipolar plates to collect the current from the anodic and cathodic reactions, gaskets to seal each component, and more (not all are shown in Figure 2.2). Advanced hardware is required for the smooth operation and the integrity of a FC. As the focus of this thesis is the catalyst layer and its degradation, only components in the MEA are discussed in the following sections.



**Figure 2.2** Schematic of a single cell within a PEMFC stack.<sup>28</sup>

### 2.2.1 The PEMFC catalyst layer

The anode and cathode catalyst layers of PEMFCs typically employ Pt or its alloys as a catalyst in nanoparticle (NP) form (2-5 nm) or as Pt black, dispersed on high surface area carbon

supports (e.g.,  $220 \text{ m}^2\cdot\text{g}^{-1}$  for Vulcan carbon), to drive the oxidation and reduction reactions (Reaction 2.1 and Reaction 2.2) at low temperatures (60-80 °C), producing electricity and  $\text{H}_2\text{O}$ . In the most advanced PEMFCs, Pt NPs are dispersed on microporous carbon (Vulcan XC-72R) to meet the total Pt group metal (PGM) loading targets of  $0.125 \text{ mg}\cdot\text{cm}^{-2}$  per MEA, set by the US Department of Energy, with a target of 2020.<sup>11</sup> The majority of the Pt catalyst loading is consumed by the cathode, as the ORR is a complex four electron process and thus high loadings of Pt ( $> 0.075 \text{ mg}\cdot\text{cm}^{-2}$  per electrode) are needed. In contrast, the ultrafast HOR needs very little Pt, typically  $< 0.01 \text{ mg}\cdot\text{cm}^{-2}$  per electrode.<sup>11, 29-30</sup>

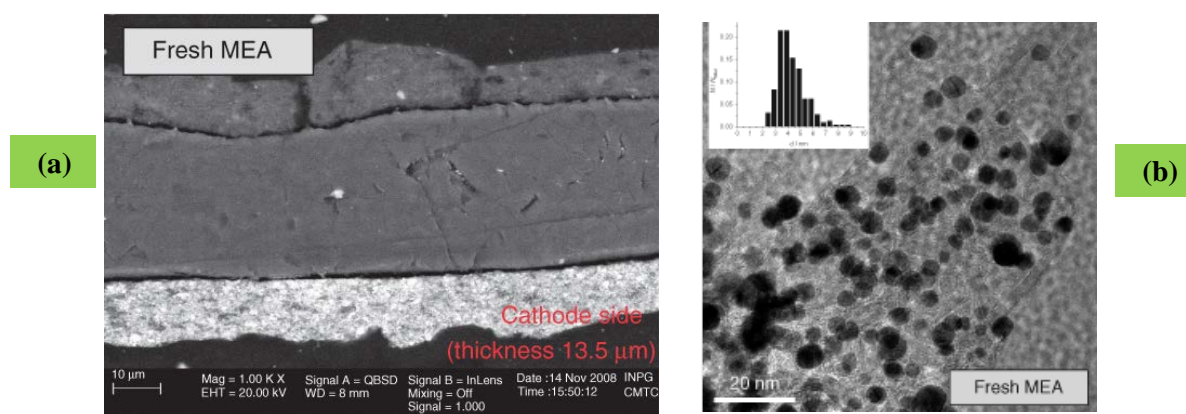


**Figure 2.3** (a) SEM image of MEA and (b) TEM image of the Pt/C catalyst layer along with the particle size distribution histogram.<sup>31-32</sup>

Figure 2.3 shows representative SEM images of a fresh MEA and the Pt NP distribution histogram, with the majority being 4-5 nm in diameter.<sup>31-32</sup> However, the particle size vs. catalytic activity (particle size effect) correlation is not yet clear.<sup>33-35</sup> While it is agreed that the

particle size effect is influenced by the type of anion adsorbed on the Pt NPs and the presence/absence of ionomer, typically Nafion,<sup>33</sup> many groups in the field are trying to achieve very small (3-5 nm) Pt NPs for electrocatalysis, since smaller NPs gives a higher surface to volume ratio.

### **2.2.2 Proton exchange membranes (polymer electrolyte membrane, PEM)**

The electrolyte sandwich between the two catalyst layers in the PEMFC is called a PEM; typically this is Nafion. Nafion consists of a fluorocarbon backbone (Polytetrafluoroethylene) with side chains that are terminated with sulfonic acid groups (Figure 2.4a). The backbone is highly hydrophobic and the side chains are hydrophilic due to their terminal sulfonic acid. These two characteristics are essential for the proper operation of PEMFCs, as membrane hydration serves to retain the water that is required for proton conduction across the membrane, while the hydrophobicity stemming from the fluorocarbon backbone prevents the flooding of the cathode layer. Flooding is a problem, since it hinders gas transport (reactants O<sub>2</sub> and H<sub>2</sub>), which eventually shuts down the FC.

There is no full agreement on the microstructure of Nafion in a PEM fuel cell, although the structure in Figure 2.4b is commonly shown. This is called the cluster network model, where the backbone forms short and narrow channels between the ionic clusters.<sup>6</sup> It is believed that protons are transported between clusters, through the channels, under the influence of the electric field.<sup>6</sup> The proton conductivity of Nafion is ca. 0.1 S·cm<sup>-1</sup> and protons are conducted as H<sub>3</sub>O<sup>+</sup> ions.<sup>6</sup>

Apart from the proton conduction, Nafion provides structural strength to the MEA, which helps prevent the collapse of the MEA.

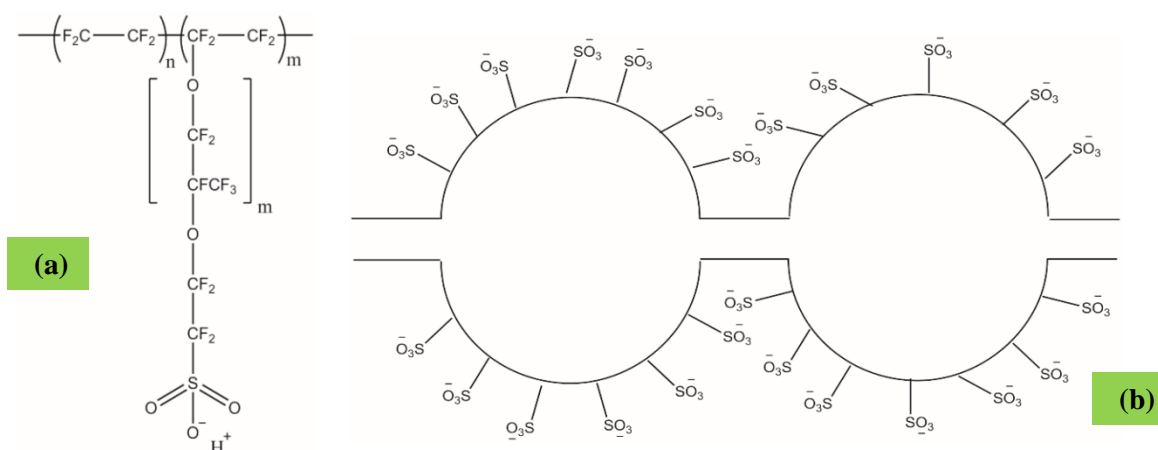


**Figure 2.4** (a) Chemical structure of Nafion<sup>®</sup> and (b) cluster network model of Nafion<sup>®</sup> in a PEMFC.

## 2.3 Challenges faced by PEMFCs

PEMFCs are faced with several challenges. As mentioned briefly in Chapter 1, two major reasons holding back PEMFC commercialization are cost and durability.

### 2.3.1 Cost

Although the end user acceptance of PEMFCs is influenced by social responsibility, by and large, implementation is still constrained to specific segments of the market. The last decade (2007-2017) saw a 52 % decrease in the cost per kW of power generation by PEMFCs for

automotive applications,<sup>36-37</sup> with this projected to be 20 \$·kW<sup>-1</sup> by 2020.<sup>11</sup> The ultimate DOE target is 15 \$·kW<sup>-1</sup>, which means that the DOE is on track for lowering PEMFC cost.

The main cost in PEMFCs (41%) is due to the catalyst, namely the Pt group metals (PGM) (Figure 2.5). Lowering this cost can occur either by decreasing the Pt loading or replacing Pt with alternatives. Since PEMFCs are operated at low temperatures, maintaining the required power output with an ultra-low Pt loading is a challenging task. Nevertheless, knowledge and experience have improved the understanding of the electrocatalysis (in terms of structure/composition vs. activity)<sup>38</sup> of the oxygen reduction reaction (ORR) and hydrogen oxidation reaction (HOR). Thus, breakthroughs are being seen in terms of the PGM loading and alternatives to PGMs. Further, with the ever-increasing choice of synthesis methods, it is not difficult to imagine the development of a ‘designer catalyst’ for the intended purpose.

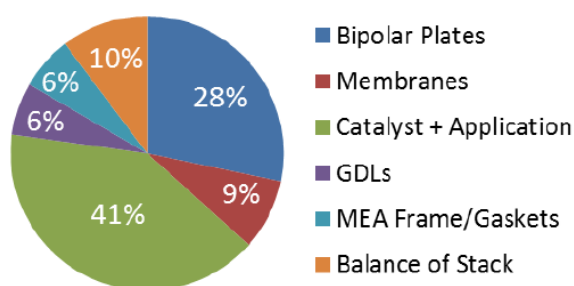


**Figure 2.5** Breakdown of the 2017 automotive PEM fuel cell stack cost.<sup>11</sup>

The design strategy for PGM catalysts is focused primarily on their morphology and composition.<sup>38</sup> This involves the use of thin films or NPs, altering the volume of the catalyst

support, or changing the catalyst packing.<sup>38</sup> Although most approaches are still in the experimental stage, three have made it to mass scale production. These are PGM thin films deposited on nanostructured thin films (NSTF) or whiskers, size/shape controlled NPs, and core/shell NPs.<sup>38</sup> All of these methods help to reduce the PGM catalyst loading and thus increase its activity.

The alternative to PGMs is catalysts made of non-precious metals (NPMs). For example, significant improvement in the catalytic activity is shown by catalysts made of porphyrins or polyaniline containing metal (M= Fe or Co) centres.<sup>39</sup> The performance of these low cost NPMs is reported as a volumetric current density instead of a mass or specific activity, with the activity for supported Fe/N/CF complex being  $450 \text{ A}\cdot\text{cm}^{-3}$  at 0.8 V (2020 DOE expects  $300 \text{ A}\cdot\text{cm}^{-3}$ ).<sup>40</sup>

Various nitrogen-containing Ta compounds ( $\text{Ta}_3\text{N}_5$ , TaON, TaCN, TaOCN) have also been shown to have some ORR activity by Ota et al.<sup>41-51</sup> Of these, the oxygenated compounds (TaON and TaOCN) were the most active, attributed to the presence of oxygen defects on the surface, which may acts as active sites for  $\text{O}_2$  adsorption and e transfer.<sup>52</sup>

### **2.3.2 Durability**

Durability is another issue that is hindering full scale commercialization of PEMFCs. Sometimes, end-users will buy highly priced product if they guarantee high durability. Therefore, durability also goes hand in hand with other essential specifications in order to market a product. For PEMFCs, the DOE and the EU fuel cell program have set similar targets for durability. For automobile applications, PEMFCs need to operate for 6000 h under real

conditions (by 2020) and DOE's ultimate goal is 8000 h, while it is 60,000 h for a 5 kW micro-combined heat and power ( $\mu$ -CHP) fuel cell energy system for stationary applications.<sup>11</sup>

Poor durability can be a problem related to the accumulated degradation of materials, components and interfaces. Therefore, addressing durability needs a broad perspective that covers the full fuel cell system. Furthermore, any approach should consider the interdependence of the different parts of the FC. However, understanding each component's durability is necessary before moving to the integrated approach. In this thesis, durability of the catalyst support material is thus one of the focal points.

## **2.4 Degradation of PEMFC Catalyst Layers (CL)**

It is not a surprise that catalyst layers, especially at the cathode, undergo degradation under the operating conditions of a PEMFC, especially due to the strong oxidizing and acidic conditions encountered. Therefore, understanding the reasons for degradation and the related mechanisms is vital for assessing and improving the durability of PEMFCs.

### **2.4.1 Catalyst degradation**

In the following discussion of degradation, only PGM catalysts, especially Pt, are considered. According to the Pourbaix diagram,  $\text{PtO}_2$  is stable at the OCP of a  $\text{H}_2$ -air PEMFC<sup>53-54</sup> and from the spectroscopic analysis of carbon-supported Pt NPs, it was shown that Pt can be oxidized at 0.8 V and reduced at 0.5 V during potential scanning.<sup>55-56</sup> High potentials also cause Pt dissolution, especially as the Pt NPs are small, thus causing a loss in Pt surface area and a consequent loss in activity.<sup>57-58</sup> Furthermore, Pt NPs can also Ostwald ripen and agglomerate,

reportedly increasing in size from a narrow distribution of 1-5 nm to a broader distribution of 1-15 nm at the cathode catalyst layer of the MEA after 1200 h of test cycles.<sup>59</sup>

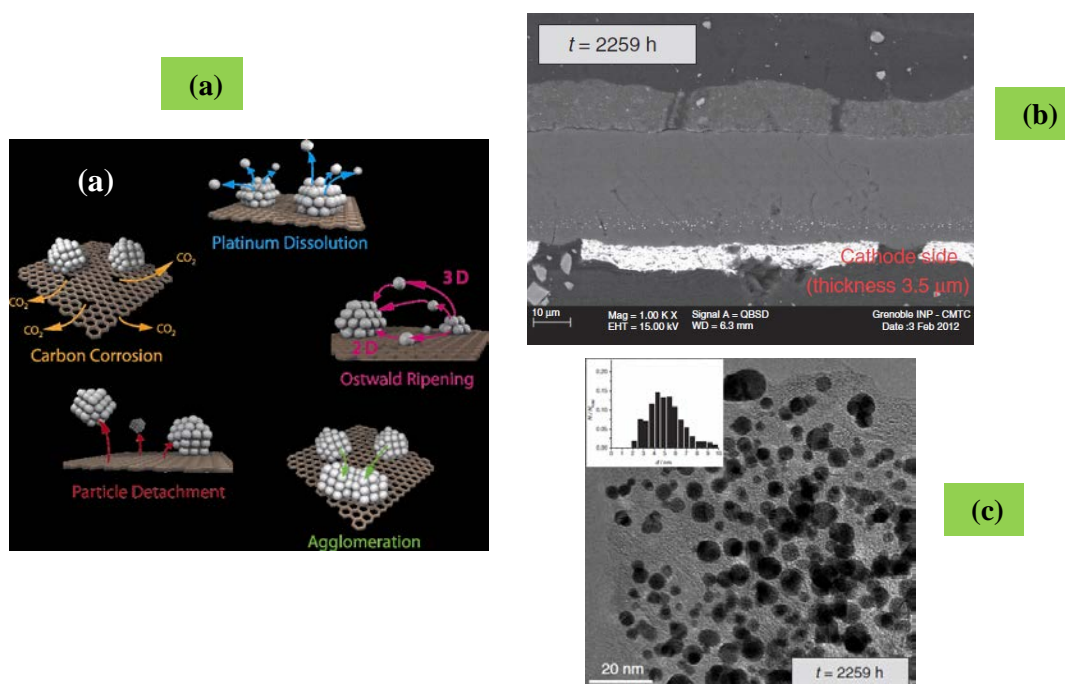


**Figure 2.6** (a) CL degradation in PEMFCs. After 2259 h of operation, (b) shows SEM images of the MEA and (c) shows a TEM image of the Pt/C catalyst layer, along with the Pt NP size distribution histogram.<sup>31-32</sup>

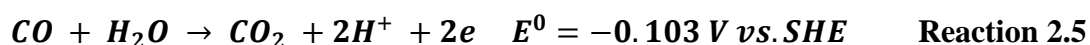
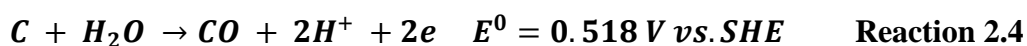
Figure 2.6 shows some of the possible methods of lowering the electrochemical surface area (ECSA) of Pt NPs, including particle detachment due to carbon corrosion (will be discussed later), Pt NP dissolution and re-deposition or Ostwald ripening, as well as NP agglomeration. Of these mechanisms, the one that contributes most significantly to lowering the Pt ECSA is yet to

be determined. An SEM image of a MEA after 2259 h of operation is shown in Figure 2.6 b (the SEM of the freshly made MEA is shown in Figure 2.3 a). Here, the thinning of the cathode CL from 13.5  $\mu\text{m}$  to 3.5  $\mu\text{m}$  can be clearly seen, while Figure 2.6c shows the growth of the Pt NPs from 5 nm to 10 nm for the same MEA.

### 2.4.2 Carbon catalyst support degradation

Heterogeneous catalysis occurs only at surface sites and thus maximizing the surface area of these types of catalysts is vital. Also, typically, catalyst materials used in PEMFC applications are precious metals. As a result, the catalysts are nanostructured in order to increase their surface to volume ratios. Furthermore, these catalyst nanoparticles must be dispersed on an appropriate high surface area support material in order to minimize their agglomeration and to ensure good electrical contact. This, in turn, can lower the amount of precious metals needed in a catalyst layer.

The most ubiquitous catalyst support used in PEMFCs is carbon because of its availability, good conductivity, high surface area (in most allotropes), high porosity for mass transport, and low cost. However, carbon undergoes electrochemical oxidation in the presence of water and at a sufficiently high potential, according to the following reactions.<sup>60</sup>



These reactions are kinetically sluggish at the typical PEMFC operating potential (0.5 – 0.9 V), even though they are thermodynamically allowed. However, the potential, temperature, time and reaction conditions can all enhance the oxidation rate, as has been determined from the spikes seen in the CO<sub>2</sub> concentration in the exhaust of the cathode.<sup>61-62</sup> Other observations, such as in-situ electrode potential measurements<sup>63</sup> and carbon support weight loss have verified this phenomenon.<sup>64</sup> Furthermore, Raman spectroscopy and PXRD have also provided evidence for the occurrence of the COR in the cathode catalyst layer.<sup>65</sup>

Carbon corrosion is promoted particularly during PEMFC shut-down/start-up, due to the formation of a H<sub>2</sub>/O<sub>2</sub> front that divides the PEMFC into two regions, where the H<sub>2</sub> rich region acts as a power source (fuel cell, with the HOR occurring at the anode and the ORR at the cathode) and the H<sub>2</sub>-free region serving as a load driven by the power source, thus electrolyzing water (Figure 2.7). The electrons generated from the HOR at the front end of the channels travel along the CL to the H<sub>2</sub>-free region and are consumed by any O<sub>2</sub> present (from the time at open circuit). Protons are generated by the oxygen evolution reaction (OER) and COR in the cathode of the H<sub>2</sub>-free region and transported across the membrane, as in plane H<sup>+</sup> transport is less facile than transport across the membrane. This causes the reverse proton current as shown in Figure 2.7. Unfortunately, in the use of PEMFCs in automobiles, the start-stop cycle event is frequently encountered and thus the carbon corrosion is a significant degradation problem.

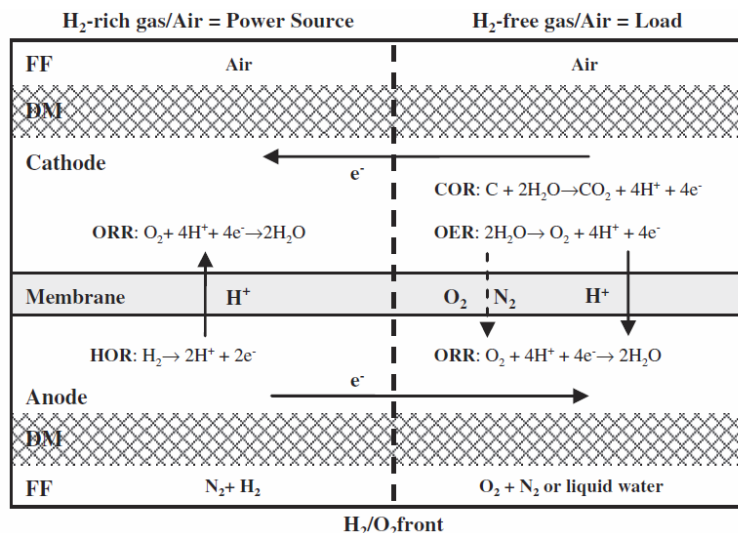
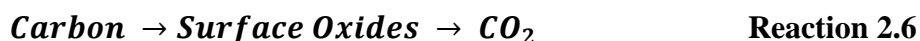


**Figure 2.7** A schematic of reverse current generation at the H<sub>2</sub>/O<sub>2</sub> front in a PEMFC during shut-down and start-up.<sup>66</sup>

#### 2.4.2.1 Mechanism of carbon catalyst support degradation [Carbon oxidation reaction (COR)].

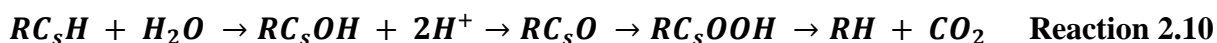
In this section, the COR mechanism is briefly discussed. Although there is no consensus about this in the literature, the accepted view is that oxygen first adsorbs on the carbon surface and after several intermediate steps, carbon is oxidized to CO<sub>2</sub> (Reaction 2.6)



In order to understand the mechanism of the COR, it is important to understand why and where these oxide groups are formed. To answer this question, some knowledge about the carbon structure is helpful. Carbon exists in allotropes, such as amorphous carbon, graphite, diamond, graphene, buckminsterfullerene, etc. For PEMFC applications, the most commonly used carbons are amorphous and graphitic carbon. Graphite consists of a purely sp<sup>2</sup> hybridized, planar, and

crystalline structure, while amorphous carbon is  $sp^2$  and  $sp^3$  hybridized, ‘planar’, and non-crystalline (although short range order does exist).

It is believed that carbon corrosion is initiated at defects, such as edges and corners of the basal plane of the carbon structure, where a high concentration of functional groups, such as phenols, lactones, ketones, carboxylic acid, etc. can be found. A generally accepted mechanism for the COR is given below.<sup>67</sup>

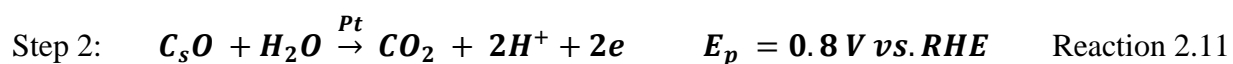


where  $C_s$  describes the surface C atom.

The first step (Reaction 2.7) of the mechanism is not always necessary for the initiation of the COR. A typical route for the oxidation of  $sp^2$  or  $sp^3$  carbon is to convert it to alcohol, then to ketone/aldehyde, then to carboxylic acid, and finally to  $CO_2$  (Reaction 2.10). This generic scheme is based on knowledge of organic chemistry and information obtained from experimental techniques, such as X-ray photoelectron spectroscopy, Boehm titration, temperature programmed desorption, FTIR/Raman spectroscopy, cyclic voltammetry (CV), contact angle measurements, etc.<sup>67</sup> Of these functional groups, certain groups (Quinone and hydroquinone- Q/QH<sub>2</sub>) participate in the reversible redox reaction during the COR, whereas others can be irreversibly oxidized to  $CO_2$ .

### 2.4.2.2 Participation of Pt NPs in carbon corrosion

It has been postulated that Pt plays a vital role in accelerating the COR. This stems from the knowledge that all Pt group metals have a strong affinity for CO, and adsorbed CO is known to block active sites. However, this unwanted adsorption phenomenon can be used for the determination of the ECSA of PGMs during the oxidative stripping of adsorbed CO at higher potentials.<sup>68</sup> Willsau et.al. have proposed that the catalysis of the COR by Pt occurs via a mechanism similar to the oxidation of CO on Pt, based on their CV analysis. In both cases, the peak potential is centered at ca. 0.8 V vs. RHE.<sup>68</sup> The proposed steps involved in the COR when Pt is present are:



They claim that surface oxides on the carbon surface are oxidized to CO<sub>2</sub> only at sites close proximity to the Pt NPs. Further, it is said that the amount of CO<sub>2</sub> produced is proportional to the distance between two neighboring Pt NPs on the carbon surface. Maass et.al proposed a similar mechanism (studies done on an MEA), but they broke down step 2 into two individual steps, where Pt reacts with water to form PtOH<sub>s</sub> and then PtOH reacts with C<sub>s</sub>O to form Pt and CO<sub>2</sub>.<sup>69-</sup>

<sup>71</sup> A recent study by Lebedeva et.al. states that first, the CO and –OH species are adsorbed on Pt and then they are oxidized to CO<sub>2</sub>, according to following reaction.<sup>72</sup>



Sugawara et. al.<sup>73</sup> and Gallagher et. al.<sup>74</sup> pointed out that cathode potentials in the range of 1.0 – 1.5 V vs. RHE facilitate the formation of a passivating oxide layer on Pt, thus preventing the COR to some degree. However, they were unable to identify the exact nature of these Pt oxide(s).

## 2.5 Protecting the PEMFC Catalyst Layer from Corrosion

Thus far, the challenges faced by PEMFC catalyst layers have been discussed. In this section, some of the remedial methods to minimize carbon and Pt oxidation/corrosion are discussed. Earlier work to replace traditional carbon supports (e.g., carbon black) concentrated on modifying the existing carbon black or graphite by heat treatment, surface modification, and other methods that lead to a higher resistance to corrosion.<sup>58</sup> Furthermore, other types of carbon, such as colloid imprinted carbons (CIC), carbon nanotubes (CNT), diamond, etc. have also been considered as a PEMFC catalyst support material.<sup>58</sup> CNTs have an excellent resistance to corrosion because of their well extended  $sp^2$  hybridized carbon network that provides good crystallinity (due to graphitization). It is known that crystalline carbons are less corrosion susceptible than non-graphitized carbon, mostly as they have fewer graphene edge sites.<sup>58</sup>

The CICs are favoured for the tunability of their pore size, with large ordered pores allowing the utilization of Pt NPs both inside and outside the pores.<sup>75</sup> Most typical carbon materials (e.g., Vulcan XR72) contain primarily micropores (pore size < 2 nm) and Pt precursors may not be able to penetrate them. Alternatively, any Pt NPs residing inside these micropores will not be easily reached by the reactants ( $O_2$  or  $H_2$ ) and challenges could also exist in getting

the ionomer (Nafion) into the pores, thus limiting the triple phase boundary (TPB) length, the sites where the gaseous reactants ( $O_2$  and  $H_2$ ), the solid phase supported catalyst (Pt/C), and the liquid phase ionomer or water all meet and the fuel cell reactions can occur. Maximizing the TPB length is crucial in order to achieve high power densities, and thus the CICs, with their high internal surface areas and accessible pores, should satisfy this criterion. Moreover, since the mesoporous CICs have more surface oxygenated functional groups than microporous Vulcan Carbon, the CICs provide a platform for the bottom up synthesis of materials mixed with carbon. In this thesis, 100 nm pore size CIC was used as a co-support for Pt, along with  $TaO_xN_y$  nanoparticles, as explained in Chapter 6.

Other non-carbonaceous materials, such as a variety of metals, oxides, nitrides, carbides, borides, mesoporous silica, conducting polymers, and conducting oxides have been considered as alternative PEMFC catalyst supports, as reported in the literature.<sup>12-13</sup> These materials can be used as a single-phase support for the cathode (Chapter 5) or as part of a co-support, normally in a mixture of carbon and the catalyst (Chapter 6). While many of these materials have been reported to be superior to carbon, their negative features have generally not yet been reported, likely related to industry involvement in the research and related intellectual property issues.

### **2.5.1 Non-carbon PEMFC catalyst support materials**

This section is focused primarily on the cathode catalyst layer as it the most vulnerable to corrosion. In Section 2.5.3, alternative supports for the anode catalyst are discussed, partly also as this is one way to potentially protect the cathode from damage. Conducting metal oxides, metal carbides, and metal nitrides are emerging as promising oxidation-resistant non-carbon

supports for PEMFCs, especially for cathodes, although initially they were considered only as potential substitutes for noble metal catalysts.<sup>12-13, 76</sup> An electrocatalyst support needs to provide not only good conductivity but also good catalyst-support interactions, a high surface area for catalyst dispersion, mesoporous channels to transport reactants/ionomer, corrosion resistance, and easy recovery of the catalyst.<sup>12-13, 76</sup> These non-carbon (alternative) support materials typically lack certain properties, such as good conductivity or sufficiently high surface area. However, they are often extremely stable under the operating conditions of a PEMFC.<sup>13</sup>

### ***2.5.1.1 Metal Oxides***

Certain metal oxides, such as the Group IV/V metal oxides, some conducting oxides, etc., have been reported to be more stable in the acidic and oxidizing conditions of a PEMFC cathode than is carbon.<sup>12-13</sup> For example, Chinna et al. reported that Pt, deposited on conducting transparent ITO (indium tin oxide), exhibits stable electrocatalytic activity for the ORR, even after 100 cyclic voltammetric (CV) cycles between 0.8 - 1.5 V, whereas the commercially available Hispec 4000<sup>®</sup> catalyst (40% Pt on carbon black from Alfa Aesar) lost most of its activity after the same number of cycles, and 40 wt.% Pt on Vulcan XC-72R lost its activity after only 50 cycles.<sup>77</sup> Un-doped-tin oxide (SnO<sub>2</sub>) has also been used as a support in several studies, and in one of them, the ECSA (electrochemical surface area) of Pt at variable temperatures was evaluated after potentials cycling (CV). Pt/C lost most of its ECSA after 1000 cycles, but it took 5000 cycles to observe a significant loss of the ECSA for Pt/SnO<sub>2</sub>.<sup>78</sup>

Although metal oxides are often semiconductors, some are very good conductors. For example,  $\text{Ti}_n\text{O}_{2n-1}$  in the Magnéli phase, where  $4 < n < 10$ , has a conductivity of ca.  $1000 \text{ S}\cdot\text{cm}^{-1}$  at room temperature, which exceeds the conductivity of graphitized carbon ( $727 \text{ S}\cdot\text{cm}^{-1}$ ).<sup>12-13, 79</sup> The Magnéli titania ( $\text{TiO}_2$ ) phase is produced by heating stoichiometric titania in a reducing environment, which creates oxygen vacancies or introduces dopants.<sup>80</sup> Kim et. al. treated titania first with urea, thiourea, or HF to make the titania Magnéli phase and then deposited Pt NPs on it. The HF-treated  $\text{TiO}_2/\text{Pt}$  had the highest  $\text{Ti}^{2+}$  or  $\text{Ti}^{3+}$  concentration (as found by XPS) and hence better charge transfer capability. Therefore, it is the material that showed the best ORR activity out of all of the samples.<sup>81</sup>

Metal oxides can be produced with a high surface area and the work done by Heung et. al. showed that a  $266 \text{ m}^2\cdot\text{g}^{-1}$  titania, decorated with Pt NPs, can withstand 4000 potential cycles between 0 V and 1.2 V vs. RHE compared to Pt/C, which can only handle 2000 cycle numbers. After corrosion testing of this sample, the Pt NP size increased from 3 nm to 8 nm, whereas for the Pt/ $\text{TiO}_2$  material, the Pt NP size did not change.<sup>82</sup>

Another commonly explored n-type oxide in this field is tungsten oxide ( $\text{WO}_x$ ), where  $2 < x < 3$ . As outlined by Antonelli et. al. in their review,  $\text{WO}_x$  can be employed in many parts of a PEMFC, including as a support and as a replacement for the Nafion proton conductor.<sup>83</sup> It is also reported that Pt/ $\text{WO}_3$  is more stable than Pt/C in 1 M  $\text{H}_2\text{SO}_4$  and that nanostructured  $\text{WO}_3$  (nanorod), decorated with Pt NPs, is even more stable than bulk  $\text{WO}_3$  with Pt.<sup>84</sup>

As demonstrated by several researchers, using metal oxides as a PEMFC catalyst support has additional benefits, such as potentially strong metal-support interactions (SMSI) that minimize nanoparticle agglomeration as well as the capability of oxidative removal of adsorbed species that usually block the catalyst surface.<sup>85-86</sup> The conductivity of some metal oxides can be further improved by replacing the oxygen anion with other elements, such as N or C.

### ***2.5.1.2 Metal Carbides***

Only a few metal carbides (Ti carbide, W carbide) have been studied as PEMFC catalyst supports to date, with W carbide seeming to be particularly promising.<sup>87-89</sup> Because WC exhibits Pt-like behaviour, it may be useful both as a catalyst and as a catalyst support.<sup>90</sup> As observed by Chinna et. al., the stability of 40 wt. % Pt/WC as a PEMFC catalyst was far better than Hispec 4000<sup>®</sup> after accelerated durability testing (ADT) of 100 CV cycles between 0.6-1.8 V vs. RHE.<sup>88</sup> It was claimed that this was due to the oxidation of WC to sub-stoichiometric  $WO_x$ , which is a moderately conductive compound.

### ***2.5.1.3 Metal Nitrides***

Ti nitride has also been studied as a Pt catalyst support in PEMFCs and also in Direct Alcohol Fuel Cells (DAFCs).<sup>91-100</sup> The Pt ECSA and the ORR catalytic activity was reported to be higher for 20 wt. % Pt on TiN cathodes than for a commercial 20 wt. % BASF<sup>®</sup> Pt/C catalyst.<sup>96, 98</sup> Also, Kakinuwa et al. showed that it takes 4000 CV cycles to decrease the Pt ECSA by 50% in a PEMFC when using Pt/TiN cathodes, whereas, for a Pt/C cathode, it takes only 300 CV

cycles.<sup>95</sup> Moreover, 19.5 wt. % Pt/TiN gave an ORR exchange current density of  $1.2 \text{ mA}\cdot\text{cm}^{-2}$ , vs.  $0.8 \text{ mA}\cdot\text{cm}^{-2}$  seen for commercially available 20 wt.% Pt/C.

TiN was also shown to be a better support than carbon for Pt-based cathode catalysts in alcohol (methanol and ethanol) fuel cells.<sup>91, 97, 99-100</sup> Tafel slopes (TS) and exchange current densities ( $i_0$ ) were obtained after 50 CV cycles of methanol oxidation at Pt/TiN and commercially available Pt-Ru/C catalysts by Thotiyl et al.<sup>100</sup> They showed that Pt/TiN gave an ORR TS of  $102 \text{ mV}\cdot\text{decade}^{-1}$  vs.  $126 \text{ mV}\cdot\text{decade}^{-1}$  for Pt-Ru/C and a better current density of  $0.81 \text{ mA}\cdot\text{cm}^{-2}$  vs.  $0.63 \text{ mA}\cdot\text{cm}^{-2}$  for Pt-Ru/C.<sup>100</sup>

Fritz et. al. investigated mesoporous Ti nitride and Nb nitride as a cathode catalyst support for Pt NPs in a PEMFC environment.<sup>101</sup> Although the surface area of these materials was not very high ( $49 \text{ m}^2\cdot\text{g}^{-1}$  Nb nitride and  $60 \text{ m}^2\cdot\text{g}^{-1}$  for Ti nitride), the mesoporous structures of these nitrides was maintained, with an average pore size of 27 nm and 19 nm for Ti nitride and Nb nitride, respectively. Between the two nitrides, Ti nitride withstood 2000 cycles of potential cycling up to 1.4 V vs. RHE, whereas Nb nitride was stable to the same number of cycles, but only to 0.85 V. Pt electrochemistry was clearly seen for the Pt/TiN composite, but it was not subjected to ADT.

### **2.5.2 Non-carbon materials as co-supports to carbon**

Although transition metal oxides/nitrides/carbides possess good stability in the PEMFC environment, their conductivity (ca.  $10^{-3} \text{ S}\cdot\text{cm}^{-1}$  at room temperature)<sup>102</sup> is generally not on par with that of graphitized carbon (ca.  $727 \text{ S}\cdot\text{cm}^{-1}$ )<sup>12-13</sup>, which imposes certain limitations on

performance. If the durability is not compromised, forming a composite of these compounds with carbon may be a good way to improve their conductivity. It has been reported that composites of carbon, metal oxides/nitrides/carbides, and Pt show improved durability of PEMFC cathode catalyst layers.<sup>103-106</sup>

A further advantage of these transition metal compounds, especially the nitrides and carbides, is that they have sometimes been reported to exhibit some ORR activity. According to Rong Kou et. al., the durability and activity of graphene/ITO/Pt is better than Pt/graphene.<sup>104</sup> After 100 CVs ( $5 \text{ mV}\cdot\text{s}^{-1}$ ), the decrease in the Pt ECSA of the former was 41% and, for the latter, it was 56 %. This was explained as arising from the synergistic effect of the participating compounds and the presence of strong metal-support interactions.  $\text{Mo}_2\text{N}$  also showed promising behaviour as a methanol reforming catalyst support, which may extend to applications as a PEMFC catalyst support.<sup>107</sup>

Ti oxynitride was deposited on carbon nanotubes (CNT) by atomic layer deposition to serve as a catalyst support for Pt and Pt-Ni alloy NPs.<sup>108</sup> After 10,000 potential cycles between 0.6 V and 1.1 V vs. RHE, the ECSA of the Pt/CNT material dropped by 48%, whereas for Pt/TiON/CNT, this loss was only 24 %. However, for Pt-Ni alloys, there was no improvement in the stability observed. Moreover, Pt NP growth was also observed (average size increased from 6 nm to 29 nm).<sup>108</sup>

### **2.5.3 Protecting the cathode catalyst layer from corrosion by protecting the anode**

Another possible way to protect the cathode catalyst support from corrosion is to design an anode support that suppresses the ORR (oxygen reduction reaction), which occurs during cell reversal, without obstructing the HOR (hydrogen oxidation reaction) that must occur while in the normal fuel cell mode. This is a new research area with only a few published papers available. Efforts to date have involved coating the anode with hydrogenase enzymes<sup>109</sup> or employing chemically modified Pt surfaces (e.g., with calixarene) to catalyze the HOR selectively in the presence of O<sub>2</sub>.<sup>110</sup>

Although selectivity for the HOR has been achieved, the stability of the catalysts is still under scrutiny in these works. If the support material is conductive at cathodic potentials (ca. < 0.8 V vs. RHE), but is not conducting at more positive potentials, this would make the material ideal for this application. The TaO<sub>x</sub>N<sub>y</sub> material under investigation in this thesis work shows exactly this behaviour. On the whole, most metal oxides, nitrides and oxynitrides should show this diode effect at high potentials, although the conductivity switching potential should vary with the material. Banham et. al. tested this concept with a Nb-doped Ti oxide support and it showed better stability than conventional Pt/C catalysts, even after 5400 cycles of potential.<sup>111</sup>

## **2.6 Protocols for Evaluation of Catalyst Layer Degradation**

Accelerated testing of PEMFCs is essential in order to determine the possible failure modes of the system. Several agencies, including the US DOE, the US Fuel Cell Council, the EU Fuel Cell Programme and the Japan Fuel Cell Commercialization Program, have been working

together to establish a standard protocol for the rapid, reliable and cost effective testing of fuel cell performance and durability. Accelerated durability tests (ADTs) or sometimes called Accelerated Stability Tests (ASTs) provide a way to analyze the failure mode of each part of the FC. Since this thesis is focused on the catalyst layer of PEMFCs, only the ADT relevant to this component is discussed here.

As mentioned earlier, the CL has two parts, the electrocatalyst and its support. Therefore, separate ADTs need to be considered. The DOE and EU together developed a multiyear plan in 2017 to evaluate the catalyst and its matrix according to following method, which they adopted from Gasteiger et.al.<sup>11, 112</sup> A 25-50 cm<sup>2</sup> single cell should be subjected to 30,000 square wave cycles at 0.6 V for 3 s and 0.95 V for 3 s. The rise time should be ca. < 0.5 s or less. After a specified number of cycles (0, 10, 100, 1k, 3k, 10k, 20k, and finally 30k) at controlled humidity, temperature and gas flow, a CV (20 mV/s) needs to be run to obtain the changes in the ECSA of the Pt catalyst, with the upper potential limit not > 1.2 V vs. RHE. After correcting for double layer charge, the HUPD charge should be calculated based on the standard value of 210  $\mu\text{C}\cdot\text{cm}^{-2}_{\text{Pt}}$ , with a loss of 40% or less considered tolerable. The ADT for the catalyst support layer involves 5,000 CVs at 500 mV·s<sup>-1</sup> run on a 25-50 cm<sup>2</sup> single cell between 1.0 to 1.5 V vs RHE and the ECSA is evaluated at specified number of cycles (0, 10, 100, 200,500, 1k, 2k and 5k), with a 40% loss of ECSA considered acceptable.

In a typical laboratory set-up, these experiments are performed in a three-electrode cell with a catalyst-containing ink deposited as a film on a working electrode (WE) surface, typically a GC electrode. Gasteiger et. al. has argued that the three-electrode system is suitable as a

method for testing improved or new catalysts and that the results can be extrapolated to the full MEA performance.<sup>112</sup> They compared four different commercially available catalyst inks [46 and 47 % Pt/C (TKK) and 20 and 40 % Pt/VC (ETEK)] with the fully constructed MEA and obtained similar specific (170-210 and 180  $\mu\text{A}\cdot\text{cm}^{-2}_{\text{Pt}}$ , respectively) and mass activity (0.11-0.16 and 0.11  $\text{A}\cdot\text{mg}^{-1}$ , respectively) at 0.9 V vs RHE.

Since establishing standard ADTs is in an ever evolving task, several research groups, including the Birss group, have developed their own ADT protocols to mimic the PEMFC start-up/shutdown cycles. Shao et.al. used potential stepping and holding to evaluate carbon corrosion of a Pt/C catalyst.<sup>113</sup> Under potential holding conditions (1.2 V and 1.4 V vs. RHE for 120 h), less carbon degradation was observed than during potential stepping (1.4 V for 150 s and 0.85/0.6 V for 30 s). The same group investigated the corrosion of carbon without Pt, but changed the lower potential limit and holding time.<sup>114</sup> They used CV and X-ray photoelectron spectroscopy (XPS) to analyze for the oxygenated functional groups present on the carbon surface, before and after the ADT. The quinone/hydroquinone pseudocapacitive charges became larger after corrosion when using the protocol with the lower potential limit of 0.1 V and a holding time of 30 s. The XPS results showed more functional groups on the surface (carbonyl, carboxylic,  $\text{sp}^3$  carbon, etc.) after ADT, but a decrease in the  $\text{sp}^2$  carbon percentage. They attributed the acceleration of the COR by potential stepping to the generation and consumption of functional groups. In Chapter 3, the ADT protocol used in this thesis work and in the Birss group, in general, is explained in detail.

## 2.7 Oxygen Reduction Reaction (ORR)

Whether it is biological (e.g., respiration) or artificial (e.g., in a fuel cell), the ORR is part of an energy conversion process. Therefore, it is not an exaggeration to say that this is an essential chemical reaction. The complete conversion of molecular O<sub>2</sub> to oxide anions (O<sup>2-</sup>) or water needs four electrons, and depending on several factors, its mechanism can go through 1, 2 or 4 electron pathways. Table 2.2 shows the known values of the standard reduction potentials for each of these steps.

**Table 2.2 ORR in different solutions**

Electrolyte	ORR reactions	Thermodynamic electrode potential at standard conditions, V
Acidic aqueous solution	$O_2 + 4H^+ + 4e^- \rightarrow H_2O$	1.229
	$O_2 + 2H^+ + 2e^- \rightarrow H_2O_2$	0.70
	$H_2O_2 + 2H^+ + 2e^- \rightarrow 2H_2O$	1.76
Alkaline aqueous solution	$O_2 + H_2O + 4e^- \rightarrow 4OH^-$	0.401
	$O_2 + H_2O + 2e^- \rightarrow HO_2^- + OH^-$	-0.065
	$HO_2^- + H_2O + 2e^- \rightarrow 3OH^-$	0.867
Non-aqueous aprotic solvents	$O_2 + e^- \rightarrow O_2^-$	a
	$O_2^- + e^- \rightarrow O_2^{2-}$	b

Note: The a and b values are strongly dependent on the organic solvent used and therefore are not listed here.<sup>115</sup>

### 2.7.1 Relevant electrochemistry of the ORR

The formulation to express the current-potential relationship of an electrochemical reaction for which charge transfer kinetics are rate limiting is called the Butler–Volmer (BV) equation (Equation 2.1) and it takes the following form for a general multistep reaction.<sup>116-117</sup>

$$i = i_0 \left[ e^{\frac{\alpha_a \eta_a F}{RT}} - e^{\frac{-\alpha_c \eta_c F}{RT}} \right] \quad \text{Equation 2.1}$$

The notations have their usual meaning and their meanings are given in the abbreviation section. The most important parameters of the BV equation that pertain to fuel cell research are the overpotential ( $\eta$ ), the exchange current density ( $i_0$ ) and the transfer coefficients ( $\alpha$ ), as they govern the kinetics of the reaction. High values of the latter two parameters means that the kinetics are fast, which is critical for a fuel cell, for which efficiency is determined by the electrical power. These two parameters are material/catalyst dependent and for the ORR, the best values are obtained for Pt.<sup>115</sup>

In the Tafel approximation, for example at large cathodic  $\eta$  values, the contribution from the anodic reaction is small ( $< 1\%$ ) and then the BV equation (Equation 2.1) reduces to:

$$i = i_0 \left[ - e^{\frac{-\alpha_c \eta_c F}{RT}} \right] \quad \text{Equation 2.2}$$

A Tafel plot ( $\log i$  vs.  $\eta$ ) then gives a slope of  $2.303RT/\alpha_c \eta_c F$  [Tafel slope (TS)], indicating how much overpotential is needed to increase the rate of the reaction (current) by a factor of ten. The Tafel slope contains information about the number of electron transferred, the number of chemical steps involved during and preceding the rate determining step, etc. in a non-elementary

reaction.<sup>116-117</sup> Although the Tafel slope is used to interpret the kinetic results in this thesis work, its use should meet certain requirements for proper interpretation, including that a uniform current density is present, the ohmic resistance should be negligible, the kinetic currents should be much smaller than diffusion limiting currents, and there should not be any parallel reactions occurring.

Typically for the ORR, two Tafel slopes are reported in the literature for Pt, Pt (111), Pt (100), Pt alloys etc. The most common value is  $120 \text{ mV}\cdot\text{decade}^{-1}$  ( $\alpha_c = 0.5$ ), seen at higher current densities/higher overpotentials and suggesting that the first electron transfer step is rate determining.<sup>118-119</sup> However, at low current densities and lower overpotentials (ca. 0.8 V vs. RHE), even though the same reaction step is slow, the kinetics are influenced by the presence of Pt oxide surface groups, giving a  $60 \text{ mV}\cdot\text{decade}^{-1}$  Tafel slope.<sup>120</sup>

Anion adsorption can also play a role in changing the Tafel slope. Studies on particular Pt crystal facets (Pt 111) have shown that strongly adsorbed  $\text{HSO}_4^-$  can change the 60 mV slope to  $120 \text{ mV}\cdot\text{decade}^{-1}$  at  $> 0.6 \text{ V}$  vs. RHE. This is because the  $\text{HSO}_4^-$  adsorption coverage does not change and the number of available sites for  $\text{O}_2$  adsorption also remains constant, while for weakly adsorbed  $\text{ClO}_4^-$  anions, a continuously changing Tafel slope is seen in the potential region of 0.6 – 1.0 V.<sup>121-122</sup>

The ORR mechanism on Pt is known to involve a series of electron and proton transfer steps, with at least two generic mechanisms proposed in the literature. These include the single and dual site mechanisms, with Figure 2.8 showing the dual site mechanism on a Pt surface.

Here,  $O_2$  adsorbs onto two neighboring Pt atoms, followed by the electron and proton transfer steps, producing  $H_2O$  and releasing the Pt sites for further adsorption of  $O_2$ .

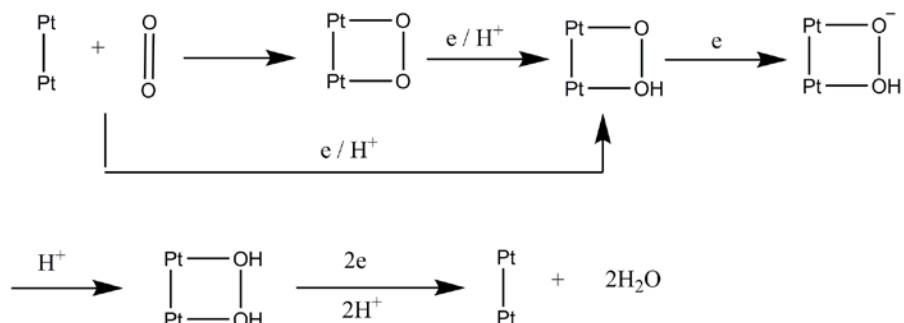


**Figure 2.8** Dual site ORR mechanism on Pt surfaces.

## 2.8 Hydrogen Oxidation Reaction (HOR)

The HOR is one of the fundamental reactions of electrochemistry and much of the knowledge in the area of electrochemistry has been developed based on this reaction. The HOR is the anode reaction in a PEMFC and is thus a major part of the  $H_2$  economy, which is yet to materialize. The kinetics and mechanism of the HOR on various metal surfaces have been studied extensively, showing the Pt is the best catalyst for the HOR, due to its metal-hydrogen (M-H) bond strength, which is shown to be in the intermediate range (at the apex of Figure 2.9). The Sabatier principle states that a reaction is most rapid when the bond strength between a reactant and the catalyst is 'just strong enough'. This statement is usually translated in a Volcano plot as being moderate bond strength between the two species. Because of the very rapid rate of

the HOR and its reverse process, hydrogen evolution, the Pt/H<sub>2</sub> system has been chosen to define the standard electrode potential for the H<sub>2</sub>/H<sup>+</sup> redox half-reaction.

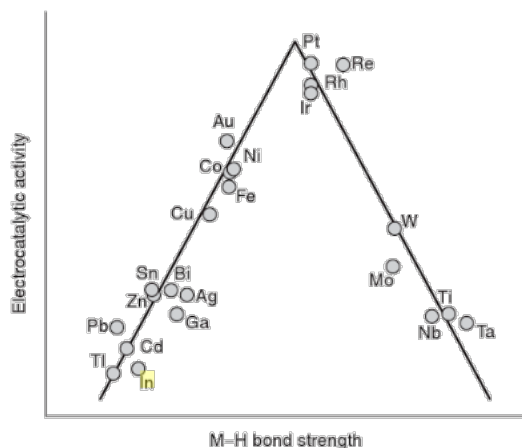


**Figure 2.9** Volcano plot for Metal-Hydrogen (M-H) bond strength.<sup>123</sup>

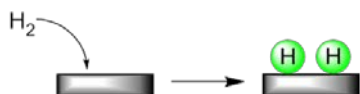
In a PEMFC, only a very small amount of Pt is needed at the anode for the electro-oxidation of hydrogen (HOR) ( $0.05 \text{ mg}_{\text{Pt}} \cdot \text{cm}^{-2}_{\text{geo}}$ ), largely due to the rapid HOR kinetics discussed above. The cost imparted to the full PEM fuel cell by adding Pt to the anode is thus negligible, compared to the cathode, due to the sluggish ORR, and therefore replacing Pt at the anode is not a high priority. While an anode material that can conductivity switch could have some benefits in enhancing the durability of the cathode (explained in Section 2.5.3), few efforts have been directed towards this goal.

In this thesis, the focus is on the HOR at Pt, deposited on a non-carbon support material, while the HOR literature is focused primarily on the HOR on bulk Pt or Pt supported on carbon. However, no differences have been reported in terms of the mechanism and kinetics of the HOR whether or not carbon supports are present. Consequently, it is assumed that the mechanism of the HOR may be independent of the presence of a support material. However, this assumption needs to be validated.

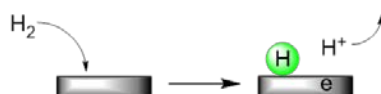
Three mechanistic steps have been proposed for the HOR (Reaction 2.1), namely the Tafel (1905), Heyrovsky (1940) and Volmer (1930) steps, as shown in Figure 2.10, with at least two of these three steps involved. For e.g., in the Tafel-Volmer reaction sequence, if the Volmer step is rate determining (rds), then the Tafel slope is  $120 \text{ mV}\cdot\text{decade}^{-1}$ , while for the Heyrovsky-Volmer (rds) sequence, the TS is  $40 \text{ mV}\cdot\text{decade}^{-1}$ . The observed Tafel slope (anodic and cathodic) and exchange current density ( $i_0$ ) values obtained in the research community are 60 or 120  $\text{mV}\cdot\text{decade}^{-1}$  and ca.  $1 \text{ mA}\cdot\text{cm}^{-2}_{\text{Pt}}$ , respectively. However, recently, it has been suggested that the  $i_0$  values obtained in 3-electrode studies in acidic solutions may be incorrect, due to the very fast kinetics of the HOR.<sup>124</sup>

Studies of the HOR on Pt (or PGMs) deposited on a non-carbon support is a relatively new field of work, as the Pt/C anode behaves so well overall. However, Pt on a non-carbon support catalyst has been used when the fuel was reformed  $\text{H}_2$ , as even with extensive purification, trace amounts of CO are present. It is well known that CO binds strongly to Pt, easily poisoning Pt NPs, with the notion being that a different support material may weaken the CO/Pt bond.

Tafel step:  $H_2 + 2^* \leftrightarrow 2H_{ad}$



Heyrovsky step:  $H_2 + ^* \leftrightarrow H_{ad} + H^+ + \bar{e}$



Volmer step:  $H_{ad} \leftrightarrow ^* + H^+ + \bar{e}$

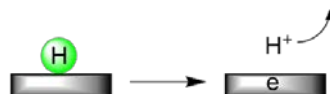


**Figure 2.10** Possible steps involved in the HOR and HER. \* denotes a site on the surface where the reaction occurs.

Typical non-carbon supports that have been studied as a support material for Pt for the HOR include metal oxides and carbides, such as Ti oxides, W oxides or carbides, Sn oxides, etc.<sup>125-126</sup> Liu et. al. reported a higher HOR activity for hexagonal  $WO_3$  modified with polyethyleneimine as compared to Pt/C, attributed to modified interactions between Pt and the support material.<sup>126</sup> Further, a bifunctional effect may help to oxidize CO at lower potentials at this Pt/ $WO_3$  based material. For Pt/C, the CO oxidation (stripping) peak is seen at 0.67 V vs. Ag/AgCl, while for this new composite, two peaks at ca. 0.05 V and 0.53 V vs Ag/AgCl were

seen. This shows that it is easier to remove CO from Pt on the WO<sub>3</sub> substrate than when Pt is deposited on carbon.

Wand and coworkers have shown that the exchange current density for the HOR at Pt supported on several transition metal carbides (TMC) is comparable to what is seen for Pt/C.<sup>127</sup> They tested a range of TMCs and the exchange current densities seen for V, W, and Ti carbides were 1.80, 1.51, and 1.38 mA·cm<sup>-2</sup><sub>disk</sub>, respectively, which is quite close to what is seen for Pt/C (1.63 mA·cm<sup>-2</sup><sub>disk</sub>). A Pt/SnO<sub>2</sub> catalyst showed a stable HOR current (4.25 mA·cm<sup>-2</sup>) over an extended range of potential > 0.8 V vs. RHE, whereas for Pt/C, the current (4.75 mA·cm<sup>-2</sup>) started to decrease at > 1 V, likely due to Pt oxide formation<sup>128</sup> Although transition metal nitrides and oxynitrides are good photoelectrocatalysts for the HER, their catalytic behavior towards the HOR has not been tested as yet. These types of experiments on the HOR are carried out in this thesis work for a Ta oxynitride catalyst, as described in Chapter 7.

## 2.9 Evaluation of Electrocatalyst Activity

The normal electrochemical techniques that are used to establish electrocatalyst activity include cyclic voltammetry (CV), with and without a rotating disk electrode configuration, electrochemical impedance spectroscopy (EIS), and steady state polarization. In CV, the potential is scanned at a certain rate ( $v = \Delta E / \Delta t$ ) over a selected potential range, with the currents that flow indicating which redox processes can occur and how active they are, often just from the onset potential. For activation controlled conditions, CV data can also be used to obtain a Tafel plot and hence a Tafel slope. Furthermore, for quiescent, diffusion controlled reactions, by

changing the scan rate, valuable information can be obtained on the number electrons ( $n$ ) involved in the redox reaction from a peak current and the application of the Randles-Sevcik equation (Equation 2.2),<sup>116, 129</sup>

$$i_p = (2.69 \times 10^5) n^{\frac{3}{2}} A D^{\frac{1}{2}} C_0^* \nu^{\frac{1}{2}} \quad \text{Equation 2.2}$$

When a RDE is used, the diffusion controlled currents are constant (steady state) and sweep rate independent. Using proper boundary conditions, the Levich equation can be applied.

$$i_l = 0.62 n F D^{2/3} \omega^{1/2} \nu^{-1/6} C \quad \text{Equation 2.3}$$

The symbols in the above two equations have their usual meaning, given in the abbreviation section. Further, if the electrochemical reaction exhibits activation control at low overpotentials and diffusion controlled conditions at higher overpotentials, then the Koutecky-Levich (KL) equation can be applied.

$$\frac{1}{i} = \frac{1}{i_k} + \frac{1}{i_l} \quad \text{Equation 2.4}$$

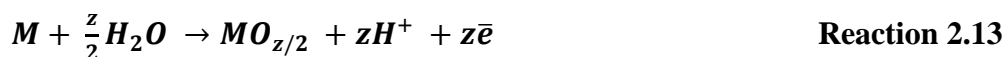
The activation controlled current is given by  $i_k$  and is independent of the diffusion controlled current ( $i_l$ ) as long as the reactants are supplied to the electrode surface rapidly enough. Equation 2.4 can then be used and from the plot of  $1/i$  vs.  $1/i_l$ , the kinetic current ( $i_k$ ) can be obtained, then giving the number of electron involved in the electron transfer (ET) process.

## 2.10 Catalyst Layer Nanostructuring by Anodization

Since electrocatalysis is dependent on the electrode surface area, a high ratio of the surface area to volume of the catalyst is vital and is typically achieved by nanostructuring the catalyst material. Nanostructuring of materials by anodization is considered a low cost method, as it employs a simple set-up, which consists of an electrode (metal), a counter electrode/pseudo reference electrode, a power supply, and a conducting aqueous/organic solution. Although valve metals (e.g., Al, Ti, V, Zr, Nb, Mo, Hf, Ta, and W) have been most commonly used for anodization, other metals and metalloids, such as Mn, Fe, Ni, Co, Bi or Sb, can also be anodized under specific conditions.<sup>130</sup>

The term ‘valve’ is used because of the rectifying effect of the oxide films on the measured current and the oxide acts like a diode. Thus, the current flows preferentially in one direction, making these metals easy to oxidize but their oxides are very difficult to reduce. Most valve metals form an oxide film (e.g., a native oxide layer) almost instantaneously on the bare metal surface upon exposure to air or water, with the native oxide being only 3-5 nm thick.<sup>130</sup>

In the anodization process, the metal electrode is oxidized, causing it to react with water and producing an initially very thin oxide film on its surface (Reaction 2.13).



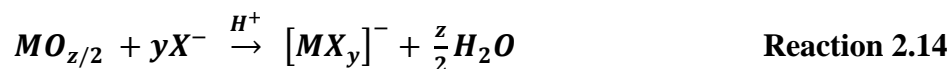
Further growth of the oxide film requires metal cation migration from the metal/oxide interface to the oxide/solution interface or anion migration in the opposite direction. This requires a high electric field, which is typically in the range of 0.1 to 1 x 10<sup>9</sup> V·m<sup>-1</sup>, as the valve

metal oxide films are poorly conducting.<sup>130</sup> The relationship between applied voltage and oxide film thickness is the anodization constant. For example, for Ta oxide formation by anodization, 1 V of applied potential will thicken the Ta oxide film by 1.7 nm.<sup>131</sup>

In order for a metal to be suitable for anodization, it must be susceptible to forming an oxide in the presence of water, and the oxide must be a poor electronic conductor and be relatively insoluble in the anodizing medium.<sup>132</sup> At the same time, some solubility is essential as this is how the pores in a porous anodic film form. Typically, fluoride ions are used to solubilize the anodically formed oxide film and, as a result, several different nanostructures, including a hexagonal (organized) porous film and a nanoarray of oxide nanotubes, can be produced.<sup>133</sup>

Since Masuda et. al. reported the anodically formed, highly ordered hexagonal pattern of Al oxide nanopores, they have attracted much interest.<sup>134</sup> In fact, these porous oxide films can be produced on valve metals in both acidic and alkaline solutions, conditions under which the metal oxide dissolves sparingly. The type of valve metal and electrolyte used, as well as the applied anodic potential and time of anodization, all determine the final morphology of these porous oxide films. For example, Al can form hexagonal nanoporous oxide layers, while the analogous Ta oxide film is nanotubular in nature. In both situations, it is believed that a dense, uniform compact oxide film is formed initially (Reaction 2.13), which then begins to dissolve under polarization in the electrolyte (Reaction 2.14), forming the porous oxide. At long times, a steady-state is reached, leading to one-dimensional growth (thickening) of the nanostructured oxide (Figure 2.11). This explanation was presented by O'Sullivan and Wood<sup>135</sup> for the first time in

their comprehensive study of porous Al oxide formation, and the theory has evolved over time with additions and modifications.



In terms of the formation of nanotubular oxide films at valve metals (e.g., Ta<sub>2</sub>O<sub>5</sub> NTs), rather than porous oxides, the growth mechanism is not very well understood as yet. Over the years, several theories have been proposed, such as the mechanical stress model<sup>136</sup>, the equifield model<sup>137-138</sup>, etc., in order to explain pore initiation, the dissolution of the oxide to form nanotubes and gaps between them, and their self-ordering and continuous growth. Hebert et. al. reported that metal oxide dissolution and metal and oxide ion transport play a critical role in the morphological instability in the initial pore formation stage.<sup>139</sup> They found that the spacing between pores and NTs is determined at the initial stages of anodization and that this depends on several other factors, such as anodization bath condition. In parallel work, the present author carried out a study of the early stages of Ta oxide NT formation, helping to determine that pore initiation occurred significantly earlier in the anodization process than previously thought.<sup>140</sup>

In an effort to understand why nanoporous oxides are formed by anodization of some valve metals, vs. nanotubular oxides on others, or under other conditions, Schmuki et.al. has argued that this relates primarily to the solubility of the metal fluoride complex in water. His group was able to produce a nanoporous TiO<sub>2</sub> film when Ti was anodized in an organic medium containing ultra-low level of water and fluoride ions<sup>141</sup>, as also observed for other valve metals, such as Hf and Zr.<sup>142-145</sup> Al also produced nanopores, while Ti gave NTs, if they are made under

similar conditions with reasonable water content. This was argued to be due to the lower solubility of Al fluoride than Ti fluoride in water.<sup>146-147</sup>

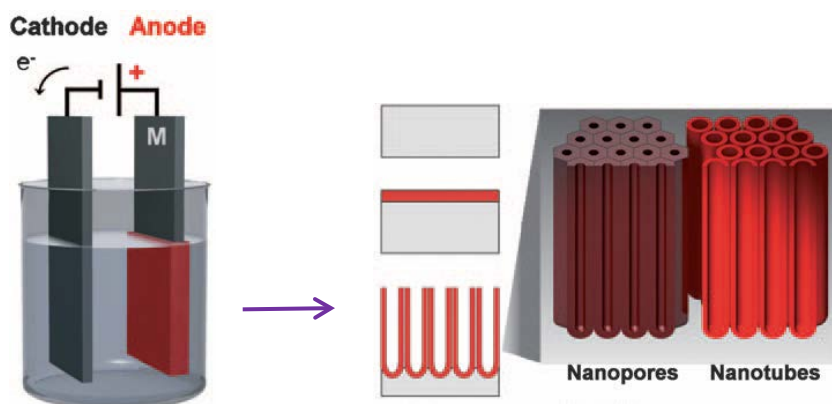


**Figure 2.11** Anodization of valve metals to produce nanopores and nanotubes.<sup>148</sup>

Ta is another valve metal that has been used to make compact oxide films<sup>131, 149-150</sup>, nanotubes (NTs)<sup>15, 17, 140, 151-152</sup> and nanorods<sup>151</sup> by anodization. Compact oxide films are typically made by using 98% H<sub>2</sub>SO<sub>4</sub> solutions, while to achieve any of the other nanoporous morphologies, small amounts of HF are normally added to the electrolyte.<sup>15</sup> In organic media, NTs with very smooth walls have been produced by controlling the water content of the anodization solution. However, Allam et. al. also formed longer (ca. 20 μm long) NTs, which adhered very well to the Ta substrate, by adding 5-10 % dimethyl sulfoxide or ethylene glycol to H<sub>2</sub>SO<sub>4</sub> and HF, but they were unable to produce smooth NT walls as the water content was too

high.<sup>151</sup> Also, it was shown that the Ta NTs do not adhere well when formed in aqueous media for the same anodization time, due to the high solubility of the Ta fluoride complex.<sup>16</sup>

In the Birss group, the preparation of Ta oxide NTs by anodization in ca. 16 M H<sub>2</sub>SO<sub>4</sub> plus varying concentrations of HF, ranging from 0.15 M to 3 M, has been extensively studied, with the aim being to control the nanotubular array properties and to better understand Ta oxide NT growth [Figure 2.12(1)].<sup>15-17, 140</sup> Further, preliminary work has also been carried out on the two step anodization of Zr in an aqueous mixture of [(NH<sub>4</sub>)<sub>2</sub>SO<sub>4</sub> (1 M) + (NH<sub>4</sub>)<sub>4</sub>F (0.5 – 4.5 % wt), also successfully forming nanotubular Zr oxide arrays [Figure 2.12(3)].<sup>153</sup> By anodization of Ta in solutions with a volume ratio of H<sub>2</sub>SO<sub>4</sub> to HF of 9:1 in a two electrode cell, using a cell voltage of 15 V for 2 mins, NTs that were ca. 3 μm in length were formed.<sup>15</sup> However, these NTs were found to be unstable on the Ta substrate and easily detachable, leaving a patchy coverage of NTs on the underlying Ta metal. In fact, under still longer times of anodization (> 10 min) in a 0.85 M HF + 16.4 M sulfuric acid solution, producing NTs up to 20 microns in length, the entire nanotubular array could be removed, giving a free-standing film of the Ta oxide NTs and leaving behind a mirror-like surface.<sup>16, 154</sup>

In fact, one of the original goals of long term anodization of Ta and related valve metals in these HF-containing solutions was to electropolish their surfaces in this way.<sup>19-20, 155</sup> In work carried out by the Kruse group, it was first reported that this shiny Ta surface was covered with an array of nanodimples, having the same dimensions as the original NTs, being roughly 30-50 nm in diameter and separated from each other (center to center) by ca. 50 nm.<sup>19</sup> These dimples

were shown by cross-sectional TEM studies to be covered with a thin, conformal Ta oxide film, roughly 3-5 nm in thickness.<sup>155</sup>

In later work in the Birss group, these dimpled Ta (DT) surfaces were sputter-coated with thin layers (2 – 10 nm) of metals, such as Au, Pt, and later Ag, followed by thermal treatment at 450-900 °C for 0.5 -12 h (temperature and time were different for each metal).<sup>21, 23, 156</sup> This caused these thin film to dewet, forming a surface array of metal nanoparticles (NPs), with one NP per dimple [Figure 2.12(4)], also allowing these NPs to be electrochemically addressable. Recent collaborative work between the Birss and Shi groups has taken this work with DT further, employing high vacuum laser dewetting methods, to better control the temperature and prevent air-oxidation of the Ta substrate.<sup>22</sup>

It was also found that, by further dilution of the acids, e.g., using  $\leq 0.5$  M HF, shorter and more stable NTs can be formed (100-1000 nm in length), with the charge passed during anodization correlating linearly with the NT length, as determined from SEM analysis [Figure 2.12(2)].<sup>17</sup> One of the other interesting features of these short NTs was their interference colors, which is a common phenomenon observed for thin films. However, what was of particular interest is that the color changed quite dramatically when the films were wet or dry, attributed to their differing refractive index when either water or air filled both the NTs and the gaps between neighboring NTs.<sup>18</sup>

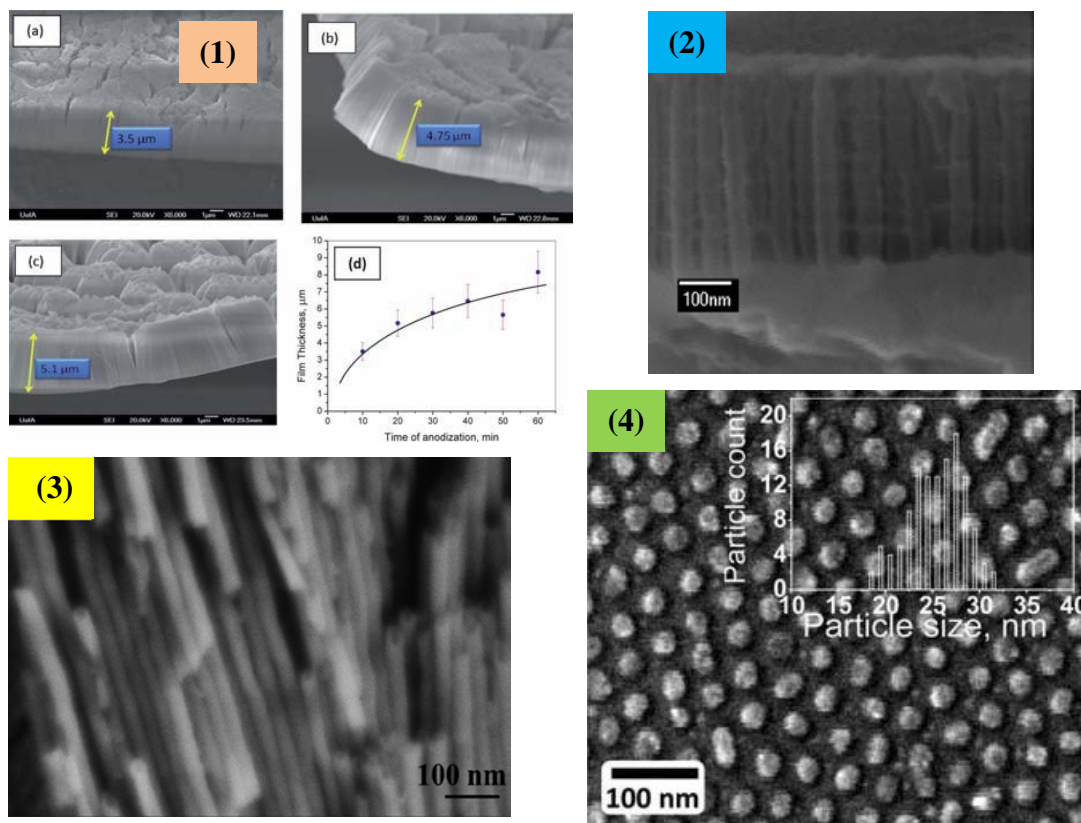


**Figure 2.12** (1) Ta oxide NTs made by anodization of Ta at 15 V vs. Pt CE in 16.4 M  $\text{H}_2\text{SO}_4$  + (a) 0.51 M, (b) 0.85 M, (c) 1.17 M HF for 10 min and (d) NT's length as a function of time in 16.4 M  $\text{H}_2\text{SO}_4$  + 0.51 M HF<sup>16</sup>, (2) Short Ta oxide NTs formed by anodization of Ta at 15 V vs. Pt CE in 16 M  $\text{H}_2\text{SO}_4$  + 0.6 M HF for 23.9 seconds<sup>17</sup>, (3) 2 μm long Zr oxide NTs formed by two step anodization of Zr. First step at 20 V vs. Pt CE in 1 M  $[(\text{NH}_4)_2\text{SO}_4]$  and 4.5 % wt  $\text{NH}_4\text{F}$  for 30 min<sup>153</sup>, and (4) Au NPs were made on the Ta oxide dimples (formed after detaching Ta oxide NTs) by dewetting. 3-4 nm sputter Au thin film is annealed in  $\text{N}_2$  environment for 30 min at 450 °C<sup>21</sup>.

In this thesis, Ta oxide NTs were formed using the methods described above, focusing on NT lengths of 1 μm by using a 0.85 M HF + 16.4 M sulfuric acid solution and anodizing at a cell voltage of 15 V for 5 min. Compact Ta oxides were also formed both as received and dimpled

Ta surfaces and anodizing in 98 %  $\text{H}_2\text{SO}_4$  at 15 V vs. a Pt counter electrode. All of these Ta oxide nanomaterials were then converted to Ta oxynitride by high temperature treatment in ammonia, with Ta oxynitride being the material that is the full focus of this thesis work.

## **Chapter 3 : Experimental Methods**

This chapter summarizes the experimental methods that were used for the work presented in the following chapters.

### **3.1 Preparation of Ta oxide samples**

#### **3.1.1 Anodization of Ta metal**

Unless otherwise stated, Ta foil (99.95% purity, 0.127 mm thickness, annealed) and Pt (mesh and wire) were purchased from Alfa Aesar. Hydrofluoric acid (48% v/v), sulfuric acid (98% v/v), acetone, and isopropanol were purchased from Sigma-Aldrich, and were used as received.

Anodization was performed using a Princeton Applied Research 263A potentiostat or HP Harrison 6824A power supply. The anodization solution was placed in clear Teflon® PFA bottle with a cylindrical (2.5 cm in diameter and 2 cm in height) Pt mesh used as a counter electrode (CE)/reference electrode (RE) [Figure 3.1]. The Ta foil working electrode (WE) was placed in the centre of the cylinder to ensure an even electrical field around it and, for that purpose, a distance of ca. 1 cm between the WE and the CE was maintained.

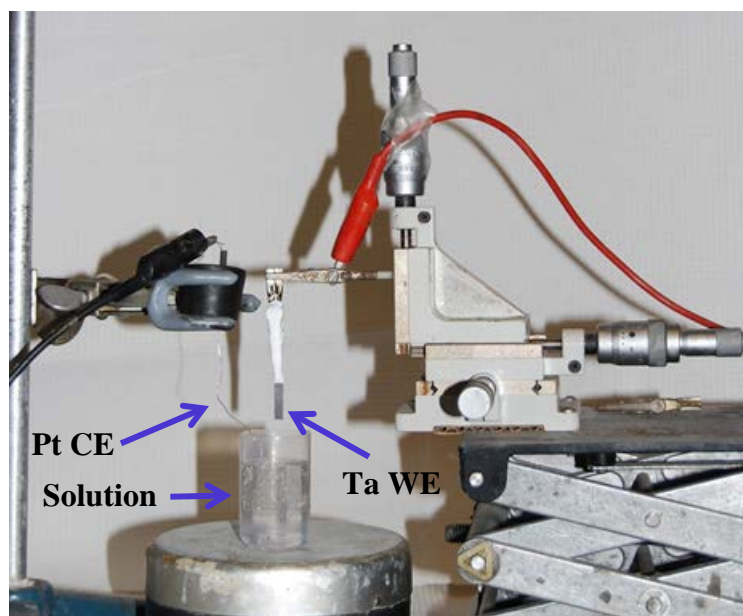


**Figure 3.1** Anodization set-up used for preparing Ta oxide compact layers and nanotubes.

### *3.1.1.1 Preparation of Ta oxide compact layers (CLs)*

1.0 × 0.5 cm Ta foil specimens were cleaned by sonication, successively with acetone, isopropanol, ethanol, DI water, and then dried with Kimwipes®. Compact Ta oxide layers (CLs) were prepared by anodizing the cleaned Ta foil at 15-30 V vs. a Pt mesh counter electrode (CE) for 5 minutes in a room temperature quiescent solution of concentrated H<sub>2</sub>SO<sub>4</sub> (99.999%). The Ta oxide CL was then rinsed with water and air dried. The current vs. time (I vs. t) transient was monitored during the anodization when the potentiostat was used. However, with the power supply, the I vs. t transients were not monitored, but a multi-meter, placed on the voltage measuring mode, was used for tracking the applied potential.

### ***3.1.1.2 Preparation of Ta oxide nanotubes (NTs)<sup>15-16</sup>***

1.0 cm × 0.5 cm Ta foil specimens were cleaned by sonication, successively with acetone, isopropanol, ethanol, DI water, and then dried with Kimwipes®. Ta oxide nanotubes (NTs) were prepared by anodizing the cleaned Ta foil at 15 V vs. a Pt mesh counter electrode (CE) for different times (X min) in a room temperature quiescent solution composed of H<sub>2</sub>SO<sub>4</sub> (16.29 M), HF (0.85 M), and H<sub>2</sub>O (4.72 M). The times of anodization (X min) were 2.5 min, 5 min, 7.5 min and 10 min, and by changing the time of anodization, different NTs lengths were obtained. The Ta oxide nanotubular array was then rinsed with water and air dried. Then, the current vs. time (I vs. t) transient was monitored during the anodization when the potentiostat was used. However, with the power supply, a multimeter, placed on the voltage measuring mode, was used for tracking the applied potential and displaying the current transient, allowing the success of NT formation to be gauged.

## **3.2 Preparation of Ta oxynitride (TaO<sub>x</sub>N<sub>y</sub>) samples**

Ta oxide samples that were prepared as described in Section 3.1 were subjected to ammonolysis/nitriding to obtain TaO<sub>x</sub>N<sub>y</sub> NTs or CLs. This was done by heat treating the samples in a tube furnace at 700 °C under anhydrous ammonia gas, flowing at 10 ml·min<sup>-1</sup> for 7 h. During this nitriding process, the white/grey coloured Ta oxide NTs became yellow-orange in colour, but in the case of the CLs, the brown-yellow Ta oxide samples were converted to a faint yellow color. By changing the flow rate of ammonia, the annealing temperature and the annealing time,

it was found that  $10 \text{ ml}\cdot\text{min}^{-1}$  for 7 h at  $700 \text{ }^\circ\text{C}$  was the best condition to obtain the yellow-orange  $\text{TaO}_x\text{N}_y$  samples.

### **3.3 Deposition of Pt nanoparticles (NPs) on $\text{TaO}_x\text{N}_y$ CLs and NTs<sup>157</sup>**

$\text{TaO}_x\text{N}_y$  CLs or nanotubular samples were left in the 8 mL acetone solution containing 0.1333 g of  $\text{H}_2\text{PtCl}_6\cdot 6\text{H}_2\text{O}$  (Sigma Aldrich,  $\geq 99.99 \%$  trace metal basis) while stirring for  $> 12$  h. Occasionally, additional acetone was added to maintain the volume at 8 mL. The samples were then dried at  $60 \text{ }^\circ\text{C}$  in an oven for  $> 12$  h to remove any remaining acetone solution. The  $\text{Pt}^{4+}$  salt was reduced to  $\text{Pt}^0$  by heating in a tube furnace (Lindberg/Blue 55030A1 Mini-Mite) under a  $\text{H}_2$  environment. The temperature was ramped from room temperature (RT) to  $300 \text{ }^\circ\text{C}$  for 2 h in  $\text{H}_2$  gas and subsequently the samples were maintained at  $300^\circ\text{C}$  under  $\text{N}_2$  for another 2 h to remove excess  $\text{H}_2$  gas from the samples. Finally, the furnace was cooled down to RT for 2 h.

### **3.4 Preparation of colloid imprinted carbon (CIC) based materials**

#### **3.4.1 Synthesis of CIC100**

The synthesis of the CIC powder with a pore size of 100 nm (CIC100) followed a procedure previously reported by the Birss group and others.<sup>75, 158-159</sup> The 100 nm pore diameter was introduced to mesophase pitch (MP) by mixing it with 100 nm colloidal silica particles. Specifically, 1 g of ground Mitsubishi AR mesoporous pitch (MP; particle size of  $< 45 \text{ }\mu\text{m}$ ) was mixed with 20 mL of a  $\text{EtOH}:\text{H}_2\text{O}$  (3:2 v/v) solution and stirred for 1 h. To this mixture, 10 g of silica colloid (Ludox HS-100, with an average particle size of 100 nm) was added dropwise

while vigorously stirring. The temperature of this mixture was raised and held at 80 °C until all of the solvent had evaporated.

The MP/silica mixture was ground to a powder and heated in a N<sub>2</sub> environment from RT to 400 °C for 2 h and then held at that temperature for 2 h for imprinting, followed by cooling to RT. The samples were then carbonized by heating to 900 °C at the rate of 2.5 °C·min<sup>-1</sup> and holding at that temperature for 2 h in a N<sub>2</sub> environment. Finally, the carbonized mixture was cooled down to RT, again at the rate of 2.5 °C·min<sup>-1</sup>. The softening temperature of the MP depends on the starting materials and the process that was used to make the MP, as well as on the addition of silica. To ensure a constant pore size of 100 nm, the MP/silica composite powder was carbonized at 900 °C.

After carburization, the removal of the silica NPs can be done either by immersion in HF or hot concentrated NaOH. Since the latter medium requires prolonged heating at reflux and multiple rinsing steps, it ensures the complete removal of the silica. With HF, however, this technique can be quite rapid and thus the HF medium was used to remove the silica from the composite. Specifically, 1 g of the carbon/silica mixture was treated with 7.5 mL of 50 % HF and 2 mL of H<sub>2</sub>O and stirred for ca.12 h. The resulting CIC100 material was filtered, rinsed and dried in the oven at 120 °C for > 12 h. Finally, the resulting cake-like CIC100 structure was ground using an agate mortar and pestle to decrease the particle size. Figure 3.2 shows the overall CIC100 synthesis route used in this work and described above.

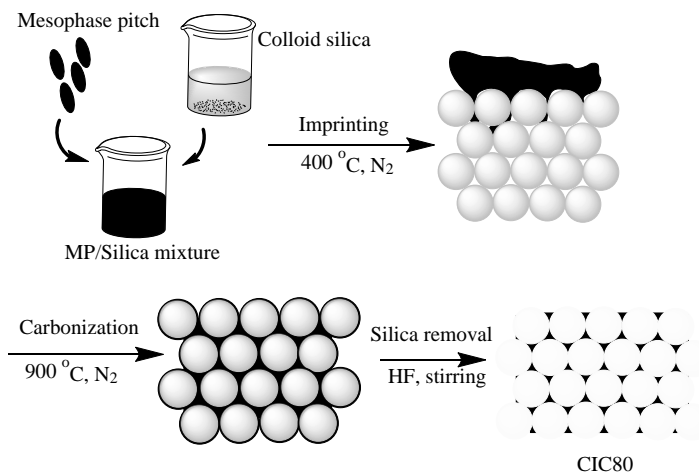


**Figure 3.2** Synthesis scheme for CIC100.

### 3.4.2 Synthesis of TaO<sub>x</sub> NPs on CIC100 (TaO<sub>x</sub>N<sub>y</sub> NPs/CIC100)

Since there is no literature precedent for the synthesis of TaO<sub>x</sub> NPs (nanoparticles) on a carbon powder, such as CIC100, a new procedure was designed and executed. A key consideration was not to hydrolyze the Ta alkoxide too rapidly on the CIC100, because this could result in the formation of rather large NPs. Therefore, the hydrothermal method was eliminated and instead a solvothermal method was employed. Pinna et. al. used the solvothermal method [solvent was benzyl alcohol (BnOH)] to synthesize Ta<sub>2</sub>O<sub>5</sub> NPs with a small size of 3-6 nm in diameter and upon heat treatment, they became 20-30 nm in size.<sup>160-162</sup> The challenge in the work described here was that these TaO<sub>x</sub> NPs had to be made on a solid surface with a high density of oxygenated functional groups. The theory behind the bottom-up synthesis of TaO<sub>x</sub> NPs on the CIC100 was to utilize these functional groups for the anchoring of the NPs.

Under a N<sub>2</sub> blanketed environment, 16 mL of BnOH was charged with 0.1 g of CIC100 and 0.05 mL of Ta(OEt)<sub>5</sub> in a Teflon® cup, which was then transferred to a steel autoclave and sealed. The autoclave was slowly heated to 260 °C in an oven and held at that temperature for 24 h. After cooling to RT, the TaO<sub>x</sub> NPs/CIC100 colloidal suspension was filtered and rinsed thoroughly with EtOH and finally with CHCl<sub>3</sub>. The resulting precipitate was dried at 60 °C for > 12 h.

### **3.4.3 Synthesis of TaO<sub>x</sub>N<sub>y</sub> NPs on CIC100 (TaO<sub>x</sub>N<sub>y</sub> NPs/N-CIC100)**

TaO<sub>x</sub> NPs/CIC100 powders were synthesized according to the procedure outlined in Section 3.4.2 and then nitriding according to the procedure described in Section 3.2. Briefly, 1 g of TaO<sub>x</sub> NPs/CIC100 was placed in a quartz boat, which was then slid into a quartz tube and heated to 700 °C at a rate of 2.5 °C·min<sup>-1</sup> for 7 h under an ammonia flow rate of 10 mL·min<sup>-1</sup>. The resulting TaO<sub>x</sub>N<sub>y</sub> NPs/N-CIC100 powder was cooled down to RT and stored in a vial for further experiments.

### **3.4.4 Synthesis of CIC100 treated with benzyl alcohol (BnOH)**

This material was made as a control for the TaO<sub>x</sub> NPs/CIC100 sample, because during the preparation of the TaO<sub>x</sub> NPs/CIC100 material, the CIC100 powder was also treated in BnOH during the solvothermal synthesis. The procedure is the same as what was outlined in Section 3.4.2.

### **3.4.5 Synthesis of nitrogen-doped CIC100 (N-CIC100)**

This material was made as a control for the TaO<sub>x</sub>N<sub>y</sub> NPs/N-CIC100 because, in the preparation of the TaO<sub>x</sub>N<sub>y</sub> NPs/N-CIC100 material, the CIC100 powder was also treated in NH<sub>3</sub> gas during the nitriding process. The procedure used was the same as what was outlined in Sections 3.2 and 3.4.3.

### **3.4.6 Synthesis of Pt NPs on TaO<sub>x</sub>N<sub>y</sub> NPs/N-CIC100 material**

To be consistent with the preparation of the Pt NPs, the incipient impregnation method was used as the standard procedure, with the details given in Section 3.3. Briefly, 0.05 g of TaO<sub>x</sub>N<sub>y</sub> NPs/N-CIC100 was treated dropwise with 1 mL of an acetic solution of H<sub>2</sub>PtCl<sub>6</sub>.6H<sub>2</sub>O (0.034 g) while vigorously stirring. After evaporation of the acetone in an oven at 60°C for > 12 h, the Pt<sup>6+</sup> was reduced to Pt<sup>0</sup> in H<sub>2</sub> gas at 300 °C for 3 h to yield 20 wt % Pt on TaO<sub>x</sub>N<sub>y</sub> NPs/N-CIC100.

## **3.5 Electrochemical Characterization of Samples**

### **3.5.1 Buffer and electrolyte solution preparation**

All compounds used to make the electrolyte solutions were purchased from Sigma-Aldrich, and were used as received. The pH = 7 phosphate buffer (KH<sub>2</sub>PO<sub>4</sub> and K<sub>2</sub>HPO<sub>4</sub>) and aqueous electrolyte (0.5 M H<sub>2</sub>SO<sub>4</sub> and KOH) solutions were prepared with deionized water purified to a resistivity of 18.2 MΩcm<sup>-1</sup> using a Corning<sup>®</sup> MEGA-PURE MP3A system. To carry out the organic solution electrochemistry, CH<sub>3</sub>CN, obtained from a MBRAUN<sup>®</sup> solvent purification

system, was used with a concentration ratio of analyte to supporting electrolyte maintained at 1:100.

### **3.5.2 Instruments and general experimental methods**

All cyclic voltammetry (CV) experiments were performed using either a CHI 660B (CHI Instrument Inc., Austin, TX) or an EG&G 263A (Princeton instrument, USA) or EG&G 173 in conjunction with a PARC 175 function generator potentiostat. Electrochemical Impedance Spectroscopy (EIS) experiments were carried out using either a Solartron 1287 potentiostat/1255 frequency response analyzer or a Gamry REF-3000 at various applied dc potentials vs the reference electrode, with a superimposed 10 mV AC excitation signal. The sweeping frequency range was from 1 MHz to 0.01 Hz, with the collection of 10 data points per decade. All data analysis and electrochemical experiments were controlled by the built-in software of the CHI instrument (Corrware software, version 3.1) or the Gamry built-in software. ADInstrument Power lab 2/25 was used for recording of the data from the EG&G 173 and ADInstrument chart 5 was used for data analysis. The RDE experiments were performed using a Pine Instrument® compact Pine rotator.

All of the electrochemical work was carried out using a standard three electrode set-up with the Ta/TaO<sub>x</sub>N<sub>y</sub> or carbon-based materials as the working electrode (WE), a platinized Pt mesh as the counter electrode, and a reversible hydrogen electrode (RHE) as the reference electrode (RE). In the studies in acetonitrile, an Ag/Ag<sub>2</sub>O pseudo reference electrode was employed. All potentials in this thesis are referenced to the RHE.

For all CV (with and without the RDE configuration) and EIS experiments, the solutions were purged with N<sub>2</sub> for 30 min before the experiments began and a N<sub>2</sub> blanket was maintained over the cell solution during data acquisition. The oxygen reduction reaction (ORR) and hydrogen oxidation reaction (HOR) experiments were initially performed in deaerated solutions and then they were repeated with their respective gas (O<sub>2</sub> for ORR and H<sub>2</sub> for HOR) saturated solution. Experiments were normally repeated minimum 3 times in order to establish the WE integrity and data reproducibility.

### **3.5.3 Working Electrodes (WE)**

In this thesis, basically two types of WEs were used, namely the Ta oxide/TaO<sub>x</sub>N<sub>y</sub> CL or NTs that were formed on a Ta foil or rod and an ink made of CIC100-based materials deposited on a glassy carbon (GC) electrode.

#### ***3.5.3.1 Working electrodes made with Ta foils or rods***

Upon anodization, the materials of interest were coated on a Ta foil or rod and were used directly as the WE. The Ta foil-based WEs were attached to a Cu clip and the Ta rod-based WEs were part of the RDE connected via the shaft of the rotor to the potentiostat.

#### ***3.5.3.2 Glassy Carbon (GC) working electrodes made with CIC100-based materials***

Catalyst inks based on the CIC100 materials were prepared and then drop-casted on the GC (Alfa Aesar; 5 mm dia) electrode surface. Prior to ink deposition, the GC surface was

cleaned thoroughly by mechanical polishing with 0.03  $\mu\text{m}$  alumina slurry on a microcloth and sonicating successively in EtOH and water for 5 mins. Finally, it was dried in a stream of  $\text{N}_2$ .

Determining the best composition of the inks was quite challenging, as several alcohols (EtOH,  $i\text{PrOH}$ ,  $n/\text{sec}/i/\text{tert}$  BuOH) had to be tested to improve the dispersion of the composite. Out of all of the alcohols,  $n\text{BuOH}$  gave the best dispersion of the composite. However, spreading of the ink onto the shroud of the electrode (Figure 3.2) made the amount of material that participated in the electrochemistry somewhat uncertain. This is probably due to the fact that the intermolecular interactions between  $n\text{BuOH}$  and the shroud material, polyether ether ketone (PEEK), were too strong. The ink spreading problem was not confined to  $n\text{BuOH}$ , but rather it was observed with other alcohol-based inks as well, although to a lesser extent. After several attempts, it was decided that the approach used previously in the Birss group<sup>163-164</sup> was preferred for better comparison with these prior results. The ink formulation is always involves a tuning of the inter- and intramolecular forces of the materials used. Furthermore, the shimming of the electrode on the balance played a minor role in removing the spreading issue.

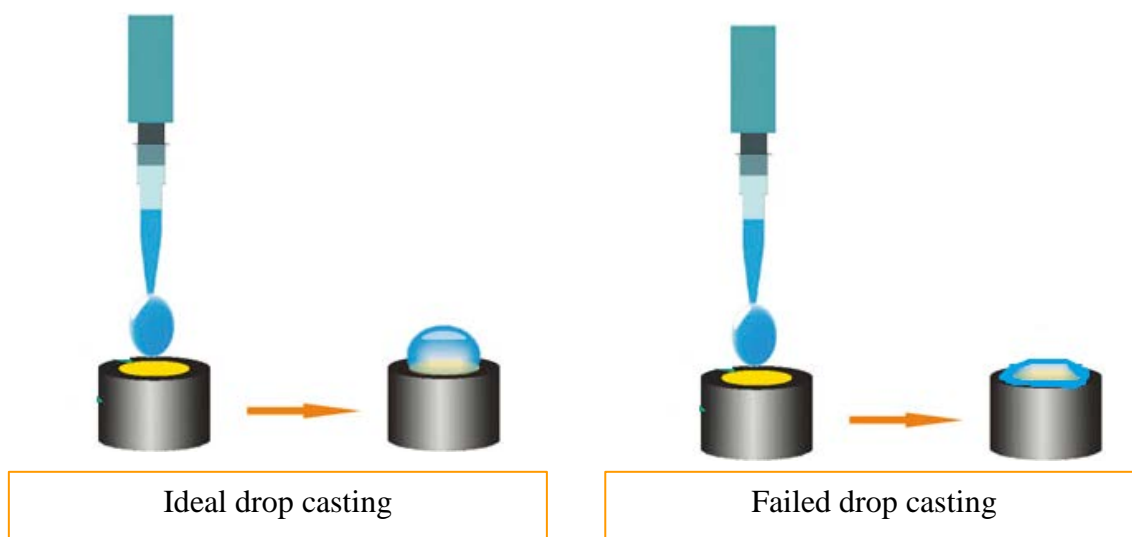


**Figure 3.3** Ink spreading onto the shroud of the GC electrode.<sup>165</sup>

The next step is catalyst ink drying to obtain a uniform film on the electrode surface. Garsany et. al. at the National Renewable Energy Laboratory (NREL) has tried three methods to obtain a uniform film on a GC electrode.<sup>166-167</sup> The first method involves stationary film drying, where a drop-casted catalyst ink is air dried at 40 °C. The second method involves ‘spin coating’ of the ink, where the deposited ink on the inverted RDE is rotated and finally, for thin films, the <sup>i</sup>PrOH drying method has been used, where the ink is dried in a beaker with <sup>i</sup>PrOH at 40 °C. In the present work, a minor variation was made in order to accommodate the available resources. The drop casted ink, deposited on the GC electrode surface, was air dried using two methods, using an oven at 40 °C and on the lab bench at room temperature. The film made by the former method showed visible cracks and less uniformity, while the films formed under ambient

conditions exhibited fewer cracks and more uniformity. Finally, after several attempts, the optimum conditions for preparing the ink were identified.

In this work, the catalyst or catalyst support ink was prepared by adding 0.12 g of 12% wt H<sub>2</sub>SO<sub>4</sub>/EtOH solution to 0.01 g of a CIC100 based sample and sonicated for 5 min to disperse the carbon based material in the solvent. Then, 0.4 g of 1% wt Nafion/EtOH solution was added and the mixture was sonicated again for 30 min, after which a 10 µL drop of the ink was drop casted on the cleaned GC electrode surface and dried at room temperature.

### **3.5.4 Corrosion Evaluation Protocols**

There are two protocols used in the thesis to assess the corrosion susceptibility of the catalysts and support materials investigated in this work, namely assessing the changes in the cyclic voltammograms (CVs) after accelerated durability testing (ADT) and calculating the corrosion charge from the potentiostatic ADT. For the CIC100 based materials, the double layer (DL) and pseudocapacitance (PC) charges were calculated separately from the CV results.

#### ***3.5.4.1 Corrosion Evaluation protocol based on CV***

For the TaO<sub>x</sub>N<sub>y</sub> NTs, with and without Pt deposited, 100 CV cycles were run, with the first and the last CVs compared for the loss in electrochemical features (current, charge) and an increase in real surface area. Also, CVs were collected before and after the potentiostatic ADT experiments to determine the changes in the double layer (DL) and pseudocapacitance (PC) charges.

(a) *Calculation of PC charge for CIC100 based materials*

The CVs were collected between 0.05 V to 1.1 V vs. RHE at  $10 \text{ mV}\cdot\text{s}^{-1}$  and a typical CV trace obtained is shown in Figure 3.3. The peaks in the CV are believed to be due to the oxidation/reduction of the quinone/hydroquinone redox couple (further information is given in Chapter 6, Section 6.6.2). After baseline correction, the peak charges were obtained using the OriginPro® 2017 data analysis and graphing software, with this software also used for baseline correction. Unless otherwise mentioned, the PC charge is the average of the anodic and cathodic PC charges seen with the CVs.

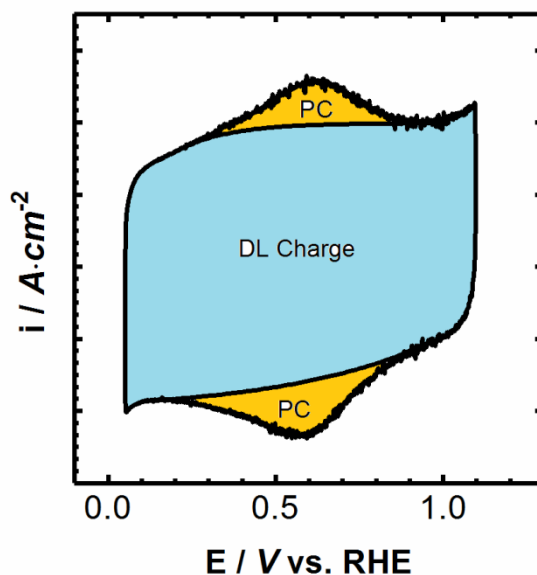


**Figure 3.4** Graphical representation showing the potential range over which the double layer (DL) and pseudocapacitance (PC) features are seen and how charges were obtained from the CVs of the carbon-based materials under study here.

*(b) Calculation of DL charge for CIC100 based materials*

The entire anodic and cathodic segment of a CV was integrated separately to determine the charge passed and the respective peak charges were deducted from the total charge. Generally, the average DL charge was used for further analysis in the thesis.

**3.5.4.2 Corrosion evaluation protocol based on potentiostatic ADT**

The potentiostatic ADT protocol used in this work is discussed in Section 2.6 in detail but is explained briefly here. This is a modified DOE protocol, in which a mimic of the PEMFC start up/shut down process was created in a laboratory environment.<sup>11</sup> The potentiostatic ADT involves holding the WE at 1.4 V vs. RHE for 50 s and then at 0.8 V for 10 s. These anodic and cathodic steps are considered a single full cycle (Figure 3.5c) and 18 of these cycles were repeated for 1080 s. Further, a steady state CV was collected before and after this potentiostatic stepping experiment (Figure 3.5b and d).

The charge passed in each ADT cycle was obtained by integrating the I vs. t curve. The anodic ( $q^+$ ) and cathodic ( $q^-$ ) charges were thus obtained at 1.4 V and 0.8 V vs RHE, respectively. The corrosion charge [Equation 3.1] was assumed to be the difference between the anodic and cathodic charges.<sup>164</sup> After obtaining these charges, they were often subjected to further analysis to establish the corrosion stability of the materials studied here.

$$\text{Corrosion Charge} = [(q^+) - (q^-)] \quad \text{Equation 3.1}$$

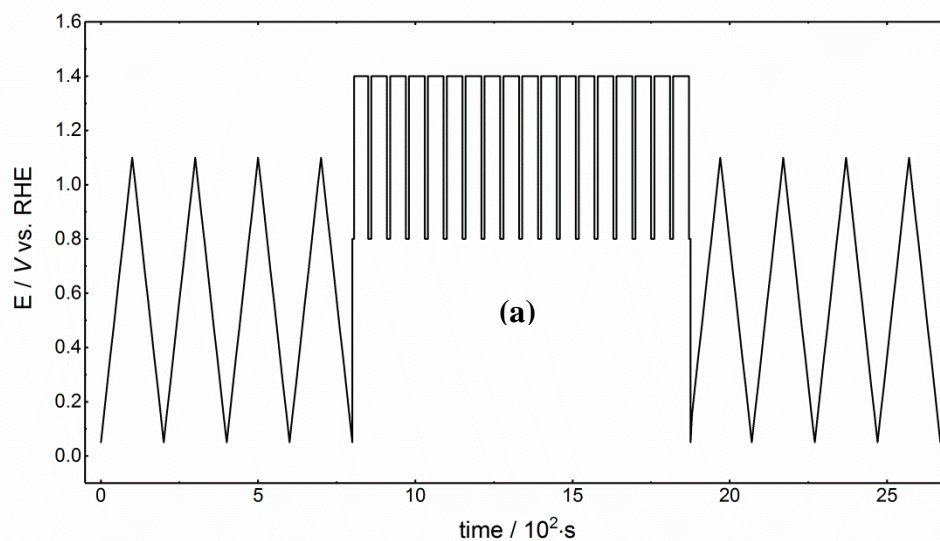
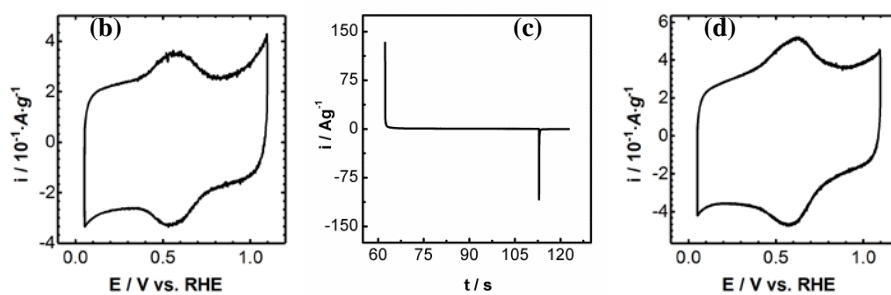


**Figure 3.5** (a)  $E$  vs.  $t$  program used for corrosion evaluation of catalysts and supports, based on the potentiostatic ADT. Steady-state CVs were collected before and after potential stepping, as shown in (b) and (d), respectively. (c) shows the  $I$  vs  $t$  transient for one cycle of potentiostatic stepping (1.4 V for 50 s and 0.8 V for 10 s).

### 3.6 Material Characterization Techniques

Several techniques were used to characterize the materials studied in this thesis to determine their morphology, composition and structure.

#### 3.6.1 Field Emission Scanning Electron Microscopy/Energy Dispersive X-Ray Spectroscopy (FESEM/EDX) Analysis

Because of the limitations of optical imaging, electron microscopy (EM) was developed to image the surface morphology of samples, assuming that they are sufficiently conducting. When an accessory, such as EDX, is attached, the composition of the imaging sample can also be obtained. Figure 3.6 shows a schematic of an SEM and various detectors that can be positioned at different locations to capture the electrons emitted from a sample, with these electrons eventually used for imaging. In this thesis, a secondary electron detector was used primarily.

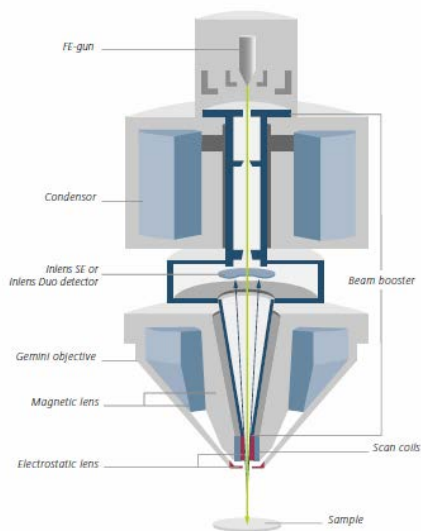


**Figure 3.6** Schematic diagram of the Zeiss Sigma VP SEM at the University of Calgary.<sup>168</sup>

All Field Emission Scanning Electron Microscope (FESEM) images were obtained using a Zeiss SIGMA VP FESEM (Carl Zeiss Microscopy Canada Ltd, Toronto, ON) using the following parameters: 2.0 kV accelerating voltage, mostly secondary electron detector (occasionally an in-lens detector was used) at various magnifications, and a slow capture scan. All Ta foil and rod samples were supported on an Al stub with conducting carbon tape (Ted Pella, Inc.) and Ag paint (Ted Pella, Inc.), while all CIC100-based powder samples were supported on an Al stub with conducting carbon tape (Ted Pella, Inc.). EDX (Inca EDX attached to SEM) analysis was performed to determine the composition of the samples.

### **3.6.2 Transmission Electron Microscopy/ Energy Dispersive X-Ray Spectroscopy (TEM/EDX)**

TEM is another electron microscopic method that can be used for imaging, with the electron beam passing through the sample. Unlike SEM, the acceleration voltage in TEM is > 200 keV, giving a theoretical wavelength of ca. 2.5 pm. Also, detectors with various capabilities can be attached to the TEM. All of the TEM images in this thesis were obtained with a Tecnai TF20 G2FEG-TEM instrument (FEI, Hillsboro, Oregon, USA), located in the Microscopy Imaging Facility (Health Sciences Centre) at the University of Calgary.

TaO<sub>x</sub>N<sub>y</sub> nanotubular samples were immersed in ethanol and sonicated to remove them from the Ta substrate. A few drops of the suspended NTs were then placed on one side of a Lacey Carbon grid for TEM imaging. The CIC100-based powder samples were also dispersed in ethanol (10 mg of sample in 1 mL of EtOH) by sonication and a drop was placed in a Lacey Carbon grid. Images were obtained in dark and bright field modes and EDX analysis was

performed to obtain the composition. Further, the ImageJ image processing program was used to determine the NPs size.

### 3.6.3 X-Ray Photoelectron Spectroscopy (XPS)

In XPS, a sample to be analyzed is irradiated with photons that are in the X-Ray energy range. The core level electrons of the atoms in the sample absorb the irradiated energy and emit photoelectrons. The emitted photoelectrons from the surface can be captured, based on their energy, which, in turn, relates to nature of the material and the atomic environments. From the captured photoelectrons, valuable information, such as the binding energy of the emitted electron, can be calculated based on the Einstein equation ( Equation 3.2).

$$h\nu = KE + BE + \varphi \quad \text{Equation 3.2}$$

where  $h\nu$ , KE, BE and  $\varphi$  are the energy of the irradiation source, and the kinetic energy, binding energy and work function of the emitted electron, respectively.

All X-ray Photoelectron Spectroscopy (XPS) analyses were performed using a PHI VersaProbe 500 (Catalyst Surface Science Laboratory, Department of Chemical and Petroleum Engineering, University of Calgary) with a 15 keV Al source (monochromatic) at 50 W and a beam diameter of 200.0  $\mu\text{m}$ . The samples were loaded in a custom-made sample holder and the spectra were collected with double beam neutralization, i.e., using low energy electron and  $\text{Ar}^+$  beams. All peaks were reported against the C1s peak at  $284.8 \pm 0.2$  eV and peak fitting was performed with Multipak 9.2.0.5 (Physical Electronics, USA) software. The depth profile calibration was carried out using 100 nm  $\text{SiO}_2$  particles on a standard carbon wafer. The

sputtering of the SiO<sub>2</sub> wafer was performed using a fixed ion gun (2 kV, 1.5 μA, 2x2 mm) at a standard sputtering rate of 10.5 nm·min<sup>-1</sup>.

#### 3.6.4 X-Ray Diffraction (XRD)

XRD is a technique that can be used to study the structure of a solid sample. When a solid sample is struck with X-rays, the atomic planes in the solid sample can cause interference in the incident X-rays when they exit the sample, which is called X-ray diffraction. Constructive interference occurs when the path length difference between the two X-ray waves is equal to the integer of the path length, which is the basis of Bragg's law (Equation 3.3) and hence the X-ray diffraction.

$$2 d \sin\theta = n \lambda \quad \text{Equation 3.3}$$

Here,  $d$  is the interatomic distance ( $d$  spacing),  $\theta$  is the X-ray incident angle,  $\lambda$  is the wavelength of the X-ray, and  $n$  is an integer. Since the  $d$  spacing is unique to a solid sample, specific information about the structure of the sample can be obtained from the XRD data.

All XRD measurements were performed at room temperature with a Rigaku Multiflex X-Ray Diffractometer (Department of Geoscience, University of Calgary) using Cu K $\alpha$  ( $\lambda=0.15406$  nm) radiation. The operating conditions were 40 kV and 40 mA and the samples were scanned at 2 min-degree<sup>-1</sup> with a sample width of 0.020°. Samples were placed on an Al stub covered with a silica plate. Reitveld (with the LeBail technique) refinement, using the General Structure Analysis System (GSAS) package<sup>169</sup> with an EXPGUS interface<sup>170</sup>, was performed on

the XRD data sets through a collaboration with Dr. Wang Hay Kan, currently at the Australian Nuclear Science and Technology Organization.

### **3.6.5 Diffuse reflectance UV-Visible Spectroscopy (DRUV-Vis)**

In this thesis work, DRUV-Vis spectroscopy was used to obtain the band gap of the TaO<sub>x</sub>N<sub>y</sub> NTs, with the thin layer of yellow-orange TaO<sub>x</sub>N<sub>y</sub> NTs being ideal for diffuse reflectance measurements. From the reflection edge of the spectrum, the band gap of the TaO<sub>x</sub>N<sub>y</sub> was calculated.

Diffuse reflectance spectra of the nanotubular arrays were collected using a double beam scanning Cary 5000 UV-Vis-NIR spectrophotometer (Dr. Todd Sutherland Laboratory, Department of Chemistry, University of Calgary), equipped with an external diffuse reflectance accessory. Typically, a fast scan between 200 nm to 800 nm was used, and then depending on the reflection edge, a slow scan with a narrow wavelength range was selected to obtain the appropriate data.

### **3.6.6 Elemental Analysis (EA)**

The carbon, nitrogen, and hydrogen content of some of the samples was determined by combustion EA. Since a combustion process is involved, the oxygen content cannot be directly determined. However, if the other elements present are analyzed using other techniques, then the missing mass is considered to arise from the sample's oxygen content. In this work, a Perkin Elmer 2400 EA instrument (Department of Chemistry, University of Calgary) was used for EA.

### 3.7 Error Analysis

All materials used in this thesis were weighed using an AB204 Metler-Toledo balance that has a reported error of  $< 2$  % wt. All solutions were prepared in volumetric flasks, which have a ca. 0.1% error in volume. For anodization solution preparation and catalyst or catalyst support ink drop casting, Eppendorf pipettes (10-1000  $\mu\text{L}$ ) were used, with the 10  $\mu\text{L}$  pipettes having an error of  $\pm 1.4$  % and a 1000  $\mu\text{L}$  pipette having an error of  $\pm 0.8$  %. The proper liquid drawing and delivery methods were used in order to minimize any errors while using Eppendorf pipettes. The error in the EA data was estimated at  $< 3$  % wt.<sup>171</sup>

All electrochemical measurements were repeated for consistency at least three times and the representative data are presented in this thesis, with the error between data sets found to be  $< 5$  %. The error in the potentiostats was periodically evaluated by obtaining EIS (between 100 kHz to 0.1 Hz) or I vs E data using a dummy cell (with known circuit elements) and comparing the measured and theoretical values. Typically,  $< 5$  % of errors were then found. Furthermore, the reference electrode (RHE) was always purged with  $\text{H}_2$  30 min prior to the experiments to ensure accuracy of the WE potential against the RE.

The NP and NT sizes were typically determined using ImageJ processing software and histograms were constructed based on the findings. 82-90 % of the NPs were normally within the standard deviation of the histogram, above the theoretical natural distribution of 68 %. The scale bar error for the Tecnai F20 is reported to be in the range of  $\pm 0.2$  Å.<sup>172</sup> The calculation of the

specific area of the Pt NPs was based on the NP size obtained from TEM imaging, where the NPs were assumed to have a spherical shape.

The NT lengths were measured using the FESEM for at least 25 different samples and the relative standard deviation error was found to be  $\pm 30\%$ .

In terms of the reproducibility of the Ta oxide and TaO<sub>x</sub>N<sub>y</sub> NT dimensions, the most significant error arose from the variability in the Ta foil that was purchased from Alfa Aesar, although the foil purity, density and hardness remained the same. Ta foil from the new source had a matte finish and efforts made to polish it did not produce the desired finish. The surface roughness of this foil could be seen clearly and, as a result, some of the NTs were situated on steps or have larger grain boundaries.

The Cary 5000 UV-Vis-NIR spectrophotometer typically has a resolution of  $4\text{ cm}^{-1}$  with an error of  $2\text{ cm}^{-1}$ .

## Chapter 4 : General Electrochemical Characteristics of TaO<sub>x</sub>N<sub>y</sub> Nanotubes

The majority of the work shown in this chapter has been published: Abhayawardhana, A. D.; Birss, V. I., Conductivity Switching N-Doped Ta Oxide Nanotubular Arrays, **Journal of Physical Chemistry C** 2015, 119, 24, 13847-13857.

### 4.1 Introduction

The primary goal of this Chapter is to present and explain the electrochemistry of the TaO<sub>x</sub>N<sub>y</sub> nanotubes (NTs), developed in this work, and then to be used as an electrocatalyst or electrocatalyst support material for application in proton exchange membrane fuel cells (PEMFCs). This chapter also includes aspects of the electrochromism of TaO<sub>x</sub>N<sub>y</sub>, which is blue coloured in the reduced state of Ta and yellow-orange coloured in the oxidized state of Ta.

A general overview of this material is provided in Chapters 1 and 2 (Sections 2.3.1 and 2.5.1.3). It is noted there that TaO<sub>x</sub>N<sub>y</sub> is an n-type semiconductor (SC) due to the formation of anion vacancies in the lattice, having a relatively small band gap (2.4 eV).<sup>173</sup> Although semiconductor electrochemistry is quite well established, the focus to date has been primarily on elements in Group IIIB to VB [CAS group names of 13 to 15], whereas there is less literature on semiconductors derived from transition metal compounds.

Semiconductor (SC) electrochemistry can be different from the electrochemistry observed with normal conducting electrodes, as the potential drop is located both at the electrode/solution interface and within the semi-conductor itself. As a result, a space charge layer (SCL) is formed inside the SC phase, which has a capacitance that is much higher than the Helmholtz layer at

metal/solution interfaces, with the width of the SCL typically being in the range of 100 nm. Further, the formation of a SCL decreases the charge carrier density inside the semi-conducting layer, thus increasing the electrical resistance. Band bending of the SC complicates the situation further, such that most of the potential drop occurs in the band bending region of the SC. For n-type materials, the SCL becomes wider as the applied potential is made more positive and vice-versa. In these situations, the SCL is called the depletion and enrichment layer, respectively.

Here, we examine the electrochemistry of  $\text{TaO}_x\text{N}_y$  nanotubes (NTs) in comparison with that of the Ta oxide ( $\text{Ta}_2\text{O}_5$ ) NT precursors. The results show that the  $\text{TaO}_x\text{N}_y$  NTs, which are shown to contain evenly spaced holes ca. 25 nm in diameter along their length, are electrochemically inactive at potentials  $> 0.6$  V, but active at potentials at  $< \text{ca. } 0.6$  V vs. RHE in aqueous solutions and also in dry acetonitrile (containing tetrabutylammonium hexafluorophosphate as the electrolyte). This electroactivity is assumed to be related to the reversible  $\text{Ta}^{5+}/\text{Ta}^{4+}$  oxide redox process, which involves proton or cation insertion and expulsion. An analysis of the charge passed during this reaction is consistent with a surface reaction of this kind. Both  $\text{Ta}_2\text{O}_5$  and  $\text{TaO}_x\text{N}_y$  NTs are shown to be n-type semiconductors, with their semiconducting behaviour also depending on the pH. This chapter also reveals that the  $\text{TaO}_x\text{N}_y$  NTs exhibit electrochromism, being orange-yellow in color in the oxidized state ( $\text{Ta}^{5+}$ ) at 1.5 V vs. RHE and black-bluish at -0.4 V vs. RHE when they are reduced ( $\text{Ta}^{4+}$ ). In this work, the exact x and y coefficients in  $\text{TaO}_x\text{N}_y$  are not given, although the ratio of x:y is likely close to 1, based on the X-ray photoelectron spectroscopy results reported here. It is also of interest that the morphology of the  $\text{TaO}_x\text{N}_y$  NTs is a bit different from their precursors, the  $\text{Ta}_2\text{O}_5$  NTs, as the

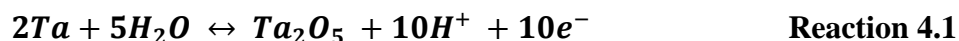
TaO<sub>x</sub>N<sub>y</sub> NTs have regular holes along the NT walls, whereas the walls of the oxide NTs are fully intact. Finally, this chapter also examines the effect of TaO<sub>x</sub>N<sub>y</sub> NT length on their electrochemistry, showing that a 5 min anodization time (giving a ca. 1 μm NT length) has the most stable structure as well as the optimum electrochemistry.

## 4.2 Results and Discussion

### 4.2.1 Morphology and composition of Ta<sub>2</sub>O<sub>5</sub> and TaO<sub>x</sub>N<sub>y</sub> nanotubes (NTs):

Anodization of Ta metal at 15 V vs. the combined pseudo-reference/counter electrode (Pt gauze) in a solution containing H<sub>2</sub>SO<sub>4</sub> (16.3 M) and HF (0.85 M) results in the formation of a Ta oxide nanotubular surface array (Figure 4.2a),<sup>15</sup> according to Reactions 4.1 and Reaction 4.2

Anodic Oxidation:



Chemical Dissolution:



A typical current density (i) vs. time (t) curve obtained during Ta<sub>2</sub>O<sub>5</sub> NT formation is shown in Figure 4.1a, with the inset of the figure showing the i vs t behaviour in the first few seconds. At ca. 250 sec, a small current peak is seen, similar to what has been observed by other members of the Birss group.<sup>18</sup> This peak has been attributed to the dissolution of the Ta oxide close to the Ta metal substrate or due to the detachment of some of the NTs from the Ta substrate. The i vs. t curve is traditionally divided into three stages, as dictated by the characteristics of the curve, namely (i) compact oxide formation (Reaction 4.1), (ii) dissolution

of oxide in the presence of  $F^-$  ions (Reaction 4.2) and NT formation, and (iii) steady-state lengthening of the NTs. However, this classical interpretation of the  $i$ - $t$  data has been modified recently.<sup>174</sup>

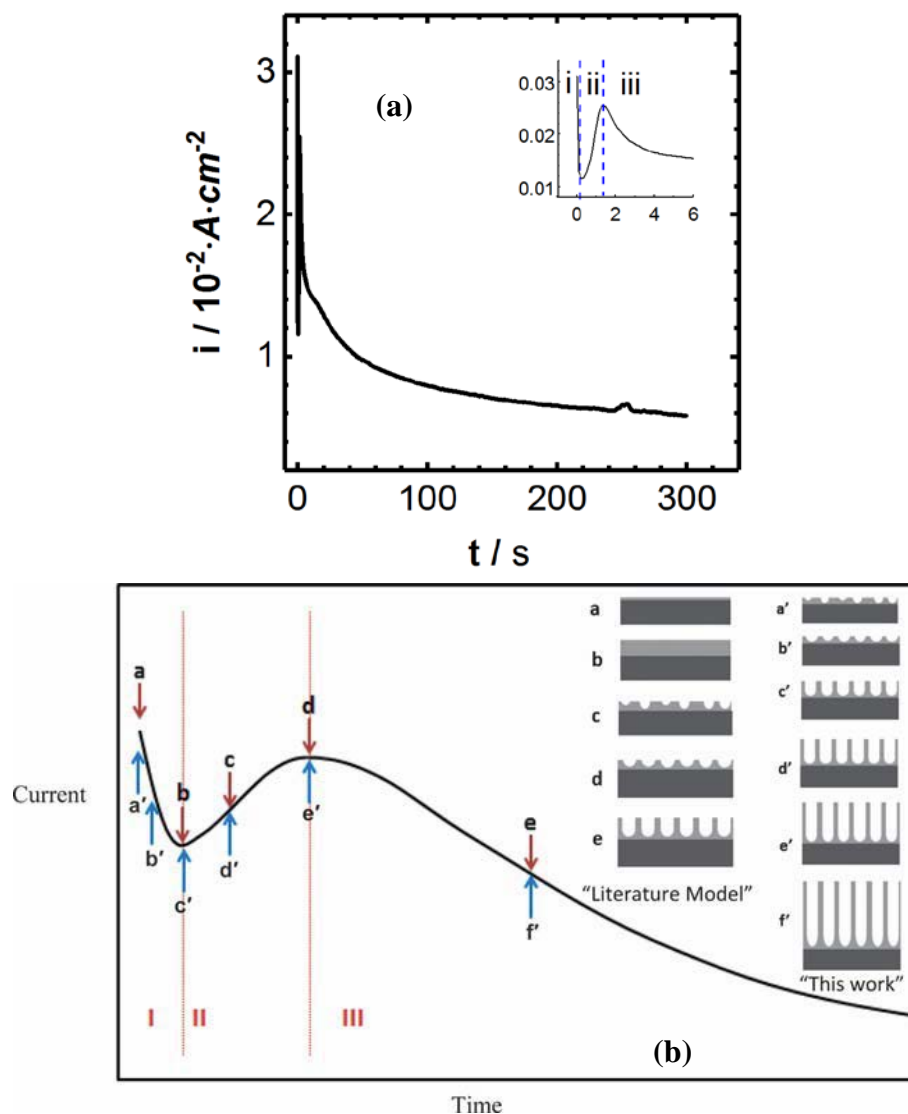


**Figure 4.1** (a) Typical current density vs. time curve obtained during Ta oxide NT preparation. The inset shows the expansion of the first few seconds of the  $i$  vs.  $t$  results, with (b) showing a comparison of the  $i$  vs.  $t$  data obtained here relative to the literature.<sup>140</sup>

In this previous work, it was reported that initiation of Ta oxide dissolution and NT formation (Figure 4.1b) takes place simultaneously with compact oxide formation, while at the local minimum in stage (ii), oxide formation ceases. Then the current starts to increase due to dissolution of the oxide layer, resulting in its thinning, and in stage (iii), steady-state lengthening of the NTs occurs. Although the  $i$  vs.  $t$  curves were explained using the FESEM images at these specific stages, a full theory of NT formation is yet to materialize, with a summary of the proposed literature mechanisms given in Section 2.10.

In this thesis work, four different lengths of the Ta oxide NTs were synthesized by varying the time of anodization (2.5 min, 5 min, 7.5 min, and 10 min), with the NTs formed in 5 min of anodization being the main focus of the thesis. Figure 4.2a shows that 5 min of anodization and 30 min of annealing in  $N_2$  at  $450^\circ C$  results in a nanotubular film (which is white in color) that is ca.  $1 \mu m$  in thickness. This is seen most clearly from the edge of a cracked region, where some NTs have been lost, consistent with what has been reported previously.<sup>15-16</sup> The NTs are roughly 30 nm in diameter, similar to what has been seen in previous reports for Ta oxide,<sup>15</sup> as well as for oxide NTs formed on metals such as Ti,<sup>175</sup> Zr,<sup>176</sup> and Hf.<sup>177</sup>

In regions where the NTs have fallen off, Figure 4.2a also shows that the underlying Ta substrate is patterned with close packed hexagonal shallow pores, or nanodimples (NDs),<sup>15</sup> demonstrating that each NT was housed in a dimple (Figure 4.2a). Also, it is clearly visible in Figure 4.2a that the NTs are separated from each other at their base but not closer to the outer surface of the array, due to the presence of a surface overlayer that is not removed, even after annealing at  $450^\circ C$  for 30 min. It is believed that the surface overlayer represents the un-

dissolved compact/barrier oxide layer that was formed in the initial stages of the anodization process.<sup>178</sup>

In comparison, Figure 4.2b shows what appears to be a very similar structure for the nitrated NTs, formed after 7 h of ammonolysis of the Ta oxide NTs at 700 °C. These NTs, which are now a yellow-orange color, are still roughly 40 nm in diameter, similar to what is seen for the Ta oxide NT precursor (Figure 4.2a). Also, they appear to have adhered very well to the Ta substrate during exposure to the high temperatures required to form  $\text{TaO}_x\text{N}_y$ , as the Ta surface is still essentially fully covered by the nanotubular array. However, it is interesting that the thin overlayer seen on the Ta oxide arrays in Figure 4.2a is now no longer present.

Figure 4.2c and d show the high resolution TEM (HRTEM) images of the base of the ca. 1  $\mu\text{m}$  long Ta oxide and  $\text{TaO}_x\text{N}_y$  NTs, respectively. Similar to the NT diameter seen in the FESEM images in Figure 4.2a and b, when the Ta oxide NTs were formed at 15 V for 5 minutes, the outer and inner diameters of the Ta oxide NTs are 40 nm and 20 nm, respectively. As revealed by the TEM image (Figure 4.2c), the base of each Ta oxide NT has a hemispherical or scalloped shape (the inverse of the nanodimples left on the surface when NTs are removed). Further, HRTEM images of the Ta oxide NT walls (Figure 4.2c) do not show any phase contrast, suggesting that these NTs are amorphous, not crystalline, in nature.

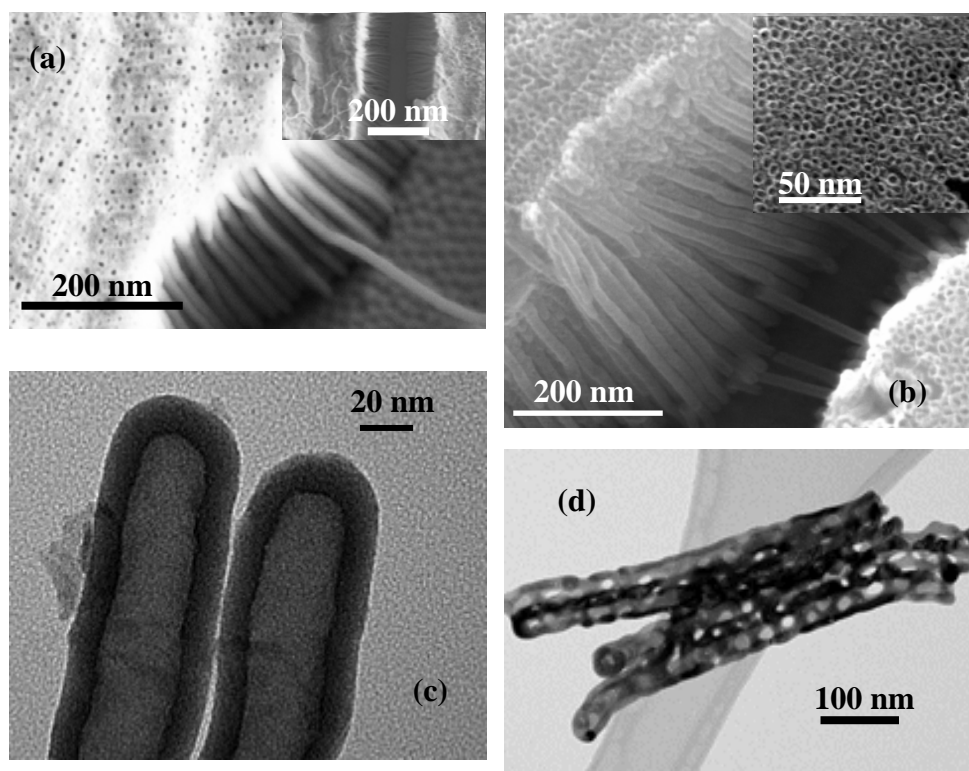


**Figure 4.2** (a) High magnification FESEM image of Ta oxide nanotubes at a ‘crack’ in the film (annealed at 450 °C for 30 min), with the inset showing the same crack, but at a lower magnification, (b) FESEM image of TaO<sub>x</sub>N<sub>y</sub> nanotubes at a ‘crack’ in the film after formation by ammonolysis of Ta oxide, with the inset showing the top view of the same film, (c) TEM image of the base of two Ta oxide nanotubes, and (d) TEM image of a few TaO<sub>x</sub>N<sub>y</sub> nanotubes, showing periodic holes in their walls.

The SEM and HRTEM images also confirm that the wall thickness of the Ta oxide NTs is uniformly ca. 10 nm, even at their base. This uniformity is expected, as these NTs were formed in aqueous solutions. It is known that if they had been formed in fluoride containing organic solutions, the wall thickness would vary along the length of NT,<sup>179</sup> as the movement of fluoride ions is restricted in these more viscous solvents.

After nitriding the Ta<sub>2</sub>O<sub>5</sub> NTs to form TaO<sub>x</sub>N<sub>y</sub>, significant structural differences occurred, as seen in Figure 4.2d. While the yellow-orange TaO<sub>x</sub>N<sub>y</sub> NTs remain attached to the Ta substrate and their outer diameters have not changed significantly (40 nm, Figure 4.2b), their walls have developed an interesting pattern of holes, each roughly 24 nm in diameter (Figure 4.2d). These holes and voids in Figure 4.2d have also been reported by others for Ta nitride (Ta<sub>3</sub>N<sub>5</sub>)<sup>180</sup> and Mo nitride (MoN)<sup>181</sup> nanoparticles, formed by ammonolysis. We believe that the formation of these holes is likely due to the increased density of TaO<sub>x</sub>N<sub>y</sub> (14.1 g·cm<sup>-3</sup>) relative to Ta oxide (8.2 g·cm<sup>-3</sup>)<sup>182</sup>. As supported by Domen and coworkers, these voids in the lattice of Ta<sub>3</sub>N<sub>5</sub> develop after replacing three oxygen anions with two nitride ions.<sup>180</sup>

To verify that the holes seen in Figure 4.2d developed as a result of nitriding and not just from exposure to the annealing temperatures, a layer of Ta<sub>2</sub>O<sub>5</sub> NTs on Ta was annealed under N<sub>2</sub> instead of NH<sub>3</sub>, but using otherwise the same conditions as employed for TaO<sub>x</sub>N<sub>y</sub> formation, and no holes are seen (Figure 4.3). Moreover, Ta<sub>2</sub>O<sub>5</sub> (Figure 4.3), annealed in N<sub>2</sub>, and the TaO<sub>x</sub>N<sub>y</sub> NTs show phase contrast, indicating that, after annealing, the as-formed amorphous Ta<sub>2</sub>O<sub>5</sub> NTs and TaO<sub>x</sub>N<sub>y</sub> NTs have become crystalline in nature.

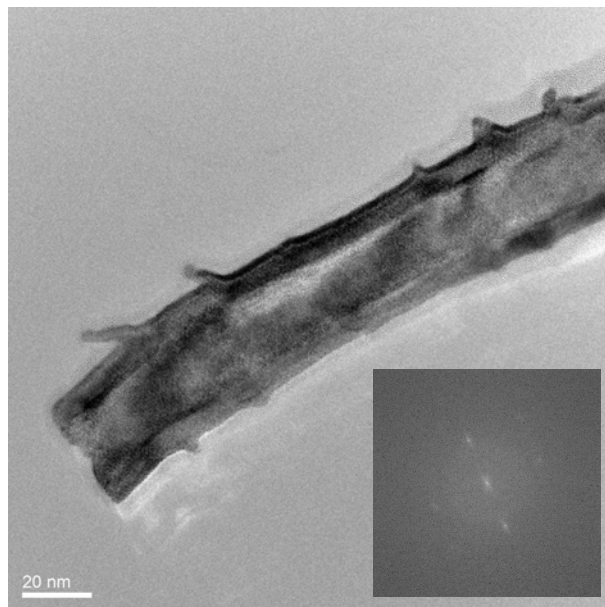


**Figure 4.3** Single Ta oxide NT formed after annealing the Ta oxide nanotubes in  $N_2$  at  $700\text{ }^\circ\text{C}$  for 7 h at a flow rate of  $10\text{ ml}\cdot\text{min}^{-1}$ . Inset shows the FFT pattern of the nanoarray of Ta oxide NTs.

The chemical composition of the  $Ta_2O_5$  and  $TaO_xN_y$  NTs was established by X-ray photoelectron spectroscopy (XPS) (Figure 4.4). The Ta  $4f_{5/2}/Ta\ 4f_{7/2}$  peaks of the Ta oxide NTs are seen to have moved to a higher binding energy (BE) compared to Ta metal (Figure 4.4a-green), as expected, indicating the more ionic character of the Ta oxide bond. On the other hand, the Ta  $4f_{5/2}/Ta\ 4f_{7/2}$  peaks in  $TaO_xN_y$  moved to lower BE values with respect to Ta oxide, presumably as a result of the introduction of more covalent character to the  $TaO_xN_y$  bonds (Figure 4.4a, blue).

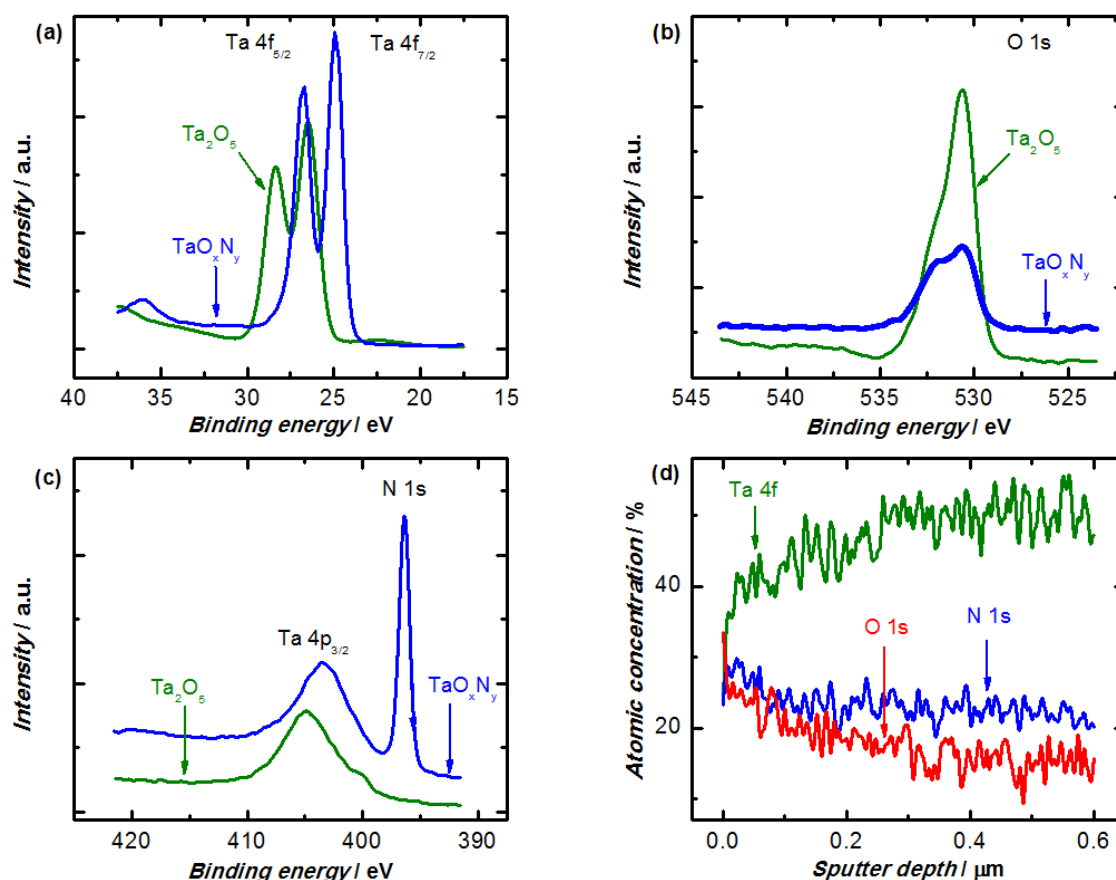


**Figure 4.4** Top-down XPS analysis of  $\text{Ta}_2\text{O}_5$  and  $\text{TaO}_x\text{N}_y$  nanotubular array (ca.  $1\ \mu\text{m}$  thick) on a Ta substrate, showing the (a) Ta 4f, (b) O 1s, and (c) N 1s spectra, as well as (d) depth profile XPS analysis of a  $1\ \mu\text{m}$  film of  $\text{TaO}_x\text{N}_y$  NTs.

Comparison of the literature binding energies of Ta  $4f_{5/2}$ /Ta  $4f_{7/2}$  with those observed here (Figure 4.4a) for the  $\text{TaO}_x\text{N}_y$  nanotubular array suggests that the Ta oxide nanotubes were not fully nitrated ( $\text{Ta}_3\text{N}_5$ ) but are also not pure TaON. While the ratio of the XPS-determined O to N peak areas is close to one near the NT/air interface, the ratio is clearly less than one deeper inside the nanotubular array (Figure 4.4d). Further, the yellowish-orange colour of our films also

supports the fact that the ratio of O:N is less than 1:1, as the powder form of TaON is reported to be yellow.<sup>183-184</sup> In fact, it is known that the flow rate of ammonia, the annealing temperature, and the time of annealing, could all affect the TaO<sub>x</sub>N<sub>y</sub> composition.<sup>185-186</sup> Attempts to obtain the exact composition of the TaO<sub>x</sub>N<sub>y</sub> NT films formed here by standard X-ray Diffraction (XRD) analysis (data not shown) were unsuccessful, primarily as the peaks arising from the parent compound, Ta<sub>3</sub>N<sub>5</sub>, overlap fully with those for TaO<sub>x</sub>N<sub>y</sub>, where  $x$  and  $y$  can have quite a wide range of values.<sup>184</sup>

Unfortunately, the nanotubular film is very thin (ca. 1  $\mu\text{m}$ ) and thus it is challenging to collect reliable XRD data using standard methods. Consistent with this, Figure 4.5 shows that the peak intensities are large for the underlying Ta metal substrate, but quite small for the nanotubes.

The XRD determination of the composition of the nanotubes after nitriding of Ta oxide is a challenging task. This is because Ta<sub>3</sub>N<sub>5</sub> (which is the parent compound; Pearson crystal data code 1409825) is in the same space group (Cmcm) as Ta<sub>3</sub>O<sub>x</sub>N<sub>y</sub> for many different  $x$  and  $y$  values, and thus these compounds cannot be distinguished from each other. This was shown by refining the PXRD data sets with the LeBail refinement using the General Structure Analysis System (GSAS) package with the EXPGUS interface to obtain the cell parameters of Ta<sub>3</sub>N<sub>x</sub>O<sub>y</sub>.

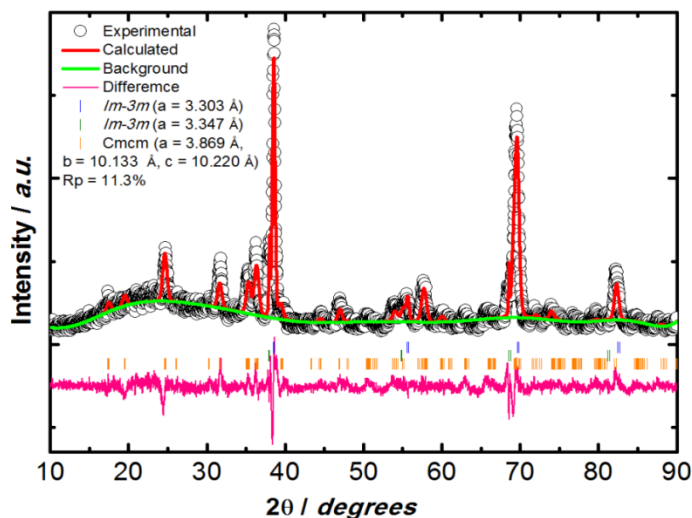


**Figure 4.5** Powder XRD experimental and fitting pattern for  $TaO_xN_y$  NTs. The PXRD data sets were refined by LeBail refinement using the General Structure Analysis System (GSAS) package with the EXPGUS interface to obtain the cell parameters of Ta (Pearson Crystal Structure code 261169),  $TaN_{0.1}$  (Pearson Crystal Structure code 531979) and  $Ta_3N_xO_y$  (Pearson Crystal Structure code 1409825). The background, zero-point position, cell parameters, and profile coefficients for the Pseudo-Voigt/Finger–Cox–Jephcoat (FCJ) asymmetric peak function were refined until convergence was achieved.

As stated above, the XPS data (Figure 4.4), collected as a function of depth into the nanotubular film, show that the N:O ratio is not 1:1, but rather, that there is more N present than O. Furthermore, the color of the nanotubular films (yellow-orange) is the same as the color of  $TaO_xN_y$  in previous work, while  $Ta_3N_5$  is ruby red in color and TaON is yellow.<sup>183-186</sup> For these reasons, the material is referred as  $TaO_xN_y$  in the remainder of this thesis.

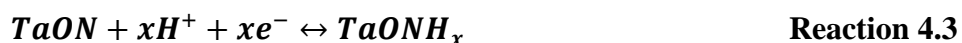
## 4.2.2 Electrochemistry of TaO<sub>x</sub>N<sub>y</sub> NTs

### 4.2.2.1 Cyclic Voltammetry (CV)

Typical cyclic voltammograms (CVs) of the TaO<sub>x</sub>N<sub>y</sub> NTs are shown in Figure 4.6, with the CVs collected in deaerated 0.5 M H<sub>2</sub>SO<sub>4</sub> (black), in pH 7 phosphate buffer (PB) (Figure 4.6, red), and in 0.5 M KOH (Figure 4.6, green), in the same potential range, from 0.05 V to 1.5 V vs. RHE, at 50 mV·s<sup>-1</sup>, in comparison with the CV response of the Ta oxide NTs under the same conditions and in same solutions (Figure 4.6, blue, magenta, and yellow, respectively). Only a small double layer charging response is seen for Ta oxide over the full potential range, as expected, as Ta oxide is not a good conductor<sup>24</sup> and does not have any other oxidation states in these aqueous solutions.<sup>187</sup>

In comparison, the CVs for the TaO<sub>x</sub>N<sub>y</sub> nanotubular array (Figure 4.6) at potentials between 0.8 and 1.5 V are also relatively featureless and essentially overlay the response for Ta oxide in the same potential range. However, in the negative scan, a small cathodic peak/shoulder is seen for the TaO<sub>x</sub>N<sub>y</sub> NTs at ca. 0.35 V vs. RHE in Figure 4.6 (black, red and green), after which the reduction current increases steadily as the potential is made still more negative, revealing a large redox feature. In the reverse scan (anodic direction), a matching (reversible) oxidation peak is seen, centered at ca. 0.05 V, although a corresponding anodic peak to the cathodic peak at 0.33 V is not always obvious. Importantly, the shape of the CVs in the three solutions is very similar, as is the magnitude of the peak currents.

While the reversible, pseudocapacitive CV response, seen for the  $\text{TaO}_x\text{N}_y$  nanotubes in Figure 4.6, has not been reported previously, it is well known that some other metal oxides, such as  $\text{WO}_3$ , exhibit similar electrochemical behaviour. This has been attributed to the redox chemistry of the metal sites within the films, accompanied by ion intercalation/deintercalation, forming metal bronzes in the case of cations.<sup>188</sup> Therefore, it is assumed that the electrochemical behaviour shown in Figure 4.6 is related to the  $\text{Ta}^{5+}/\text{Ta}^{4+}$  redox process within the  $\text{TaO}_x\text{N}_y$  NTs, also involving proton insertion and expulsion in aqueous solutions, as shown in Reaction 4.3.



The origin of the peak at ca. 0.33 V is not definitively known, but it may be attributed to the reduction/oxidation of surface defects, as claimed by Grätzel et al in their work on  $\text{TiO}_2$  electrochemistry.<sup>189</sup> This peak is seen more prevalently in acidic solutions (Figure 4.7) than in neutral media, but even in acidic media, it is not always present, suggesting a surface contaminant or defect which is only occasionally present.

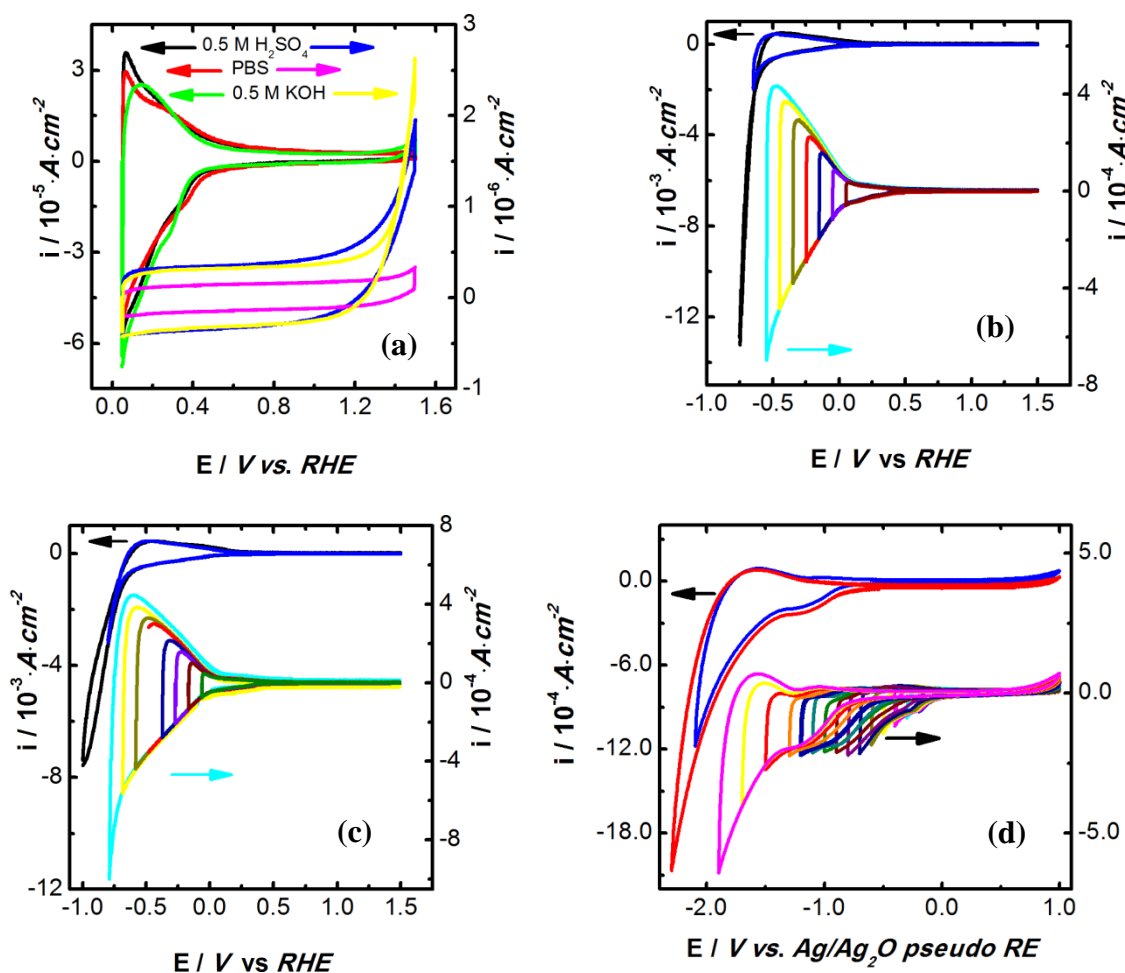


**Figure 4.6** CVs ( $50 \text{ mV}\cdot\text{s}^{-1}$ ) of TaO<sub>x</sub>N<sub>y</sub> NTs in (a) 0.5 M H<sub>2</sub>SO<sub>4</sub> (black), pH 7 PB solution (red) and 0.5 M KOH (green) and those for the Ta oxide NTs in 0.5 M H<sub>2</sub>SO<sub>4</sub> (blue), pH 7 PB solution (magenta) and 0.5 M KOH (yellow). All of these CVs were collected for the same TaO<sub>x</sub>N<sub>y</sub> or Ta oxide samples. (b) and (c) are CVs obtained at  $50 \text{ mV}\cdot\text{s}^{-1}$  at variable cathodic switching potentials for the same TaO<sub>x</sub>N<sub>y</sub> NTs in 0.5 M H<sub>2</sub>SO<sub>4</sub> and PB solutions, respectively. (d) shows the CVs ( $50 \text{ mV}\cdot\text{s}^{-1}$ ) obtained for the TaO<sub>x</sub>N<sub>y</sub> NTs in anhydrous acetonitrile using 0.1 M tetra-n-butylammonium hexafluorophosphate as the electrolyte and a Ag/Ag<sub>2</sub>O pseudo-reference electrode.

By varying the cathodic switching potential (Figure 4.6b), more insight can be obtained about the  $\text{TaO}_x\text{N}_y$  electrochemistry. In this experiment, the scan rate was kept at  $50 \text{ mV}\cdot\text{s}^{-1}$  and the cathodic switching potential was changed in 50 mV increments until significant evolution of hydrogen was observed. The most notable feature in these CVs is the excellent reversibility of the system. Also, it is seen that the hydrogen evolution reaction (HER) interferes with the  $\text{TaO}_x\text{N}_y$  electrochemistry at cathodic potentials in the  $\text{H}_2\text{SO}_4$  solution (Figure 4.6b), while in the pH 7 PB solution, the HER is slower, thus revealing more of the  $\text{TaO}_x\text{N}_y$  response (Figure 4.6c). It is also of interest that the HER Tafel slope is ca.  $90 \text{ mV}\cdot\text{decade}^{-1}$ , whereas for  $\text{Ta}_2\text{O}_5$  NTs, it is ca.  $230 \text{ mV}\cdot\text{decade}^{-1}$ . It seems that the  $\text{TaO}_x\text{N}_y$  NTs are reasonable HER catalysts, while the  $\text{Ta}_2\text{O}_5$  NTs are clearly not. A ‘double Tafel slope’, being roughly two times the expected highest Tafel slope at room temperature (120 mV), has been reported previously for the HER at  $\text{ZrO}_2$ , explained as being due to the ‘dual barrier’ effect (this has been discussed in detail in Chapter 5).<sup>190</sup>

Figure 4.6b and c shows that the HER overlaps with the  $\text{TaO}_x\text{N}_y$  redox process in both pH 0 and 7 aqueous solutions, such that it is not possible to determine the full charge associated with this process. For this reason, CVs were collected in an anhydrous acetonitrile ( $\text{CH}_3\text{CN}$ ) solution (Figure 4.6d), where the HER should be significantly inhibited. Figure 4.6d shows that the general characteristics of the CV are very similar to those obtained in aqueous solutions, showing that Equation 4.3 is also occurring in this medium, with the tetrabutylammonium cation apparently serving the role of the proton in aqueous solutions.

At -2.3 V vs. the Ag/Ag<sub>2</sub>O pseudo-RE, significant cathodic current is passed, possibly due to the HER arising from the reduction of trace water in the solvent. Tetra-*n*-butylammonium hexafluorophosphate (Bu<sub>4</sub>N<sup>+</sup>PF<sub>6</sub><sup>-</sup>) in acetonitrile is stable over a wide potential range (-2.75 to +3.0 V vs. SCE) at Pt<sup>116</sup> and thus the cathodic current in Figure 4.6d should not be due to organic solvent breakdown. Therefore, a Pt WE was used instead of the TaO<sub>x</sub>N<sub>y</sub> NTs to determine how much water was present in the solvent (results not shown). Typically, a fresh anhydrous CH<sub>3</sub>CN contains ≤ 0.001 % H<sub>2</sub>O, but, over the course of the experiment (~ 2 h), it can be expected that the solvent will absorb up to 10 times this amount of water in a 70% humid environment, according to Webster et. al.<sup>191</sup> The relatively high currents (ca. 17 mA) passed at the Pt WE at potentials negative of -1.6 V thus do suggest the presence of water in the solvent.

Consistent with the rapid redox kinetics observed qualitatively in Figure 4.6, it is seen (Figure 4.7) that the relationship between peak current ( $i_p$ ) and scan rate ( $\nu$ ) is linear up to relatively high sweep rates of 0.6 V·s<sup>-1</sup> in acidic media and at least 0.1 V·s<sup>-1</sup> in PB solution. This indicates that the reaction is acting like a pseudocapacitive surface process,<sup>192</sup> while at higher sweep rates, especially in PBS, the TaO<sub>x</sub>N<sub>y</sub> redox process (Reaction 4.3) is likely diffusion controlled, with the peak currents being proportional to the square root of the potential sweep rate.

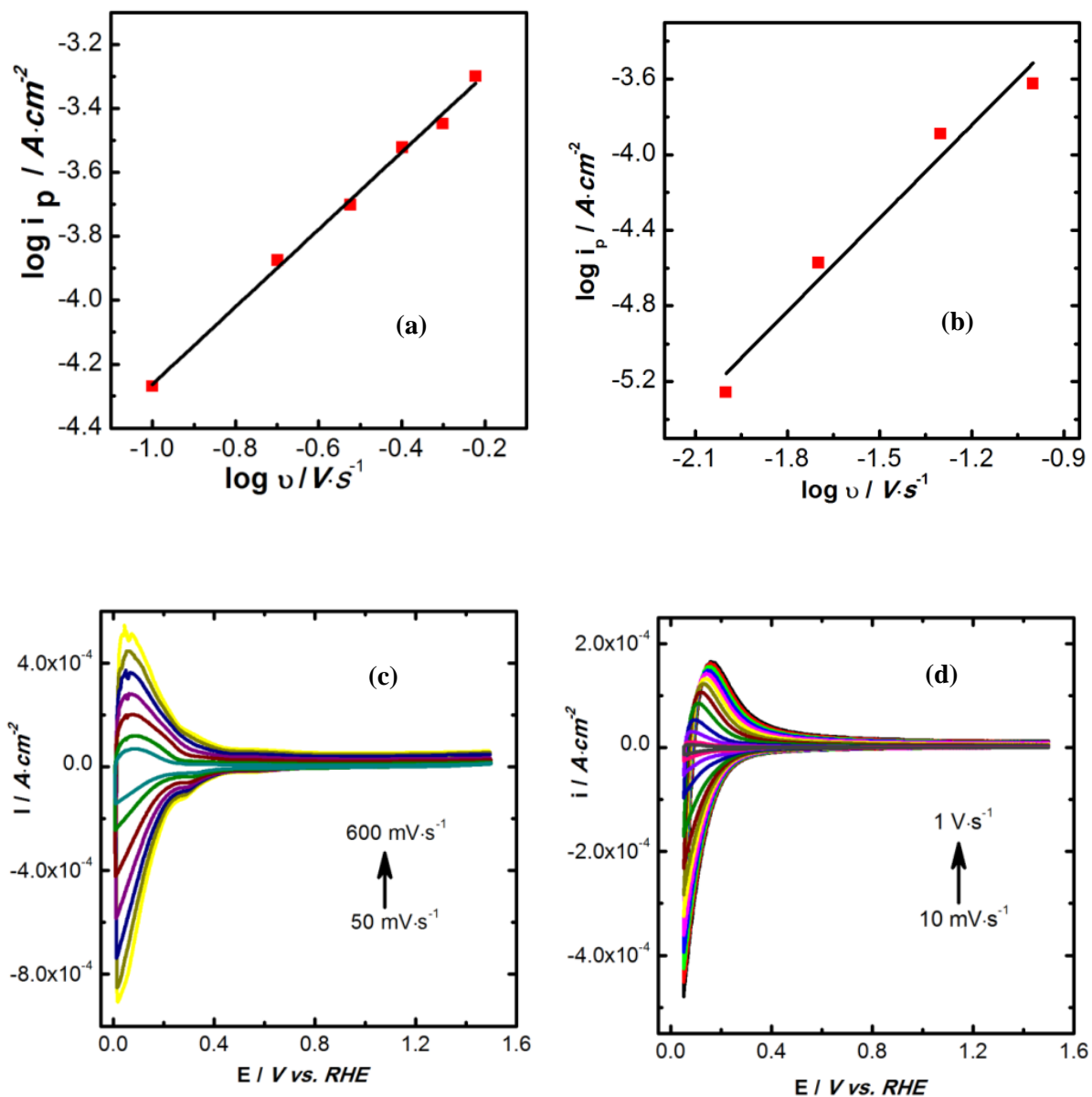


**Figure 4.7** Logarithm of anodic peak current vs. logarithm of scan rate ( $\nu$ ) for TaO<sub>x</sub>N<sub>y</sub> NTs in (a) 0.5 M H<sub>2</sub>SO<sub>4</sub> and (b) pH 7 PBS. Solid lines are best fit lines. (c) and (d) show the CVs obtained at various scan rates for TaO<sub>x</sub>N<sub>y</sub> NTs in 0.5 M H<sub>2</sub>SO<sub>4</sub> and pH 7 PBS, respectively.

It remained of interest to determine whether the pseudocapacitive response of the TaO<sub>x</sub>N<sub>y</sub> NTs, in the range of -0.1 V to -0.6 V vs. RHE in aqueous solutions (and ca. -0.1 V to -0.6 V vs. Ag/Ag<sub>2</sub>O in acetonitrile), is due to the redox activity of the full nanotubular array or just a fraction of the full volume of the NTs. To determine this, the number of moles of Ta present on the surface and in the bulk of the NTs was estimated, based on the SEM and TEM morphology shown in Figure 4.2.

Assuming an average outer NT diameter of 30 nm and an inner NT diameter of 10 nm (and thus an average wall thickness of 10 nm), a NT length of 1 μm, and a void/hole diameter within the TaO<sub>x</sub>N<sub>y</sub> NTs of roughly 25 nm (Figure 4.1d), the total real surface area of a 1 cm<sup>2</sup> array of NTs is estimated to be 1.4 × 10<sup>2</sup> cm<sup>2</sup>. This is equivalent to 3.6 × 10<sup>-7</sup> moles of Ta present on the exposed surface of the NTs, assuming a P2<sub>1/c</sub><sup>193</sup> unit cell size of 0.25 nm<sup>2</sup>, each containing 4 Ta cations. This equates to a predicted charge density of ca. 35 mC·cm<sup>-2</sup> if all of the surface Ta ions, exposed to the solution, are electrochemically active. In contrast, the total number of moles of Ta present in a 1 cm<sup>2</sup> array of TaO<sub>x</sub>N<sub>y</sub> nanotubes, ca. 1 μm in length and having the characteristics described above, is close to 2 × 10<sup>-6</sup> moles·cm<sup>-2</sup> (roughly 200 mC·cm<sup>-2</sup>).

In comparison, the experimental charge densities seen in the CVs in Figure 4.6 in a scan to ca. -0.5 V vs. RHE are in the range of 3-5 mC·cm<sup>-2</sup>. This is significantly smaller (only 10-15%) than what would be expected if every Ta<sup>5+</sup> ion on the surface of the nanotubular array underwent reduction to Ta<sup>4+</sup> (Reaction 4.3) in the CV scans. This argues that only a fraction of the exposed

(to the solution) outer surface of the TaO<sub>x</sub>N<sub>y</sub> NTs is undergoing redox chemistry in the CV scans shown in Figure 4.6. This would be consistent with the rapid redox kinetics observed (Figure 4.7), as if protons (Reaction 4.3) or the bulky tetra-*n*-butylammonium cation (in acetonitrile) were moving into the TaO<sub>x</sub>N<sub>y</sub> NT walls, transport limitations would have been expected. Notably, the charge measured in the pseudocapacitive region in Figure 4.6b is limited at the negative end by the onset of the hydrogen evolution reaction (HER) and thus further reduction of Ta<sup>5+</sup> to Ta<sup>4+</sup> would likely occur if the HER could be blocked. Even so, it seems unlikely that the full surface area of the TaO<sub>x</sub>N<sub>y</sub> NTs would be electrochemically active, even under these conditions.

The FESEM images in Figure 4.8 were used to determine the NT lengths, and the maximum NT length is obtained at 10 minutes of anodization [ca. 4 μm NT length (Figure 4.8c)]. As can be seen in Figure 4.8b and c, the NTs are lost from the surface at longer times of anodization. This results in a larger area of TaO<sub>x</sub>N<sub>y</sub> compact layer, covering the nanodimpled (ND) surface, being exposed to solution during anodization. The loss of NTs during the anodization is thought to be caused by the accumulation of F<sup>-</sup> anions (from the electrolyte) at the NT/metal interface, forming the soluble [TaF<sub>7</sub>]<sup>2-</sup> (Reaction 4.2). This accumulation of soluble species at the NT/metal interface causes nanotubes greater than ca. 4 μm in length to be unstable on the metal surface and thus, the NTs reach a limiting thickness.

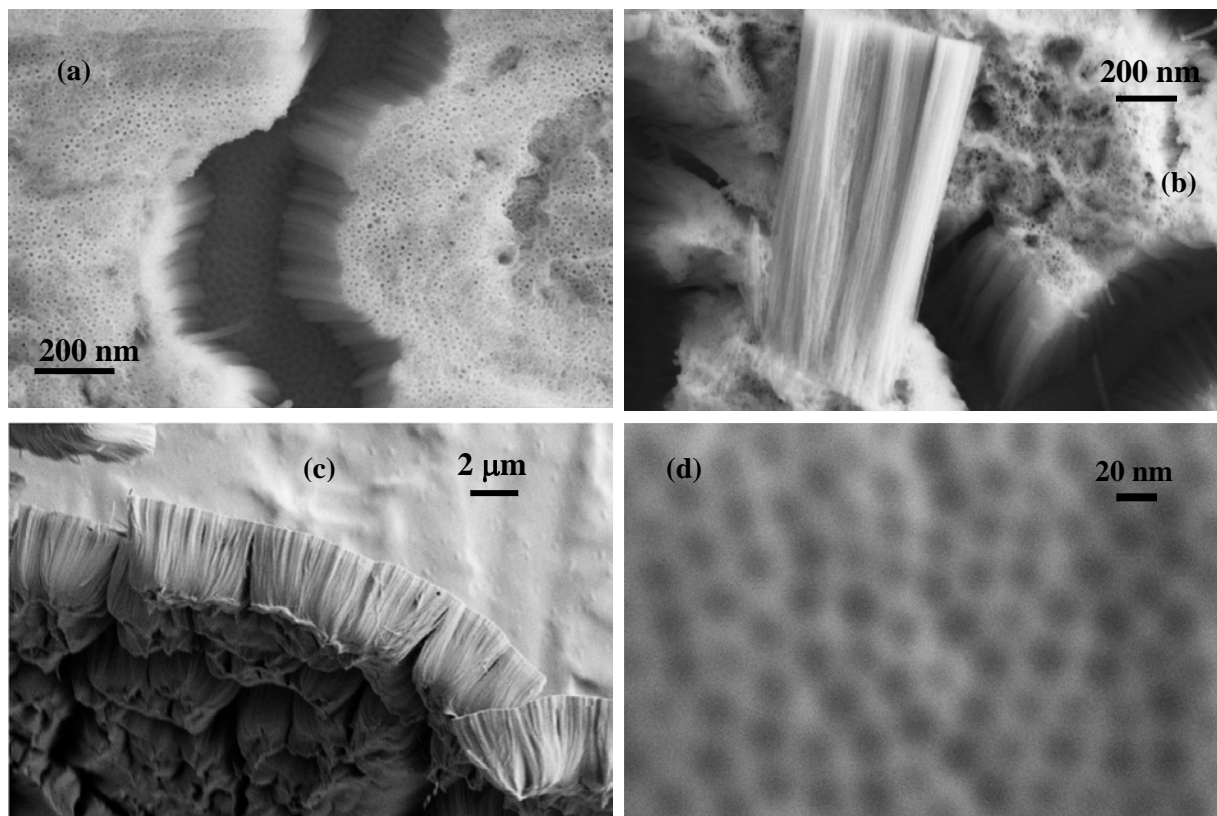


**Figure 4.8** TaO<sub>x</sub>N<sub>y</sub> NTs as a function of anodization times of (a) 2.5 min, (b) 7.5 min, and (c) 10 min, and (d) nanodimples covered by TaO<sub>x</sub>N<sub>y</sub> compact film.

In Figure 4.9a, the CV response of the TaO<sub>x</sub>N<sub>y</sub> nanotubular array is shown as a function of NT length, obtained by varying the anodization time, as well as for dimpled Ta coated with a thin film of TaO<sub>x</sub>N<sub>y</sub> ('0 anodization time'), while Figure 4.9b shows the charge calculated from the CVs for each respective material. The average charge increment is proportional to the NT length for the 2.5 and 5 mins anodization. The charges for the 7.5 min and 10 min anodization films are lower than the 5 min anodization time although the NT length has increased by 2.5 and 7 times, respectively. This observation can be attributed to the only a part of the longer NTs are

redox active, or detachment of some of the NTs from the base and exposure of the  $\text{TaO}_x\text{N}_y$  compact film that covers the NDs. The partially detached NTs still present, but not well connected to surface and hence electrochemically cannot be addressable. Furthermore, the exposure of the underlying compact  $\text{TaO}_x\text{N}_y$  film allows more Ta oxidation to occur, as can be seen in the CV at  $> 1.3$  V vs. RHE.

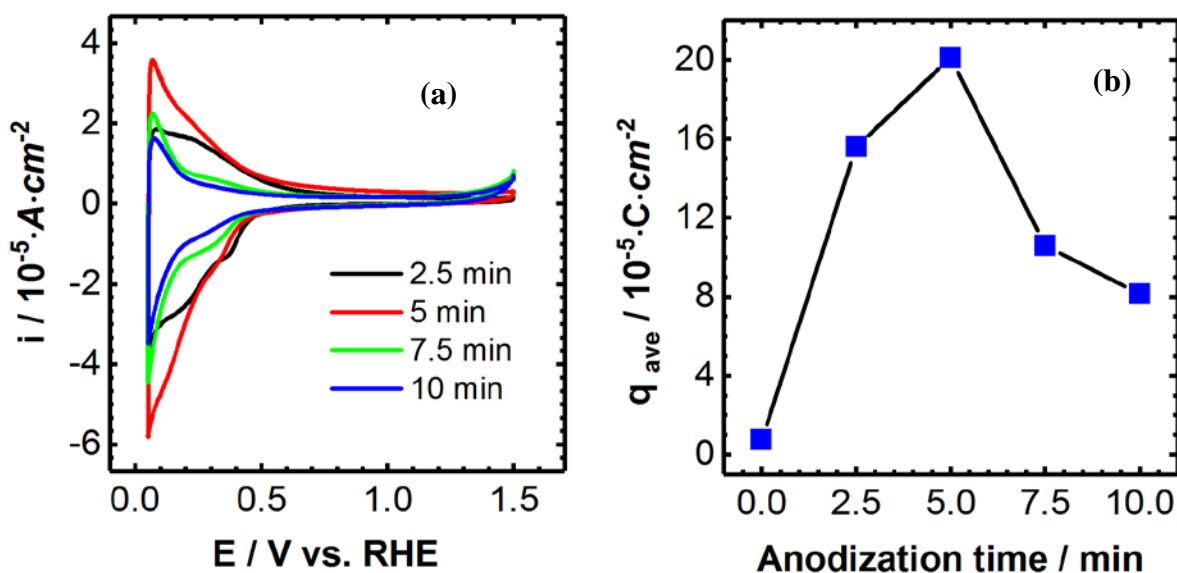


**Figure 4.9** (a) CV response of the  $\text{TaO}_x\text{N}_y$  NTs as a function of their length, all in deaerated 0.5 M  $\text{H}_2\text{SO}_4$  at  $50 \text{ mV} \cdot \text{s}^{-1}$ . (b) Average charge obtained from the CV redox features in (a) for the NTs and also for the case when the NTs were removed from the surface ('0 anodization time').

#### 4.2.2.2 Electrochemical impedance spectroscopy (EIS)

EIS data were collected for the  $\text{TaO}_x\text{N}_y$  NTs in  $\text{H}_2\text{SO}_4$  and PBS solutions at various applied potentials ( $E_{\text{app}}$ ), as shown in the Nyquist and Bode plots in Figure 4.10 and Figure 4.11 (a and b), respectively. It is seen that the impedance response at potentials between 0.6 and 1.4 V is

very similar, in both solutions, to what is seen for the Ta oxide nanotubular film precursor, shown in Figure 4.9c and Figure 4.10c.

In the acidic medium, the data for the Ta oxide (Figure 4.10c) and TaO<sub>x</sub>N<sub>y</sub> NTs (Figure 4.10a), at between 1.4 and 0.6 V, were fitted to a circuit containing one time constant (Figure 6 a). For Ta oxide, it is seen that a capacitance of ca.  $5.5 \times 10^{-7}$  F·cm<sup>2</sup> is obtained (Table 4.2), independent of potential, with an associated n parameter of 0.98. This capacitor (with essentially no dispersion) must be arising from the barrier film at the base of the Ta oxide nanotubes, consistent with what has been reported previously for other valve metal oxide NTs,<sup>194</sup> as the nanotubes themselves are too long and resistive to be detected by the EIS technique. When using the theoretical dielectric constant for Ta<sub>2</sub>O<sub>5</sub> ( $\epsilon_r \sim 18$ ) and assuming a roughness factor of 1, the observed capacitance (ca.  $5 \times 10^{-7}$  F·cm<sup>2</sup>) is consistent with a film thickness of roughly 32 nm, which is quite reasonable ( $16 \text{ V} \times 1.76 \text{ nm}\cdot\text{V} = 28 \text{ nm}^{131}$ ). In fact, the real surface area at the base of the NTs is likely a little larger than the geometric area, due to its curvature (Figure 4.1c), and if a roughness factor of 1.3 is assumed, the oxide film thickness at the base of the NTs is predicted to be ca. 40 nm. However, the degree of fluoride doping of the oxide film is not known and thus  $\epsilon_r$  is not known with certainty for our materials.

In comparison, the capacitance of the TaO<sub>x</sub>N<sub>y</sub> nanotubular film at 0.6 – 1.4 V vs. RHE in the acidic solution is ca.  $8\text{-}15 \times 10^{-7}$  F·cm<sup>2</sup> (Table 4.1), only a little larger than for the Ta oxide NTs, and the n parameter is a bit smaller, ca. 0.8 (Table 4.1). The fact that the capacitance values for the TaO<sub>x</sub>N<sub>y</sub> and Ta oxide NTs are so similar to each other suggests that the response

from the TaO<sub>x</sub>N<sub>y</sub> NTs is also coming from the barrier film at the base of the nanotubes. In this potential range (0.6 to 1.4 V), Figure 4.6 shows that the redox capacitance of the TaO<sub>x</sub>N<sub>y</sub> NTs has not yet been switched on and only what appears to be double layer charging current passes. Indeed, Figure 4.10d shows how similar the CV responses of Ta oxide and TaO<sub>x</sub>N<sub>y</sub> are in this potential range, consistent with the EIS data.

The fact that the capacitance is a little larger for the TaO<sub>x</sub>N<sub>y</sub> NTs than Ta oxide (Table 4.1 vs. Table 4.2) at all potentials may be due a higher degree of surface roughening, as well as some change in the electronic properties of the two materials. Ta oxide is known to be a wide band gap semiconductor (3.86 eV band gap, Figure 4.13) from diffuse reflectance measurements, while TaO<sub>x</sub>N<sub>y</sub> is expected to be a weakly conducting semiconductor having a band gap of 2.26 eV (Figure 4.13, obtained from diffuse reflectance measurements) in this potential range (0.7 to 1.4 V). This is also consistent with the difference in the R1 values (Table 4.1 vs. Table 4.2) for the two materials in acidic media, which are 50-100 times larger for the Ta oxide vs. the TaO<sub>x</sub>N<sub>y</sub> NTs. These same trends were found for the Ta oxide and TaO<sub>x</sub>N<sub>y</sub> NTs in neutral solutions (Table 4.3).

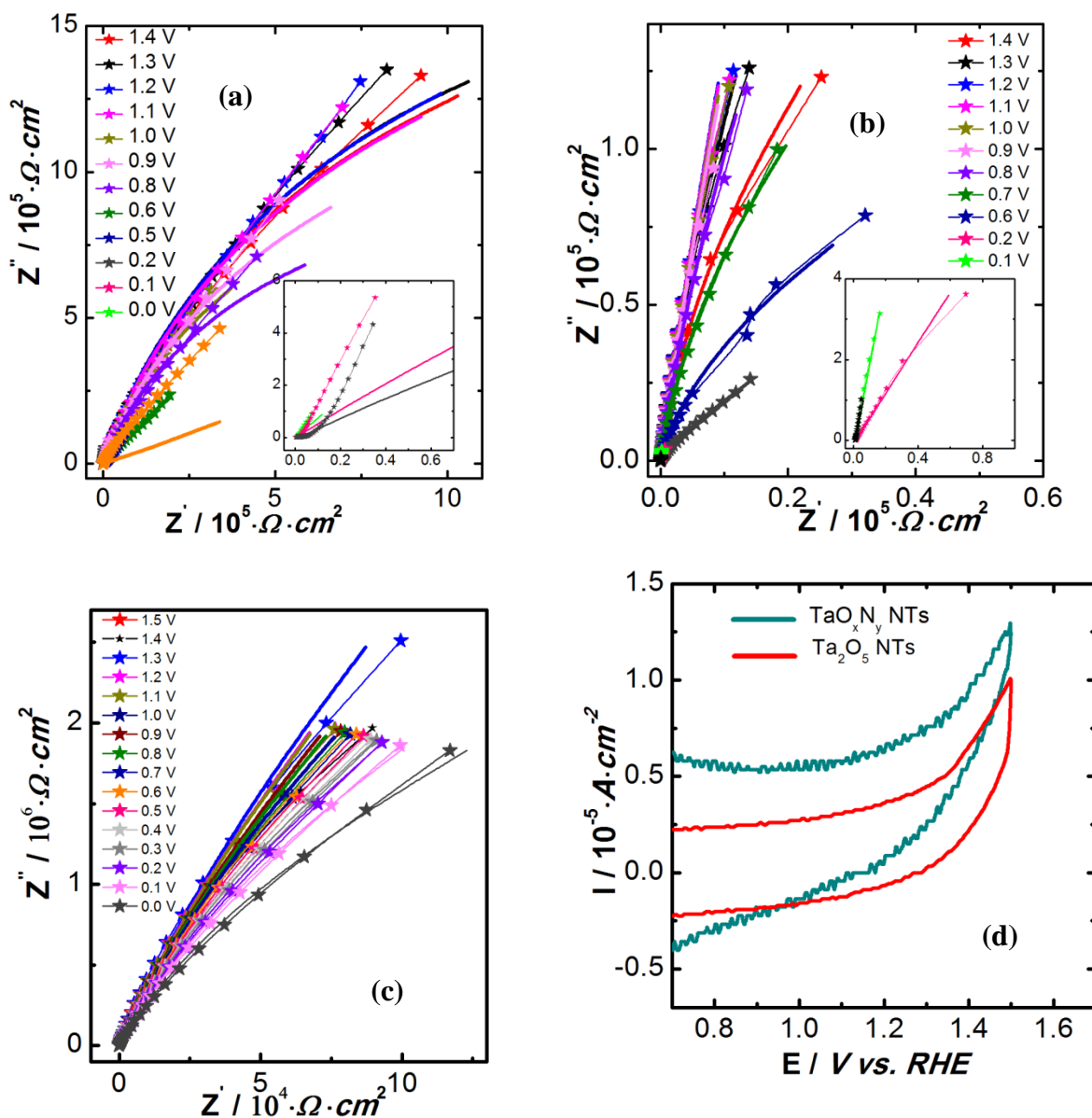


**Figure 4.10** (a) and (b) Nyquist plots obtained for the TaO<sub>x</sub>N<sub>y</sub> NTs at various potentials vs. the reference electrode in (a) 0.5 M H<sub>2</sub>SO<sub>4</sub>, and (b) in the PB solution, and (c) Nyquist plots for Ta<sub>2</sub>O<sub>5</sub> NTs in 0.5 M H<sub>2</sub>SO<sub>4</sub> for comparison with (a). Symbols are experimental data while solid lines are fitted data. (d) shows the comparison CV (50 mV/s) of the Ta<sub>2</sub>O<sub>5</sub> NTs and TaO<sub>x</sub>N<sub>y</sub> NTs in the potential range of 0.8-1.5 V in 0.5 M H<sub>2</sub>SO<sub>4</sub>. Insets in (a) and (b) show Nyquist plots obtained at more cathodic potentials.

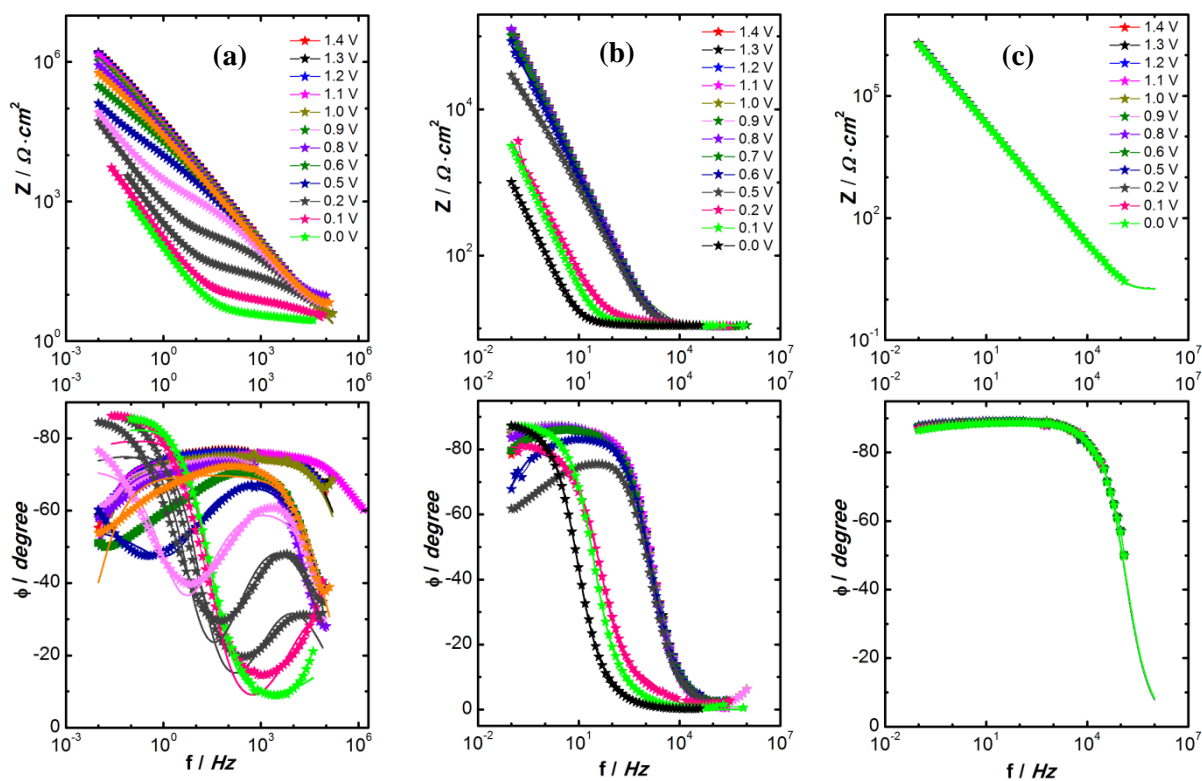


**Figure 4.11** (a) and (b) Bode plots obtained for the TaO<sub>x</sub>N<sub>y</sub> NTs at various applied potentials in (a) 0.5 M H<sub>2</sub>SO<sub>4</sub> and in (b) PB solution, and (c) Bode plots obtained for the Ta<sub>2</sub>O<sub>5</sub> NTs in 0.5 M H<sub>2</sub>SO<sub>4</sub>, for comparison with (a). Figures at top are for the total impedance ( $Z$ ) and figures at bottom of for the phase angle. Symbols are experimental data while solid lines are fitted data.

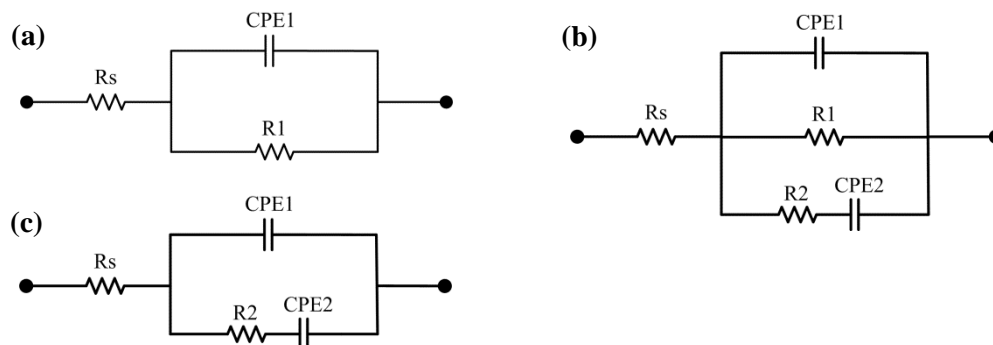


**Figure 4.12** (a), (b) and (c) show the equivalent circuits used to fit the EIS experimental data.

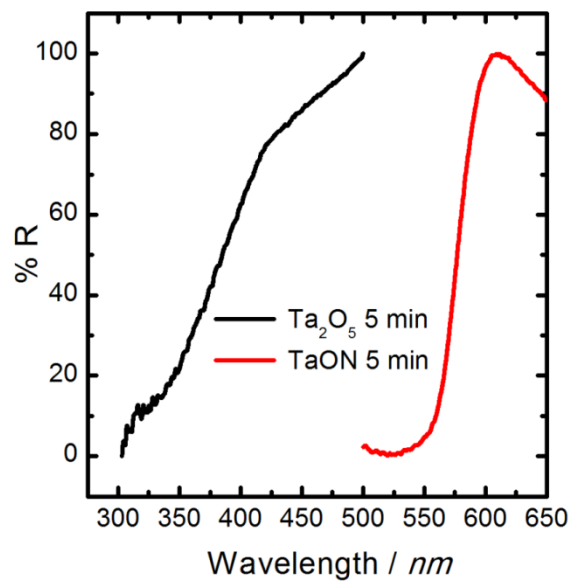
At lower potentials of ca. 0 V, however, the response for the two types of films is quite different in both of the aqueous solutions. For the TaO<sub>x</sub>N<sub>y</sub> films, the EIS response (Figure 4.9a) begins to show low frequency pseudocapacitive behaviour, which is not seen for Ta oxide (Figure 4.9c). This is consistent with the CVs shown in Figure 4.6, where the pseudocapacitive response of the TaO<sub>x</sub>N<sub>y</sub> nanotubes is clearly seen to begin at potentials < 0.6 V, while above this, only the double layer charging/discharging process (R1/CPE1) is seen, identical to the situation at the Ta oxide NTs.

Table 4.1 shows that the CPE (constant phase element) obtained for the TaO<sub>x</sub>N<sub>y</sub> NTs has a value of ca.  $2.5 \times 10^{-4} \text{ F}\cdot\text{cm}^{-2}$  at 0 V, very similar to what is obtained from the CV response (Figure 4.6) in acidic media, i.e., ca.  $2\text{-}4 \times 10^{-4} \text{ F}\cdot\text{cm}^{-2}$ . CPE2 is related to the redox reaction of the TaO<sub>x</sub>N<sub>y</sub> NTs (Equation 4.3), while CPE1 is due to the interfacial response of TaO<sub>x</sub>N<sub>y</sub> at the base of the NTs. It can be clearly seen that the resistance of the redox reaction (R2) decreases as the applied potential is made more negative, dropping from  $1.8 \times 10^4$  to  $2 \text{ }\Omega\cdot\text{cm}^2$ . A similar trend can be seen for the nanotubular arrays in phosphate buffer (PB) solution (Table 4.3), but, in this

case, both CPEs increase in magnitude as the potential is extended into the pseudocapacitive range (below 0.6 V).

It can be seen in Table 4.1 and Table 4.3 that the power factor (n value) associated with CPE2 is close to or even less than 0.5 at both 0.6 and 0.5 V, possibly indicating that mass transport (Warburg impedance) plays a role at low frequencies, potentially related to transport within the porous TaO<sub>x</sub>N<sub>y</sub> nanotubular array.<sup>195-197</sup> However, the n value is closer to 1 at lower potentials when the TaO<sub>x</sub>N<sub>y</sub> redox process is well underway. It is known that the redox switching of the TaO<sub>x</sub>N<sub>y</sub> NTs starts at ca. 0.6 V (Figure 4.6 and Figure 4.7) and therefore the resistance (R2) to the pseudocapacitive charge transfer (CT), including counter ion injection/expulsion, would be higher at 0.6 and 0.5 V compared to at lower potentials. As a result, the slow kinetics of these processes are seen as a Warburg impedance in the EIS results. However, the charge transfer resistance (R2) is much smaller when the potential is 0 V (2 Ω compared to 10<sup>4</sup> Ω at 0.6 V), indicating that the kinetics of the TaO<sub>x</sub>N<sub>y</sub> redox reaction are now much faster, and the Warburg impedance disappears. Related to this, the n value of CPE2 is now much closer to 1 (~ 0.9 in both 0.5 M H<sub>2</sub>SO<sub>4</sub> and in PBS at 0 V, as seen in Table 4.1 and Table 4.3).

It should be noted that EIS analysis was not carried out at potentials below 0 V in the case of the TaO<sub>x</sub>N<sub>y</sub> nanotubular films in either of the two aqueous solutions. This is because the response was so strongly capacitive and exhibited such a small resistance (due to the onset of the hydrogen evolution reaction) that the EIS data could not be accurately collected.



**Figure 4.13** Diffuse reflectance UV-Visible analysis of Ta oxide and TaO<sub>x</sub>N<sub>y</sub> NTs, with the data obtained using a Cary 5000 double beam scanning spectrophotometer, equipped with a diffuse reflectance accessory.

**Table 4.1** Values of circuit elements for TaO<sub>x</sub>N<sub>y</sub> NTs studied by EIS in 0.5 M H<sub>2</sub>SO<sub>4</sub> solution and employing the equivalent circuits shown in Figure 4.11<sup>a</sup>.

$E_{app}/V$ vs. $RHE$	$R_s/\Omega \cdot cm^2$	CPE <sub>1</sub>			CPE <sub>2</sub>			$\chi^2$ <sup>b</sup>
		$Q/F \cdot cm^2$	$n$	$R_1/\Omega \cdot cm^2$	$Q/F \times cm^2$	$n$	$R_2/\Omega \cdot cm^2$	
1.4	0.605	7.53E-07	0.828	3.89E+06				4.33E-03
1.3	0.663	7.37E-07	0.831	4.07E+06				5.93E-03
1.2	0.601	7.83E-07	0.829	4.08E+06				2.06E-03
1.1	0.628	8.27E-07	0.825	3.87E+06				2.20E-03
1.0	0.664	8.81E-07	0.820	2.53E+06				5.11E-03
0.9	0.686	1.10E-06	0.807	3.17E+06				2.09E-03
0.8	0.680	1.24E-06	0.797	2.18E+06				2.75E-03
0.7	0.632	1.53E-06	0.776	1.13E+06				6.19E-03
0.6	0.654	1.41E-06	0.792	7.64E+08	1.45E-06	0.473	1.85E+04	6.79E-04
0.5	0.671	2.08E-06	0.758	4.27E+15	5.22E-06	0.586	8.75E+03	1.43E-03
0.4	0.671	4.23E-06	0.697	1.71E+15	1.34E-05	0.797	1.91E+03	3.79E-03
0.3	0.671	7.32E-06	0.667	4.58E+11	2.92E-05	0.895	2.21E+02	1.01E-02
0.2	0.644	1.65E-05	0.617	1.81E+09	7.49E-05	0.890	3.61E+01	9.30E-03
0.1	0.644	1.52E-05	0.642	1.51E+09	1.58E-04	0.909	7.87E+00	1.37E-02
0	0.612	2.93E-05	0.801		2.53E-04	0.912	1.95E+00	3.54E-03

<sup>a</sup> Data obtained in the potential ranges of 1.4-0.7 V, 0.6-0.1 V, and 0 V were fitted with equivalent circuits (a), (b) and (c) in Figure 4.11, respectively.

<sup>b</sup>  $\chi^2$  is the measure of the goodness of fit to the data using equivalent circuit models.

**Table 4.2** Values of circuit elements for Ta oxide NTs studied by EIS in 0.5 M H<sub>2</sub>SO<sub>4</sub> solution and employing the equivalent circuit (a) shown in Figure 4.11.

$E_{app}/V$ vs. <i>RHE</i>	$R_s/\Omega \cdot cm^2$	$CPE_1$			$R_1/\Omega \cdot cm^2$	$\chi^2{}^a$
		$Q/F \cdot cm^2$	<b>n</b>			
1.5	1.82	4.97E-07	0.98	3.65E+07	1.04E-03	
1.4	1.81	4.99E-07	0.98	1.32E+08	9.80E-04	
1.3	1.81	5.00E-07	0.98	2.03E+08	9.69E-04	
1.2	1.81	5.01E-07	0.98	2.18E+08	9.70E-04	
1.1	1.81	5.02E-07	0.98	2.26E+08	9.54E-04	
1	1.80	5.03E-07	0.98	2.04E+08	9.51E-04	
0.9	1.80	5.05E-07	0.98	1.95E+08	9.35E-04	
0.8	1.80	5.06E-07	0.98	1.77E+08	9.16E-04	
0.7	1.80	5.07E-07	0.98	1.56E+08	9.27E-04	
0.6	1.80	5.09E-07	0.98	1.42E+08	9.51E-04	
0.5	1.80	5.11E-07	0.98	1.27E+08	9.49E-04	
0.4	1.80	5.13E-07	0.98	1.15E+08	8.81E-04	
0.3	1.80	5.15E-07	0.98	1.03E+08	8.79E-04	
0.2	1.79	5.18E-07	0.98	9.78E+07	8.32E-04	
0.1	1.80	5.22E-07	0.98	8.04E+07	8.35E-04	

<sup>a</sup>  $\chi^2$  is the measure of the goodness of fit to the data using equivalent circuit models

**Table 4.3** Values of circuit elements obtained for TaO<sub>x</sub>N<sub>y</sub> NTs by EIS in phosphate buffer solution and employing the equivalent circuits shown in Figure 4.11<sup>a</sup>.

$E_{app}/V$ vs. RHE	CPE <sub>1</sub>			CPE <sub>2</sub>			$\chi^2$ <sup>b</sup>	
	$R_s/\Omega \cdot cm^2$	$Q/F \cdot cm^2$	n	$R_1/\Omega \cdot cm^2$	$Q/F \cdot cm^2$	n		$R_2/\Omega \cdot cm^2$
1.4	10.97984	1.95E-06	9.60E-01	1.04E+06			7.22E-04	
1.3	10.96019	1.95E-06	9.61E-01	3.66E+06			6.99E-04	
1.2	10.99164	1.98E-06	9.60E-01	1.12E+07			7.38E-04	
1.1	10.9995	2.01E-06	9.60E-01	1.05E+07			7.01E-04	
1	10.95232	2.05E-06	9.59E-01	9.85E+06			1.14E-03	
0.9	10.96019	2.10E-06	9.58E-01	9.96E+06			1.07E-03	
0.8	11.03488	2.15E-06	9.57E-01	2.83E+06			6.41E-04	
0.7	10.90515	2.29E-06	9.52E-01	8.87E+05			2.77E-04	
0.6	10.94053	2.70E-06	9.35E-01		7.16E-07	2.22E-01	1.34E+04	6.22E-04
0.5	10.85797	4.12E-06	8.95E-01		3.83E-06	5.05E-01	3.37E+03	1.37E-04
0.2	10.99557	1.74E-05	8.98E-01		4.69E-05	8.99E-01	5.24E+00	2.29E-03
0.1	10.9995	3.55E-05	9.80E-01		4.26E-05	9.62E-01	4.90E+00	9.52E-05
0	10.91694	1.39E-04	9.82E-01		1.02E-04	9.53E-01	6.31E+00	4.36E-05

<sup>a</sup> Data obtained in the potential ranges of 1.4-0.7 V and 0.6-0 V were fitted with equivalent circuits (a), and (b) in Figure 4.11, respectively.

<sup>b</sup>  $\chi^2$  is the measure of the goodness of fit to the data using equivalent circuit models.

To examine the semi-conducting properties of the TaO<sub>x</sub>N<sub>y</sub> NTs more closely, Mott-Schottky plots were constructed using data obtained at particular constant frequencies of 100, 75, 50, and 25 kHz, as well as from the EIS-determined (full frequency range) capacitance value, from 1.4 to 0.7 V. Figure 4.14 shows plots of  $1/C^2$  vs. E for TaO<sub>x</sub>N<sub>y</sub> NTs in 0.5 M H<sub>2</sub>SO<sub>4</sub> solution at various

frequencies. This figure shows that there are two linear regions in the Mott Schottky plots, perhaps due to the presence of different donor levels, where shallower donor levels would be ionized before the ionization of the deeper donor levels.<sup>198</sup> Another important observation is the positive slope of the MS plots, indicating that the TaO<sub>x</sub>N<sub>y</sub> NTs are n-type semiconductors, consistent with the literature.<sup>173</sup> In order to calculate the donor density ( $N_D$ ) from the gradient of the MS plot, the permittivity of TaN<sub>y</sub> (~26) was used.<sup>199</sup> This analysis gives an  $N_D$  value of  $1.7 \times 10^{21} \text{ cm}^{-3}$  at 100 kHz and  $5.7 \times 10^{21} \text{ cm}^{-3}$  at 25 kHz, which is quite similar to previously reported values for N-doped TiO<sub>2</sub> NTs ( $3.9 \times 10^{20} \text{ cm}^{-3}$ ).

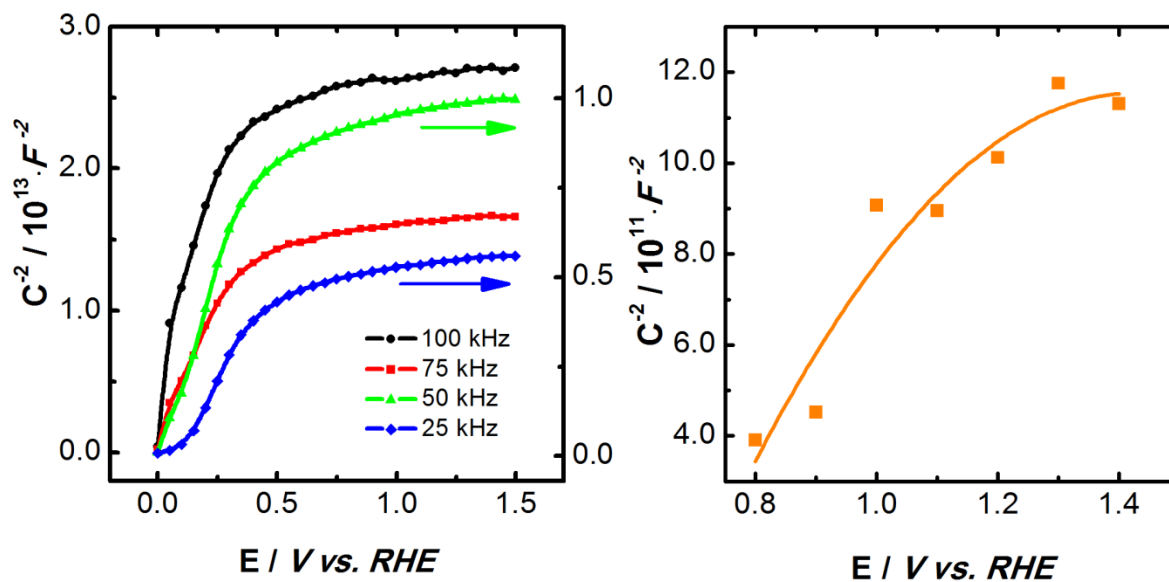


**Figure 4.14** Mott-Schottky (MS) plots obtained for TaO<sub>x</sub>N<sub>y</sub> NTs in 0.5 M H<sub>2</sub>SO<sub>4</sub> at various perturbation frequencies (a) and an MS plot of the same material using capacitance values from CNLS fitting (b).

### 4.2.3 Electrochromic response

Another interesting feature of the electrochemical behavior of these materials is that the TaO<sub>x</sub>N<sub>y</sub> nanotubular films undergo a color change (electrochromism) as the potential is swept over the CV peaks negative of 0.5 V, transitioning from a yellow-orange colour to a blue-black. The potential at which the blue-black colour appears in the PB solution is ca. -0.4 V vs RHE, whereas in 0.5 M H<sub>2</sub>SO<sub>4</sub>, this begins already at ca. -0.1 V vs RHE, when even smaller fractions of the TaO<sub>x</sub>N<sub>y</sub> NTs have been reduced.

It is known that transition metal oxides, such as those that form at W, Ir, Ce, Cr, Ta, Ti, Nb, V, etc., show electrochromism.<sup>200</sup> Typically, oxides of  $d^0$  metal ions (W, Mo, etc.) show an intense colour when they are in the reduced state, while  $d^{10}$  metal ions show the most intense colour in their oxidized state,<sup>200</sup> e.g.,  $\text{Ir}^{4+}$  oxide is blue-grey or blue-black, depending on the number of water molecules present around the metal site. Although oxides of W, Ni, Ir and Mo show the most intense colour changes, W oxide has been the most widely studied.<sup>201</sup> The exact mechanism of colouration/decolouration of  $\text{WO}_3$  is still not established, although this could relate to the participation of crystal defects in the colouration/decolouration process, such as in F centres, inter-valance charge transfer, polaronic absorption, interband excitation, and splitting of the  $\text{W}^{5+}$  state by charge transfer from the valence band. It is assumed that the mechanism of the electrochromism of the  $\text{TaO}_x\text{N}_y$  nanotubular array is comparable to that of  $\text{WO}_3$ , as its electrochemistry is also very similar, involving the insertion of a cation into the lattice while  $\text{Ta}^{5+}$  is reduced to  $\text{Ta}^{4+}$  (analogous to the  $\text{W}^{6+/5+}$  redox reaction).<sup>201</sup>

In electrochromism, a counter ion balances the charge as the transition metal ion changes its redox state,<sup>201</sup> consistent with Reaction 4.3. Counter ion insertion may also play a role in the expansion of the lattice, which, in turn, would provide space for lattice expansion caused by metal ion reduction (and vice versa during oxidation). Moreover, electrochromism can still often be observed when bulky ions that are unable to insert into the lattice of the material are used, due to Drude-type free carrier absorption.<sup>202-203</sup> Thus, in our CV experiments in  $\text{CH}_3\text{CN}$ , electrochromism was still observed, with the  $\text{TaO}_x\text{N}_y$  nanotubes changing from an orange-yellow color to a dark brownish color as the potential is extended from -1.5 to -2.3 V vs. the  $\text{Ag}/\text{Ag}^+$

pseudo-RE. However, the colour and its intensity seem to depend on the water concentration in the solvent.

### 4.3 Summary

TaO<sub>x</sub>N<sub>y</sub> nanotubular arrays were formed by the nitriding of Ta oxide nanotubes (NTs) at 700 °C in a NH<sub>3</sub> atmosphere, converting the white Ta oxide surface film to a yellow-orange color. TEM analysis showed that the TaO<sub>x</sub>N<sub>y</sub> NTs contained evenly spaced holes, ca. 25 nm in diameter, along the NT walls, while the NTs otherwise retained their length and other features after conversion from the Ta oxide state. XPS and XRD analyses, combined with the yellow-orange colour of the TaO<sub>x</sub>N<sub>y</sub> arrays, indicated that the O to N ratio is close to, but not quite, 1:1. NTs that were 300 nm, 1 μm, 2.5 μm and 4 μm in length were formed by varying the anodization time from 2.5 to 10 min, showing that CV redox charges are proportional to the NT length for the shorter NTs, but not for the longer ones. This is likely due to the detachment of the NTs from the base as they become longer.

The electrochemical properties of the TaO<sub>x</sub>N<sub>y</sub> nanotubes were studied by cyclic voltammetry (CV), showing the switching from a non-conducting state at > 0.6 V vs RHE, while at potentials below this, a new set of reversible, pseudocapacitive redox peaks are seen in both acidic and basic media, as well as in a neutral phosphate buffer solution and in acetonitrile solutions. This is associated with an electrochromic phenomenon, with the color switching from yellowish-orange at > 0.6 V to blackish-blue at potentials near -0.4 V. An analysis of the charge passed in these peaks at slow sweep rates, conditions under which the peak currents depend

linearly on scan rates, showed that only ca. 10-15% of the charge expected from the  $\text{Ta}^{4+/5+}$  redox chemistry of the surface of the NTs is passed. In the potential range between 0.6 – 1.5 V vs. RHE, the  $\text{TaO}_x\text{N}_y$  NTs behave as an insulator, almost identical to the parent Ta oxide NTs.

Electrochemical impedance spectroscopy (EIS) studies were also carried out, confirming that a pseudocapacitive response dominates the electrochemical properties at potentials negative of 0.5 V. Also, a Mott-Schottky analysis of the  $\text{TaO}_x\text{N}_y$  NTs at potentials  $> 0.6\text{V}$  revealed that they are n-type semiconductors with a donor density of  $6 \times 10^{21} \text{ cm}^{-3}$  under these conditions. The conductivity and color switching characteristics of  $\text{TaO}_x\text{N}_y$  NTs, observed in a wide range of aqueous solutions and also in acetonitrile solutions, in this work, have not been reported previously.

These properties significantly broaden the range of applications of these interesting nanostructured materials. Specifically, the 1D nanotubular structure of the  $\text{TaO}_x\text{N}_y$  films formed here is vital for the facilitation of electron transport in photocatalytic processes, while the circular holes seen in the tube walls are ideal for enhanced transport of ions and gases in fuel cell applications, where porosity and accessibility of internal surfaces are essential. The fast reversible conductivity switching behavior is of particular importance for the rapid insertion/expulsion of cations from the lattice of the  $\text{TaO}_x\text{N}_y$  NTs, applicable to battery electrodes. Finally, another application of these materials is as a highly conducting catalyst support for hydrogen oxidation in the anode, likely then switching off (becoming poorly conducting) the oxygen reduction reaction at higher potentials and thus protecting the cathode (Chapter 7).

In Chapters 5 and 7, the TaO<sub>x</sub>N<sub>y</sub> NTs are examined for their applicability as either a catalyst or support material for both oxygen reduction (ORR) and hydrogen oxidation (HOR). It will be shown that the TaO<sub>x</sub>N<sub>y</sub> NTs, supporting the catalytic Pt nanoparticles, give reasonable activities towards both the ORR (Chapter 5) and the HOR (Chapter 7).

## Chapter 5 : Evaluation of TaO<sub>x</sub>N<sub>y</sub> nanotubes for use in PEM Fuel Cell Cathode Catalyst Layers

### 5.1 Introduction

In Chapter 4, the general properties of the TaO<sub>x</sub>N<sub>y</sub> nanotubes (NTs) and how their conductivity changes with applied potential were presented and discussed. It was shown that TaO<sub>x</sub>N<sub>y</sub> NTs are electrochemically inactive at potentials ca. > 0.6 V, but active at < ca. 0.6 V vs. RHE. This was assumed to be related to the switching-on of the reversible Ta<sup>5+</sup>/Ta<sup>4+</sup> oxide redox process, a reaction that also involves proton or cation insertion and expulsion during TaO<sub>x</sub>N<sub>y</sub> reduction and oxidation, respectively, at potentials below 0.6 V. From the CV analysis of the charge passed in the CVs, it was also shown that only a fraction (10-15 %) of the Ta sites within the TaO<sub>x</sub>N<sub>y</sub> NTs are electrochemically active, although this seems to be enough to convert the color of the NTs from yellow-orange in the oxidized state to dark blue/black when fully reduced. Both the Ta<sub>2</sub>O<sub>5</sub> and TaO<sub>x</sub>N<sub>y</sub> NTs were suggested to be n-type semiconductors, with their semiconducting behaviour also depending on the solution pH.<sup>204</sup>

Ta oxynitrides have been reported to be promising as a catalyst support to replace carbon, which is susceptible to oxidative degradation, and also as a catalyst for the oxygen reduction reaction (ORR) under proton exchange membrane fuel cell (PEMFC) conditions.<sup>44-47, 51</sup> TaO<sub>x</sub>N<sub>y</sub> mixed with carbon has been used as an ORR catalyst and is on the Department of Energy's (DOE) alternative catalyst list as a prospective replacement for Pt in fuel cell applications.<sup>205</sup>

Several other Group IV metal oxynitrides, such as  $\text{TiO}_x\text{N}_y$ ,  $\text{HfO}_x\text{N}_y$ , etc., have been tested for their stability as a catalyst support in PEM and methanol fuel cells.<sup>206-212</sup>

For these reasons, this chapter examines the stability (corrosion resistance) as well as the electrochemical characteristics of  $\text{TaO}_x\text{N}_y$  NTs and Pt nanoparticles (NPs) loaded (expected 20 wt %)  $\text{TaO}_x\text{N}_y$  NTs as an ORR catalyst support or as the catalyst itself. Notably, this is the first time in the literature that one dimensional (1D) nanotubular structures of  $\text{TaO}_x\text{N}_y$  have been tested for this purpose. If  $\text{TaO}_x\text{N}_y$  NTs can replace costly Pt (which can be easily poisoned by the residual CO in  $\text{H}_2$  fuel) as an ORR catalyst, the cost of PEMFCs could be significantly lowered. Even if this material could serve as a stable catalyst support for Pt, the problematic electro-oxidation (corrosion) of carbon (Section 2.4.2) could be overcome, thus enhancing PEMFC durability and lifetime.

In this chapter,  $\text{TaO}_x\text{N}_y$  NTs (with/without deposited Pt nanoparticles) were examined for their resistance to electrochemical oxidation at the relatively high potentials (up to 1.4 V vs RHE) encountered during PEMFC start-up and shut-down. These materials were also studied for their electrochemical response and activity in the presence of oxygen. This chapter focuses primarily on  $\text{TaO}_x\text{N}_y$  NTs (attached to Ta substrates) that are ca. 1  $\mu\text{m}$  in length, chosen as a representative form of the material, although some experiments with shorter NTs (ca. 0.3  $\mu\text{m}$  in length) and with a compact layer of  $\text{TaO}_x\text{N}_y$  formed on Ta were also carried out.

Pt/C has been used for many years as the main ORR catalyst in PEMFCs and yet a full understanding of its function and its interplay with other components in the fuel cell is still not

available. Therefore, this chapter includes a study of a TaO<sub>x</sub>N<sub>y</sub> compact layer (CL), formed by the anodization of Ta, and then moves to a study of the TaO<sub>x</sub>N<sub>y</sub> NTs, with and without Pt NPs, in both cases. These studies were carried out using a range of electrochemical techniques, including cyclic voltammetry (CV), accelerated durability testing using potential step methods, and a rotating disc electrode configuration.

It is shown that the Pt NPs/ TaO<sub>x</sub>N<sub>y</sub> CL material behaves like Pt and the characteristic electrochemistry of Pt can be seen, an indication that the interface between the Pt NPs and the TaO<sub>x</sub>N<sub>y</sub> CL is strong. The CVs show a high ORR activity, whereas the TaO<sub>x</sub>N<sub>y</sub> NTs alone are inactive. Oddly, however, the other electrochemical features of Pt [e.g., hydrogen underpotential peaks (HUPD) and PtO<sub>x</sub> formation/reduction peaks] are not seen for the long NTs. For the shorter NTs, the HUPD features are seen, but not the PtO<sub>x</sub> peaks, attributed to the diode effect of the TaO<sub>x</sub>N<sub>y</sub> material. Importantly, the TaO<sub>x</sub>N<sub>y</sub> material shows excellent stability under PEMFC conditions, as determined by used a modified DOE protocol.<sup>11</sup> Therefore, the TaO<sub>x</sub>N<sub>y</sub> NTs are seemed to be a potential candidate for the replacement of the Pt/C catalyst in PEMFCs.

## 5.2 Results and Discussion

### 5.2.1 Structure, Morphology and Compositional Characterization

#### 5.2.1.1 Compact TaO<sub>x</sub>N<sub>y</sub> Layer (CL)

In order to evaluate the Pt/ TaO<sub>x</sub>N<sub>y</sub> interfacial properties in later experiments, TaO<sub>x</sub>N<sub>y</sub> compact layers (CLs) were prepared by anodizing Ta metal at 15 V for 15 min in conc. H<sub>2</sub>SO<sub>4</sub> solution to obtain a ca. 26 nm thick compact Ta oxide. The thickness was calculated based on the

anodization constant for Ta metal, which is  $1.7 \text{ nm}\cdot\text{V}^{-1}$ . The Ta oxide CL was then nitrided in the normal reducing ammonia environment to convert it to the  $\text{TaO}_x\text{N}_y$  CL. Pt NPs were deposited on the  $\text{TaO}_x\text{N}_y$  CL by incipient impregnation method, where  $\text{TaO}_x\text{N}_y$  CL coated Ta metal foil was dipped in a  $(\text{CH}_3)_2\text{CO}$  solution containing  $\text{H}_2\text{PtCl}_6\cdot 6\text{H}_2\text{O}$  to impregnate the  $\text{Pt}^{4+}$  salt, then reducing the metal ions to  $\text{Pt}^0$  in a  $\text{H}_2$  environment to obtain the Pt NPs/  $\text{TaO}_x\text{N}_y$  CL composite.

Figure 5.1a and b show the SEM images of the  $\text{TaO}_x\text{N}_y$  and Pt NPs/  $\text{TaO}_x\text{N}_y$  CL, respectively. The  $\text{TaO}_x\text{N}_y$  CL does not have a very smooth surface and follows the contours of the original Ta metal surface, which was somewhat rough. Notably, attempts to make it smoother by mechanical polishing did not succeed.

After depositing Pt, the morphology of the surface of the  $\text{TaO}_x\text{N}_y$  CL is seen to have become quite different (Figure 5.1b). Unlike the  $\text{TaO}_x\text{N}_y$  NTs, where almost spherical or oval shaped Pt NPs of similar sizes (3-5 nm diameter) are seen decorating the NT surfaces (Figure 5.2a), here, various sizes and shapes of Pt NPs can be seen on the surface, while the EDX spectrum confirms just that Pt is present in the material. The origin of the sulphur is likely from the electrolyte (95-98 %  $\text{H}_2\text{SO}_4$  acid) that was used for anodizing the Ta metal. Apart from that, all other elements have the same origin as for the  $\text{TaO}_x\text{N}_y$  NTs.

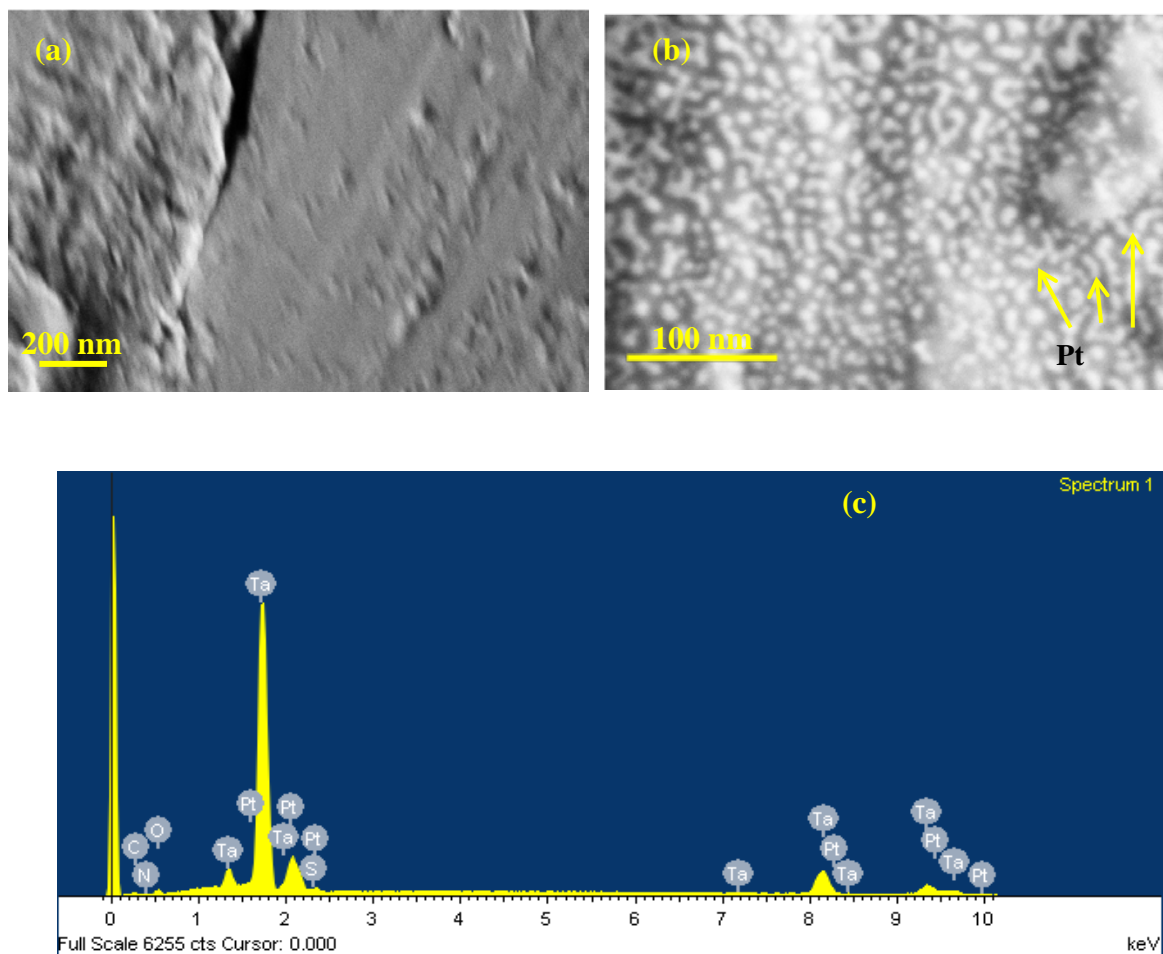


**Figure 5.1** (a) and (b) FESEM images of TaO<sub>x</sub>N<sub>y</sub> CL and Pt NPs/TaO<sub>x</sub>N<sub>y</sub> CL, respectively, while (c) shows the EDX spectrum of the Pt NPs/ TaO<sub>x</sub>N<sub>y</sub> CL.

### 5.2.1.2 Pt nanoparticle-loaded TaO<sub>x</sub>N<sub>y</sub> Nanotubes (NTs)

According to our previously reported procedure, TaO<sub>x</sub>N<sub>y</sub> NTs were synthesized by anodizing Ta foils or rods to make Ta oxide NTs and subsequently heat treating them in ammonia gas.<sup>25</sup> NTs of various lengths were obtained by anodizing the Ta for 2.5 minutes to

obtain NTs ca. 300 nm in length or 5 minutes for 1  $\mu\text{m}$  long NTs. These NTs remained attached to the Ta metal substrate and were then used as the substrate for Pt NP deposition using incipient impregnation.<sup>157</sup> In this method, Ta supported  $\text{TaO}_x\text{N}_y$  NTs were dipped in an acetic chloroplatinic acid solution for > 12 h and subsequently reducing under  $\text{H}_2$ .

The SEM images of the  $\text{TaO}_x\text{N}_y$  NTs and the Pt NPs/  $\text{TaO}_x\text{N}_y$  NTs composite, illustrated in Figure 5.2, show the top and side views of arrays attached to a Ta foil substrate, with the side views obtained from cracks within the film. These images show that the NT array is well-decorated with Pt NPs. The representative NTs are ca. 1  $\mu\text{m}$  in length (Figure 5.2a-c) but the diameter is difficult to determine because of the presence of the deposits around the NTs. However, the NT diameter ranges from 30 to 40 nm without Pt NPs present. Furthermore, these images not only show that the NTs are well-adhered to the Ta metal base, but they also show the appearance of periodic holes along the NT walls, caused by nitriding, consistent with previously reported data (Figure 4.2d).<sup>25</sup> The SEM images of shorter ca. 0.3  $\mu\text{m}$  NTs are presented in Figure 5.2d.

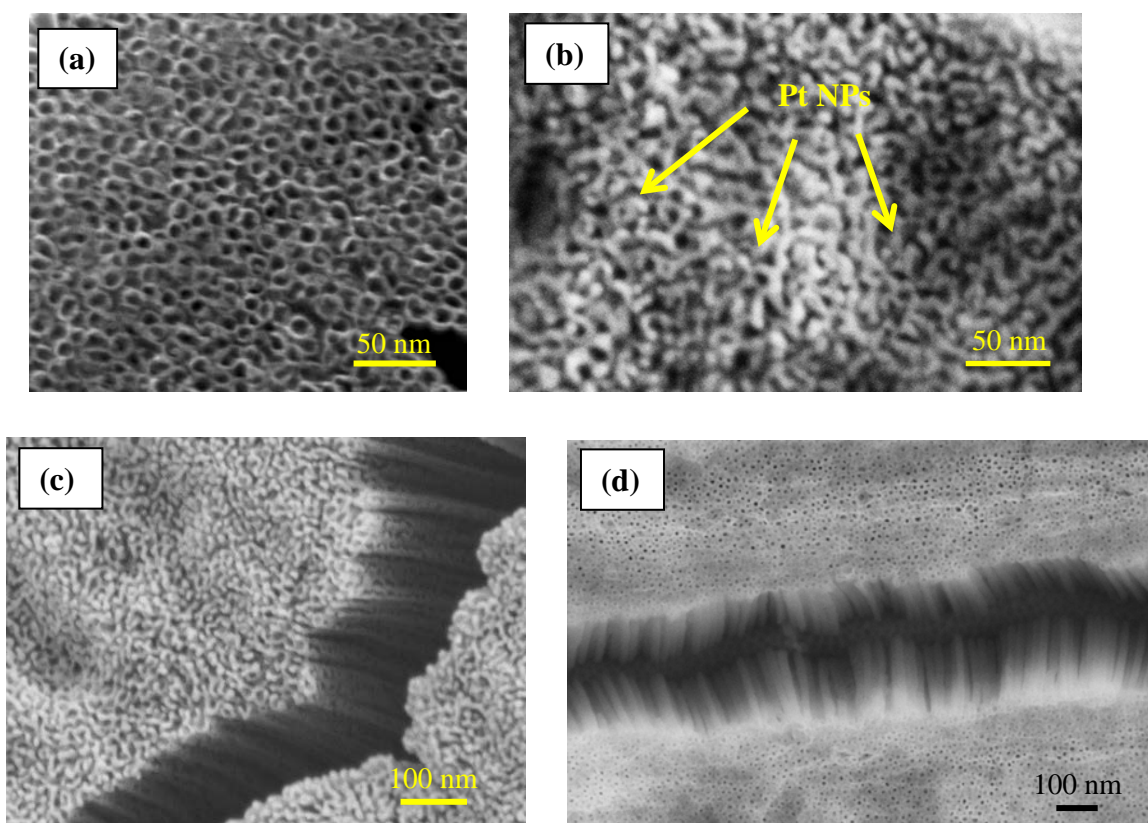


**Figure 5.2.** Top view SEM images of TaO<sub>x</sub>N<sub>y</sub> NTs (anodized for 5 min, giving 1  $\mu$ m long nanotubes) before (a) and after (b and c) the deposition of Pt on these NTs. (d) TaO<sub>x</sub>N<sub>y</sub> NTs (anodized for 2.5 min, giving ca. 0.3  $\mu$ m long tubes), viewed from within a crack in the NT film.

Although the details of the deposits around the NTs are not clear in the SEM images, the TEM image (Figure 5.3a) shows that they are composed of Pt NPs and that the NPs are well separated from each other. Figure 5.3b shows the histogram of the NP size distribution, showing that they are in the range of 1-6 nm. The average NP diameter is 2-4 nm, which is the ideal size for electrocatalysis of the ORR.<sup>34-35, 213</sup> No Pt NPs that are separated from the NTs are seen in Figure 5.3a, although the TEM samples were prepared by sonicating the Pt NPs/TaO<sub>x</sub>N<sub>y</sub> NTs

composite electrode in ethanol. This is an indication that the Pt NPs are well adhered to the  $\text{TaO}_x\text{N}_y$  NTs surfaces. These Pt NPs should reside both on the inner and outer surfaces of the NTs because of the way they were impregnated.

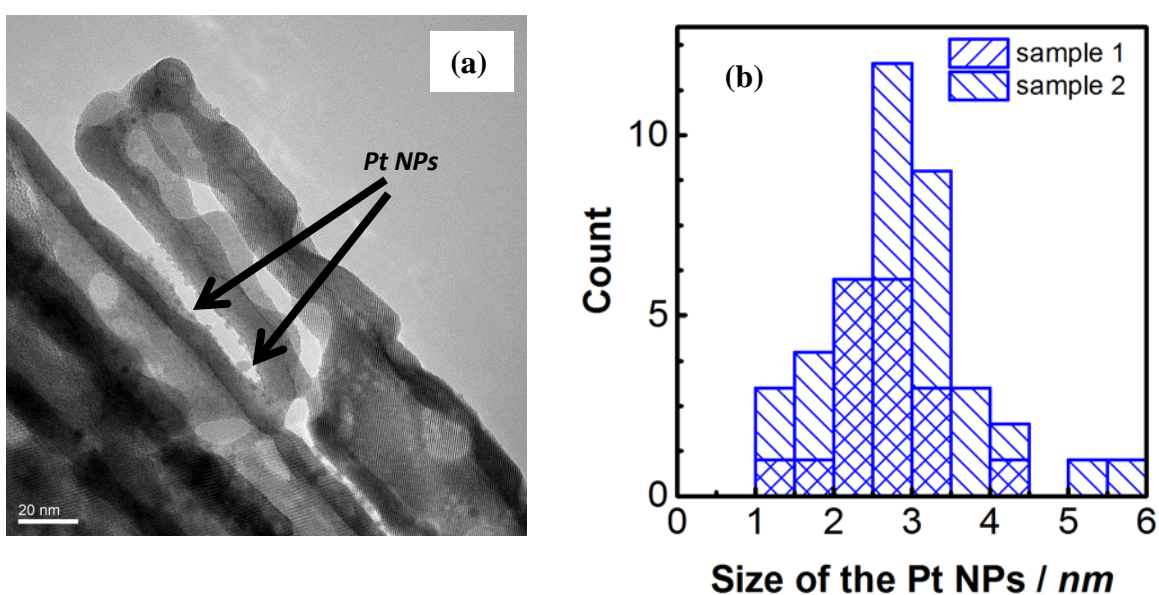


**Figure 5.3** (a) TEM image and (b) histogram of the Pt NPs in the Pt NPs/ $\text{TaO}_x\text{N}_y$  NTs composite.

The Energy Dispersive X-ray (EDX) analysis of the Pt NPs/ $\text{TaO}_x\text{N}_y$  NT composite is shown in Figure 5.4. It is seen that the composite definitely contains Pt. The additional peaks, identified as Ta and Cu, have their origin from the  $\text{TaO}_x\text{N}_y$  NTs and Cu grid, respectively.

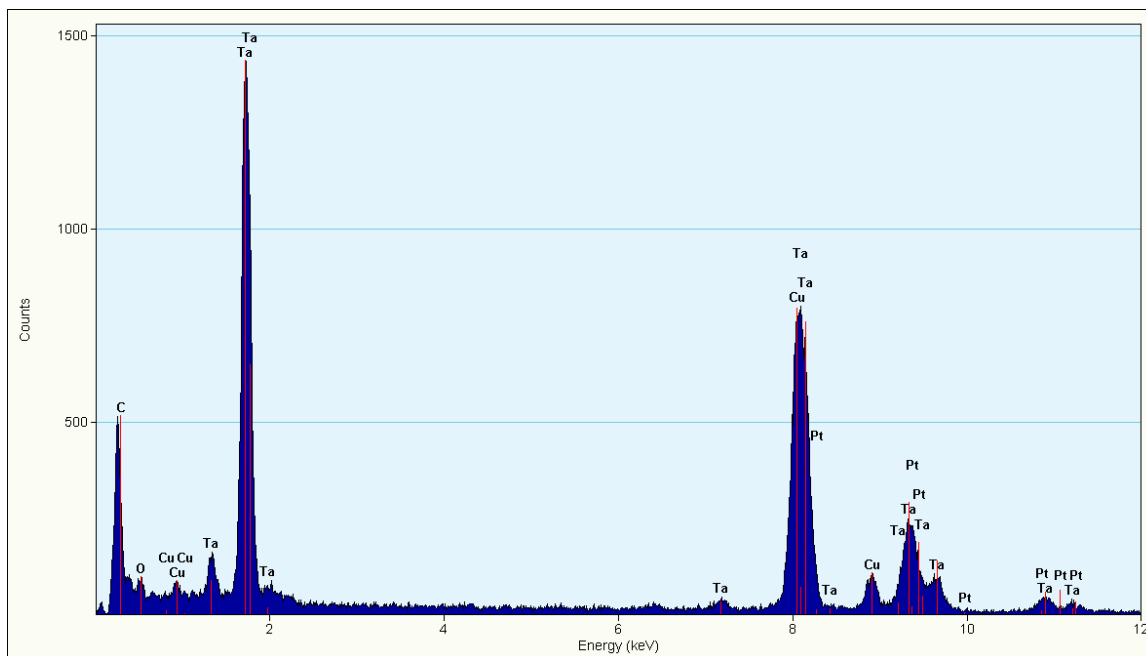


**Figure 5.4** EDX spectrum of Pt NPs/TaO<sub>x</sub>N<sub>y</sub> NTs composite.

It is believed that the surface N and O sites in the TaO<sub>x</sub>N<sub>y</sub> NTs and possibly the OH/H<sub>2</sub>O groups on the TaO<sub>x</sub>N<sub>y</sub> NT surface serve to anchor the Pt salt to the surface. The exact nature of the chemical bond involved is uncertain, but a Lewis acid-base interaction is possibly involved. Furthermore, the periodic holes in the walls of the NTs (Figure 4.2 and Figure 5.3b) may also be good anchoring sites for the Pt NPs because of their expected higher energy.<sup>25</sup> To facilitate the controlled reduction of Pt ions by hydrogen (forming protons) and to prevent unnecessary Pt NP growth, the reaction vessel was protected from stray light by wrapping it with Al foil because Pt ions can be reduced by oxidizing H<sub>2</sub>O/CH<sub>3</sub>COCH<sub>3</sub> in the presence of photons.<sup>214-215</sup> To obtain a single Pt NP, several Pt atoms need to come together, with the Pt salt reduced by H<sub>2</sub>. Contrary to

the present case of TaO<sub>x</sub>N<sub>y</sub> NTs, on carbon supports, some of the oxidizable surface functional groups, such as –COOH, -OH, etc., may help to reduce the Pt ions before treatment in H<sub>2</sub>, and as a result, the Pt NPs may be formed more readily.

### **5.2.2 Oxygen reduction at TaO<sub>x</sub>N<sub>y</sub> nanomaterials, with and without Pt NPs present**

In this section, the research was directed towards the activity of TaO<sub>x</sub>N<sub>y</sub> NTs, with and without Pt NPs present, as an oxygen reduction (ORR) catalyst or as a catalyst support material. The ORR is the cathodic reaction in the majority of fuel cells and its activity is commonly tested using a three electrode half-cell system, as well as within a full membrane-electrode assembly. There are many electrochemical techniques used in the screening of the ORR activity of a catalyst, including steady state polarization, cyclic voltammetry, and electrochemical impedance spectroscopy. All of these techniques can be used with or without a rotating disk electrode (RDE) configuration.

Cyclic voltammetry (CV), with and without the use of a RDE, was performed in 0.5 M H<sub>2</sub>SO<sub>4</sub> without (N<sub>2</sub> saturation) or with O<sub>2</sub> saturation, to characterize the TaO<sub>x</sub>N<sub>y</sub>-based materials as an ORR catalyst. The research began with the TaO<sub>x</sub>N<sub>y</sub> compact layer (CL) in order to later distinguish the effects of electrode porosity (as in the case of the nanotubular array) from the normal characteristics of the ORR.

#### ***5.2.2.1 ORR at TaO<sub>x</sub>N<sub>y</sub> compact layer coated with Pt NPs (Pt NPs/ TaO<sub>x</sub>N<sub>y</sub> CL)***

The ORR studies of the Pt NPs, deposited on the TaO<sub>x</sub>N<sub>y</sub> compact layer (CL), were undertaken first as a proof-of-concept that these Pt NPs could be electrochemically addressed

and then function as an ORR catalyst on the TaO<sub>x</sub>N<sub>y</sub> substrate. The CV obtained for this material in N<sub>2</sub>-saturated solutions is shown in Figure 5.5a (blue trace), where it is seen that the normal CV for Pt metal is obtained. Two pairs of peaks in the 0.05 - 0.3 V window are due to the underpotential deposition/removal of H atoms on Pt (the 'HUPD' process).<sup>216</sup> The charge passed in these HUPD peaks allows the calculation of the electrochemically active surface area (ECSA) of the Pt on the electrode surface.<sup>217</sup> At higher potentials (ca. > 0.70 V), evidence for both Pt oxide formation and reduction in the peak centered at 0.75 V is also seen, as expected.<sup>216</sup>

Based on the SEM images in Figure 5.1b, the average Pt NP size for this sample is ca. 20 nm and thus, assuming a spherical NP shape, the maximum Pt ECSA would be 300 cm<sup>2</sup> for 1 cm<sup>2</sup> of geometric electrode area. However, the SEM image shows that only ca. 50% (qualitatively) of the compact layer area is covered by the Pt NPs. Therefore, the active Pt ECSA is expected to be in the range of 150 cm<sup>2</sup> for 1 cm<sup>2</sup> of geometric electrode area. However, the HUPD charge passed in Figure 5.5a (blue) gives an ECSA of only ca. 1.1 cm<sup>2</sup>.<sup>217</sup> This very large difference in the predicted vs. observed ECSA values shows clearly that not all of the deposited Pt NPs are electrochemically addressable when on the surface of the 30 nm thick TaO<sub>x</sub>N<sub>y</sub> CL. It is possible that those Pt NPs that are electrochemically addressable are surrounded by Ta ions that can undergo a redox reaction and thus conduct electrons to/from the Pt NPs, suggesting then that the TaO<sub>x</sub>N<sub>y</sub> phase is present only in domains on the CL surface.

It is known that wide band gap valve metal oxides, such as Ti oxide, become conductive if there is a Magneli phase present, where a Magneli phase is an insulating phase, but in a substoichiometric state.<sup>80</sup> This state can sometimes be formed due to exposure to H<sub>2</sub> and then it

can show conducting properties.<sup>218</sup> Here, the Magneli phase would have formed within the Ta oxide CL while undergoing reduction during the high temperature ammonolysis/nitriding step. In terms of why only such a small fraction of the Pt NPs is responding electrochemically, this question remains unanswered here. However, it should be noted that the notion that the contact between the Pt NPs and the TaO<sub>x</sub>N<sub>y</sub> CL surface is eroding by CV cycling can be ruled out, since the first and last CV of the Pt NPs on the CL are superimposable.

In O<sub>2</sub>-saturated 0.5 M H<sub>2</sub>SO<sub>4</sub>, the ORR is clearly seen to be occurring at the Pt NPs/TaO<sub>x</sub>N<sub>y</sub> CL material (red trace in Figure 5.5a), with the CV being offset in the negative current direction, as expected. The green trace shows the CV after subtracting the CV collected in deaerated conditions (blue trace), showing that the onset potential for the ORR is typical of a Pt/C catalyst [ca. 0.9 V vs. RHE (Figure 5.11d)]. However, it is odd that there are two peaks seen at 0.75 and 0.6 V vs RHE, even after the CV obtained in the N<sub>2</sub>-saturated acid solution is subtracted from the CV obtained in the aerated environment. This cannot be due to Pt oxide reduction, as this would have subtracted out.

It is possible that the two peaks reflect the 2-e ORR mechanism, with the ORR occurring via the H<sub>2</sub>O<sub>2</sub> pathway as the formation of H<sub>2</sub>O<sub>2</sub> occurs at 0.67 V vs. RHE, but this should not occur at Pt, where the ORR is known to occur via the 4e pathway. However, it is known that metal oxides can promote the indirect 2e H<sub>2</sub>O<sub>2</sub> pathway for the ORR and therefore perhaps the ORR is being influenced by the underlying TaO<sub>x</sub>N<sub>y</sub> compact film.<sup>219</sup> Figure 5.5b shows that this peculiar ORR behaviour persists even over a range of sweep rates, with the peaks shifting cathodically with increasing sweep rate, suggesting some kinetic sluggishness.

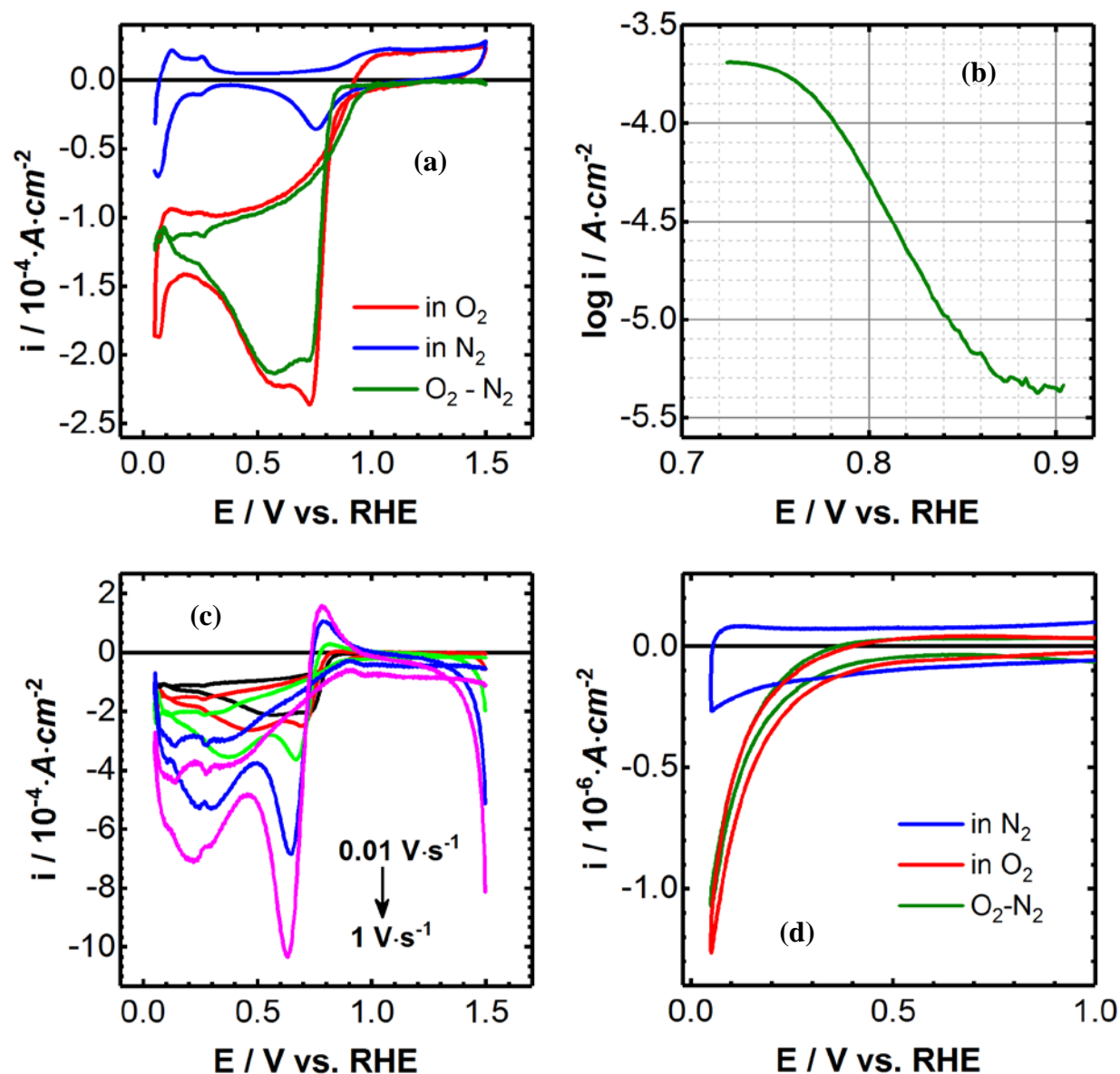


**Figure 5.5** (a) CVs obtained in quiescent 0.5 M H<sub>2</sub>SO<sub>4</sub> at 10 mV·s<sup>-1</sup> in N<sub>2</sub> (blue) and O<sub>2</sub> (red) saturated conditions, also showing the difference between these two CVs (green) for the Pt NPs/TaO<sub>x</sub>N<sub>y</sub> CL material. (b) shows the cathodic scan Tafel plot obtained from (a) between 0.7-0.9 V at 10 mV·s<sup>-1</sup>, while (c) shows the CVs at various scan rates (0.01, 0.05, 0.2, 0.6, and 1 V·s<sup>-1</sup>) in O<sub>2</sub>-saturated 0.5 M H<sub>2</sub>SO<sub>4</sub>. (d) shows the ORR activity of TaO<sub>x</sub>N<sub>y</sub> CL without Pt. Note: The currents in all of the CVs have been divided by the geometrical area of the electrode.

As explained in Chapter 2 (Section 2.7), the key parameters extracted from a CV for a reaction such as the ORR are the current at a particular potential (or the exchange current density), also described as the ‘overpotential’ at a particular current density, and the Tafel slope. On the best catalysts, such as Pt/C, the ORR commences at ca. 1 V vs. RHE (Figure 5.11d) and the overpotential is then typically already ca. 0.23 V.<sup>220</sup> However, on the Pt NPs/ TaO<sub>x</sub>N<sub>y</sub> CL material, the overpotential appears to be ca. 0.35 V at the potential where the ORR is seen to commence, which is ca. 0.88 V vs. RHE (Figure 5.5). This could be consistent with a relatively small fraction of the Pt NPs being active.

However, it is believed to be best to report the ORR activity from the current passed at a particular potential, or by the potential at a particular current density. Here, the chosen potential is 0.9 V vs. RHE, because for Pt/C, it is the most widely reported and compared.<sup>112</sup> At 0.9 V, Pt/C gives a current density of ca. 300  $\mu\text{A}\cdot\text{cm}^{-2}_{\text{Pt}}$ ,<sup>221</sup> while for the Pt NPs/TaO<sub>x</sub>N<sub>y</sub> CL material, the current is only 6  $\mu\text{A}\cdot\text{cm}^{-2}_{\text{Pt}}$ , again indicating that only some of the Pt NPs are active.

The Tafel slope (TS) for the ORR at low currents (low overpotentials, > 0.77 V vs. RHE) at Pt catalysts is normally ca. 60  $\text{mV}\cdot\text{decade}^{-1}$  of current, while here, it is 61  $\text{mV}\cdot\text{decade}^{-1}$  (Figure 5.5b). This good agreement suggests that the ORR is indeed occurring at the Pt NPs. This value of the TS is consistent with the proposed mechanism of the ORR at Pt, namely that the first electron transfer step is slow, but that the Pt surface is partly covered by an oxide film with the surface O groups repelling each other laterally, leading to kinetics influenced by the Temkin isotherm.<sup>222-226</sup>

Figure 5.5d presents the ORR results at the TaO<sub>x</sub>N<sub>y</sub> CL, without any Pt NPs present. It can be seen the ORR activity for this material is negligible when compared with the Pt NPs/ TaO<sub>x</sub>N<sub>y</sub> CL.

Overall, these results (Figure 5.5) do show that the Pt NPs on the TaO<sub>x</sub>N<sub>y</sub> CL substrate behave as metallic Pt and are active towards the ORR, although only some of the Pt NPs seem to be active. A comparison was then made to the ORR activity at the Pt NPs present on the surface of the TaO<sub>x</sub>N<sub>y</sub> NTs, formed identically to the method used for Pt NP deposition on the TaO<sub>x</sub>N<sub>y</sub> CL, as described in the following section.

### ***5.2.2.2 Electrochemistry and ORR at TaO<sub>x</sub>N<sub>y</sub> NTs (~1 μm in length)***

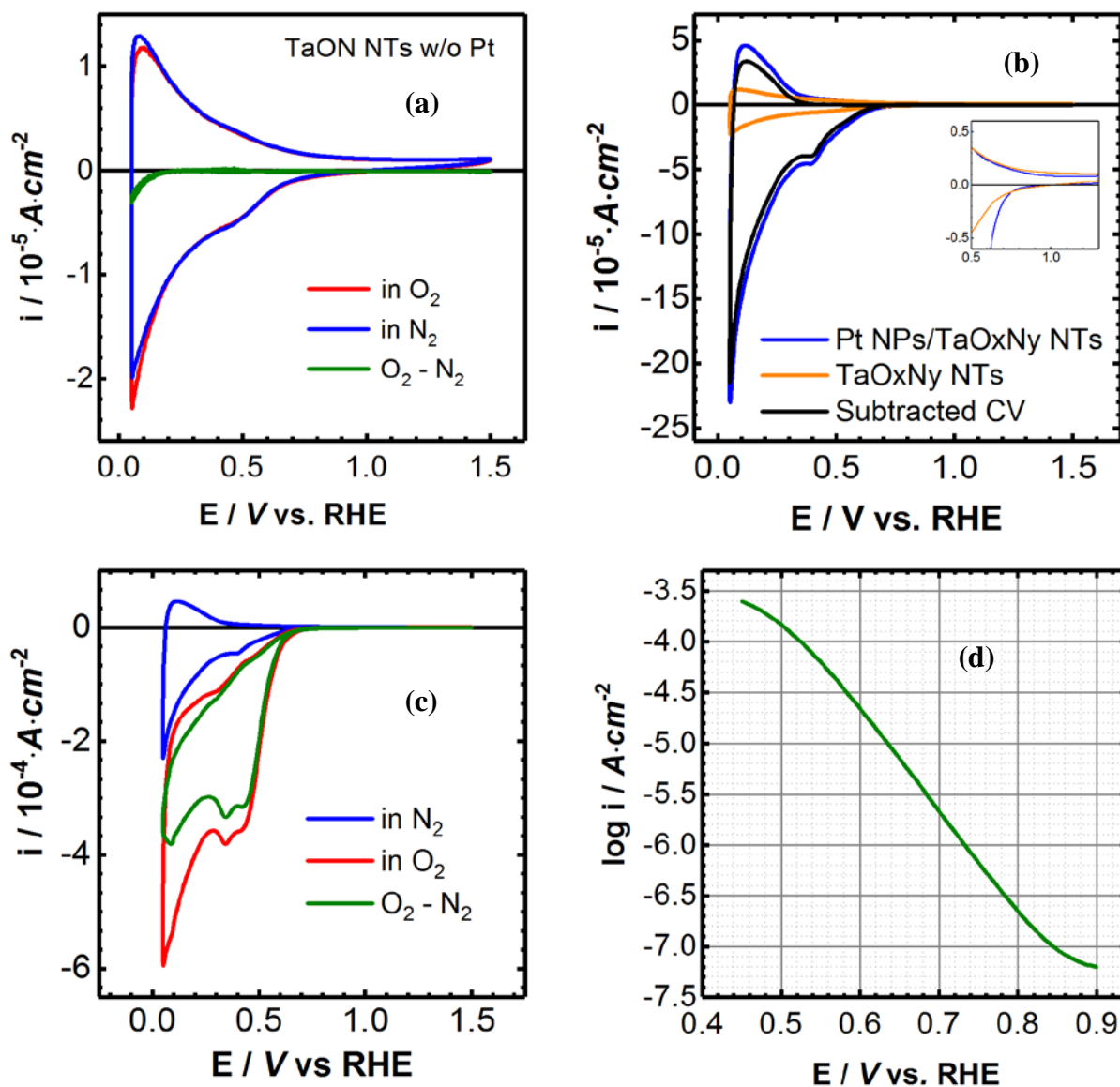
#### ***(a) In the absence of Pt NPs***

Figure 5.6a shows an example of the CVs obtained for the TaO<sub>x</sub>N<sub>y</sub> NT coated electrodes in 0.5 M H<sub>2</sub>SO<sub>4</sub> solution saturated with either N<sub>2</sub> (blue) or O<sub>2</sub> (red) at a scan rate of 10 mV·s<sup>-1</sup> over the potential range of 0.05 V – 1.5 V vs. RHE. In the deaerated solution, the TaO<sub>x</sub>N<sub>y</sub> NTs are clearly electrochemically inactive from ca. 0.6 V to 1.5 V vs. RHE. However, the NTs are redox active at < 0.6 V, attributed in Chapter 4 to the redox chemistry of Ta<sup>5+/4+</sup> coupled with proton intercalation/de-intercalation.<sup>25</sup> As explained earlier, this process could be due to the presence of Magneli phase in the TaO<sub>x</sub>N<sub>y</sub> NTs.



Furthermore, this CV (Figure 5.6a, blue) reveals that the material is behaving like an n-type semiconductor, which is normally electrochemically inactive at relatively positive potentials vs. the RHE.<sup>25</sup> As the potential is made more positive, n-type semi-conductors are deprived of the electrons that are responsible for their conductivity and hence their CVs tend to show only double layer charging, as seen in Figure 5.6a (blue).<sup>227</sup>

Figure 5.6a (red) shows that, even with O<sub>2</sub>-saturation of the acidic solution, the redox chemistry of the TaO<sub>x</sub>N<sub>y</sub> NTs does not change significantly, although a very slight cathodic offset is seen when compared to the situation under N<sub>2</sub> saturation. This result, seen more clearly in the subtracted CV in Figure 5.6a (green), indicates that the TaO<sub>x</sub>N<sub>y</sub> NTs may have a very minor ORR activity, but definitely not enough to compete with the benchmark material, Pt/C.



**Figure 5.6** (a and c) CVs obtained at  $10 \text{ mV} \cdot \text{s}^{-1}$  in  $0.5 \text{ M H}_2\text{SO}_4$  saturated with  $\text{N}_2$  (blue) or  $\text{O}_2$  (red), and the subtracted CV (red minus blue = green) for (a)  $\text{TaO}_x\text{N}_y$  NTs and (c) Pt NPs/ $\text{TaO}_x\text{N}_y$ , with Pt NPs deposited by the incipient impregnation method. (b) CVs obtained in  $\text{N}_2$ -saturated acid for  $\text{TaO}_x\text{N}_y$  NTs and Pt NPs/ $\text{TaO}_x\text{N}_y$  NTs, as well as the subtracted CV. Inset shows double layer charging region. Pt NPs were deposited on the NTs by incipient impregnation method. (d) shows the Tafel plot for the ORR in the cathodic scan at the Pt NPs/ $\text{TaO}_x\text{N}_y$  NTs [data from (c)]. Note: All currents have been divided by the geometric area of the electrode.

To quantify the ORR activity, the ORR current at 0.9 V vs. RHE (Figure 5.6a) at the TaO<sub>x</sub>N<sub>y</sub> NTs was obtained, showing that it is in the range of nanoampere (ca. 900 nA·cm<sup>-2</sup>) and even at 0.6 V vs RHE, the current is still in the nanoampere range. These results confirm that the TaO<sub>x</sub>N<sub>y</sub> NTs are a very poor ORR catalyst compared to Pt/C, which gives currents in the mA range at a similar potential.

It should be noted that there are literature claims that TaO<sub>x</sub>N<sub>y</sub>, in the form of nano- and micron-size particles as well as thin films, is active for the ORR, giving between 20 to 0.14 μA·cm<sup>-2</sup> at 0.3 V vs RHE.<sup>44-46</sup> However, in much of this past work, Ta oxynitride was mixed with carbon, except for in the work of Pasqualetti et.al.<sup>45</sup> and Ota et.al.,<sup>46</sup> where they obtained current densities of 0.14 and 20 μA·cm<sup>-2</sup> at 0.3 V for a single phase Ta oxynitride powder and thin film, respectively. Other groups have reported that Ta nitride, the fully nitrated version of oxynitride, is a reasonable catalyst for the ORR.<sup>228-229</sup> However, in most cases, the catalyst inks were prepared with 7 - 50 wt % carbon present, which would have provided an alternative pathway for electronic conduction within these catalysts vs. for TaO<sub>x</sub>N<sub>y</sub> alone, as it is known from Chapter 4 that TaO<sub>x</sub>N<sub>y</sub> is not a good conductor at > 0.6 V vs. RHE (without Pt).

In some of the past literature, Ta oxynitride was not only mixed with carbon but also that carbon was incorporated into the oxynitride lattice, making carboxynitride (TaO<sub>x</sub>N<sub>y</sub>C<sub>z</sub>), materials that are believed to be more electronically conducting due to additional vacancies in the lattice.<sup>41, 48, 50</sup> One other difference between most of the prior and present work is that the TaO<sub>x</sub>N<sub>y</sub> catalysts used in these previous literature studies were not attached to a Ta substrate, as is the case here, most typically being nanopowders. At this point, the lack of ORR activity of

TaO<sub>x</sub>N<sub>y</sub> alone, as observed here (Figure 5.6a, green), makes sense in the light of the fact that TaO<sub>x</sub>N<sub>y</sub> should not be an electronic conductor in the potential range of the ORR. Thus, it remains unclear why this material was found to be active on its own in some prior literature reports.

***(b) Electrochemistry of TaO<sub>x</sub>N<sub>y</sub> NTs (1 μm length) + Pt NPs in deaerated solutions***

As the ~1 micron long TaO<sub>x</sub>N<sub>y</sub> NTs, attached to the Ta metal substrate, appear to be essentially inactive towards the ORR on their own, as described in the above section, efforts were made to determine whether the NTs could serve as a support material for Pt NPs during the ORR. Thus, the CV response of the TaO<sub>x</sub>N<sub>y</sub> NTs after Pt deposition (Figure 5.6b, blue trace) was first examined in N<sub>2</sub>-saturated 0.5 M H<sub>2</sub>SO<sub>4</sub> and compared to the activity of the NTs without Pt (Figure 5.6b, orange trace).

It can be clearly seen in Figure 5.6 that both materials give a reversible CV in the potential range of 0 to 0.8 V. In fact, the currents in the presence of Pt are much larger, as expected from the fact that HUPD currents should be seen when Pt is present. However, the CV features in the presence of Pt (blue) have the characteristics primarily of TaO<sub>x</sub>N<sub>y</sub>, rather than of the HUPD process on Pt, which is a rather puzzling outcome, and the subtracted CV (Figure 5.6b, black) shows only the characteristics of TaO<sub>x</sub>N<sub>y</sub>. The HUPD features typical of Pt NPs, deposited on some other valve metals oxides, such as Ti oxide<sup>230</sup> and Nb oxide<sup>219, 231</sup>, have been seen by others<sup>111</sup>, but are not observed in Figure 5.6b at these relatively long (1 μm) TaO<sub>x</sub>N<sub>y</sub> NTs. Because the CV currents are significantly enlarged in the presence of the Pt NPs, but the peak

shapes are those of the  $\text{TaO}_x\text{N}_y$  redox reaction, we refer to this phenomenon here as ‘Pt enhanced  $\text{Ta}^{5+/4+}$  redox currents’.

Another feature to note in Figure 5.6b is that there is no sign of the Pt oxide formation/reduction currents that were seen in Figure 5.5a for the Pt NPs on the compact thin film of  $\text{TaO}_x\text{N}_y$ . In the potential window (0.8 V - 1.5 V) over which  $\text{TaO}_x\text{N}_y$  is not redox active (Figure 5.6a), Pt normally forms  $\text{PtO}_x$ . However, it would be difficult to form  $\text{PtO}_x$  as  $\text{TaO}_x\text{N}_y$  does not conduct electrons in this potential range, especially through the long NTs, as compared to the thin (30 nm) compact layer (Figure 5.5). The inset in Figure 5.6b also shows that the Pt NPs do not seem to be adding to the observed double layer capacitance, which should be higher for Pt than for the  $\text{TaO}_x\text{N}_y$  CL. Thus, the absence of the CV features of Pt is a clear indication that the electroactive Pt NPs are not residing just on the base of the NTs. If this had been the case, these NPs should have exhibited the typical Pt CV characteristics, as was the case at the  $\text{TaO}_x\text{N}_y$  CL, which had an additional thickness (3-5 nm) similar to what is expected to be present at the base of the NTs (Figure 5.5a).

Overall, the results in Figure 5.6 suggest that the Pt NPs on these long  $\text{TaO}_x\text{N}_y$  NTs are not generating their expected CV characteristics. At the same time, the Pt NPs are causing a significant increase in the  $\text{TaO}_x\text{N}_y$  redox currents, based on an as yet not understood process or phenomenon. It will also be shown below that the presence of the Pt NPs does result in much higher ORR currents at the Pt NPs/  $\text{TaO}_x\text{N}_y$  NTs composite material as compared to the  $\text{TaO}_x\text{N}_y$  NTs alone.

**(c) ORR at TaO<sub>x</sub>N<sub>y</sub> NTs with deposited Pt NPs**

To evaluate the ORR activity of the composite Pt NPs/ TaO<sub>x</sub>N<sub>y</sub> NTs electrodes, CVs were again obtained in both N<sub>2</sub> and O<sub>2</sub> saturated 0.5 M H<sub>2</sub>SO<sub>4</sub> solutions (Figure 5.6c), with significant differences seen in the CVs in these two gas environments. In O<sub>2</sub>-saturated 0.5 M H<sub>2</sub>SO<sub>4</sub>, the CVs in Figure 5.6c clearly show significantly enhanced ORR activity at the Pt NPs/ TaO<sub>x</sub>N<sub>y</sub> NTs. Despite the absence of the HUPD and oxide CV features of Pt, the observed ORR electrochemistry confirms that the Pt NPs are catalytically active and must be communicating with the underlying Ta electrode. Further analysis of the CVs (Figure 5.6c) in O<sub>2</sub>-saturated conditions reveals that the ORR currents begin to flow at ca. 0.8 V vs. RHE, similar to the situation at the compact TaO<sub>x</sub>N<sub>y</sub> layer after Pt NP deposition (Figure 5.5a), but significant currents are seen only at < 0.65 V vs. RHE, when more of the Ta<sup>5+</sup> sites within the TaO<sub>x</sub>N<sub>y</sub> NTs switch on their conductivity.

Figure 5.6d shows the Tafel plot for the ORR at the Pt NPs/TaO<sub>x</sub>N<sub>y</sub> NTs, giving a Tafel slope (TS) in the cathodic scan of 0.105 V·decade<sup>-1</sup> obtained between 0.5 V to 0.85 V. Only the cathodic Tafel plot is again shown here, as often, the anodic plot was not very linear, which could indicate that a mixture of pathways or slow steps are present, making interpretation difficult. The 105 mV·decade<sup>-1</sup> slope is different from what was seen at lower overpotentials (between 0.76 to 0.85 V vs. RHE) at the Pt/TaO<sub>x</sub>N<sub>y</sub> compact film (0.061 V·decade<sup>-1</sup> of current in Figure 5.5b).

Another possible explanation for the roughly twice the Tafel slope value, obtained for the ORR at Pt NPs deposited on the  $1\ \mu\text{m}$   $\text{V}\cdot\text{decade}^{-1}$  NTs vs. on the compact  $\text{V}\cdot\text{decade}^{-1}$  layer, is related to the ‘dual barrier mechanism’.<sup>232-234</sup> Due to the resistance of the catalytic material, which will be much higher for the NTs than the CL, it has been hypothesized that there are two potential drops, one down the length of the NTs, driving the transport of ions and electrons through the  $\text{V}\cdot\text{decade}^{-1}$  walls, and the other at the Pt/solution interface, driving the charge transfer process during the ORR.<sup>232-234</sup> This could then double the Tafel slope from 60 to 120  $\text{mV}\cdot\text{decade}^{-1}$  (60 to 105  $\text{mV}\cdot\text{decade}^{-1}$ , in our case).

A third possible explanation is related to ‘porous electrode theory’, where a Tafel slope can be doubled due to the mass transport limitations down the length of the pores within a catalytic layer, e.g., the flooded agglomerate model and the cylindrical gas pore model<sup>235</sup>, as shown from de Levie’s limiting case.<sup>195</sup> The Birss group and others have reported the doubling of the slope for porous carbon electrodes, based on this argumentation.<sup>236-237</sup>

Typically, the kinetics and thermodynamic properties of ORR on carbon supported catalysts (either novel carbon support or carbon mixed with other compounds) in FCs are compared with the state-of-the art catalyst Pt/C. On Pt/C two values for TS are obtained, 60  $\text{mV}\cdot\text{decade}^{-1}$  in the low overpotential range (potential at  $< 0.77\ \text{V}$  vs. RHE) and 120  $\text{mV}\cdot\text{decade}^{-1}$  in the high overpotential range ( $> 0.77\ \text{V}$  vs. RHE). This change in the TS is attributed to the formation of  $\text{PtO}_x$  at lower overpotential. The  $\text{PtO}_x$  participate in the rate determining step of the ORR, which changes the TS of the reaction.<sup>238</sup> However, comparison of Pt/C ORR data with the Pt/TaO<sub>x</sub>N<sub>y</sub> system to evaluate the efficiency of the catalyst and their corrosion stability raise

questions, because, mechanistically, ORR on Pt/C could be different from the Pt/TaO<sub>x</sub>N<sub>y</sub>. In this thesis, the mechanistic aspect of the ORR on Pt NPs/TaO<sub>x</sub>N<sub>y</sub> NTs is not studied and it was proposed as the future work. Therefore, ORR data on Pt/C is reported here only for readers to have a broader perspective on the subject, not intended for comparison.

Another interesting feature of the ORR CV data shown in Figure 5.6c is the multiple cathodic peaks (at least three peaks before subtraction) seen between 0.3 V and 0.5 V vs. RHE, even after subtraction of the CV collected in N<sub>2</sub>-saturated sulfuric acid solutions from the data under aerated conditions. One of the peaks, centered ca. 0.4 V (Figure 5.6a), has been attributed to the redox chemistry of surface states in the TaO<sub>x</sub>N<sub>y</sub> NTs. (Section 4.2.2.2) Two more peaks, centered ca. 0.35 V and 0.45 V, appear in the O<sub>2</sub>-saturated solution and are not subtracted out (Figure 5.6c). The broad peak at ca. 0.45 V in O<sub>2</sub>-saturated conditions is still present as a small peak after subtraction of the CV collected in the N<sub>2</sub>-saturated sulfuric acid solution. Further, this peak is not always reproducible and may arise from the presence of variable surface states on the NTs.

Because these two peaks may be ‘transport sensitive’, a scan rate study was performed to understand whether the processes involved are diffusion controlled. A plot of the cathodic peak current (at ca. 0.3 V) vs. both the scan rate and the square root of scan rate is shown in Figure 5.7, demonstrating that the relationship between peak current vs. square root of scan rate is linear. This does suggest a diffusional element to the measured currents, as expected, considering that this is in the potential range at which a plateau (diffusional) current is observed at Pt/C catalysts when solution agitation is present (or in a membrane-electrode-assembly, where

convection is provided by gas flow).<sup>166</sup> Since the peak centered at ca. 0.45 V is not easily discernable at all sweep rates, the data for this peak are not presented here.

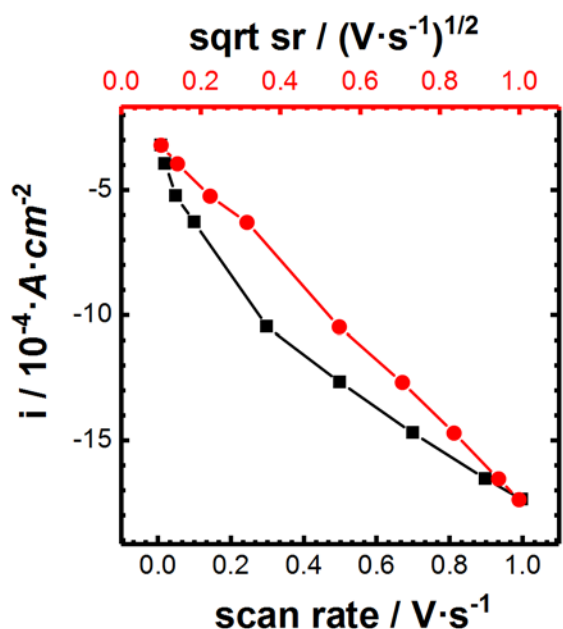


**Figure 5.7** Cathodic peak current (at -0.3 V vs RHE) vs. scan rate and square root of scan rate for Pt NPs/TaO<sub>x</sub>N<sub>y</sub> NTs in O<sub>2</sub>-saturated 0.5 M H<sub>2</sub>SO<sub>4</sub> solution (see Figure 5.6c).

Because of the evidence for diffusion controlled currents in the quiescent sulfuric acid solution (Figure 5.6b and Figure 5.7), also seen in the ORR literature for Pt/C,<sup>166, 236</sup> the Pt NPs/TaO<sub>x</sub>N<sub>y</sub> NTs were also used in rotating disc electrode (RDE) work. In the RDE configuration, the mass transport of the electroactive species under investigation should be controlled by convection and a limiting current should be seen due to the fixing of the Nernst diffusion layer thickness. As a result, the kinetic region of the electrochemical reaction should be extended, allowing a more detailed kinetic analysis.

To carry out the RDE work, the end of a Ta rod with a 4.75 mm diameter was anodized to form ca. 1  $\mu\text{m}$  Ta oxide NTs and it was then subjected to the standard high temperature ammonia treatment to obtain the  $\text{TaO}_x\text{N}_y$  NTs, followed by Pt NP deposition (Section 3.3), giving a Pt NPs/ $\text{TaO}_x\text{N}_y$  NTs electrode. The prepared electrode was then embedded in a polyether ether ketone (PEEK) shroud to serve as the RDE tip, which was connected to the RDE shaft (Figure 5.8b) for further electrochemical analysis.

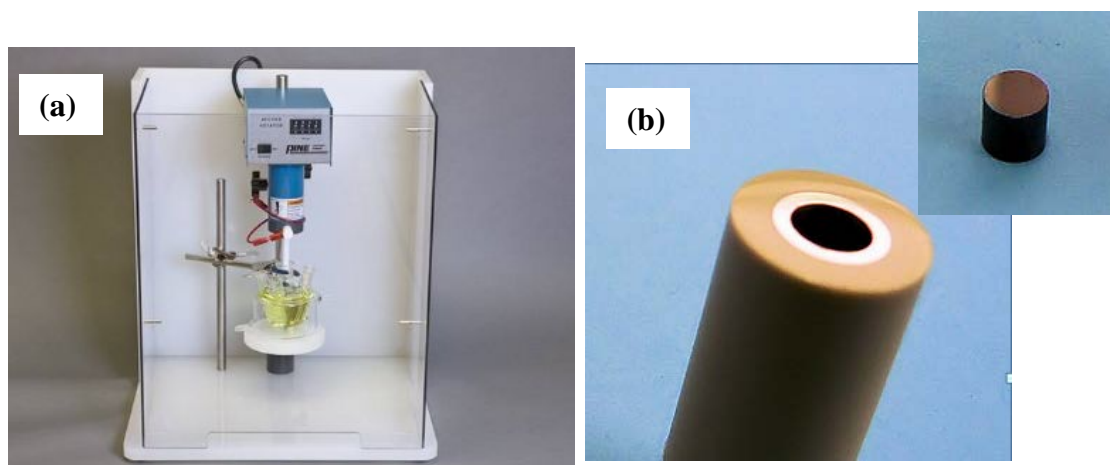


**Figure 5.8** (a) RDE set up and (b) the RDE tip, with the electrode shrouded in an insulating layer.<sup>239</sup>

The RDE data for the Pt NPs/ $\text{TaO}_x\text{N}_y$  NTs in the  $\text{N}_2$ -saturated and  $\text{O}_2$ -saturated 0.5 M  $\text{H}_2\text{SO}_4$  solution at various rotation speeds are shown in Figures 5.9a and b, respectively. Also, prior to the RDE work, a steady-state CV of each material was obtained in the same solution at

scan rates as low as  $10 \text{ mV}\cdot\text{s}^{-1}$ , as shown in Figure 5.9c. Typically, in a RDE experiment aimed at screening Pt catalysts for their ORR activity, a potential window of between 0.05 – 1.1 V vs. RHE is used.

Figure 5.9a (in  $\text{N}_2$ -saturated conditions) shows the typical features of Pt NPs on  $\text{TaO}_x\text{N}_y$  NTs, similar to what was shown in curve c in Figure 5.6, even though a tilt is present in the CVs, likely arising from an IR drop associated with some solution leakage at the edge of the embedded Ta disc. This leak adds an additional series resistance to the system, due to the IR drop associated with current passing in the small gap between the electrode and the shroud. This ohmic drop results in the tilted CV seen in Figure 5.9. Since the face of the custom-made RDEs was quite delicate, extreme care had to be taken during the fabrication not to destroy the face of the RDE and thus the leakage problem could not be easily resolved. When a Pt/C ink is drop-casted, typically on a glassy carbon (GC) RDE, the GC electrode is firmly fixed in the shroud before drop-casting the ink. However, for the Pt NPs/ $\text{TaO}_x\text{N}_y$  NTs RDE, the RDE was fixed in the shroud after preparing the Pt NPs/ $\text{TaO}_x\text{N}_y$  NTs. Therefore, the face of the RDE had to be protected carefully in order to not destroy the active material, and hence the final step of inserting the RDE into the shroud was challenging.

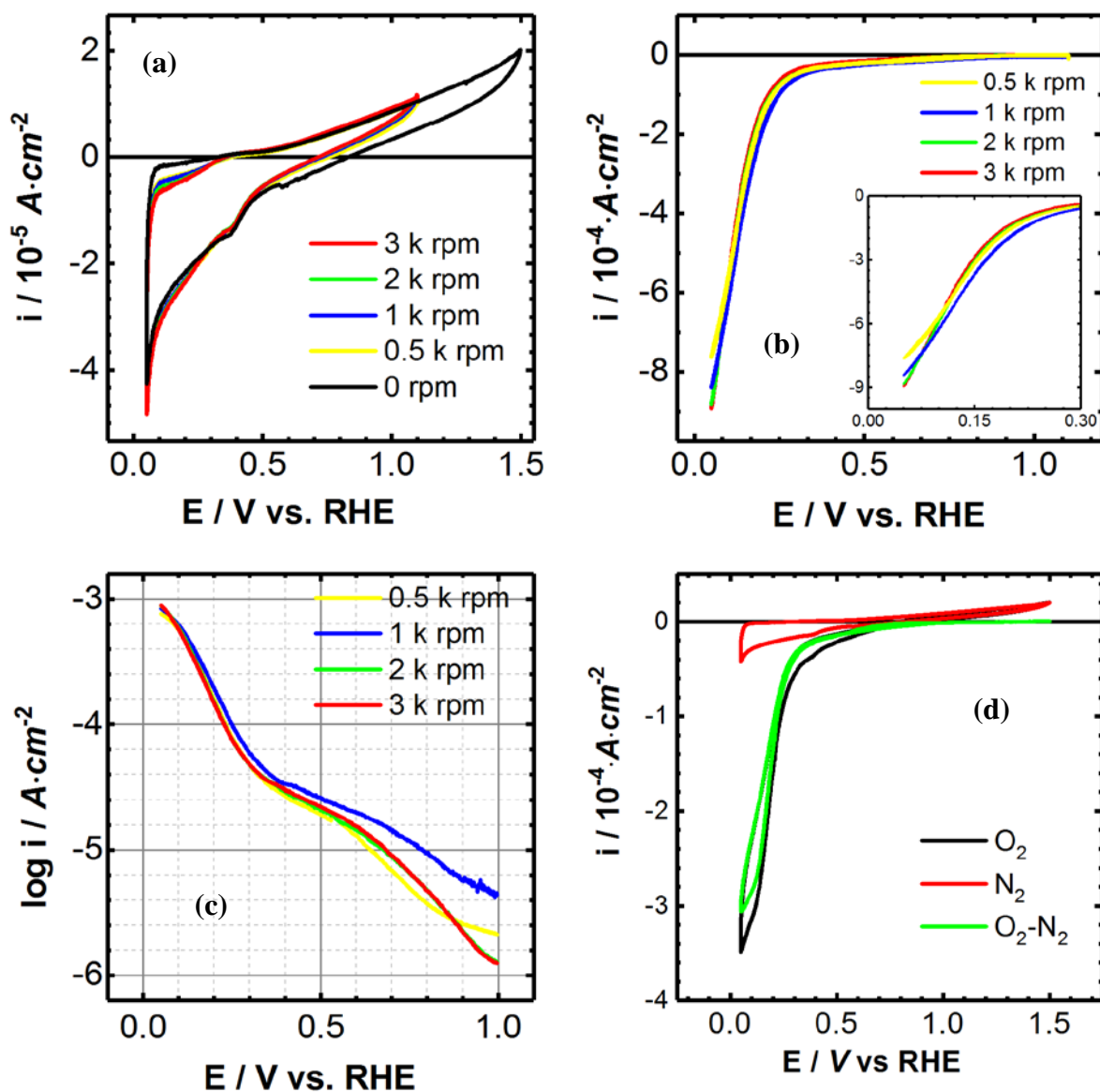


**Figure 5.9** CVs obtained at 0.05 -1.1 V vs RHE for the Pt NPs/TaO<sub>x</sub>N<sub>y</sub> NTs at 10 mV·s<sup>-1</sup> at various RDE rotation rates in (a) N<sub>2</sub>-saturated 0.5 M H<sub>2</sub>SO<sub>4</sub> and (b) O<sub>2</sub>-saturated 0.5 M H<sub>2</sub>SO<sub>4</sub> after subtracting the data from N<sub>2</sub>-saturated electrolyte. (c) Cathodic scan Tafel plot for the ORR at the Pt NPs/TaO<sub>x</sub>N<sub>y</sub> NTs from the data in (b). (d) CVs obtained in N<sub>2</sub> and O<sub>2</sub> saturated 0.5 M H<sub>2</sub>SO<sub>4</sub> without rotation, as well as subtracted data. Note: all currents are corrected for WE geometrical area.

In the O<sub>2</sub>-saturated solution (Figure 5.9b), the ORR current can be easily seen at ca. 0.7 V vs. RHE, while the currents are very small at > 0.8 V vs. RHE, where the TaO<sub>x</sub>N<sub>y</sub> NTs are non-conducting. Also, Figure 5.9a and b suggest that, for the NTs on the RDE, no diffusion controlled reactions are occurring. The current rises slowly initially and then more rapidly, but without reaching a limiting value, even at 0.05 V, an indication that the fully mass controlled current has not been realized yet. Typically, a sigmoidal shape is seen in a CV with a RDE configuration for any electroactive species and the polarization curve can there be divided into two regions, a kinetic/Butler-Volmer controlled region (exponential part) and a mass-controlled region (plateau part). It is clear that the Pt NPs/TaO<sub>x</sub>N<sub>y</sub> NTs composite is not a highly active ORR catalyst, as the kinetically controlled region begins only at fairly cathodic potentials and as the currents increase only slowly with increasingly cathodic applied potentials. Specifically, for cutting edge catalysts (Pt/C), the kinetic region starts at ca. 1 V vs. RHE and the diffusion limiting current is reached in the negative scan already at ca. 0.8 V vs. RHE.<sup>240</sup>

A cathodic scan Tafel plot was then constructed from the data in Figure 5.9b, shown in Figure 5.9c. Two linear regions are seen at all rotation rates, as well as for the data without electrode rotation (Figure 5.9d). These two regions are defined here as being from 1 V - 0.5 V (low overpotential) and from 0.3 V to 0.1 V (high overpotentials). Note, these high and low overpotential ranges are not the overpotential ranges that typically used on Pt/C catalyst work. Here, the terminology is used based on the linear regions that were seen in the Tafel plot. The respective ORR Tafel slopes for the high and low overpotentials were then calculated and are shown in Table 1. Except for the 1000 rpm data at low overpotentials, the Tafel slopes are

independent of the rotation rate, with a higher value of 300-400  $\text{mV}\cdot\text{decade}^{-1}$  at low overpotentials (1.0 - 0.5 V) and values of ca. 180  $\text{mV}\cdot\text{decade}^{-1}$  is seen at high overpotentials (0.3 – 0.1 V). These values are all much higher than what is obtained from the quiescent CV experiments, suggestive of challenges in oxygen transport through the NT pores and between adjacent NTs, preventing good access of oxygen to the Pt NPs within the porous structure.

**Table 5.1** Cathodic ORR Tafel slopes for the data shown in Figure 5.9b and d\*

rpm / (k)	overpotential **	Tafel Slope / $\text{V}\cdot\text{decade}^{-1}$
0	Low	0.314
	High	0.182
0.5	Low	0.463
	High	0.174
1	Low	0.498
	High	0.186
2	Low	0.360
	High	0.169
3	Low	0.339
	High	0.170

\* Data obtained from Figure 5.9 b and d in 0.5 M  $\text{H}_2\text{SO}_4$  at  $10 \text{ mV}\cdot\text{s}^{-1}$  after subtraction of the data obtained in the  $\text{N}_2$ -saturated solution from the aerated data.

\*\* Low and high overpotential ranges are defined here as being 1 V - 0.5 V and 0.3 V – 0.1 V vs RHE, respectively.

It was shown in Chapter 4 that the  $\text{TaO}_x\text{N}_y$  NTs are not a very good hydrogen evolution reaction (HER) catalyst on their own (Figure 4.6) with essentially no HER currents seen until a

potential of ca. -0.4 V vs. RHE was applied, and with a very high Tafel slope observed (ca. 0.240 V-decade<sup>-1</sup>).<sup>25</sup> However, in the presence of the Pt NPs, considerable HER currents can be seen, even at potentials near 0 V vs. RHE (Figure 5.6b). This argues that the sulfuric acid solution is present deep inside the NTs, thus accessing the Pt NP catalysts, and it appears the hydrogen product can also be expelled from the pores fairly well.

A Koutecky-Levich plot (Section 2.9) was constructed from the activation-controlled RDE data at two different potentials (0.35 V and 0.8 V vs. RHE) to attempt to evaluate the number of electrons ( $n$ ) involved in the ORR (Figure 5.10 c and d). It is seen that  $n$  is then very small (0.05), indicative again of the problems with the RDE testing of the NT-based WE.

Thus,  $n$  was also calculated from the CV peak ORR currents in quiescent solutions (Figure 5.7), using the Randles-Sevcik equation. (Section 2.9) From this analysis, the  $n$  value was found to be 2, suggesting that the ORR on the Pt NPs/TaO<sub>x</sub>N<sub>y</sub> NTs goes through a 2 electron H<sub>2</sub>O<sub>2</sub> pathway. This seems much more probable than the very low  $n$  value of 0.05, obtained from the RDE experiments. In terms of the low sensitivity of the Pt NPs/TaO<sub>x</sub>N<sub>y</sub> NTs electrode to rotation in the O<sub>2</sub>-saturated sulfuric acid solution, it seems most likely that the catalytically active Pt NPs are located deep within the NTs, regions that cannot be convected by the RDE. This then produces substantial transport problems for oxygen, such that the Pt NPs inside the NTs are not very well accessed.

In terms of the more reasonable  $n$  value of 2, obtained from the non-convected experiments (Figure 5.7), it is known that the ORR can take the indirect 2e pathway in the conversion of O<sub>2</sub> to

H<sub>2</sub>O via H<sub>2</sub>O<sub>2</sub> on many metal oxide catalysts.<sup>219</sup> This seems to be true also for the TaO<sub>x</sub>N<sub>y</sub> NTs, as metal oxides and oxynitrides have similar electrical properties, although metal oxides are generally more insulating than oxynitrides.

However, in the present work, the ORR at the Pt NPs on TaO<sub>x</sub>N<sub>y</sub> is occurring via the indirect 2e pathway, whereas the ORR at Pt on carbon goes through a 4e (direct) pathway. This may be due to problems with the interfacial properties between the TaO<sub>x</sub>N<sub>y</sub> support and the metal catalyst (Pt). Toroker et. al. have shown, using DFT calculations, that the interface between metals and metal oxides play a vital role in electrocatalysis. Although this seems counter-intuitive, the work suggests that, when the potential energy mismatch of the interface between the two phases is large, the barrier thickness between the metal/metal oxide interfaces will be small. As a result, charge transport between the phases would be enhanced.<sup>241</sup> If this statement is correct, then it is possible that the Pt/TaO<sub>x</sub>N<sub>y</sub> interface has a low energy and thus it could be presumed that the interfacial barrier is large. Therefore, this produces inefficient charge transport between the two phases. Therefore, the ORR occurs via the 2e indirect pathway at these Pt NPs/TaO<sub>x</sub>N<sub>y</sub> NTs materials. A DFT study of the Pt/TaO<sub>x</sub>N<sub>y</sub> system would thus be warranted in order to validate this argument.

These issues may be compounded by an insufficiently high electronic conductivity of the semiconducting TaO<sub>x</sub>N<sub>y</sub> NTs as well as the transport limitations discussed above. Some of these explanations are tested in the section below.

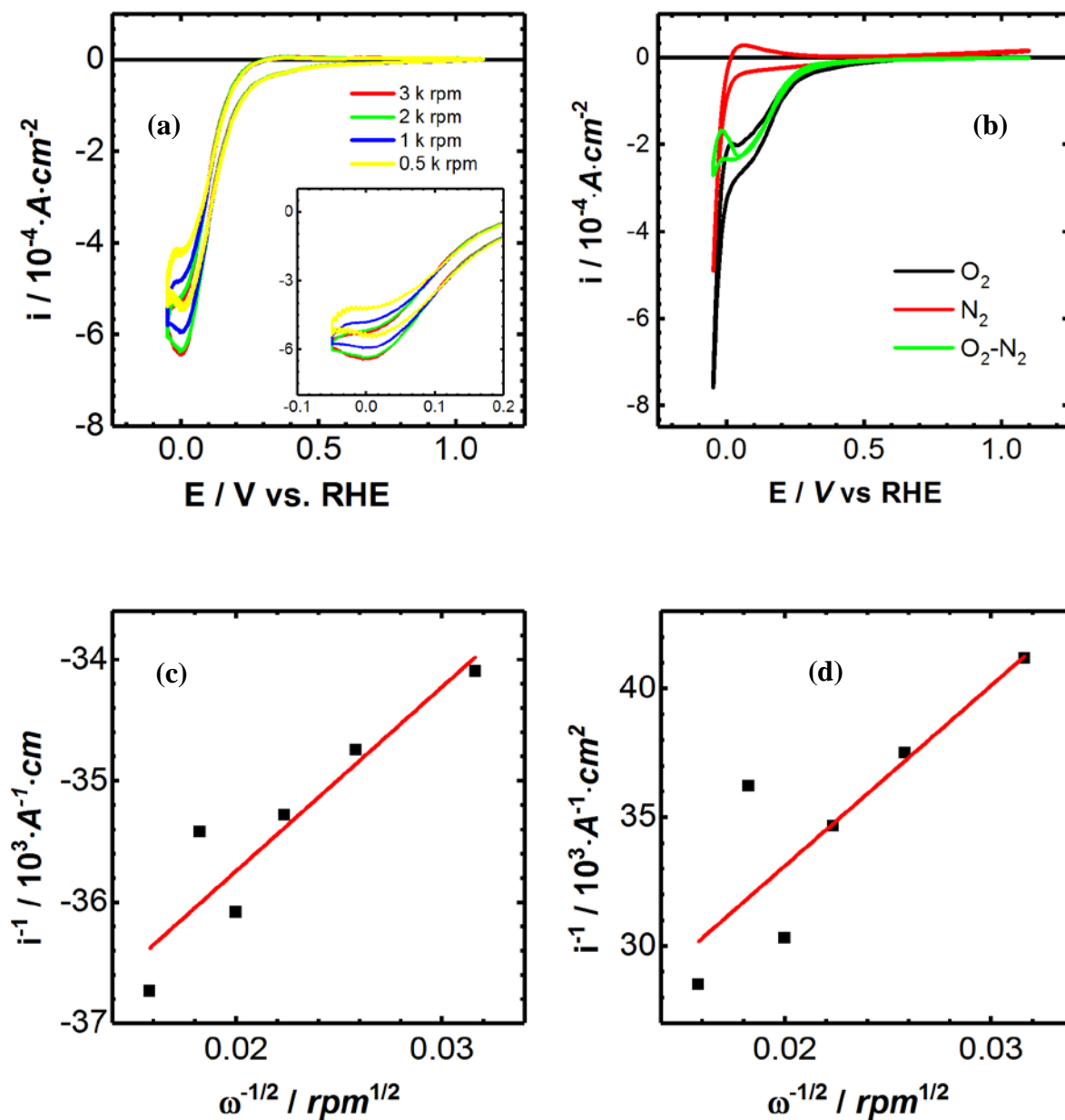


**Figure 5.10** CVs obtained for the Pt NPs/TaO<sub>x</sub>N<sub>y</sub> NTs composite over the extended potential range of -0.05 to 1.1 V vs RHE in N<sub>2</sub>-saturated and O<sub>2</sub>-saturated 0.5 M H<sub>2</sub>SO<sub>4</sub> solutions at 10 mV·s<sup>-1</sup> (a) at various rotation speeds and (b) without electrode rotation. (c) and (d) are Koutecky-Levich plots at 0.35 V and 0.8 V vs. RHE, respectively.

### 5.2.2.3 *Electrochemistry and ORR at Pt NP decorated shorter (0.3 $\mu\text{m}$ ) TaO<sub>x</sub>N<sub>y</sub> NTs*

In order to investigate the possibility that the relatively low conductivity of the TaO<sub>x</sub>N<sub>y</sub> NTs could be playing a role in the low catalytic activity of the Pt NPs/TaO<sub>x</sub>N<sub>y</sub> NTs composite towards the ORR, shorter NTs were formed, thus lowering the carrier migration length in the catalyst support. The NT length was thus decreased to ca. 300 nm by decreasing the anodization time of Ta metal from 5 to 2.5 minutes, noting that still shorter NTs tend to have a slightly different microstructure, with thin connections between NTs seen at regular intervals down the NT length. Except for shorter NT length, all other synthetic steps were kept the same as in the previous study of the 1  $\mu\text{m}$  long NTs.

These Pt NPs/TaO<sub>x</sub>N<sub>y</sub> NTs composites (ca. 0.3  $\mu\text{m}$  NTs) were then subjected to ORR studies. Figure 5.11a shows the CVs obtained in N<sub>2</sub>-saturated (blue curve) and O<sub>2</sub>-saturated (red curve) 0.5 M H<sub>2</sub>SO<sub>4</sub>, while the green CV shows the activity only in the presence of O<sub>2</sub>, i.e. the ORR current only. Unlike the CV for the 1  $\mu\text{m}$  NTs, decorated with Pt NPs (Figure 5.6b) in N<sub>2</sub>, the 0.3  $\mu\text{m}$  NT composite shows the typical HUPD peaks of Pt NPs and yet the peaks related to Pt oxidation/PtO<sub>x</sub> reduction are still not visible.

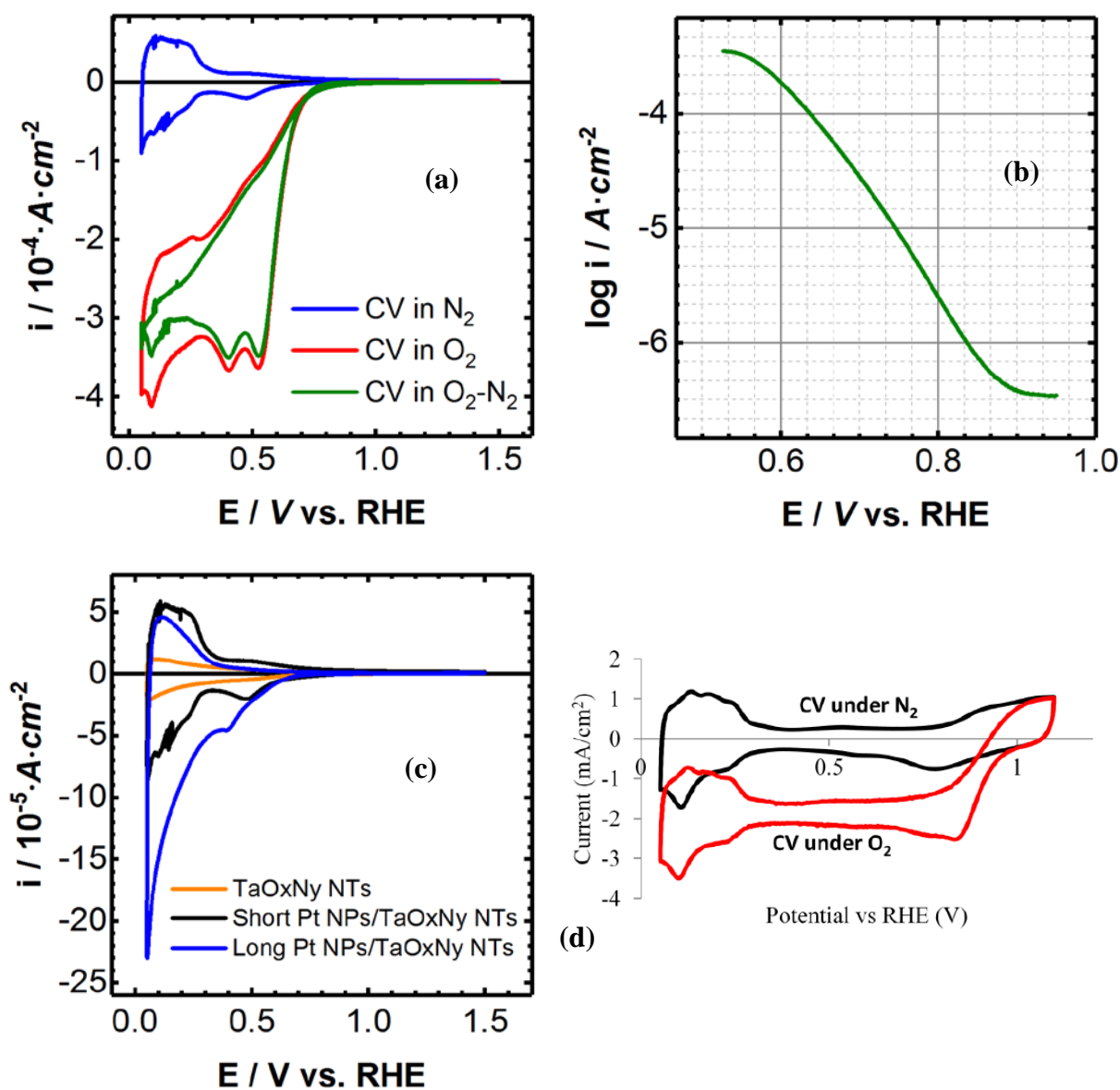


**Figure 5.11** CVs obtained at 10 mV·s<sup>-1</sup> in N<sub>2</sub> and O<sub>2</sub> saturated 0.5 M H<sub>2</sub>SO<sub>4</sub> for (a) Pt NPs/TaO<sub>x</sub>N<sub>y</sub> NTs (shorter length of 0.3 μm), where the Pt NPs were deposited on the NTs by the incipient impregnation method, and (b) the cathodic scan Tafel plot for the ORR at this material. (c) shows the CVs obtained in N<sub>2</sub>-saturated 0.5 M H<sub>2</sub>SO<sub>4</sub> for both shorter (0.3 μm) and longer (1 μm) TaO<sub>x</sub>N<sub>y</sub> NTs decorated with Pt NPs. Current is normalized to geometrical area of the electrode. (d) CV responses of the 20 wt % Pt/C catalyst in N<sub>2</sub> (black) and O<sub>2</sub> (red) saturated 0.5 M H<sub>2</sub>SO<sub>4</sub> at 10 mV·s<sup>-1</sup> scan rate.<sup>242</sup>

To determine if any improvement is seen in the ORR activity at the Pt NPs deposited on the shorter TaO<sub>x</sub>N<sub>y</sub> NTs, Figure 5.11a and b show the CVs and cathodic scan Tafel plots for both materials. For Pt on the 0.3 μm TaO<sub>x</sub>N<sub>y</sub> NTs, the current density at 0.9 V is ca. 3.2 μA·cm<sup>-2</sup>. When this current is converted to an activity per Pt ECSA (using the HUPD charges from Figure 5.11a), this gives 90 nA·cm<sup>-2</sup><sub>Pt</sub>, still quite a bit lower than seen for standard Pt/C catalysts, which is typically 300 μA·cm<sup>-2</sup><sub>Pt</sub>.<sup>221</sup> Nevertheless, the Tafel slope observed for the ORR in the cathodic scan for the Pt NPs deposited on the 0.3 μm NTs is 0.101 V·decade<sup>-1</sup>, similar to the values obtained for Pt NPs deposited on the 1 μm NTs (0.105 V·decade<sup>-1</sup>).

#### ***5.2.2.4 Summary of Section 5.2.2***

Table 5.2 shows a summary of the electrochemical results obtained for the ORR at the three Pt NPs/TaO<sub>x</sub>N<sub>y</sub> NTs materials examined in Section 5.2.2. This table does not include the RDE data, as the results obtained with the 1 μm long Pt-loaded NTs using this configuration were too difficult to interpret. This includes Pt NPs deposited on the compact thin layer of TaO<sub>x</sub>N<sub>y</sub> and on the two TaO<sub>x</sub>N<sub>y</sub> NTs of different lengths, in comparison with TaO<sub>x</sub>N<sub>y</sub> alone (in the absence of the Pt NPs), all in non-convected conditions.

It is seen that the TaO<sub>x</sub>N<sub>y</sub> NTs, without Pt, are essentially inactive towards the ORR, which contradicts several reports from other groups that have suggested that TaO<sub>x</sub>N<sub>y</sub> shows some ORR activity and can be considered as a potential replacement for Pt in PEMFC cathodes. However, in all of these previous reports, TaO<sub>x</sub>N<sub>y</sub> was used as a thin films, as a powder mixed with carbon powder or with carbon incorporated into the lattice, forming a carboxynitride. The introduction

of carbon may have provided an electronically conducting pathway to the semiconducting n-type  $\text{TaO}_x\text{N}_y$ . This may explain why  $\text{TaO}_x\text{N}_y$  was reported to be a reasonable ORR catalyst.

Table 5.2 also shows that the Pt NPs, deposited on the  $\text{TaO}_x\text{N}_y$  compact layer (CL), show reasonable ORR activity and exhibit a low Tafel slope of 60 mV per decade of current density. This argues that the Pt/ $\text{TaO}_x\text{N}_y$  interface should not be a problem and that a 30 nm  $\text{TaO}_x\text{N}_y$  layer is conductive enough to allow current to tunnel through it to carry out the ORR. For the NT-supported Pt NPs, it is seen that the ORR activity is between 6-15 times lower than at the Pt NPs/ $\text{TaO}_x\text{N}_y$  CL samples. Also, the Tafel slope is bit higher, perhaps indicating mass transport limitation in the porous catalyst layer or high resistance from the  $\text{TaO}_x\text{N}_y$  NT support, which may have influenced the mechanism of ORR.

Overall, the lower activity of the ORR at the Pt NPs/ $\text{TaO}_x\text{N}_y$  CL or NTs vs. what is seen for Pt/C may be due to many issues, including transport limitations of  $\text{O}_2$  into the NTs and the resistance of the  $\text{TaO}_x\text{N}_y$  NTs (electrons must move through the full length of the NTs to reach any ORR-active Pt NPs that are located towards the solution side of the nanotubular array). It is also seen that the 0.3  $\mu\text{m}$  NTs (shorter NTs) are somewhat more active than the 1  $\mu\text{m}$  ones, arguing that the NT length and/or the length of the pores is influencing the ORR activity.

**Table 5.2** Summary of salient electrochemical results for the ORR of Pt NPs deposited TaO<sub>x</sub>N<sub>y</sub> CL and TaO<sub>x</sub>N<sub>y</sub> NTs (1 μm and 0.3 μm in length)

	Pt NPs/TaO <sub>x</sub> N <sub>y</sub> CL	Pt NPs/TaO <sub>x</sub> N <sub>y</sub> NTs (0.3 μm)	Pt NPs/TaO <sub>x</sub> N <sub>y</sub> NTs (1 μm)
ORR Current density at 0.9 V / μA·cm <sup>-2</sup>	5.4	3.2	0.9
ORR Tafel Slope / V·decade <sup>-1</sup>	0.06	0.101	0.105
HUPD peaks	Yes	Yes	No
PtO peaks	Yes	?	?

Another uncertainty in the work is the nature and electrochemical state of the Pt NPs deposited on the TaO<sub>x</sub>N<sub>y</sub> NT surfaces. Although it is clear that ORR activity has been generated by the presence of the Pt NPs, the characteristic electrochemical features of Pt (Pt oxide formation at 0.8 V vs. RHE, Pt oxide reduction at ca. 0.7 V vs. RHE, and the symmetrical HUPD peaks at 0-0.3 V vs. RHE) are not seen on the nanotubular supports, rather seen only when the Pt NPs are deposited on the TaO<sub>x</sub>N<sub>y</sub> compact layer. At the same time, the magnitude of the currents associated with the redox reaction of the TaO<sub>x</sub>N<sub>y</sub> material is often increased. As this potential range is the same as for the HUPD reaction at Pt and as ORR activity is seen in the presence of Pt NPs, it is conceivable that the additional charge seen is actually due to the HUPD process, although the peak shapes are now different than seen at bulk Pt or Pt/C. The absence of the Pt oxide formation/reduction features could be explained more easily, attributed to the rectifying nature and redox inactivity of TaO<sub>x</sub>N<sub>y</sub> at > 0.8 V.

In summary, it appears that the TaO<sub>x</sub>N<sub>y</sub> NTs can serve as a support for Pt NPs, but there may be limitations in terms of particle size/NT length and the Pt/TaO<sub>x</sub>N<sub>y</sub> interfaces, leading to relatively poor activity. Thus, the physical and morphological characteristics of these materials may well have to be further optimized. In the next section, the resistance of the TaO<sub>x</sub>N<sub>y</sub> NTs to electrochemical corrosion is analyzed for its potential future use as a PEMFC catalyst support material.

### 5.2.3 Corrosion Stability of TaO<sub>x</sub>N<sub>y</sub> NTs and Pt NPs/TaO<sub>x</sub>N<sub>y</sub> NTs composite

Although carbon is a ubiquitous catalyst support material for use in many electrochemical devices, it can undergo electrochemical oxidation or carbon corrosion. Under PEM fuel cell operating conditions, the corrosion of carbon is one of the major challenges encountered. Carbon is thermodynamically unstable in aqueous media, producing CO<sub>2</sub> and CO at > 0.207 V vs. RHE and > 0.518 V vs. RHE, respectively (Section 2.4.2).<sup>243</sup> Thus, carbon is not thermodynamically stable at PEMFC cathodes at room temperature. Notably, even at elevated temperatures and at the potentials associated with the cathode (0.7-1.0 V), the carbon oxidation reaction (COR) or carbon corrosion kinetics are quite slow. However, at still higher potentials of > 1.2 V, which can be experienced by the cathode during the start-up or shut-down of a PEM fuel cell, carbon corrosion can become a major problem, leading to significant durability problems.

Thus, in this section, the resistance of the TaO<sub>x</sub>N<sub>y</sub> nanotubes towards corrosion in acidic solutions was investigated. TaO<sub>x</sub>N<sub>y</sub> NTs were expected to be quite stable, as Ta is already primarily in the +5 oxidation state in TaO<sub>x</sub>N<sub>y</sub> and thus cannot be easily oxidized. However, in the

XRD refinement, discussed in Section 4.2.3, some of the peaks are consistent with a Ta oxidation state lower than +5, with  $\text{TaN}_{0.1}$  possibly being a minor component. (Section 4.2.3) Further, during anodic polarization,  $\text{TaO}_x\text{N}_y$  could potentially lose some of its nitrogen, replacing it with oxygen from water, thus altering its properties.

Many metal oxides, metal nitrides, metal oxynitrides, metal carbides, etc. are n-type materials and thus should not be electrochemically active in the potential range of the cathode of a PEMFC. However, many of these alternative materials, such as  $\text{TiO}_2$ <sup>244-245</sup>,  $\text{ATO}$ <sup>246-247</sup>, etc., have shown remarkable electrochemical stability during potential cycling between 0.05 V and 1 V vs. RHE in acidic solutions. Although the durability is an asset, their relatively low conductivity is a problem. This has been overcome by adding a more conducting material, such as carbon, to form composites.<sup>104, 248</sup>

To test the durability of a material under PEMFC operating conditions, the Department of Energy's (DOE) protocols are useful. There are two methods that are crucial in these protocols, 5,000 CV cycles between 1.0 V and 1.5 V vs. RHE and potential stepping (3 s at 0.6 V and 3 s at 0.95 V) repeated 30,000 times.<sup>11</sup> However, in this work, the accelerated durability tests (ADT) were changed slightly, in relation to a parallel project in the Birss group with Ballard Power Systems, to intensify the corrosion of the materials. First, a steady-state CV was obtained between 0.05 V and 1.1 V, followed by potentiostatic stepping (pstep) [50 s at 1.4 V and 10 s at 0.8 V (66 cycles)] and then CVs again between 0.05 V and 1.1 V. Further, the CVs were repeated for 100 cycles instead of 30,000 cycles to reduce the time required for the assessment of the  $\text{TaO}_x\text{N}_y$  materials. The charge density related to corrosion from the pstep experiment was

calculated by taking the differences between the anodic charge density ( $q^+$ ) and the cathodic charge density ( $q^-$ ) and considering this as the corrosion charge density of the material under investigation. (Section 2.6) The CV charges, before and after the pstep experiments, were also calculated.

### ***5.2.3.1 Corrosion resistance of 1 $\mu\text{m}$ $\text{TaO}_x\text{N}_y$ NTs without Pt***

It can be seen in Figure 5.14a that the CVs for the  $\text{TaO}_x\text{N}_y$  NTs do not show any electrochemical changes even after 100 cycles. In terms of stability, this is a very promising result. Further, the CVs resemble all of the other CVs shown in this work, an indication that the  $\text{TaO}_x\text{N}_y$  NTs do not undergo any significant corrosion or change in either their oxidation state or chemical composition. If the entire N within the  $\text{TaO}_x\text{N}_y$  NTs had been replaced by oxygen, the NTs would have converted to Ta oxide NTs, which give a very different CV response (Figure 4.6).

Figure 5.14b and c show the current vs. time data for the  $\sim 1$  micron long  $\text{TaO}_x\text{N}_y$  NTs, obtained during the potential stepping experiment, and the corresponding charge density plot, respectively. The anodic charge is due to double layer charging plus material corrosion, while the cathodic charge is due to double layer discharge only. The corrosion charge density is the highest in the first five cycles, as highlighted in Figure 5.14c by the red rectangle, and in cycles 6-18, the corrosion rate slowly decreases, shown by the black rectangle. After 18 cycles, there is no difference in the corrosion rate of the material (magenta rectangles) between cycles and hence a plateau is seen (Figure 5.14c). This trend is also seen in the literature for the corrosion of typical

carbon supports, studied in parallel by our group, using the same corrosion protocol.<sup>249</sup> What is important is that the plateau charge density in cycles 19-66 (magenta rectangles) should be as low as possible and that the difference between the highest corrosion charge and the plateau charge is as small as possible.<sup>249</sup>

The CVs of the TaO<sub>x</sub>N<sub>y</sub> NTs, presented in Figure 5.14a, are almost identical to the CV shown in Chapter 4 (Figure 4.6). A representative TaO<sub>x</sub>N<sub>y</sub> NTs CV shows the Ta<sup>4+/5+</sup> redox chemistry at < 0.6, and at > 0.6 V, only DL charging can be seen. The same features are seen in Figure 5.14a before and after the potentiostatic stepping (pstep) experiment. This is an indication that the electrochemistry of the TaO<sub>x</sub>N<sub>y</sub> NTs does not change after extensive anodic polarization of this material, under the conditions found in a fuel cell operating system, i.e. the pstep experiment.

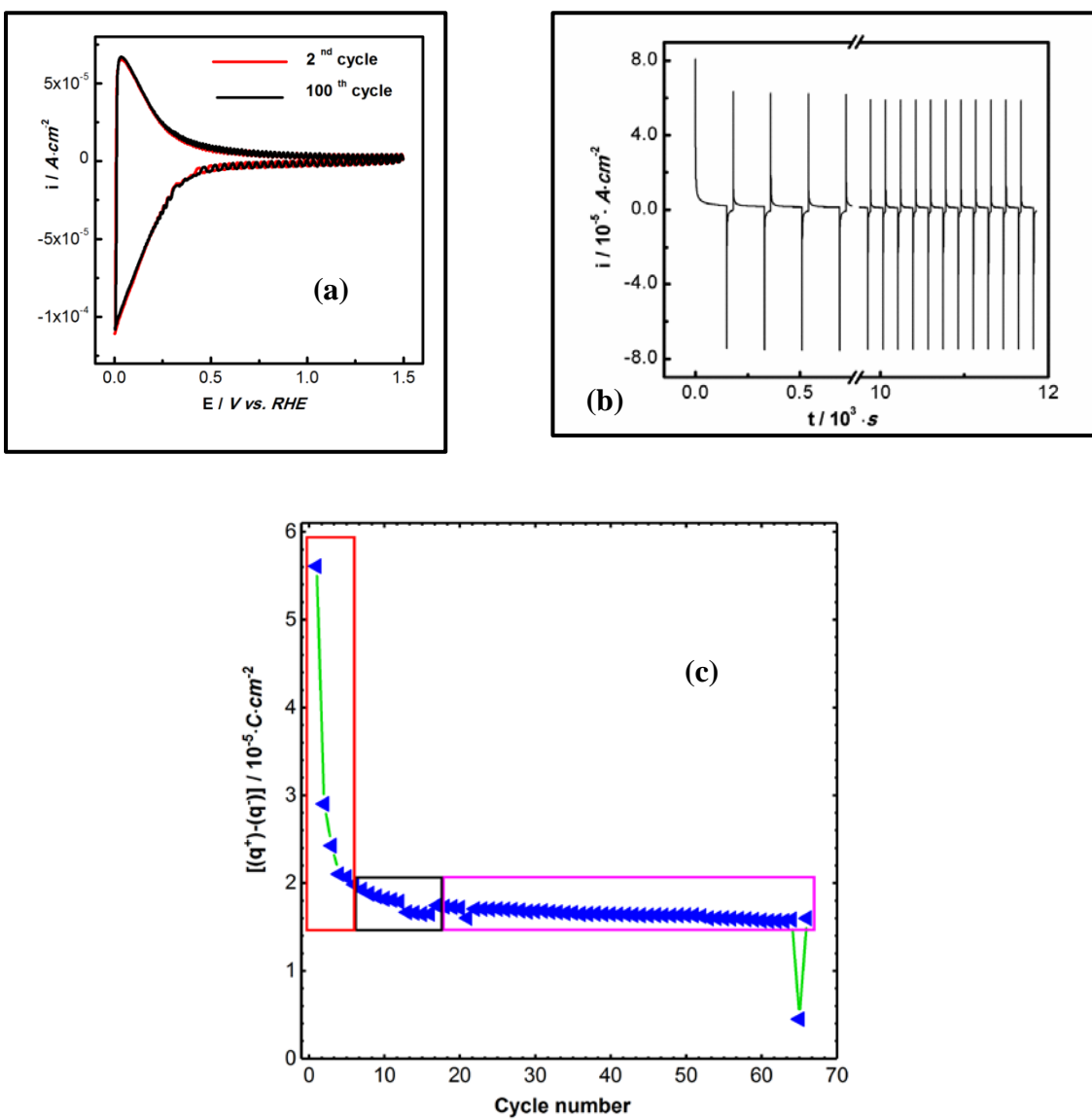


**Figure 5.12** Accelerated durability test (ADT) used for the testing of the TaO<sub>x</sub>N<sub>y</sub> NTs in 0.5 M H<sub>2</sub>SO<sub>4</sub>. (a) 2<sup>nd</sup> and 100<sup>th</sup> CVs obtained at 10 mV·s<sup>-1</sup>, (b) 66 cycles (note a break in the x axis) of potential stepping (pstep), and (c) corrosion charges obtained from the pstep experiment. The corrosion charges were calculated by taking the difference between  $q^+$  and  $q^-$ .

To claim that the TaO<sub>x</sub>N<sub>y</sub> NTs have good corrosion stability, the corrosion data should be compared with the results obtained from a benchmark material, Vulcan carbon powder (Figure 5.15a), studied by others in the Birss group. In this comparison, only a qualitative discussion is presented, based on the before/after CVs. After ADT of any type of carbon support, some degree of degradation can be seen, consistent with the increased double layer and pseudocapacitive charges seen in Figure 5.15b.<sup>114, 249</sup>

The extent of corrosion of different types of carbon is known to vary, with Vulcan carbon showing among the lowest susceptibilities for electrochemical corrosion to date.<sup>114, 249</sup> However, for the TaO<sub>x</sub>N<sub>y</sub> NTs, Figure 5.14a verifies that the electrochemical stability of this material is truly excellent.

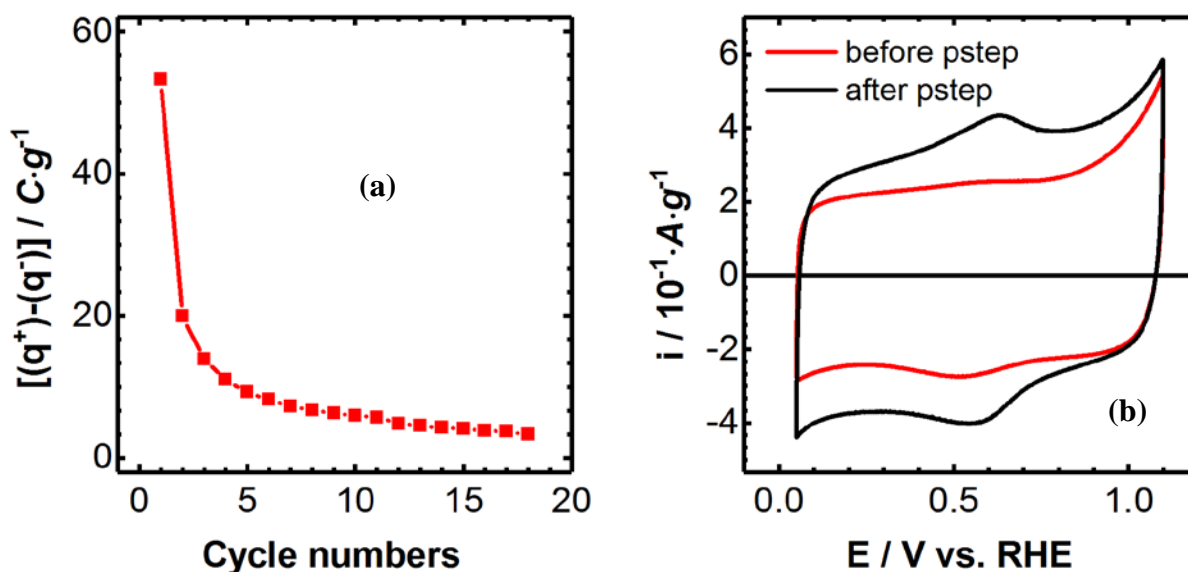


**Figure 5.13** Accelerated durability test (ADT) results for Vulcan carbon (VC) in 0.5 M H<sub>2</sub>SO<sub>4</sub>. (a) Corrosion charges related to pstep experiment (18 Cycles). Corrosion charges are calculated by taking the difference between  $q^+$  and  $q^-$ . (b) CVs (10 mV/s) obtained for the same material before and after the pstep experiment.<sup>164</sup>

### 5.2.3.2 Corrosion resistance of Pt NP-loaded TaO<sub>x</sub>N<sub>y</sub> NTs

As the previous section showed that the TaO<sub>x</sub>N<sub>y</sub> NTs are completely stable to corrosion, the goal in this section of the work was to ascertain that the presence of the Pt NPs do not exacerbate the TaO<sub>x</sub>N<sub>y</sub> oxidation susceptibility. In the case of carbon corrosion, it is well known that Pt aggravates this problem, largely as the Pt NPs catalyze oxygen evolution, which in turn, attacks the carbon.<sup>250</sup>

Figure 5.16 shows the results for the oxidation of the Pt NPs/TaO<sub>x</sub>N<sub>y</sub> NTs sample. The CV data (Figure 5.16) look very promising, as they were collected before and after the potential step

experiment, with no significant differences observed. Only a very small difference is seen in that the CVs are less negatively offset after the corrosion pstep experiments. It is possible that this is an indication of the loss of some of the Pt NPs, which may have promoted early hydrogen evolution and thus a net cathodic current. Notably, the characteristic electrochemistry of Pt hydrogen adsorption/desorption and Pt oxide formation/reduction is not observed in this CV, as already discussed in detail in Section 5.2.2.2.

Figure 5.16b shows the corrosion charges related to the Pt NPs/TaO<sub>x</sub>N<sub>y</sub> NTs sample. The shape of the plot does not match the typical exponential decay seen for carbon (Figure 5.15b) and the TaO<sub>x</sub>N<sub>y</sub> NTs without Pt NPs (Figure 5.14c). Rather, the curve has a ‘sigmoidal’ shape. Here, the difference between the ‘corrosion charge’ in the first and last cycle is very minimal (ca.  $< 0.2 \text{ C}\cdot\text{cm}^{-2}$ ), indicative of a highly corrosion resistant material. However, in the later cycles (cycles  $> 10$ ), more corrosion charge is seen than in the initial cycles.

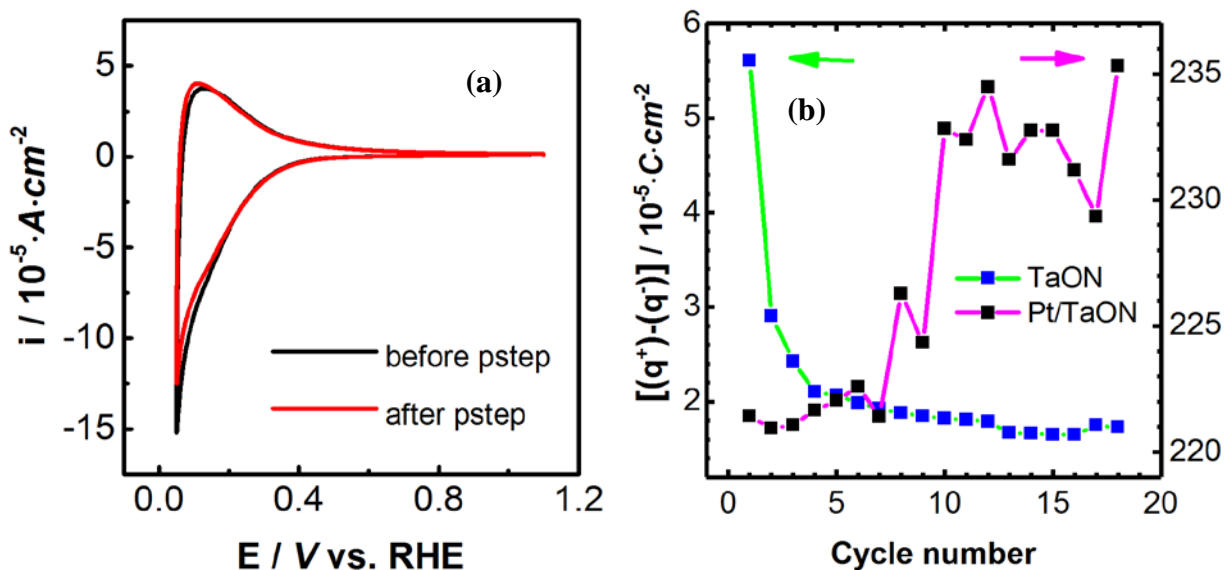


**Figure 5.14** Results of accelerated durability testing (ADT) of Pt NPs/TaO<sub>x</sub>N<sub>y</sub> NTs in 0.5 M H<sub>2</sub>SO<sub>4</sub>. (a) CVs obtained at 10 mV·s<sup>-1</sup> before and after potential stepping experiment and (b) corrosion charge as a function of step number in the ADT experiment for Pt NPs/TaO<sub>x</sub>N<sub>y</sub> NTs and TaO<sub>x</sub>N<sub>y</sub> NTs.

The typical method of assessing alternative catalyst supports is to perform a large number of CV cycles and then to evaluate the changes in the hydrogen underpotential deposition (HUPD) charges, thus giving the changes in the electrochemical surface area (ECSA) of the Pt NPs.<sup>11</sup> However, as stated above, these electrochemical features associated with Pt are not seen clearly in the CVs of the Pt NPs/ TaO<sub>x</sub>N<sub>y</sub> NTs samples. To our knowledge, potential cycling and potential stepping, while also tracking the Pt ECSA, are the only methods that have been used by others to determine the corrosion susceptibility of non-carbon catalyst support materials.

### 5.3 Summary

In this chapter, a Ta oxide compact layer (CL), and short (ca. 0.3  $\mu\text{m}$ ) and long nanotubes (NTs) (ca. 1  $\mu\text{m}$ ) were successfully converted to  $\text{TaO}_x\text{N}_y$  and Pt nanoparticles (NPs) were subsequently deposited on these surfaces using the incipient impregnation method. The proof of the presence of the Pt NPs was obtained by SEM/TEM and EDX analysis. On the NTs, the size of the Pt NPs was 3-5 nm diameter, but on the CL, they were closer to 10-20 nm in diameter.

The electrochemistry of the Pt NPs/ $\text{TaO}_x\text{N}_y$  CL material revealed the normal electrochemistry of Pt, such as the hydrogen underpotential deposition peaks (HUPD) and Pt oxide formation/reduction features. When the oxygen reduction reaction (ORR) was studied in quiescent 0.5 M  $\text{H}_2\text{SO}_4$  solutions, a Tafel slope (TS) of ca. 60  $\text{mV}\cdot\text{decade}^{-1}$  was obtained, similar to what is seen at Pt/C catalysts at low ORR overpotentials. However, the currents were substantially smaller than on Pt/C, suggesting that not all of the Pt particles were well interconnected.

The ORR activity at the Pt NPs/ $\text{TaO}_x\text{N}_y$  NTs sample (NTs were  $\sim 1 \mu\text{m}$  in length), also in quiescent conditions, is quite different from that seen at the Pt NPs/ $\text{TaO}_x\text{N}_y$  CL layer, as now, the conventional Pt CV features are no longer seen. At the same time, the currents in  $\text{N}_2$ -saturated solutions in the  $\text{Ta}^{4+/5+}$  redox chemistry regions were enhanced by the presence of Pt. The absence of the normal Pt features was attributed largely to the diode nature of the  $\text{TaO}_x\text{N}_y$  NTs. When  $\text{O}_2$  was introduced to the cell solution, the ORR was seen to be enhanced on the  $\text{TaO}_x\text{N}_y$  NTs when Pt is present and a Tafel Slope of 105  $\text{mV}\cdot\text{decade}^{-1}$  was obtained, more similar to

what would be seen on Pt/C at high overpotentials. Furthermore, the redox switching potential in TaO<sub>x</sub>N<sub>y</sub> NTs (without Pt NPs) is found to be ca. 0.6 V vs. RHE in the Chapter 4, but here in the presence of Pt, it is ca. 0.8 V. This is clearly seen in the Tafel plot of the ORR work.

Other directions taken include the use of a rotating disc electrode (RDE) to study the ORR at the Pt/TaO<sub>x</sub>N<sub>y</sub> NTs samples, which were formed by anodization of Ta and then nitriding of the Ta oxide NTs. Under these conditions, the ORR appeared to be quite inactive, showing an activation-controlled regions starting at ca. 0.8 V, but never reaching a plateau current. This suggests that the long pores within and between NTs result in oxygen transport limitations, or that the NTs are too long, and thus too resistive, to allow the NTs to become fully charged. Thus, shorter NTs were examined (0.3 μm in length) as a Pt NP support material, following by the testing of the ORR activity. This showed that the Pt CV features were more readily observed and the ORR was also more active, pointing more towards a resistance and/or pore length limitation in these materials.

Finally, the Pt NPs/TaO<sub>x</sub>N<sub>y</sub> NTs samples were also subjected to a modified version of the proposed DOE accelerated durability tests to examine the stability of the TaO<sub>x</sub>N<sub>y</sub> NTs catalyst support layer, with/without Pt NPs present. It was shown that the TaO<sub>x</sub>N<sub>y</sub> material is very stable, and can withstand the severe condition found in a PEMFC cathode during cell operation. These results suggest that the Pt NPs/TaO<sub>x</sub>N<sub>y</sub> NTs is qualified to serve as a candidate for a PEMFC cathode catalyst, as long as the NTs are not too long. However, more work is needed in order to understand the physiochemical nature of the Pt/TaO<sub>x</sub>N<sub>y</sub> interfaces within this material.

## Chapter 6 : Electrochemistry of TaO<sub>x</sub>N<sub>y</sub> NPs (with/without Pt) mixed with Carbon Powder

Part of the work in this chapter has been published: Abhayawardhana, A. D.; Birss, V. I., Ta-Based Catalyst Support for Proton Exchange Membrane Fuel Cell Applications. *ECS Transactions* 2015, 69 (17), Polymer Electrolyte Fuel Cells 15, 1227-1235.

### 6.1 Introduction

In Chapter 5, the suitability of the TaO<sub>x</sub>N<sub>y</sub> NTs (nanotubes) as either an alternative catalyst or a catalyst support material to replace carbon for use primarily in PEMFC cathodes was examined. In that work, TaO<sub>x</sub>N<sub>y</sub> NTs were subjected to Accelerated Durability Testing (ADT) and their potential as an oxygen reduction (ORR) catalyst, with or without Pt nanoparticles (NPs) added was explored. The results showed that the TaO<sub>x</sub>N<sub>y</sub> NTs have excellent corrosion resistance, but have only minimal catalytic activity towards the ORR and HOR. However, in the presence of Pt NPs, the catalytic activity of these mixtures could be increased, while seemingly retaining the good corrosion stability of the TaO<sub>x</sub>N<sub>y</sub> NT support.

It is known that most alternative catalyst supports do not have the needed electrical conductivity, typical of the ubiquitous carbon support (2-3 S·cm<sup>-1</sup>), and thus, if the conductivity is too low (< 0.02 S·cm<sup>-1</sup>), this will affect the operation of the fuel cell.<sup>251</sup> Our results in Chapter 5 suggested that the TaO<sub>x</sub>N<sub>y</sub> NTs may suffer from too low a conductivity, especially at potentials > 0.8 V vs. RHE when Pt NPs are also present. Thus, in this chapter, efforts have been made to increase the conductivity of TaO<sub>x</sub>N<sub>y</sub> powders through mixing with carbon, an approach that was discussed in Chapter 2 (Section 2.5.2).

Conventionally, this strategy has involved a top-down approach (carbon powder is mechanically ground together with the alternative support material to make a composite powder), although the bottom-up approach (synthesis of the composite material using small molecules) has also gained momentum, as this method has a greater chance of controlling the molecular level interactions rather than just producing physical mixtures.<sup>252</sup> Here, the bottom-up approach was thus employed, synthesizing TaO<sub>x</sub>N<sub>y</sub> NPs directly on colloid imprinted carbon (CIC) surfaces using Ta ethoxide.

Mesophase pitch (MP) was selected as the carbon precursor, with the goal being to make colloid imprinted carbon (CIC) powders using silica colloids, a material that has been worked on heavily in parallel in the Birss group.<sup>75, 163, 236-237, 253-257</sup> In the CICs, the pore size can be fully controlled by the choice of the silica colloid size. However, here, only a pore size of ca. 100 nm was used. The rationale for this choice was that the dispersed TaO<sub>x</sub>N<sub>y</sub> and Pt NPs should deposit both inside and outside the CIC pores during the synthesis. Moreover, if the pores are large enough, it should be easier to transport reactants/products (O<sub>2</sub>, H<sub>2</sub> and H<sub>2</sub>O) within these mesopores and hence most of the catalytic material should be able to participate in the catalytic process. It was also suggested in Chapter 5 that the pores within and between the TaO<sub>x</sub>N<sub>y</sub> NTs, which are in the range of 20-30 nm, may have caused oxygen transport limitations, which is why a 100 nm CIC was employed here.

During the course of the synthesis, a series of intermediate compounds and composite materials were made and all of them were then tested for their electrochemical activity and corrosion stability. This systematic analysis is vital in this type of investigation as all of the

materials are electroactive and identifying the differences at each stage of synthesis is quite important. The intermediates that were examined include the starting material (CIC100) and the product (Pt NPs/TaO<sub>x</sub>N<sub>y</sub> NPs/N-CIC100), with the intermediates examined being TaO<sub>x</sub> NPs/CIC100, TaO<sub>x</sub>N<sub>y</sub> NPs/N-CIC100 (N-CIC100 refers to nitrogen doped CIC100) and TaO<sub>x</sub> NPs/CIC100 (TaO<sub>x</sub> NPs incorporated CIC100). Bn-CIC100 (benzyl alcohol treated CIC100) and N-CIC100 are also called controlled materials because they are likely forms of the CIC100 that form during the synthesis of TaO<sub>x</sub> NPs/CIC100 and TaO<sub>x</sub>N<sub>y</sub> NPs/N-CIC100, respectively.

Here, the microstructure, morphology, composition, and electrochemistry of each of these materials, related to the synthesis of the TaO<sub>x</sub>N<sub>y</sub> NPs/N-CIC100 material, were all studied here. The addition of carbon to the TaO<sub>x</sub> or TaO<sub>x</sub>N<sub>y</sub> NPs was done in order to increase the electronic conductivity, while Pt NPs were added both to aggravate any support oxidation processes<sup>250</sup> as well as to provide a well-known CV response as a measure of material stability. In the literature, it is commonly seen that the degree of catalyst degradation is gauged from the extent of loss of the Pt ECSA (electrochemical surface area), with the goal being to retain at least 40% of the original Pt ECSA.<sup>11</sup> Therefore, Pt was added to the TaO<sub>x</sub>N<sub>y</sub> NPs/N-CIC100 material to make the Pt NPs/TaO<sub>x</sub>N<sub>y</sub> NPs/N-CIC100 material, which showed very good resistance to Pt dissolution, especially as compared to its precursors and parallel products, TaO<sub>x</sub>N<sub>y</sub> NPs/N-CIC100 and N-CIC100.

## 6.2 Results and Discussion

### 6.2.1. Structure, Morphology and Composition of Mixtures of TaO<sub>x</sub> or TaO<sub>x</sub>N<sub>y</sub> with CIC100 Powder

Chapter 3 (Section 3.4.1-6) gives the details of the synthesis of the CIC100, N-CIC100, Bn-CIC100, TaO<sub>x</sub> NPs/CIC100, TaO<sub>x</sub>N<sub>y</sub> NPs/N-CIC100 and Pt NPs/TaO<sub>x</sub>N<sub>y</sub> NPs/N-CIC100 materials. After their synthesis, they were characterized at every stage for their structure, morphology and composition using SEM, TEM, PXRD, and elemental analysis techniques. Although the synthesis of the Pt NPs/TaO<sub>x</sub>N<sub>y</sub> NPs/N-CIC100 material is described in the following paragraphs, their structure, morphology and composition are discussed in Section 6.2.3.

Figure 6.1 shows the HRTEM images of the CIC100 powder. It can be clearly seen that the average diameter of the pores is ca. 100 nm. The thickness of the pore walls differs in certain regions, likely an indication of the clustering of the silica NP template. This is expected, as will be explained here in terms of the steps of the synthesis. During the second step of the synthesis of the CIC powder (Chapter 3, Figure 3.1), the solvent that helps to disperse the silica NPs evaporates, causing the NPs to aggregate and form clusters. In the next step, called imprinting (Chapter 3, Figure 3.1), the MP particles are at their softening temperature.

It is possible that the thinner CIC100 walls seen in the majority of the images are due to penetration of pitch between close packed NPs, while the thicker walls could result from penetration of pitch between isolated silica NPs with larger gaps between them (Section 3.4.1).<sup>258-259</sup> Although they are not seen in these two-dimensional HRTEM images, one can

reasonably expect to observe additional pores along the walls that are created due to contact between two neighboring silica NPs. Those pore diameters are different from the silica NP size, with their sizes determined by the extent of contact between the two NPs.

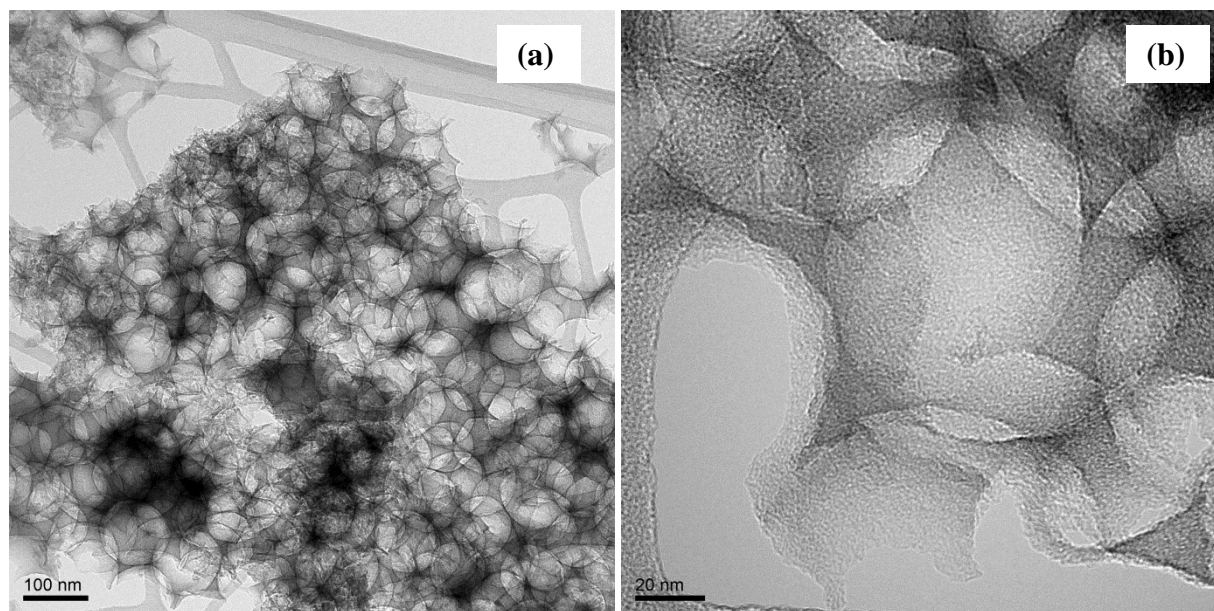
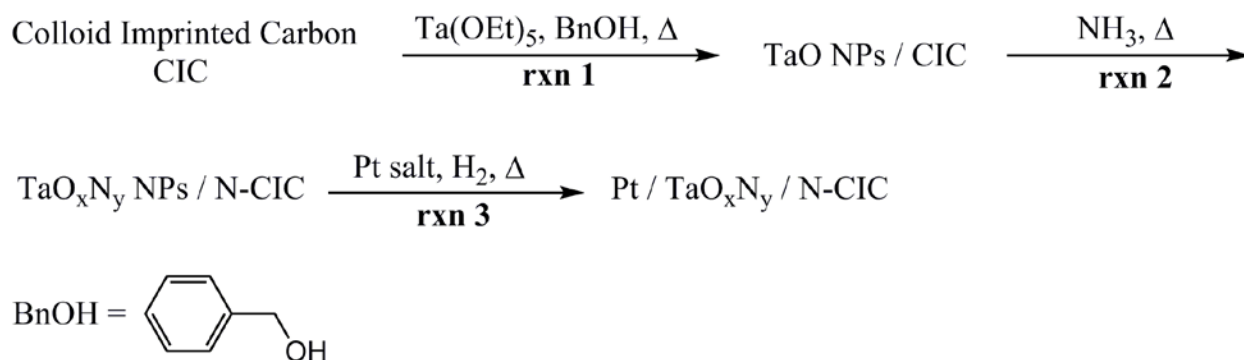


**Figure 6.1** HRTEM images of CIC100 (a) showing part of a CIC100 particle and (b) a higher magnification image of the CIC100 particle, where the diameter of the pores can be seen clearly.

To obtain the target composite, the Pt NPs/ TaO<sub>x</sub>N<sub>y</sub> NPs/N-CIC100 material, a series of synthetic steps were taken, as shown in Scheme 6.1. The second step of this procedure (Scheme 6.1, reaction 1) involves anchoring the Ta oxide NPs onto the CIC100 powder surface using the solvothermal method, in which the CIC100 was treated with Ta ethoxide in the presence of benzyl alcohol at 260 °C in an autoclave.<sup>160</sup> Unlike in the hydrothermal method, the decomposition of Ta ethoxide is controlled, which leads to better anchoring of smaller Ta oxide

NPs on the CIC100 surface.<sup>160-162</sup> It is believed that the anchoring of Ta oxide takes place on sites where the oxygen functional groups, such as quinone/hydroquinone, carboxylic acid, epoxy, lactone, etc., are present on the carbon powder surface. The steps involved in the anchoring of Ta oxide on surface sites of CIC100 could include ligand exchange, ether elimination, and/or esterification.<sup>161</sup>



**Scheme 6.1** Synthesis scheme used to form the Pt NPs/TaO<sub>x</sub>N<sub>y</sub> NPs/N-CIC100 material.

Figure 6.2 shows the possible interactions that lead to the above mentioned processes in reaction 1 of Scheme 6.1. The growth of the TaO<sub>x</sub> NPs occurs by ligand exchange between ethoxide and benzoxide, which then form Ta benzoxide and ethanol. The subsequent step results in the formation of the Ta oxo-alkoxide by condensation and then ether (diethyl ether and/or benzyl ether) formation.

Although the composition of the final mixture formed in this reaction was not analyzed to determine the by-products of the reaction in the present work, Niederberger et.al. did analyze the

final reaction mixture using  $^1\text{H}$  and  $^{13}\text{C}$  NMR spectroscopy. This showed that ligand exchange takes place, even at room temperature.<sup>260</sup> They attributed this observation to the stabilization of the intermediate carbocation by the mesomeric effect of the benzyl group.

The next step (Scheme 6.1, reaction 2) involves nitriding of the TaO<sub>x</sub> NPs/CIC100 material, according to the method used in Chapters 4 and 5, where the sample was heated at 700 °C under a reducing ammonia atmosphere for 7 hours.<sup>25</sup> During this nitriding step, it is expected that not only does TaO<sub>x</sub> convert to TaO<sub>x</sub>N<sub>y</sub>, but also that nitrogen functional groups are introduced into the surface of the CIC100 lattice, giving N-CIC100. Typically, these nitrogen functional groups are primary/secondary/tertiary amines, quaternary nitrogen, amides, pyridines, pyrroles, pyridones, pyridine N-oxide, imines, nitro and nitroso groups.<sup>261-262</sup>

In the final step of this synthesis (Scheme 6.1, reaction 3), the incipient impregnation method was used for the infiltration of the Pt salt and subsequent anchoring of Pt NPs on the TaO<sub>x</sub>N<sub>y</sub> NPs/N-CIC100 surface. It has been documented that N- functional groups on carbon surfaces help to nucleate Pt NPs. Also, they help to disperse the Pt NPs and form smaller Pt NPs compared to non-nitrogenated carbon surfaces.<sup>262-264</sup> This has been claimed to be the result of the “active sites” that are created by the introduction of the more electronegative nitrogen atoms into the carbon lattice, which behave either as Lewis acid or anionic sites for the Pt cation.

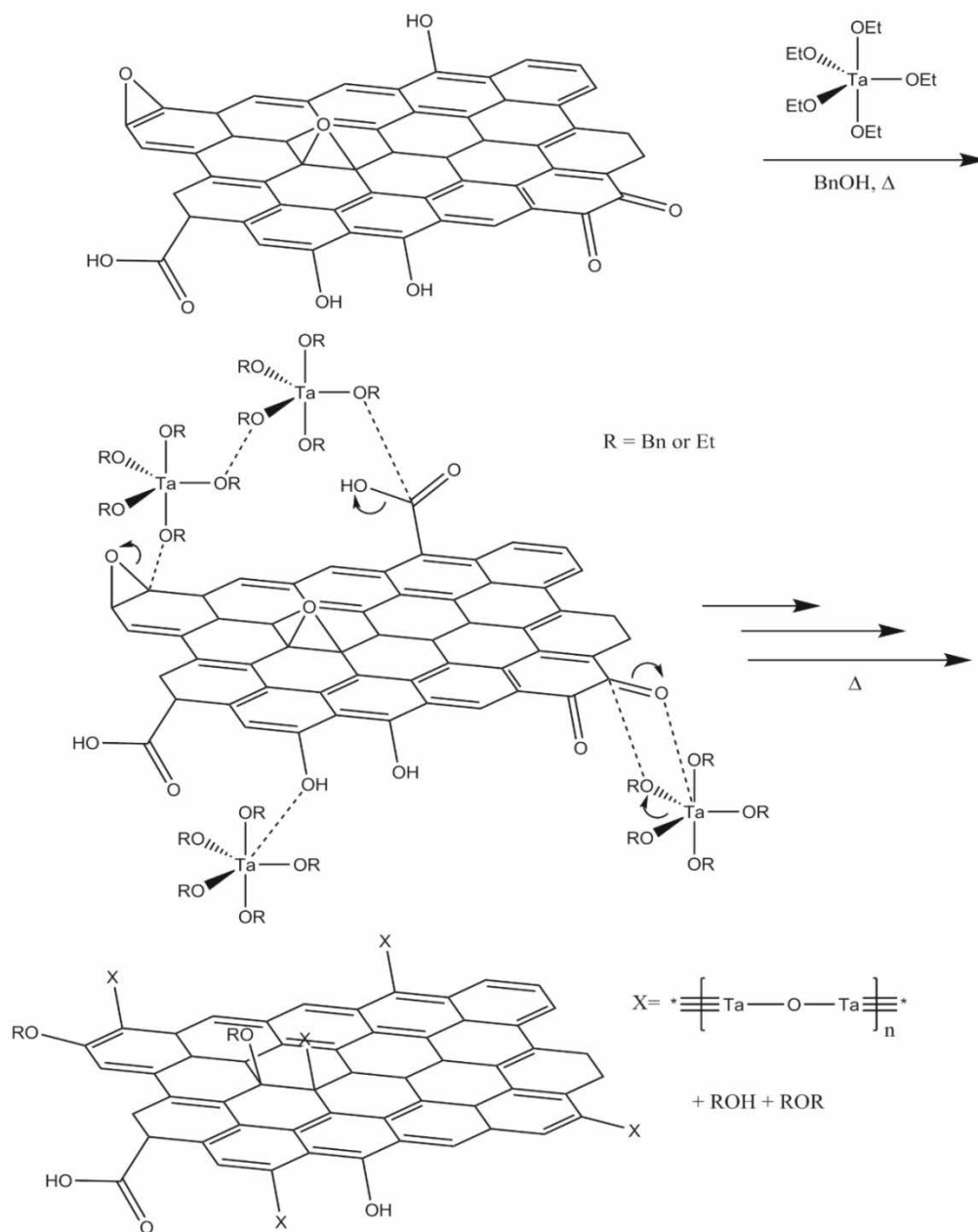


**Figure 6.2** Synthesis route for the formation of the  $\text{TaO}_x$  NPs/CIC100 composite, showing the possible interactions between  $\text{Ta}(\text{OEt})_5$  and CIC100 and the formation of the  $\text{TaO}_x$  NPs/CIC100 material.

Two additional materials were synthesized as controls in this work, including benzyl alcohol treated CIC100 (Bn-CIC100) and the nitrated Bn-CIC100 alone (N-CIC100). Bn-CIC100 was made by the solvothermal method (treating the CIC100 powder with BnOH at 260°C) that was used to form the TaO<sub>x</sub> NPs/CIC100 material in this work. (Section 3.4.2) The Bn-CIC100 was subsequently nitrated to convert it to N-CIC100 under the same conditions as used to obtain the TaO<sub>x</sub>N<sub>y</sub> NPs/N-CIC100 material.

Figure 6.3 shows the HRTEM images of the nitrated CIC100. The images obtained for N-CIC100 are much sharper and clearer than seen for the CIC100 (Figure 6.1), likely as the N-CIC100 sample was drifting less within the TEM chamber. Specimen charging can be ruled out as causing the drift, as carbon is a good conductor, so the full reason(s) for these challenges remain unknown. Notably, even after nitriding, the structure and pore size of CIC100 (100 nm) are still intact for the N-CIC100 powder.

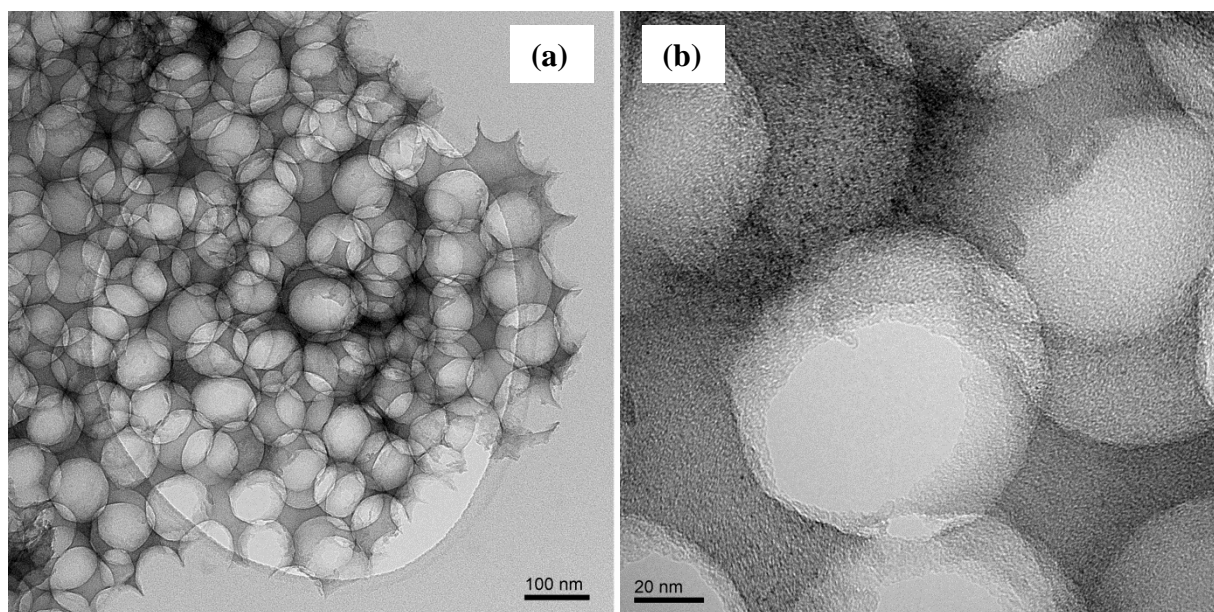


**Figure 6.3** HRTEM images of N-CIC100 with (a) showing part of an N-CIC100 particle and (b) showing the high magnification image of the CIC100 particle, where the diameter of the pores can be seen clearly.

Under HRTEM analysis, the TaO<sub>x</sub> NPs/CIC100 sample shows a string of Ta oxide NPs anchored onto the carbon surface. As this is a 2D TEM image (Figure 6.4), it is difficult to determine the exact location of the TaO<sub>x</sub> NPs. However, one can expect that they should be located both inside and outside the pores of CIC100. Determining the TaO<sub>x</sub> NP size was also difficult to achieve, since they appear as a chain of NPs, but the average particle size was estimated as being 5-8 nm. Again, image drifting was observed for this sample, which can perhaps be attributed to the charging of the specimen. Ta oxide is known to be an insulator (band gap is 3.9 eV) and hence charge building up on the surface is not a surprise with a 200 kV

applied potential in the HRTEM. On the other hand, the TaO<sub>x</sub>N<sub>y</sub> NPs/N-CIC100 sample did not show charging problems and, consistent with this, no drift was observed.

The size of the TaO<sub>x</sub>N<sub>y</sub> NPs was a little larger (10-20 nm) than the original Ta oxide NPs (5-8 nm), probably due to sintering of the TaO<sub>x</sub> NPs during the high temperature nitriding treatment. As was seen for the TaO<sub>x</sub>N<sub>y</sub> NTs sample (Figure 4.2), holes are also seen in the TaO<sub>x</sub>N<sub>y</sub> NPs (Figure 6.4b) after the conversion of the TaO<sub>x</sub> NPs to TaO<sub>x</sub>N<sub>y</sub> NPs. Further, it can be clearly seen in the HRTEM images that the original morphology and hence the pore size of the CIC100 powder is preserved after solvothermal synthesis and nitriding. The TaO<sub>x</sub> or TaO<sub>x</sub>N<sub>y</sub> loading on the CIC100 or N-CIC100 powder is 75% w/w, but the volume of TaO<sub>x</sub>N<sub>y</sub> is significantly lower, thus fewer particles are seen than perhaps expected (Figure 6.4). This is because the TaO<sub>x</sub> or TaO<sub>x</sub>N<sub>y</sub> NPs are heavier (density = 8.2 and 14.1 g·cm<sup>-3</sup>, respectively)<sup>182</sup> than the CIC100 or N-CIC100 powders (density is ca. 2 g·cm<sup>-3</sup>).

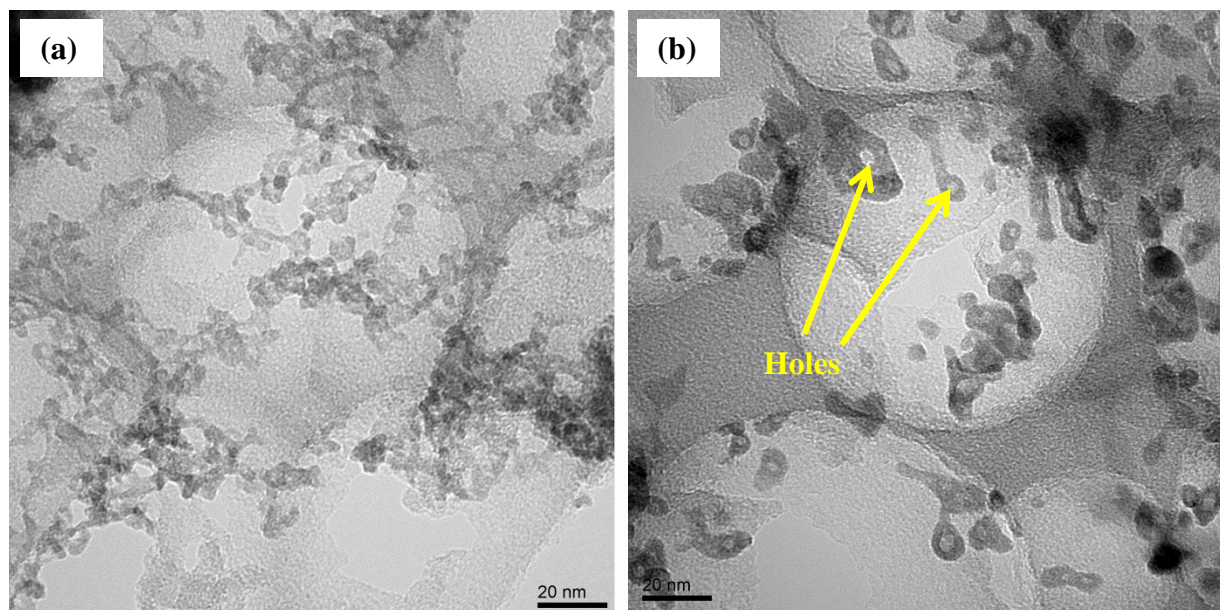


Figure 6.4 HRTEM images of the (a) TaO<sub>x</sub> NPs/CIC100 (1:3 w:w) and (b) TaO<sub>x</sub>N<sub>y</sub> NPs/N-CIC100 (1:3 w:w) powders.

The elemental analysis of this series of materials is presented in Table 6.1. Comparing CIC100 with the benzyl alcohol treated CIC100 (Bn-CIC100), there is a 6 % increment in the oxygen content. It is expected that some oxygenated functional groups may have been introduced onto the CIC100 surface during the solvothermal process. However, it seems that some of these oxygen functional groups may have been converted to nitrogen functional groups in N-CIC100 (the oxygen content was lowered by ca. 3% in N-CIC100). In N-CIC100, the nitrogen content is 2%, but for the TaO<sub>x</sub>N<sub>y</sub> NPs/N-CIC100 powder, a 4% nitrogen content is obtained. The additional 2% nitrogen may come from the decomposition of the TaO<sub>x</sub>N<sub>y</sub> NPs and/or from TaO<sub>x</sub>/

TaO<sub>x</sub>N<sub>y</sub> NPs that act as a catalyst for the further nitriding of CIC100 while forming the TaO<sub>x</sub>N<sub>y</sub> NPs/N-CIC100 material.

In an elemental analysis procedure, the oxygen content is normally determined after taking away the total weight of C, H and N from the sample's initial weight. However, the oxygen content of the TaO<sub>x</sub> NPs/CIC100 and TaO<sub>x</sub>N<sub>y</sub> NPs/N-CIC100 powders was not determined here because the residue of TaO<sub>x</sub> and TaO<sub>x</sub>N<sub>y</sub> left after combustion would make the interpretation of the results quite complex.

**Table 6.1** Elemental analysis of the CIC100, Bn-CIC100, N-Bn-CIC100, TaO<sub>x</sub> NPs/CIC100, and TaO<sub>x</sub>N<sub>y</sub> NPs/N-CIC100 materials

		Materials				
		CIC100	Bn-CIC100	N-Bn-CIC100	TaO NPs/CIC100	TaON NPs /N-CIC100
weight %	<b>Carbon</b>	94.2	91.0	92.3	29.5	27.6
	<b>Hydrogen</b>	0.8	1.3	0.7	0.8	0.5
	<b>Nitrogen</b>	0.2	0.0	2.0	0.0	4.1
	<b>Oxygen</b>	4.8	7.7	5.0		

*Note: TaO = TaO<sub>x</sub>; TaON = TaO<sub>x</sub>N<sub>y</sub>; N-Bn-CIC100 = N-CIC100*

The XRD results obtained for the benzyl alcohol treated CIC100 and N-CIC100 powders are presented in Figure 6.5. A typical graphite peak (002) is seen for both CICs at  $2\theta = 25^\circ$ , showing that prolonged high temperature nitriding, resulting in the attachment of nitrogen functional groups, does not change the graphite peak position or shape. This may be an indication that nitriding incorporated N-functional groups on the surface of the starting material (CIC100). Also, there is no PXRD pattern for N-doped carbon allotropes that can be compared

with the results shown in Figure 6.5. Since there are no differences seen in the XRD pattern for the graphite and N-doped CIC100 (N-CIC100) materials, no structure refinement was performed on the XRD patterns for CIC100 and N-CIC100.

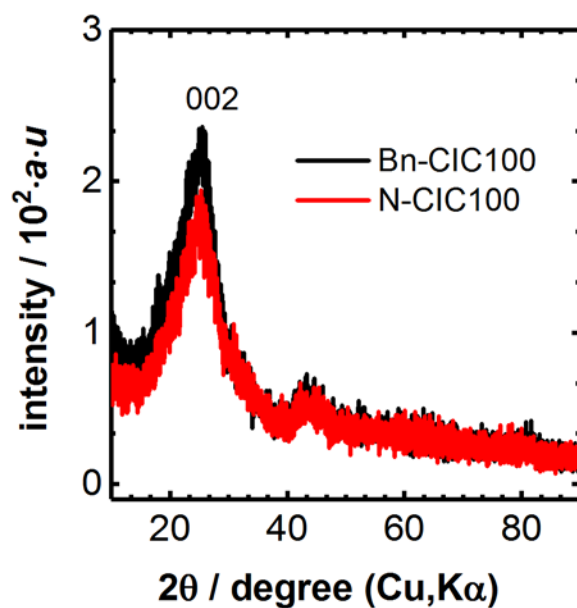


**Figure 6.5** PXRD pattern of Bn-CIC100 and N-CIC100, showing the graphite peak of 002 at  $2\theta = 25^\circ$ .

For the TaO<sub>x</sub> NPs/CIC100 and TaO<sub>x</sub>N<sub>y</sub> NPs/N-CIC100 samples, the PXRD data were refined using the Le Bail method, as shown in Figure 6.6 a and b, respectively. The TaO<sub>x</sub> pattern matches with the pattern of low temperature orthorhombic Ta<sub>2</sub>O<sub>5</sub><sup>265</sup>, while the pattern obtained

for the  $\text{TaO}_x\text{N}_y$  NPs indicates that a mixture of two compounds is present, i.e., the baddeleyite structure of both  $\beta\text{-TaON}$  and  $\text{Ta}_3\text{O}_x\text{N}_y$ .<sup>183</sup>

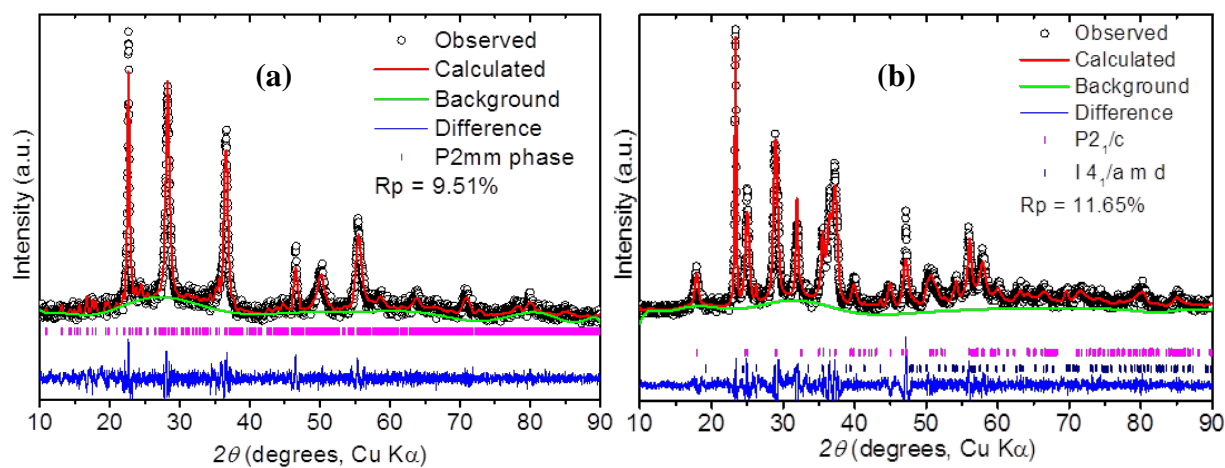


**Figure 6.6** PXRD data, after refinement, for the (a)  $\text{TaO}_x$  NPs/CIC100 and (b)  $\text{TaO}_x\text{N}_y$  NPs/N-CIC100 powder samples. The PXRD data sets were refined using the LeBail refinement method, using the General Structure Analysis System (GSAS) package with an EXPGUS interface to obtain the cell parameters of (a)  $\text{Ta}_2\text{O}_5$  and (a),  $\beta\text{-TaON}$  and  $\text{Ta}_3\text{O}_x\text{N}_y$ .

### 6.2.2 Electrochemistry of CIC100, $\text{TaO}_x$ NPs/CIC100, $\text{TaO}_x\text{N}_y$ NPs/N-CIC100, Bn-CIC100 and N-CIC100, all in the absence of Pt

Electrochemical characterization was performed for all intermediates obtained at all stages of the synthesis of the Pt NPs/ $\text{TaO}_x\text{N}_y$  NPs/N-CIC100 powders. The ink was prepared by mixing 10 mg of sample with 0.1 g of 12%  $\text{H}_2\text{SO}_4/\text{EtOH}$  and 0.4 g of 1% wt Nafion/ $\text{EtOH}$ . The mixtures were then sonicated and drop cast on a glassy carbon electrode (GC) surface. Subsequent drying of the ink produced an adherent film on the GC surface, which was subjected to electrochemical

analysis. Similar to what was used in Chapter 5, the corrosion protocol, i.e., the accelerated durability test (ADT), involved a potentiostatic stepping (pstep) experiment, where the charges passed during each cycle was determined and hence the corrosion charge could be calculated. More details about this experiment and the calculation can be found in Chapter 3 (Section 3.5.4.2). Briefly, the protocol involved subjecting the material to 1.4 V vs. RHE for 50 s, followed by 10 s at 0.8 V vs. RHE, repeated 18 times (18 cycles = 18 min). Before and after the stepping experiment, the cyclic voltammetry (CV) response was recorded, also as was done in Chapter 5. The double layer (DL) and pseudocapacitance (PC) charges were determined from the CV charges passed over a particular voltage range, as shown schematically in Figure 6.7.

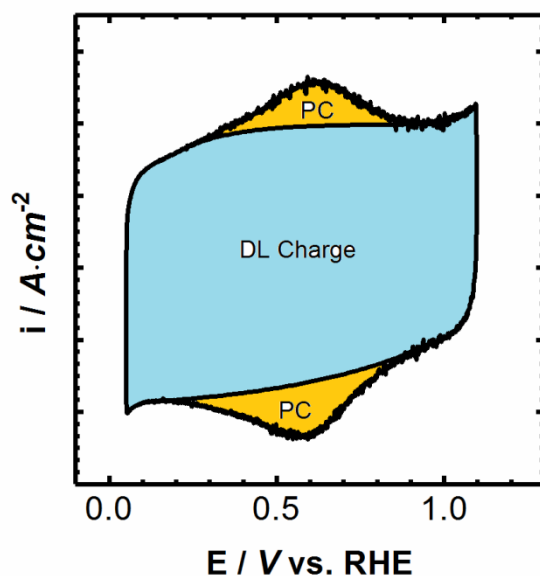


**Figure 6.7** Graphical representation showing the potential range of the double layer (DL) and pseudocapacitance (PC) and how charges were obtained from the CVs of the carbon-based materials under study here.

### 6.2.2.1 Cyclic Voltammetry analysis of carbon-based materials (no Pt)

Figure 6.8 shows the CVs of the CIC100, Bn-CIC100 (BnOH treated CIC100), N-CIC100, TaO<sub>x</sub> NPs/CIC100, and TaO<sub>x</sub>N<sub>y</sub> NPs/N-CIC100 materials, both before and after the potentiostatic stepping protocol (Accelerated Durability Test). First, a steady state CV at 10 mV·s<sup>-1</sup> was collected in the potential range of 0.05 V to 1.1 V vs. RHE, a range over which it is assumed that carbon does not corrode, especially in the absence of Pt. (Chapter 2, Section 2.4.2) It is seen that all of the CVs in Figure 6.8 look very much like the CVs of carbon alone, with no evidence for TaO<sub>x</sub> or TaO<sub>x</sub>N<sub>y</sub> electrochemistry in Figure 6.8d and e. Also, all of them clearly show that the carbon ECSA (electrochemically active surface area) has increased as a result of the ADT.

An increase in the ECSA, together with an increase in the pseudocapacitance (explained in the next paragraph), is a reliable indication that the carbon has undergone electrochemical corrosion. As discussed in Chapter 2 (Section 2.4.2), this claim has been corroborated by many other techniques, such as *in-situ* mass spectroscopy of the gases emitted in the cell<sup>61-62</sup>, showing a spike in the CO<sub>2</sub> signal, *in situ* measurements of changes in the electrode potential<sup>63</sup>, Raman spectroscopy that can detect changes in the surface functional groups<sup>65</sup>, and from carbon weight loss.

The CVs in Figure 6.8 all show double layer (DL) charging, which is proportional to the ECSA, as well as some redox peaks (pseudocapacitance, PC), centred at ca. 0.6 V vs. RHE, believed to be due to the quinone/hydroquinone (Q/QH<sub>2</sub>) redox reaction (Equation 6.1).<sup>67, 266</sup>



Notably, the equilibrium potential ( $E_{1/2}$ ) of the Q/QH<sub>2</sub> couple shifts by a few millivolts between the carbon materials and the peak shapes are also a bit variable (Figure 6.8). Even so, there are no major differences in the CV responses of the different CIC100-based materials, with the CVs looking very much like those of carbon. Consistent with this, the knowledge obtained from Chapter 4 tells us that Ta oxide and TaO<sub>x</sub>N<sub>y</sub> should not have any redox activity at > 0.6 V vs. RHE (Section 4.2.2). However, it is puzzling why the redox peaks of TaO<sub>x</sub>N<sub>y</sub> (expected at 0 – 0.6 V) are not visible in Figure 6.8e.

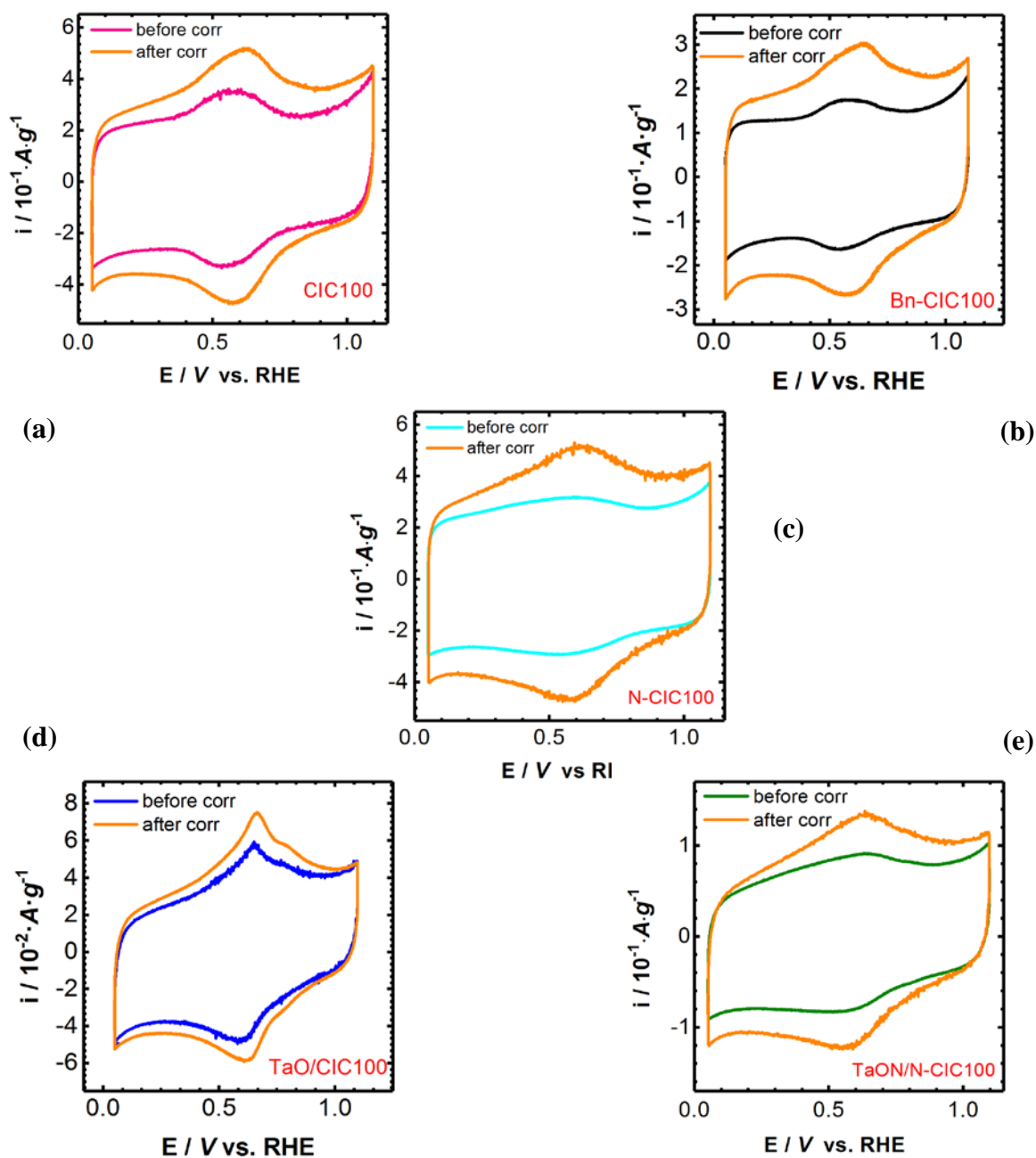


**Figure 6.8** Steady-state CVs of the materials under investigation here, before and after the potentiostatic ADT. The name of the material is shown in the respective CVs and also (a) to (e) naming is given for more clarification (a) CIC100, (b) Bn-CIC100, (c) N-CIC100, (d) TaO<sub>x</sub> NPs/CIC100 and (e) TaO<sub>x</sub>N<sub>y</sub> NPs/N-CIC100. All CVs were obtained in deaerated 0.5 M H<sub>2</sub>SO<sub>4</sub> at 10 mV·s<sup>-1</sup> and all of the currents were normalized to the carbon weight.

In the CV of the TaO<sub>x</sub> NPs/CIC100 sample, the PC peaks are a little sharper than for the other samples (Table 6.2). This may indicate that the TaO<sub>x</sub> NPs are anchored on certain redox-active surface sites, thus blocking their electrochemistry, while leaving only selected other groups exposed to solution. The pseudocapacitance peaks seen for the CIC100 sample (Figure 6.8) are well defined and sharp compared to the broader peak observed for the N-CIC100 material (Table 6.2), perhaps indicating that multiple nitrogen functional groups are participating in the PC process. Interestingly, the Bn-CIC100 material gives a PC peak width (FWHM) of 35 mV, exactly the same as seen for N-CIC100. As explained later in this section, BnOH does not participate in the observed electrochemistry, but additional oxygen functional groups could be formed during the solvothermal step. Therefore, the broad PC peak seen for Bn-CIC100 could be attributed to the presence of a range of surface redox-active functional groups that result in multiple equilibrium potentials.

**Table 6.2** The full width at half maximum for the PC peaks that are seen in the Figure 6.8.

Material	Full width at half maximum (FWHM) for Pseudo capacitance peak
CIC100	0.30
Bn-CIC100	0.35
N-CIC100	0.35
TaO <sub>x</sub> NPs/ CIC100	0.25
TaO <sub>x</sub> N <sub>y</sub> NPs / N-CIC100	0.30

Note: All CVs were obtained in deaerated 0.5 M H<sub>2</sub>SO<sub>4</sub> at 10 mV·s<sup>-1</sup> and all of the currents were normalized to the carbon weight.

The anodic and cathodic peak potentials associated with a pseudocapacitive reaction, such as seen for the predominantly quinone/hydroquinone process at 0.6 V in Figure 6.8, are normally very similar to each other. However, in Figure 6.8, a peak potential separation ( $\Delta E_p$ ) of ca. 50 mV is seen and the  $E_{p1/2}$  (full width at half-height) of the peaks are larger (up to 300 mV) than  $90.6/n \text{ mV}^{116}$ , the conditions that are normally fulfilled by Nernstian systems. These large peak separations and peak widths may be attributed to the presence of a wide range of surface redox-active functional groups and/or different micro-environments that result in multiple equilibrium potentials.

A summary of the DL and PC charges of all the materials, obtained from Figure 6.8a to e, is shown in Table 6.3. It is interesting that Bn-CIC100 gives a smaller double layer charge than the other two carbon-only materials (CIC100 and N-CIC100). This may be due to the blocking of some of the CIC pores by BnOH retained from the synthesis, thus lowering its ECSA. Since BnOH has a low solubility in aqueous media (3.5 g in 100 ml of  $\text{H}_2\text{O}$ ) it may take a while to replace the trapped alcohol with the acidic solution. Perhaps if enough time were provided for this purpose, the Bn-CIC100 sample may have shown a similar DL charge as CIC100 or N-CIC100.

The very high DL charge obtained for the N-CIC100 sample may indicate that nitriding of CIC100 causes nitrogen surface functionalization.<sup>262</sup> The nitrogen group functionalization seems to increase the hydrophilicity of the carbon surface and hence the aqueous  $\text{H}_2\text{SO}_4$  electrolyte access to the pores should be facilitated, resulting in higher DL charges.<sup>257, 267</sup> Moreover, the high temperature of the nitriding process of CIC100 may help to remove some of the BnOH

trapped inside the pores, thus potentially decreasing the impediments to electrolyte access. Otherwise, the N-CIC100 should have had a very similar DL charge as Bn-CIC100.

**Table 6.3** Pseudocapacitance (PC) and Double Layer (DL) charges from CVs for the carbon-based materials before and after ADT

<b>PC Charge / C·g<sup>-1</sup></b>	<b>CIC100</b>	<b>Bn-CIC100</b>	<b>N-CIC100</b>	<b>TaO NPs / CIC100</b>	<b>TaON NPs / N-CIC100</b>
<b>Before corr test</b>	3.0	1.1	1.8	0.4	0.5
<b>After corr test</b>	4.4	2.6	4.3	0.8	1.0
<b>after:before ratio</b>	1.5	2.5	2.4	1.8	2.2

<b>DL Charge / C·g<sup>-1</sup></b>	<b>CIC100</b>	<b>Bn-CIC100</b>	<b>N-CIC100</b>	<b>TaO NPs / CIC100</b>	<b>TaON NPs / N-CIC100</b>
<b>Before corr test</b>	23.4	13.5	25.0	3.0	6.6
<b>After corr test</b>	30.6	19.1	32.7	3.4	8.5
<b>after:before ratio</b>	1.3	1.4	1.3	1.1	1.3

*Note: TaO = TaO<sub>x</sub> ; TaON = TaO<sub>x</sub>N<sub>y</sub>*

A close look at the CVs (Figure 6.8 - CIC100 vs. N-CIC100) at the anodic and cathodic switching potentials for N-CIC100 shows a rapid change in current, indicating that N-CIC100 may be less resistive than CIC100. The same observation, i.e., less resistive CVs (Figure 6.8), can be seen for TaO<sub>x</sub>N<sub>y</sub> NPs/N-CIC100 (one of the final products without Pt, Scheme 6.1) compared to TaO<sub>x</sub> NPs/CIC100.

When comparing the composited carbon materials, the TaO<sub>x</sub> NPs/CIC100 sample (intermediate material, Scheme 6.1) gave the lowest DL charge. Recalling that the DL current or charge should be a reflection of the ECSA of the material, the low DL charge for TaO<sub>x</sub> NPs/CIC100 composite is justified by the fact that the anchored TaO<sub>x</sub> NPs would block some of

the sites of the underlying CIC100. The TEM image (Figure 6.4a) of the TaO<sub>x</sub> NPs/CIC100 material confirms this, showing that a high percentage of the CIC100 surface is covered by the TaO<sub>x</sub> NPs. Furthermore, Ta oxide is a wide band gap material and does not have good conductivity in the potential range used in these experiments. (Section 4.2.2) Finally, the charging current for Ta oxide should be in the nA range (Figure 4.6) and thus its contribution should be insignificant compared to the CIC100 DL charging current.

The magnitude of the DL charge for the TaO<sub>x</sub>N<sub>y</sub> NPs/N-CIC100 composite is higher than for the TaO<sub>x</sub> NPs/CIC100 (Figure 6.8 and Table 6.3), which can also be justified, as TaO<sub>x</sub>N<sub>y</sub> NPs/N-CIC100 should be a better conductor than TaO<sub>x</sub> and the holes present in the TaO<sub>x</sub>N<sub>y</sub> NPs should also facilitate electrolyte access to the carbon beneath the TaO<sub>x</sub>N<sub>y</sub> NPs. However, it remains unclear why the TaO<sub>x</sub>N<sub>y</sub> electrochemistry is not seen in the CV of the TaO<sub>x</sub>N<sub>y</sub> - containing materials in Figure 6.8. Although not shown in the thesis, it was found with neat TaO<sub>x</sub>N<sub>y</sub> powder that a very good electrical contact between the TaO<sub>x</sub>N<sub>y</sub> and the support material or a current collector is absolutely necessary to allow the expression of the TaO<sub>x</sub>N<sub>y</sub> electrochemistry. It is thus possible that the TaO<sub>x</sub>N<sub>y</sub> phase in the TaO<sub>x</sub>N<sub>y</sub> NPs/N-CIC100 ink may not have had a sufficiently good electrical contact to the CIC100 or to the glassy carbon surface.

Finally, it is also seen that all of the materials under study here have undergone some degree of electrochemical corrosion (Figure 6.8 and Table 6.3) after the potentiostatic stepping ADT, as both the DL and PC charges have increased (Table 6.3). It is noteworthy that the ratio of the DL charges, before and after the potentiostatic experiment, is very similar at ca. 1.3 for all

of the materials studied here (Table 6.3) except for TaO<sub>x</sub> NPs/CIC100, which gives a value of 1.1. During carbon corrosion, some of the surface carbon atoms, especially those that are already partly oxidized, are converted to CO<sub>2</sub>, which escapes as a gas from the pores, thus exposing new carbon surface sites. This will decrease the carbon particle volume, but usually will also increase the surface area, as seen by the ca. 30 % increase in the DL charge for all of the materials under study here (Table 6.3).

Table 6.3 also show that the pseudocapacitive charge (PC), stemming from the Q/QH<sub>2</sub> redox reaction, which is correlated with the degree of oxidation of the carbon surface, is lowest for the Bn-CIC100 material and highest for CIC100 before and after corrosion among all three of the carbon-alone materials. The as-formed CIC100 material is expected to have a high surface concentration of hydroxyl groups because, when the mesophase pitch is mixed with the silica NPs during CIC synthesis, it has been proposed that the -OH groups on the surface of the silica colloids end up on the carbon particle surface.<sup>256</sup> During the removal of the silica by HF, some of these oxygen-containing groups remain attached to the carbon surface, and thus the surface density of oxygenated functional groups increases.<sup>268</sup>

Having a lower value for PC charge for Bn-CIC100 is again attributed to the blocking of some of the CIC pores by unremoved BnOH. For N-CIC100, the PC charge (4.3 C·g<sup>-1</sup>) is almost the same as seen for CIC100 (4.4 C·g<sup>-1</sup>) after the ADT, even though the PC charge was much lower (1.8 C·g<sup>-1</sup>) than for the CIC100 before the ADT. As discussed earlier, the nitriding process likely introduces nitrogen functional groups into the lattice of the CIC100 powder and some of these seem to become redox active after undergoing oxidation during the ADT.

Both composited materials ( $\text{TaO}_x$  NPs/CIC100 and  $\text{TaO}_x\text{N}_y$  NPs/N-CIC100) have a very low PC charge, attributed to the blocking of the CIC100 surface. Of these two, the  $\text{TaO}_x$  NPs/CIC100 material has the lowest PC charge, perhaps because of the non-conducting nature of the  $\text{TaO}_x$  NPs and the absence of voids in the  $\text{TaO}_x$  NPs.

The PC charge ratio, before and after the potentiostatic step ADT experiment (Table 6.3), is seen to be similar for all of the materials (in the range of 1.8-2.5) except for CIC100, for which the ratio is 1.5. Even before the ADT, CIC100 exhibited a higher PC charge, attributed to the incorporation of oxygen surface functional groups during the CIC synthesis. After the ADT, the increment in the PC charge is smaller for CIC100 as compared to what is seen for the other materials. It is possible that oxygen functional groups already present on the CIC100 surface may have been converted to  $\text{CO}_2$  and those new groups are then introduced, and therefore the net increase in the PC charge for CIC100 is less than seen for N-CIC100.

For every material, the increase in the PC charge (Table 6.3 and Figure 6.8) may be the result of the oxidation of carbon. However, it is worth discussing the possible participation of BnOH in the carbon oxidation reaction (COR). The only material that was not exposed to BnOH is CIC100. Both Bn-CIC100 and  $\text{TaO}_x$  NPs/CIC100 were also exposed to the BnOH treatment, but not subjected to further treatment, while the other two materials (N-CIC100 and  $\text{TaO}_x\text{N}_y$  NP/N-CIC100) were nitrided at 700 °C for 7 h, which would definitely remove any trapped BnOH. BnOH can be electrooxidized to benzaldehyde or benzoic acid, but would likely need a metallic electrocatalyst, such as Pt, to promote these oxidation processes, which can occur at 0.05-0.2 V vs. RHE.<sup>269</sup> To date, no literature has been found that indicates that  $\text{TaO}_x$  or  $\text{TaO}_x\text{N}_y$

can act as a catalyst for these oxidation reactions. Therefore, the suggested electrooxidation of BnOH in acid can be ignored.

Importantly, Table 6.3 reveals that all of the materials studied here have undergone electrochemical corrosion, as seen from the fact that the charges after the potentiostatic stepping experiment are larger than before. The starting material and the N-CIC100: TaO<sub>x</sub>N<sub>y</sub> NPs/N-CIC100 product both exhibit a PC:DL charge ratio of ca. 4:1, respectively, while the ratios for Bn-CIC100:TaO<sub>x</sub> NPs/CIC100 are a little different, perhaps reflecting a change in the fraction of the carbon surface area that is blocked by BnOH. This is another indication that the charges (PC and DL), calculated from the CVs, arise primarily from the carbon materials. Further, the PC charge ratios, before and after ADT, for N-CIC100 and TaO<sub>x</sub>N<sub>y</sub> NPs/N-CIC100 are quite similar at 2.4 and 2.2, respectively, which can be attributed to their similar nitrogen and oxygen contents after the nitriding process.

#### 6.2.2.2 *Potentiostatic ADT analysis of carbon-based materials without Pt*

As has been shown in parallel work, the analysis of the current vs. time (i vs. t) transients during the ADT can be quite revealing<sup>249, 270-271</sup> and thus this form of analysis was also carried out in the present work. It is assumed that, in a step to 1.4 V vs. RHE, the double layer of the catalytic materials is charged, while carbon also undergoes corrosion, forming primarily CO<sub>2</sub> by a series of reactions (Reactions 2.3-2.11, Chapter 2) and possibly also forming some surface oxides (Reaction 2.6, Chapter 2). It is also assumed that the TaO<sub>x</sub> or TaO<sub>x</sub>N<sub>y</sub> NPs do not show any electrochemical activity at these potentials (Chapter 4 and 5), while the oxygen evolution

reaction (OER) could also occur at  $> 1.23$  V vs RHE. However, during the cathodic step to 0.8 V, only double layer discharge is assumed to occur.

Figure 6.9a shows the corrosion charges ( $q^+ - q^-$ ), calculated by taking the difference between the charge passed at 1.4 V ( $q^+$ ) and that at 0.8 V ( $q^-$ ) for all of the materials that were discussed above in the CV section.<sup>249, 270-271</sup> It seems that only the first few step cycles (1-5) contribute the most to the electrochemical corrosion of the material, and from cycles 6 to 18, only a small, nearly non-changing corrosion charge is seen. As mentioned earlier (Section 5.2.3), this is similar to what was seen in previous corrosion studies of carbon supports<sup>249, 270-271</sup>, with the significant lowering of the corrosion charge in latter step cycles suggested to be due to some form of passivation of the carbon surface and/or the blocking of pores, preventing access of water and acid or egress of CO<sub>2</sub> from them.

If the very first cycle is considered, then the tendency for corrosion is in the following sequence: CIC100  $>$  N-CIC100  $>$  Bn-CIC100  $>$  TaO<sub>x</sub>N<sub>y</sub> NPs/N-CIC100  $>$  TaO<sub>x</sub> NPs/CIC100, consistent with the CV results in Figure 6.8 when considering only the PC charges. The DL charges also follow the CV ranking except for CIC100 and N-CIC100, which have switched positions. However, from the eighth cycle onwards, all of the materials exhibit a relatively non-changing corrosion charge and a fairly similar corrosion charge except for CIC100, which has a slightly higher corrosion charge (ca. 4 C·g<sup>-1</sup>).

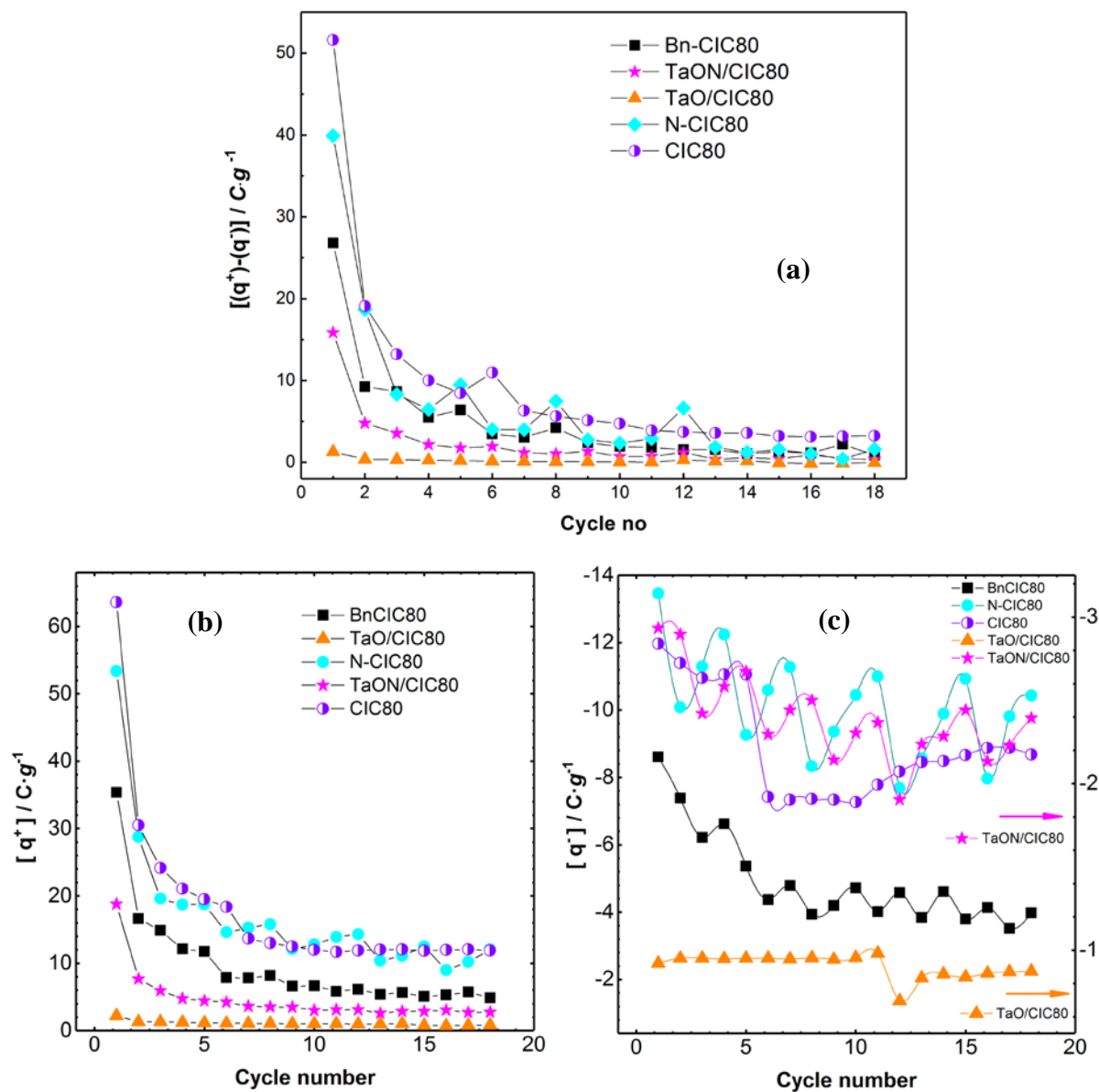


**Figure 6.9** Comparison of the (a) corrosion charge (Equation 3.1), (b) anodic charge ( $q^+$ ) and (c) cathodic charge ( $q^-$ ) for the materials under study here. Note: The  $TaO_xN_y$  NPs/N-CIC100 material is named TaON/CIC100 and  $TaO_x$  NPs/CIC100 named TaO NPs/CIC100 in the legend.

Consultation of the CV vs.  $i/t$  data shows (Table 6.3) that CIC100 and N-CIC100 both have a similar DL charge ratio (1.3), but different PC charge ratios [The ratio for CIC100 (1.5) is lower than for N-CIC100 (2.4)]. As explained earlier, it is suspected that, after the potentiostatic step ADT, some of the oxygenated functional groups on the surface of the CIC100 sample have been converted to  $\text{CO}_2$ , thus lowering the PC charge obtained from the CV data. For Bn-CIC100, the extent of corrosion is lower, likely as some trapped BnOH in the pores prevents full access of the internal CIC surface to the acidic solution.

For the composite materials, both the  $\text{TaO}_x$  NPs/CIC100 and  $\text{TaO}_x\text{N}_y$  NPs/N-CIC100 samples contain the same amount of carbon because  $\text{TaO}_x$  NPs/CIC100 is the precursor to  $\text{TaO}_x\text{N}_y$  NPs/N-CIC100. However, from the DL charge data (Table 6.3), the exposed CIC surface area of the  $\text{TaO}_x$  NPs/CIC100 composite seems to be ca. half of the carbon area exposed for the  $\text{TaO}_x\text{N}_y$  NPs/N-CIC100 composite. Again, this could be due to blocking of the CIC100 pores by BnOH, which was present during  $\text{TaO}_x$  synthesis. Also, the presence of the holes in the  $\text{TaO}_x\text{N}_y$  NP structure may have improved electrolyte access to the underlying carbon powder. Further, although the  $\text{TaO}_x\text{N}_y$  NPs/N-CIC100 sample does not exhibit the best corrosion resistance, it is better than seen for its constituent, N-CIC100.

The analysis of the individual anodic and cathodic charges passed in the potential steps (Figure 6.9b and c, respectively) can also provide some further insight into the COR at these various materials. All of the carbon materials (CIC100, BnCIC100 and N-CIC100) show the same trends, with the anodic charge being highest in the first cycle, and in the subsequent step cycles, the charge tapers down to a near-constant value between cycles 7-18. Even the

magnitude of the anodic charges in the first cycle is close to the values that were obtained previously by our group for CIC100 ( $86 \text{ C}\cdot\text{g}^{-1}$ ).<sup>272</sup> As the anodic charge represents a combination of DL charging, formation of an oxide film on the CIC surface,  $\text{CO}_2$  production and possibly OER, this suggests that carbon corrosion is more prevalent in the first few cycles, perhaps as pores gradually become blocked by corrosion products.

For the  $\text{TaO}_x\text{N}_y$  NPs/N-CIC100 composite, the decaying trend of the anodic charge is similar to what is seen for the predominantly CIC materials, whereas for the  $\text{TaO}_x$  NPs/CIC100 material, the trend is non-existence, i.e. almost a near constant values are seen for all cycles. Importantly, the anodic charges in Figure 6.9c follow the same trends as seen from the corrosion charge and the CV PC charge, i.e.  $\text{CIC100} > \text{N-CIC100} > \text{Bn-CIC100} > \text{TaO}_x\text{N}_y \text{ NPs/N-CIC100} > \text{TaO}_x \text{ NPs/CIC100}$ .

It is assumed that the DL charge represents the electrochemically accessible area of a material and thus that the cathodic charge in these potentiostatic experiments should be proportional to the electrochemically accessible surface area of the solid materials. This relationship is acceptable for the carbonaceous materials, but not valid for the composites. Even for carbonaceous materials, discrepancy is seen for the data in cathodic charge vs. CV DL charge. According to the increasing DL charge seen by the increasing size of the CVs with repeated ADT studies (Figure 6.8 and Table 6.3), the cathodic charge should increase with the number of applied cycles in the potentiostatic ADT as corrosion occurs and the surface area increases. However, this is not always seen in Figure 6.9c. In Figure 6.9c, the cathodic charges for the  $\text{TaO}_x$  NPs/CIC100 and  $\text{TaO}_x\text{N}_y$  NPs/N-CIC100 materials remain almost constant

throughout the potential steps, whereas for the carbon materials without any Ta-containing components present, most follow the decaying trend explained earlier for the anodic charge, rather than increasing.

The reason for the discrepancy between the DL charges from the CVs and the cathodic charges from the potential step ADTs may be explained by analyzing each of the CVs after the ADT experiment instead of just the steady-state CV, which is shown in Figure 6.8. Figure 6.10 shows 3 CVs after the 18<sup>th</sup> step cycle for the Bn-CIC100 material as an example. It is seen that, in the first negative scan after the potential step, a higher cathodic charge between 0.4-0.05 V than in the subsequent CVs, which are all then very similar. This higher cathodic current is very likely due to the reduction of surface oxide groups that did not get opportunity to reduce during the potentiostatic step as the lower potential applied was 0.8 V. Further, the anodic current is getting reduced after the 1<sup>st</sup> full CV. These observations give an indication that time and potential scanning allow the pores in the material to be slowly accessed by the electrolyte solution and hence DL charge reach a steady state as well as higher value. This would then mean that the cathodic charge in the ADT is smaller than it should be. Therefore, the anodic charge passed in the positive step could not be normalized to the cathodic step charge, which is normally considered to be related to the real ECSA in this work. It is important to note that all of the materials including Ta based carbon materials showed the similar phenomenon.

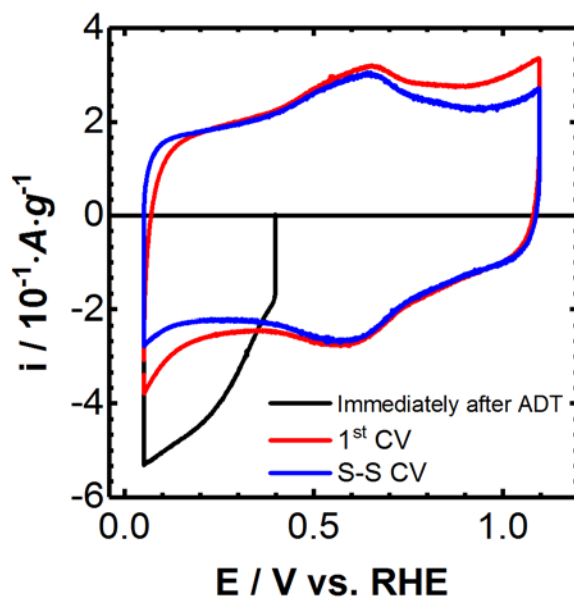


**Figure 6.10** Black trace is the cathodic segment immediately after ADT potentiostatic step, red trace is the 1<sup>st</sup> full CV between 0.05 V to 1.1 V and blue is the steady state (S-S) CV for Bn-CIC100 in 0.5 M H<sub>2</sub>SO<sub>4</sub> at a scan rate of 10 mV·s<sup>-1</sup>. The ‘before corrosion’ steady state CV is given in Figure 6.8.

The CVs (Figure 6.8 and Table 6.3) and the anodic potentiostatic step ADT results (Figure 6.9) argue that all of the materials studied here underwent some corrosion, as seen by the increasing CV charges before and after 18 cycles and the much larger anodic vs cathodic charge seen in the ADT. Similar results were obtained in parallel studies in our group (Figure 5.15) and by others for a variety of carbon materials.<sup>249, 270-271</sup> Since it is known that carbon can corrode, the samples were examined here by FESEM to detect any microstructural changes before and after the ADT protocol. Figure 6.10 shows these images for the TaO<sub>x</sub>N<sub>y</sub> NPs/N-CIC100 powder.

After ADT, some of the pores of the carbon seem to have widened ( $> 100$  nm), perhaps due to conversion to  $\text{CO}_2$ , compared to before (ca. 100 nm), while no other major changes can be seen.

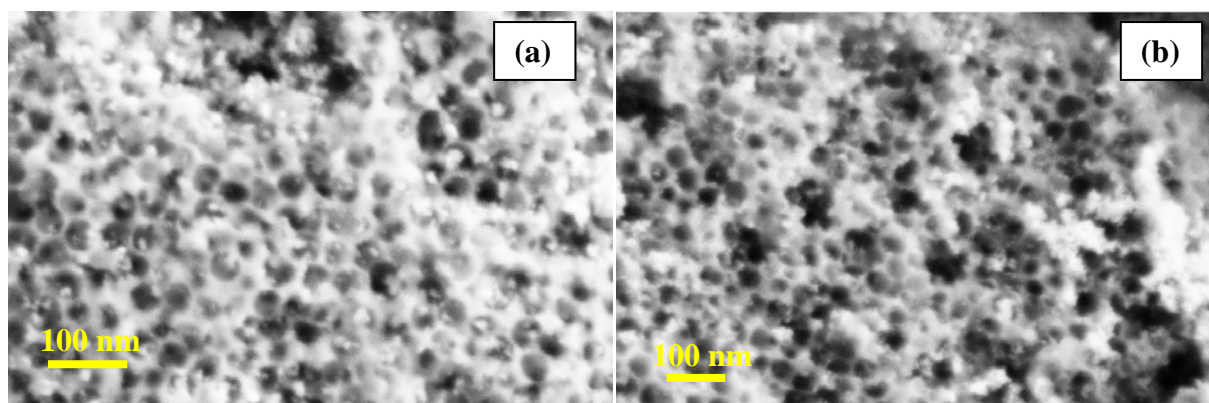


**Figure 6.11** FESEM images of  $\text{TaO}_x\text{N}_y$  NPs/N-CIC100 (a) before and (b) after the potentiostatic step ADT experiments.

What is understood from the discussion above is that the addition of  $\text{TaO}_x\text{N}_y$  NPs to CIC100 (which converted to N-CIC100 after nitriding) has blocked a certain percentage of the carbon surface. It is hypothesized that the bottom-up synthetic approach used to anchor the  $\text{TaO}_x\text{N}_y$  NPs would result in their attachment primarily to existing functional groups that were already present on the CIC100 surface. Therefore, carbon corrosion is minimized by the presence of these NPs, which serve to block some of the oxygenated functional groups that are the most prone to conversion to  $\text{CO}_2$ . However, the unblocked carbon surfaces undergo corrosion at a similar rate as any other carbon material.

### 6.2.3 Structure, Morphology, and Composition of Pt NPs/TaO<sub>x</sub>N<sub>y</sub> NPs/N-CIC100 Catalysts

The DOE has recommended that, after multiple potential steps [0.6 V (3 s), 0.95 V (3 s), (30,000 cycles)], a minimum of 40% of the initial catalytic activity or Pt ECSA should be maintained, noting that we have altered the protocol to be: [1.4 V (50 s), 0.8 V (10 s), 18 cycles].<sup>11</sup> This expectation is based on a catalyst support decorated with Pt nanoparticles. For this reason, in part, Pt NPs were impregnated into the TaO<sub>x</sub>N<sub>y</sub> NPs/N-CIC100 material, thus forming the Pt/TaO<sub>x</sub>N<sub>y</sub> /N-CIC100 composite, with the behavior of the ‘blanks’ described in detail in Section 6.2.2.

TEM images of the Pt NPs/N-CIC100 and Pt/TaO<sub>x</sub>N<sub>y</sub> /N-CIC100 composites are presented in Figure 6.12a and b, respectively. It is seen that both the TaO<sub>x</sub>N<sub>y</sub> NPs and the Pt NPs are well dispersed on the carbon support. Although the Pt NPs size is hard to determine at this magnification, the majority of the NPs are in the range of 2-3 nm. Further, the pore structure and the pore diameter (ca. 100 nm) of the N-CIC are seen to be preserved after the deposition of Pt (the ‘before Pt deposition’ images can be found in Figure 6.3 and Figure 6.4).

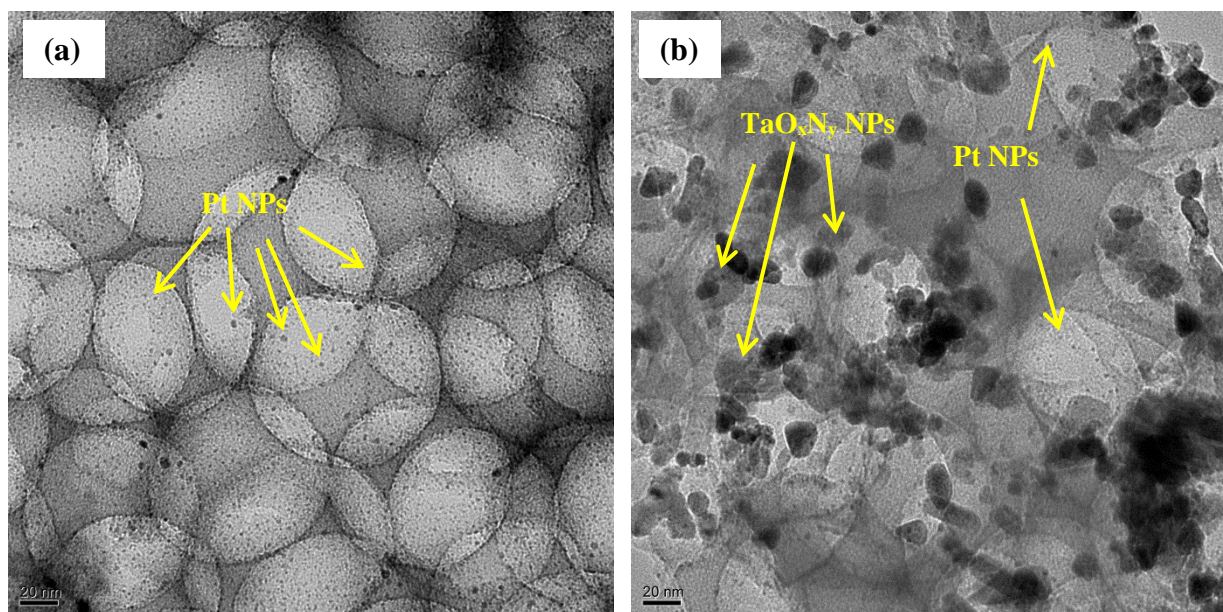


**Figure 6.12** TEM images of (a) Pt NPs/N-CIC100 and (b) Pt NPs/TaO<sub>x</sub>N<sub>y</sub> NPs/N-CIC100 composites.

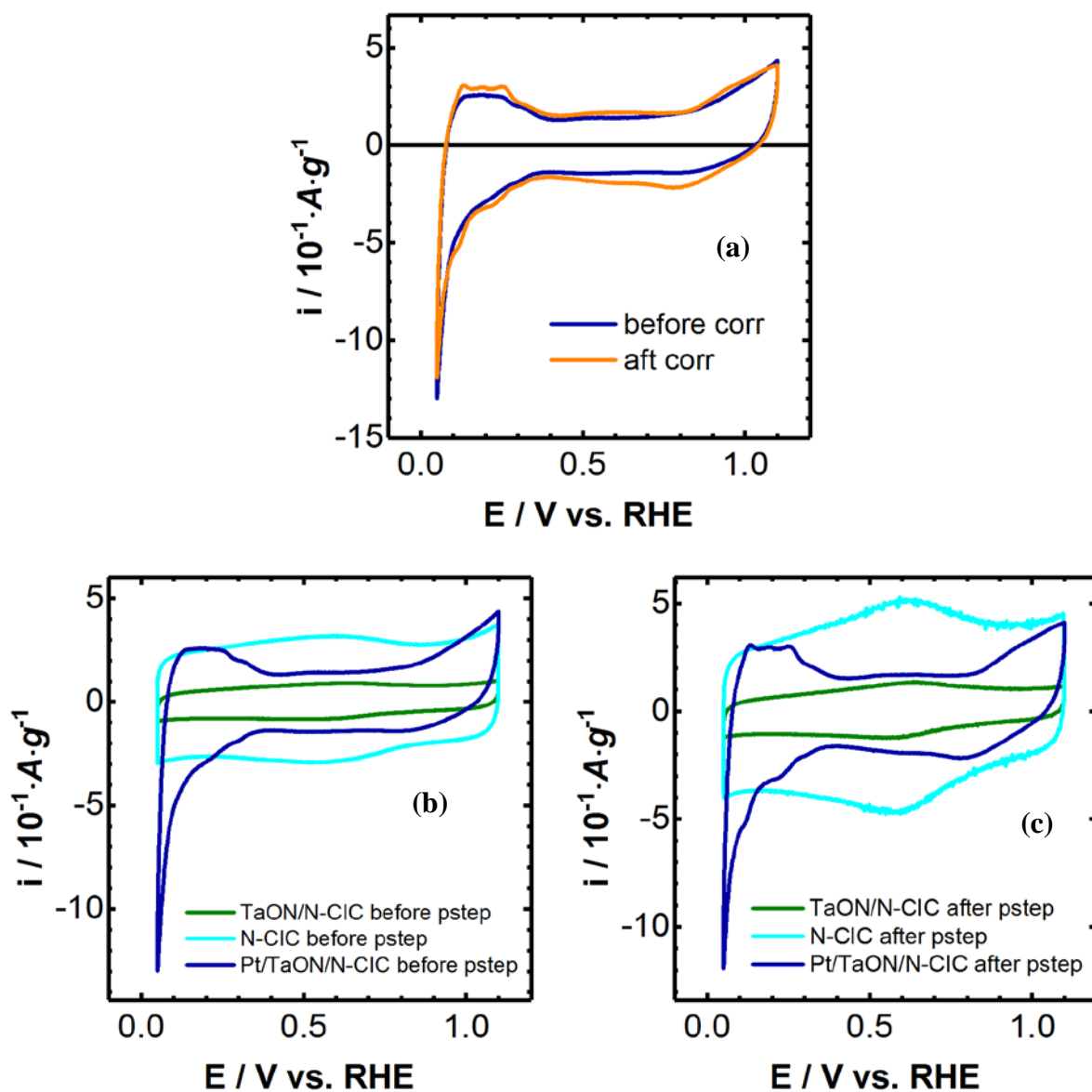
#### 6.2.4 Electrochemistry of Pt NPs/TaO<sub>x</sub>N<sub>y</sub> NPs/N-CIC100 material

Figure 6.13a shows the CVs of the Pt/TaO<sub>x</sub>N<sub>y</sub> /N-CIC100 composite, before and after the potentiostatic step ADT. These show the typical electrochemistry of Pt, including the HUPD features as well as Pt oxidation/PtO<sub>x</sub> reduction. Surprisingly, the Pt ECSA appears to have increased, rather than decreased, as a result of the potentiostatic experiments, while the double layer currents for Pt ca. 0.3 - 0.5 V vs. RHE have also increased, suggesting that the Pt NP surfaces were cleaned through the electrochemical treatment. The lack of loss of Pt ECSA is a good indication of the resistance of this support and the Pt NPs towards corrosion, Oswald ripening or agglomeration (Section 2.4.1). The presence of the Pt NPs and the good contact

between them and the TaO<sub>x</sub>N<sub>y</sub>/CIC support material is seen from the fact that the hydrogen evolution reaction (HER) is clearly being catalyzed by the Pt NPs, with the HER starting at ca. 0.1 V vs. RHE, as expected (Figure 6.13).

Unlike the discussion presented in Section 6.2.2.1, where the DL and PC charges of the materials (without Pt NPs), obtained from the CVs, were discussed, the PC and DL charges for the Pt NPs/TaO<sub>x</sub>N<sub>y</sub> NPs/N-CIC100 sample (Figure 6.13) were not analyzed here. This is because the Q/QH<sub>2</sub> redox reaction charges are partially masked by the electrochemistry associated with Pt oxide formation and reduction.

In terms of the active area of the Pt NPs, the anodic HUPD charge, after corrosion (Figure 6.13), is 170 C·g<sup>-1</sup><sub>Pt</sub>. If the Pt NPs are ca. 2 nm in diameter (based on the TEM images in Figure 6.12) and there is 20% w/w Pt present in the ink, then the surface area (ECSA) of the Pt NPs should be 120 cm<sup>2</sup>. However, based on the HUPD calculation and considering the theoretical 210 μC required for the HUPD reaction on 1 cm<sup>2</sup> real Pt area<sup>217</sup>, this gives a Pt NP SA of only 60 cm<sup>2</sup>. The discrepancy between the predicted and measured Pt ECSA argues that half of the Pt NPs are not in good electrical contact with the current collector to be addressed by the electrochemistry. They may be on TaO<sub>x</sub>N<sub>y</sub> NP surfaces or some are blocked.



**Figure 6.13** CVs before and after potentiostatic step ADT of (a) Pt NPs/TaO<sub>x</sub>N<sub>y</sub> NPs/N-CIC100, (b) and (c) Pt NPs/TaO<sub>x</sub>N<sub>y</sub> NPs/N-CIC100, TaO<sub>x</sub>N<sub>y</sub> NPs/N-CIC100 and N-CIC100, respectively. All CVs were obtained in 0.5 M H<sub>2</sub>SO<sub>4</sub> at 10 mV·s<sup>-1</sup>. Note: All currents and charges are normalized to the carbon weight.

It is also worth comparing the CVs of the Pt NPs/TaO<sub>x</sub>N<sub>y</sub> NPs/N-CIC100 sample with the CVs of its precursor material, TaO<sub>x</sub>N<sub>y</sub> NPs/N-CIC100, and the N-CIC100 control, as shown in Figure 6.13 b and c, before and after the potentiostatic step ADT, respectively. The CV for the TaO<sub>x</sub>N<sub>y</sub> NPs/N-CIC100 sample is the smallest of the three, likely as the TaO<sub>x</sub>N<sub>y</sub> NPs block some of the CIC100 surface and hence the full expression of the carbon electrochemistry is not seen. In contrast, the CV of the N-CIC100 material shows unhindered electrochemistry, giving the largest CV currents and hence the largest DL and PC charges. The CV of the Pt NPs/TaO<sub>x</sub>N<sub>y</sub> NPs/N-CIC100 material is between the other two in terms of the currents passed. Again, none of the CVs show any TaO<sub>x</sub>N<sub>y</sub> electrochemistry.

The data collected during the potentiostatic step ADT are shown in Figure 6.13. Both the anodic ( $q^+$ ) and corrosion charge ( $q^+ - q^-$ ) follow the same trends as noted in Figure 6.9 a and c for all other materials, without Pt, but the difference between the charges passed in the first and the second cycle ( $1 \text{ C}\cdot\text{g}^{-1}$ ) is smaller than was seen for the other materials ( $10\text{-}30 \text{ C}\cdot\text{g}^{-1}$  in Figure 6.9). Specifically, for the anodic and corrosion charge, these changed from 8 to  $7.2 \text{ C}\cdot\text{g}^{-1}$  and 6 to  $5.5 \text{ C}\cdot\text{g}^{-1}$ , respectively, with the plateau values (after the 5<sup>th</sup> cycle) being roughly  $7.1 \text{ C}\cdot\text{g}^{-1}$  (anodic) and  $5 \text{ C}\cdot\text{g}^{-1}$  (corrosion). This is different from the other materials that were discussed earlier, potentially attributed to interferences from Pt-based electrochemistry in the potential range between 0.8 V and 1.4 V. Further, the cathodic step charges are almost constant, as was also seen for the two other composite materials, TaO<sub>x</sub> NPs/CIC100 and TaO<sub>x</sub>N<sub>y</sub> NPs/N-CIC100. As mentioned earlier, the cathodic charge may not reflect the real DL charges as these charges are small and nearly constant in value.

When comparing the potentiostatic results obtained for TaO<sub>x</sub>N<sub>y</sub> NPs/N-CIC100, with and without Pt NPs, it is seen that corrosion charge in the first two cycles is less than for the TaO<sub>x</sub>N<sub>y</sub> NPs/N-CIC100 and N-100 materials (ca. 3 vs. 6 C·g<sup>-1</sup>). This observation is the same as seen for the anodic charge (q<sup>+</sup>). The cathodic charge, as usual, remains relatively constant throughout the 18 cycles and the magnitude is greater than that for the TaO<sub>x</sub> NPs/CIC100, but below what is obtained for the TaO<sub>x</sub>N<sub>y</sub> NPs/N-CIC100, showing the same trend as seen in the CV data (Figure 6.13a).

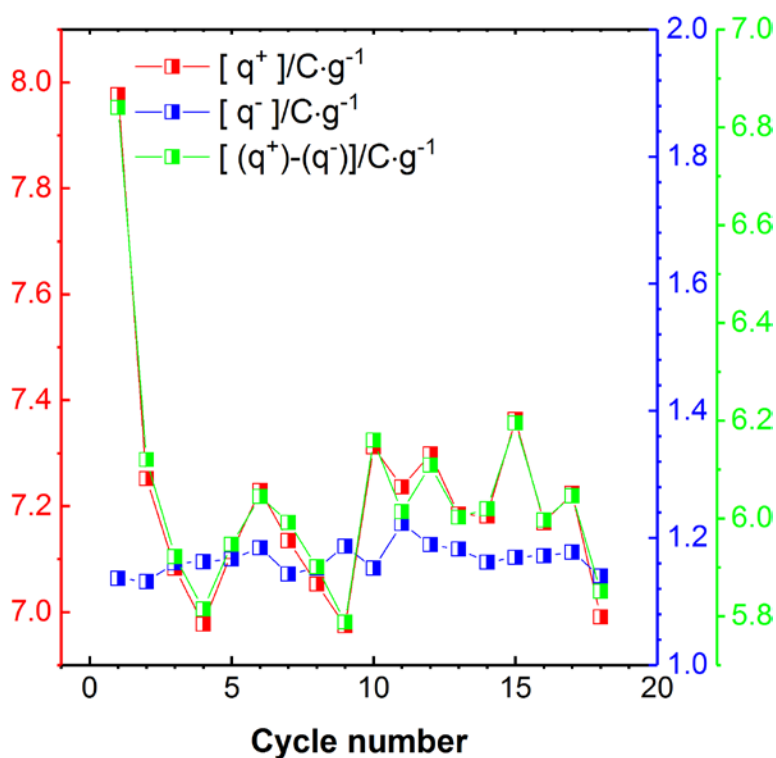


**Figure 6.14** Comparison of normalized corrosion charge (q<sup>+</sup>-q<sup>-</sup>, green), cathodic charge (q<sup>-</sup>, blue), and anodic charge (q<sup>+</sup>, red) for the Pt NPs/TaO<sub>x</sub>N<sub>y</sub> NPs/N-CIC100 material.

An interesting observation is that the CV data, before and after ADT, shows no corrosion or loss of Pt, but rather a higher Pt CV current, normally indicative of the cleaning of Pt NP surfaces. Since it is now known that corrosion occurs primarily in the first few potential steps within the ADT, the results for the TaO<sub>x</sub>N<sub>y</sub> NPs/N-CIC100 material with Pt NPs show less corrosion than the material without Pt. Based on these data, it is possible that the presence of the Pt NPs in the composite TaO<sub>x</sub>N<sub>y</sub> NPs/N-CIC100 sample does not serve to accelerate the corrosion of the support material.

### 6.3 Summary

In this chapter, the structure, morphology, composition and electrochemistry of a range of materials containing carbon powder (100 nm pore size colloid imprinted carbon, CIC100) mixed with TaO<sub>x</sub>N<sub>y</sub> NPs (nanoparticles) were studied. This was done in order to determine if TaO<sub>x</sub>N<sub>y</sub> would influence the corrosion of the CIC and also to determine whether the TaO<sub>x</sub>N<sub>y</sub> electrochemistry would be seen in CV (cyclic voltammetry) experiments when inter-connected within a conducting carbon matrix. Pt NPs were also used in some of this work, especially to track material stability under PEMFC conditions.

CIC100, with its ca. 100 nm pore diameter, was chosen to utilize any Pt NPs deposited inside the pores, as it has been reported in the literature that catalysts residing inside smaller pores are not always fully utilized. Starting with CIC100, the TaO<sub>x</sub> NPs/CIC100 material was made by solvolysis of Ta ethoxide on CIC100 powder and subsequent ammonolysis at 700 °C to obtain TaO<sub>x</sub>N<sub>y</sub> NPs/N-CIC100. Finally, Pt NPs were anchored on TaO<sub>x</sub>N<sub>y</sub> NPs/N-CIC100 by the incipient impregnation of Pt<sup>+6</sup> salt, followed by reduction in H<sub>2</sub> at 300 °C for 2 h. Between the

starting material of CIC100 and the formation of the Pt NPs/TaO<sub>x</sub>N<sub>y</sub> NPs/N-CIC100 product, several intermediates were produced, with all of them methodically characterized. Furthermore, benzyl alcohol treated CIC100 (Bn-CIC100) and nitrated CIC100 (N-CIC100) were synthesized and tested as control materials for comparison to the TaO<sub>x</sub> NPs/CIC100 and TaO<sub>x</sub>N<sub>y</sub> NPs/N-CIC100 materials, respectively.

All of the CICs retained their 100 nm pore size, as shown by TEM analysis. The XRD analysis of CIC100 and N-CIC100 show the typical graphite peak (002) at  $2\theta = 25^\circ$  and the nitriding process did not change this characteristic. The refinement of the XRD data for the TaO<sub>x</sub> NPs/CIC100 and TaO<sub>x</sub>N<sub>y</sub> NPs/N-CIC100 materials showed the presence of Ta<sub>2</sub>O<sub>5</sub> and a mixture of TaO<sub>x</sub>N<sub>y</sub> compounds, respectively. TEM images show that the TaO<sub>x</sub> NPs deposit as ‘a string of pearls’ on the CIC100 powder, but after nitriding, the TaO<sub>x</sub>N<sub>y</sub> NPs become separated and have a size of 10-20 nm. Also, it is seen that the Pt NPs were successfully deposited on the TaO<sub>x</sub>N<sub>y</sub> NPs/N-CIC100 material and that they were in the range of 2-3 nm.

After preparing inks from the materials under study, a modified DOE corrosion protocol or accelerated durability test (ADT) was employed to evaluate their corrosion stability. In this ADT, steady state CV ( $10 \text{ mV}\cdot\text{s}^{-1}$ ) between 0.05 -1.1 V vs. RHE was performed first, followed by a potentiostatic experiment, and finally CVs was collected again using the same conditions employed in the initial one. In the absence of Pt NPs and using the double layer and pseudocapacitive CV charge data, it was found that all of the materials are susceptible to corrosion, as also found in parallel studies in our group with just the CICs. Also, no evidence for the redox activity of the TaO<sub>x</sub>N<sub>y</sub> NPs was seen. However, the *i* vs. *t* data could not be rigorously

analyzed for the purpose of gauging the propensity to corrosion, as it was found that an oxidation product was clogging the catalyst layer pores, thus making the cathodic step charges anomalously small and making real ECSA corrections possible.

Notably, the Pt NPs/TaO<sub>x</sub>N<sub>y</sub> NPs/N-CIC100 material showed quite different results than the TaO<sub>x</sub>N<sub>y</sub> NPs/N-CIC100 (no Pt), where the Pt HUPD area was seen to have increased, rather than decreased, after the ADT. In a typical catalyst layer, it is seen that the HUPD charges decrease after ADT due to loss of ECSA of the Pt. The result obtained here is interpreted as indicative of the electrochemical cleaning of the Pt NPs, an encouraging result.

Overall, it appears that the CICs corrode at the same rate when examined on their own vs. when TaO<sub>x</sub> or TaO<sub>x</sub>N<sub>y</sub> NPs are present using the modified ADT developed here. The likely introduction of N into the CIC surface during nitriding also does not significantly influence the corrosion susceptibility. When Pt NPs are present, there does not seem to be significant Pt corrosion during the ADT process, although longer times of potential stepping should be used in the future.

## Chapter 7 : Hydrogen Oxidation Reaction at TaO<sub>x</sub>N<sub>y</sub> Nanotubes With/Without Pt Nanoparticles

### 7.1 Introduction

Chapters 5 and 6 were focused on the use of TaO<sub>x</sub>N<sub>y</sub> nanomaterials as an ORR (oxygen reduction reaction) catalyst or support material. It was shown that, as long as the potential was below ca. 0.8 V vs RHE, some ORR activity was seen, especially in the presence of Pt NPs. However, the activity remained relatively low, due to a combination of low conductivity of the TaO<sub>x</sub>N<sub>y</sub> materials and the assumed small fraction of the Pt NPs that was active when in contact with the TaO<sub>x</sub>N<sub>y</sub> support material. However, under the conditions of the hydrogen oxidation reaction (HOR), which occur at more negative potentials (0 V vs RHE equilibrium potential), the TaO<sub>x</sub>N<sub>y</sub> materials should be well conducting. In fact, it was shown in Chapter 4 that the hydrogen evolution reaction (HER) was quite active just on the TaO<sub>x</sub>N<sub>y</sub> nanotubular array alone, without Pt present.

Metal oxynitrides/nitrides are promising photoelectrocatalysts, especially for water oxidation, but they have yet to be tested for their activity towards the HOR.<sup>273-277</sup> One of the reasons oxynitrides/nitrides are used as photoelectrocatalyst is their colour. Oxynitrides of the noble-metal (Ti, Nb, Ta, Hf, etc.) nitrides are yellow to ruby red in color, where the nitrogen content determines the colour. When the nitrogen to oxygen ratio is 1:1, the colour is yellow and when the ratio is 1:~0, it would be ruby red.<sup>278</sup> In photochemistry, these colours are imperative as they absorb lower wavelength light, which is the major component of the solar spectrum.<sup>279</sup> As a

result, studies are underway to understand the OER and HER on these materials in the presence of photons. Furthermore, DFT calculations have shown that Ta nitride should be similar to Pt in terms of its HER activity.<sup>280</sup> By forming carbides and nitrides, the parent metal electronic properties are altered. Specifically, the d-band centre narrows, thus resembling the electronic properties of the Group 8-10 transition metals, which are highly active for electrocatalysis.<sup>102, 281-282</sup>

To the author's knowledge, this is first time that TaO<sub>x</sub>N<sub>y</sub> NTs, with or without Pt NPs present, were tested for their activity towards the HOR in an acidic medium for potential application in PEMFCs. Since there is no precedent about the catalytic activity or support characteristics of these materials, the use of metal carbides<sup>282-284</sup> and oxides<sup>126</sup> for the same purpose is overviewed here. Metal oxides, carbides, etc. are relevant in the anode of a PEMFC because they can reduce the effect of CO poisoning of Pt surfaces. CO is a contaminant in H<sub>2</sub> fuel and even a very small amount of CO can block the Pt surface, which, in turn, lowers the catalytic activity. Several factors, such as temperature, relative humidity, fuel/oxidant pressure, catalyst loading, fuel circulation method, etc. are all relevant in the CO poisoning of Pt under real operating conditions of a PEMFC.<sup>284</sup>

Based on the available data, the ISO and SAE have set the tolerance level for CO in H<sub>2</sub> at 0.2 ppm for automobile PEMFC applications, although it has been proposed to change this limit to 0.5 ppm.<sup>285</sup> These low values of the tolerable concentration of CO demonstrate how important the purity of the H<sub>2</sub> fuel is. However, removing the CO contaminant is not easy, especially from reformat H<sub>2</sub> fuel. Therefore, mitigating the damage done by CO is crucial, e.g., by finding an

alternative to Pt that would help to weaken the bond between CO and Pt. Metal oxides and carbides aid in this when they are used as a catalyst support or as an alternative catalyst for the HOR. The predominantly accepted mechanism of enhancing the tolerance of CO for the Pt/WC system is that the reduction of the W ion at cathodic potentials helps to attach –OH groups on the WC surface, with the –OH groups helping to oxidize strongly adsorbed CO on the Pt surface to CO<sub>2</sub>.<sup>286</sup> A similar mechanism can be expected from the TaO<sub>x</sub>N<sub>y</sub> NTs, as they too switch their redox state at cathodic potentials during the Ta<sup>4+/5+</sup> reaction (Reaction 4.3). This process also involves proton insertion and de-insertion, which introduces –OH groups on the TaO<sub>x</sub>N<sub>y</sub> surface.

Another point to note is that non-carbon supports, such as metal nitrides/oxynitrides, carbides, etc., typically have a low conductivity at high potentials, switching to conductive state at lower applied potentials.<sup>25</sup> If this redox switching potential is more negative than the thermodynamic potential of the ORR, then the support may help to protect the cathode catalyst layer from carbon corrosion (COR) (Section 2.5.3). Further, since these materials are conductive at the potential at which the HOR occurs, the resistance imposed by the support for electron transport is lowered. Further, in Section 2.5.3, it was discussed that using these types of materials as an anode support to protect carbon at the cathode from electro-oxidation or corrosion (COR) is a new concept. To the authors' knowledge, there is only one paper published on this topic, and in that work, a binary metal oxide (NbTiO<sub>2</sub>) was the support used for the Pt NPs.<sup>111</sup> Also, in the same section (Chapter 2, Section 2.5.3), it was pointed out that the HOR can be selectively performed in the presence of O<sub>2</sub> by using a modified Pt surface or the hydrogenase enzyme.<sup>110</sup>

Typically, the catalytic properties of a material can be modified by changing its chemical composition and morphology. Another way to enhance the catalytic performance is to add a co-catalyst that is active towards the reaction under study. Thus, in this work, instead of exploring how to improve the catalytic activity of  $\text{TaO}_x\text{N}_y$  for the HOR, a co-catalyst was added. For the HOR, Pt is the best catalyst and therefore the Pt NPs/ $\text{TaO}_x\text{N}_y$  NTs material was tested for its HOR activity, similar to what was done in the ORR study in Section 5.2.2.

It is shown that the Pt NPs/ $\text{TaO}_x\text{N}_y$  NTs behave very similarly to Pt/C at potentials positive of 0 V, although they are less active than Pt/C. Further improvements are thus needed to enhance the catalytic activity, as proposed as future work (Chapter 8). Further, from a Koutecky-Levich plot, it is seen that the HOR is controlled by both kinetics and diffusion in the potential region of 0.1 to 0.3 V vs. RHE.

## **7.2 Results and Discussion**

### **7.2.1 Structure, Morphology and Compositional Characterization of $\text{TaO}_x\text{N}_y$ NTs with and without Pt NPs**

This part of the work was carried out with ca. 1  $\mu\text{m}$  long  $\text{TaO}_x\text{N}_y$  NTs that were synthesized according to the method described in Sections 3.1 and 3.2, with the Pt NPs deposited on the NTs as per the procedure used in Section 3.3. The choice of the deposition method of Pt was described in Section 5.2.1, while the structure, morphology and composition of these materials were discussed in Sections 4.2.1 and 5.2.1.

### 7.2.2 HOR at TaO<sub>x</sub>N<sub>y</sub> NTs with and without Pt NPs

Figure 7.1 shows the hydrogen oxidation reaction (HOR) activity of the TaO<sub>x</sub>N<sub>y</sub> NTs (a) and the Pt NPs/TaO<sub>x</sub>N<sub>y</sub> NTs composite (b), as seen in cyclic voltammograms (CVs) extended to negative potentials. These CVs were obtained in quiescent 0.5 M H<sub>2</sub>SO<sub>4</sub> that had been saturated with N<sub>2</sub> gas and H<sub>2</sub> gas sequentially. The CVs (Figure 7.1a) show that the TaO<sub>x</sub>N<sub>y</sub> NTs alone are not a very promising catalyst for the HOR because both CVs (in H<sub>2</sub>- and N<sub>2</sub>-saturated conditions) are almost the same, although slightly more anodic current flows for the HOR at the TaO<sub>x</sub>N<sub>y</sub> material in H<sub>2</sub>-saturated conditions. When the TaO<sub>x</sub>N<sub>y</sub> NTs are non-conducting (ca. > 0.8 V vs. RHE), no HOR currents can be seen in the CVs (Figure 7.1a) in both gas environments. This may indicate that the NTs intrinsic kinetics of the HOR on TaO<sub>x</sub>N<sub>y</sub> is poor.

Figure 7.1b shows the CV of the Pt NPs/TaO<sub>x</sub>N<sub>y</sub> NTs composite in N<sub>2</sub>-saturated 0.5 M sulfuric acid solution (Blue), H<sub>2</sub>-saturated sulfuric acid (Red), and after subtraction of these two CVs (Green). In the N<sub>2</sub>-saturated electrolyte, the effect of the Pt NPs can clearly be seen, as significantly more current flows due to the Ta<sup>4+/5+</sup> redox chemistry enhanced by the Pt NPs, while in H<sub>2</sub>-saturated solutions, more oxidation current is seen to flow, due to the HOR. The subtracted CV in Figure 7.1b shows the net anodic current flow due to the HOR.

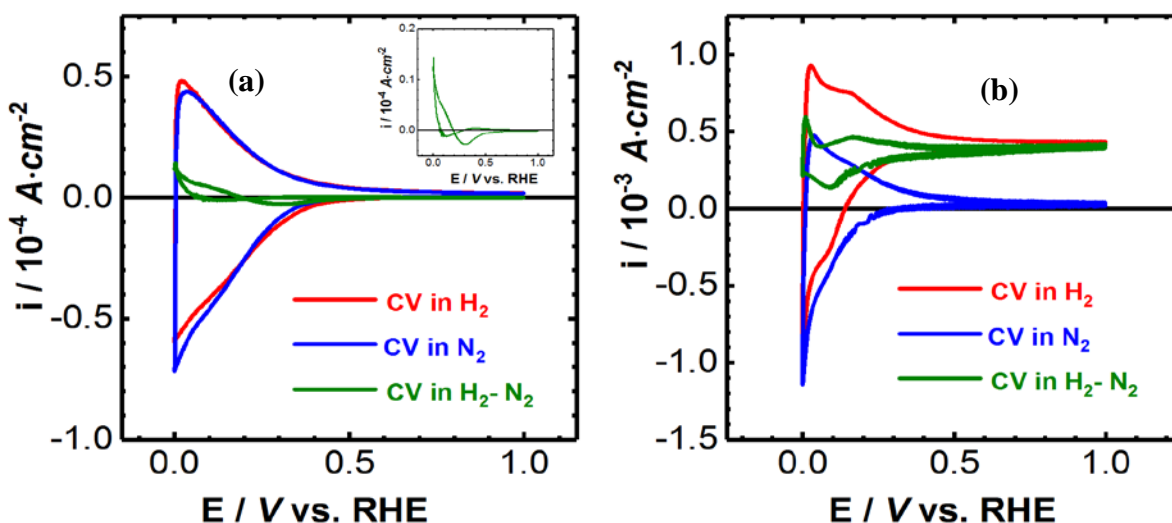


**Figure 7.1** CVs of (a) TaO<sub>x</sub>N<sub>y</sub> NTs and (b) Pt NPs/TaO<sub>x</sub>N<sub>y</sub> NTs composite at 50 mV·s<sup>-1</sup> obtained in quiescent 0.5 M H<sub>2</sub>SO<sub>4</sub>. The red CVs were obtained in H<sub>2</sub>-saturated acid solution and the blue CVs were in N<sub>2</sub>-saturated solution. The green CVs represent the subtraction of those two CVs. The inset of (a) shows subtracted CV of TaO<sub>x</sub>N<sub>y</sub> NTs.

Since the electrochemistry of the Pt NPs/TaO<sub>x</sub>N<sub>y</sub> NT materials in N<sub>2</sub>-saturated electrolyte is extensively discussed in Section 5.2.2.2, it will not be covered again here. However, briefly, at < 0.8 V vs. RHE, Ta<sup>4+/5+</sup> redox currents flow in the system, with some contribution from the onset of the HER at near 0 V (Figure 7.1b). The steady-state anodic current is indicating of the occurrence of the HOR. Notably, the presence of the Pt NPs does not cause any changes in the DL charging seen for the TaO<sub>x</sub>N<sub>y</sub> NTs. (Figure 5.6b). Generally, double layer charging current of an electrocatalyst layer is influenced by several factors, including the nature of the material, the surface area of the electrode, scan rate, catalyst loading, etc. Therefore, it is somewhat surprising that the Pt NPs do not contribute additional charging current to the CV in Figure 7.1b.

Another unexpected observation is that the HOR process continues on at  $> 0.8$  V vs. RHE, conditions under which the  $\text{TaO}_x\text{N}_y$  NTs should be non-conductive. This may be attributed to some form of hydrogen spillover phenomenon. It is known that valve metal oxides ( $\text{TiO}_2$ ,  $\text{WO}_3$ ,  $\text{Ta}_2\text{O}_5$ , etc.) participate in hydrogen spillover, where H atom transport occurs from an H atom-rich surface to an H atom-deficient surface in the presence of H-adsorbing metals. Otherwise, these surfaces do not participate in this process. For example, adsorbed H atoms on metal particles, such as Pt, move to the support, e.g.,  $\text{TiO}_2$ . If Pt metal is not present, this process will not take place on  $\text{TiO}_2$ .<sup>287</sup>

Typically, hydrogen spillover is seen only on valve metal oxides in their reduced state. However, on a non-reducible surface, such as  $\text{Al}_2\text{O}_3$  or fully oxidized valve metal oxides, it can also be observed, but with much lower efficiency.<sup>288</sup> Karim et. al. explained H atom migration from Pt metal to the  $\text{Al}_2\text{O}_3$  support, but without reducing the  $\text{Al}^{3+}$  site. This process is mediated by the 3-coordinated Al ions on the surface of the crystal lattice and the water molecules around them. Further, Karim et al mentioned that only the Al atoms that are in contact with Pt participate in this process. However, when valve metal oxides are in their reduced state, this process can occur not only very close to the Pt sites but also to metal oxide sites that are quite far away from the Pt.

It is possible that a similar explanation can be applied to the results seen in Figure 7.1b. In the anodic scan (from ca. 0.05 to 1.0 V in  $\text{H}_2$ -saturated electrolyte),  $\text{Ta}^{4+}$  is oxidized to  $\text{Ta}^{5+}$ , while the Pt NP surfaces are being enriched with adsorbed H atoms. It could thus be envisaged that the H atoms on the Pt NPs could migrate to the support surface ( $\text{TaO}_x\text{N}_y$  NTs), where  $\text{Ta}^{5+}$

can be reduced to Ta<sup>4+</sup>, as in the case of the normal spillover mechanism. This process could be mediated by water, which would serve to facilitate the removal of the proton from the TaO<sub>x</sub>N<sub>y</sub> NTs. To retain electronic conductivity, it is suggested that the Ta sites near the Pt NPs are stabilized in their Ta<sup>4+</sup> state by the H<sub>2</sub> gas, thus allowing these sites to participate in the HOR process.

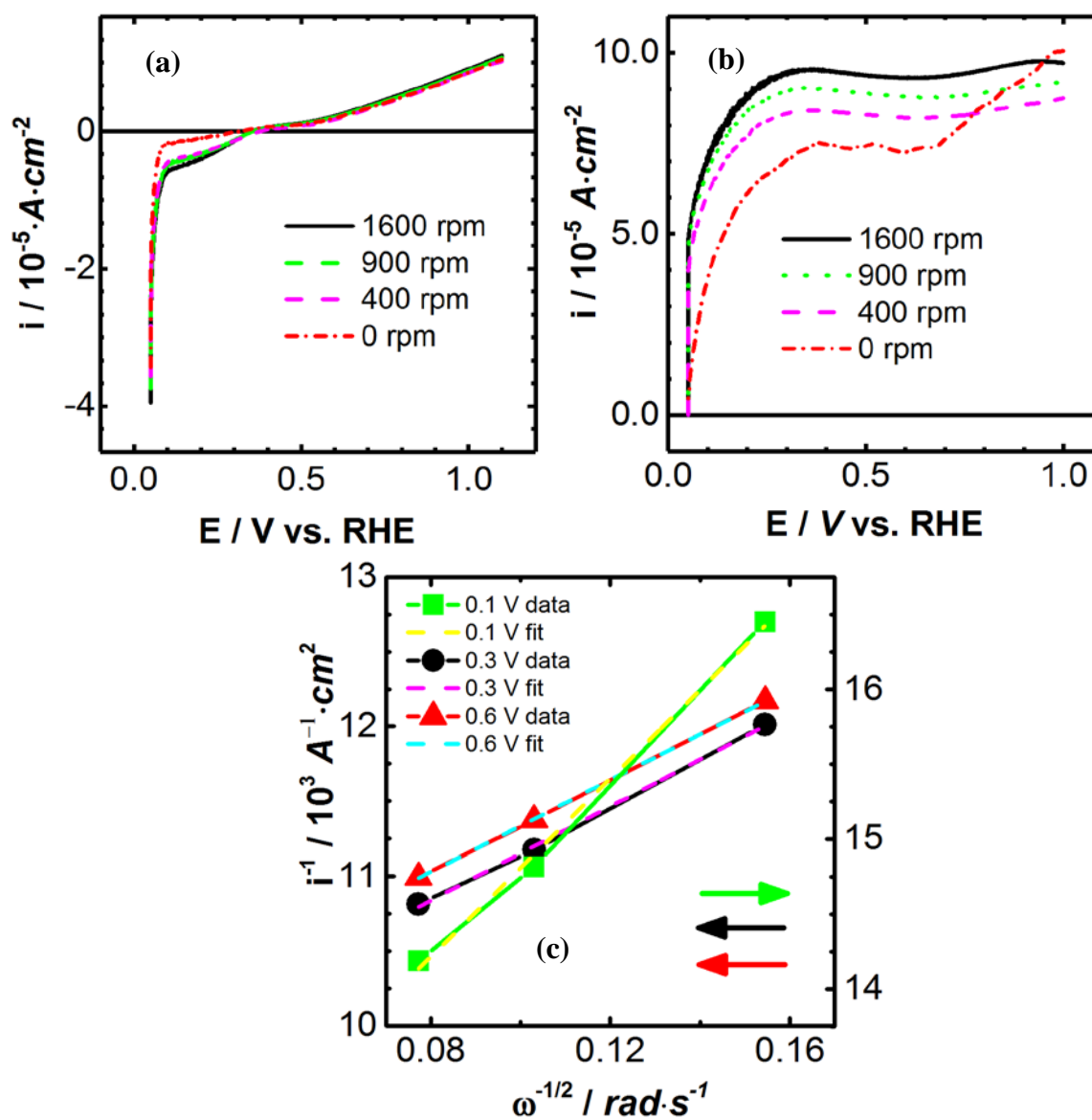
However, it is not clear why the Pt NPs/TaO<sub>x</sub>N<sub>y</sub> NTs material is active towards the HOR at these positive potentials (> 0.8 V vs RHE), but is much less for the ORR (Section 5.2.2.2). To evaluate whether this material has selectivity towards the oxidation reactions, methanol and formic acid oxidation was examined, but no oxidation activity was observed. It is therefore proposed once again that the H<sub>2</sub> environment serves to keep some Ta sites in the 4+ state, thus extending the potential range of conductivity positively and allowing the HOR to occur. Notably, Suryamas et. al. discussed the HOR activity of Pt/SnO<sub>2</sub> catalysts at higher potentials, but no explanation for this was provided.<sup>128</sup>

Figure 7.2 shows the polarization curves obtained for the Pt NPs/TaO<sub>x</sub>N<sub>y</sub> NTs composite electrode in N<sub>2</sub>-saturated 0.5 M H<sub>2</sub>SO<sub>4</sub> (Figure 7.2a) and in H<sub>2</sub>-saturated (Figure 7.2b) environments using a Rotating Disk Electrode (RDE) configuration. In the deaerated solution, it is seen that the anodic currents are rotation rate independent, consistent with the absence of any diffusion controlled reactions. At cathodic potentials (< 0.2 V), small cathodic currents that are electrode rotation dependent are seen. This is likely due to the occurrence of the ORR, as during rotation, some air could have been drawn into the cell solution via the gap between the WE

shroud and the ground glass joint of the WE inlet. Some tilt in the CV is also seen in Figure 7.2a, likely due to the imperfections in the RDE assembly, as explained in Section 5.2.2.2.

In the H<sub>2</sub>-saturated environment, the anodic currents rise at just positive of 0 V (Figure 7.2b), then plateauing. This indicates that the HOR kinetics are `fast` at the Pt NPs deposited on the TaO<sub>x</sub>N<sub>y</sub> NTs and hence a Butler-Volmer region (activation controlled kinetics) is not seen in the CVs.

The Gasteiger group explains that it is a challenge to experimentally extract the HOR/HER kinetic parameters obtained at Pt/C electrocatalysts in an acidic medium, as the reaction is extremely fast.<sup>289</sup> Consequently, there is ambiguity in the literature on reporting the values for the exchange current density ( $i_0$ ) and Tafel slope under these conditions. For example, the exchange current density ranges from 1 mA·cm<sup>2</sup><sub>Pt</sub> to 50 mA·cm<sup>2</sup><sub>Pt</sub>, and in a PEMFC, it is 400 ± 200 mA·cm<sup>2</sup><sub>Pt</sub>.<sup>290-295</sup> Further, it is indicated that, when the diffusion limited current is 10x smaller than the exchange current density, experimental quantification of the exchange current density is unreasonable.<sup>289</sup>



**Figure 7.2** CVs (anodic scan only) of Pt NPs/TaO<sub>x</sub>N<sub>y</sub> NTs obtained at 10 mV·s<sup>-1</sup> in (a) N<sub>2</sub>-saturated purged 0.5 M H<sub>2</sub>SO<sub>4</sub> and (b) H<sub>2</sub>-saturated purged 0.5 M H<sub>2</sub>SO<sub>4</sub>, and (c) the relevant Koutecky-Levich plots at various potentials for the data in the (b).

Nonetheless, here, the HOR data obtained at the Pt NPs/TaO<sub>x</sub>N<sub>y</sub> NTs are evaluated, because all previous work was reported for Pt/C catalysts, which may have very different kinetics. Figure 7.2b shows that the diffusion controlled HOR plateau is reached at ca. 0.3 V vs RHE, whereas for the state-of-the-art catalyst, Pt/C, it is reached already at ca. < 0.05 V vs. RHE.<sup>289</sup> The higher overpotential seen in the present work ( $\eta_{\text{diff}}$ ) may be attributed to the lower conductivity of the TaO<sub>x</sub>N<sub>y</sub> NT supports vs. carbon, as this will impose additional resistance to the flow of the current, hence giving more sluggish HOR kinetics. This may also indicate that only some of the Pt NPs are electroactive, as was also shown to be the case for the ORR in Chapters 5.

In the diffusion controlled region, i.e., between 0.3 V and 1.1 V vs RHE, the limiting current ( $i_{\text{lim}}$ ) increases as the electrode rotation speed is increased (Figure 7.2b). According to the Koutecky-Levich (KL) equation, a plot of the inverse of the current ( $1/i$ ) vs. the inverse of the rotation speed ( $\omega^{1/2}$ ) should go through the origin if the current is controlled by diffusion only. However, in the present work (Figure 7.2c), this is not observed at any potentials (0.1, 0.3, and 0.6 V vs. RHE). Rather, a mixture of kinetics is likely being seen, perhaps also due to sluggish diffusion of H<sub>2</sub> into and between the TaO<sub>x</sub>N<sub>y</sub> NTs. Notably, the HOR diffusion controlled currents continue to flow, even at > ca. 0.8 V, where the TaO<sub>x</sub>N<sub>y</sub> nanotubular support should be non-conducting (Chap 4, Section 4.2.2) and only charging currents (ca. nA) should be observed. This may be because of the H spill over phenomenon explained earlier.

Overall, the CV data obtained with an RDE coated with the Pt NPs/TaO<sub>x</sub>N<sub>y</sub> NTs do resemble what is obtained for Pt/C, although the kinetics is quite a bit slower. This suggests that

further optimization of the Pt NPs/TaO<sub>x</sub>N<sub>y</sub> NTs material could lead to a very promising HOR system.

### 7.3 Summary

1 μm long TaO<sub>x</sub>N<sub>y</sub> NTs were produced and Pt NPs (3-5 nm) were deposited on the NTs by using the incipient impregnation method, similar to what was done for the ORR studies described in Chapters 4 and 5. The Pt NPs/TaO<sub>x</sub>N<sub>y</sub> NTs material was then tested for its activity towards the hydrogen oxidation reaction (HOR) in both N<sub>2</sub>- and H<sub>2</sub>-saturated 0.5 M H<sub>2</sub>SO<sub>4</sub> solution.

The quiescent CV data, as well as the data collected using a rotating disc electrode (RDE), showed that the TaO<sub>x</sub>N<sub>y</sub> NTs themselves are essentially inactive towards the HOR. However, in the presence of Pt, the Pt NPs/TaO<sub>x</sub>N<sub>y</sub> NTs material showed HOR activity at potentials positive of 0 V at all rotation rates, exhibiting the expected increase in plateau currents as the rotation rate is increased. Compared to conventional Pt/C catalysts, the diffusion controlled currents are reached at ca. 0.05 V vs. RHE, whereas for the Pt NPs/ TaO<sub>x</sub>N<sub>y</sub> NTs, this is reached at ca. 0.3 V, thus showing that the kinetics are slower than at Pt/C. Unexpectedly, the Pt NPs/TaO<sub>x</sub>N<sub>y</sub> materials showed HOR activity even in the region (> 0.8 V vs. RHE) where the TaO<sub>x</sub>N<sub>y</sub> should be electrochemically inactive. This has been attributed to the possibility of a hydrogen spillover mechanism, with the TaO<sub>x</sub>N<sub>y</sub> material retaining some Ta<sup>4+</sup> sites even at high potentials due to the reducing effect of the H<sub>2</sub> environment.

Overall, this shows that the TaO<sub>x</sub>N<sub>y</sub> NTs could potentially serve as a support material for Pt NPs in order to catalyze the HOR. However, further optimization is needed in order to increase the HOR activity, and the benefits and challenges of using the NT array vs TaO<sub>x</sub>N<sub>y</sub> nanopowders would also have to be elucidated.

## Chapter 8 Conclusions and Future Work

### 8.1 Conclusions

The main focus of this thesis was to evaluate the suitability of TaO<sub>x</sub>N<sub>y</sub> nanomaterials for use in PEMFC (proton exchange membrane fuel cell) applications. TaO<sub>x</sub>N<sub>y</sub> was explored as an alternative catalyst support material to carbon and also as in comparison to Pt for both the hydrogen oxidation reaction (HOR) and oxygen reduction reaction (ORR). The need to identify new materials for PEMFCs is due to the high cost of Pt and durability challenges for both Pt and carbon, which is impeding the full scale commercialization PEMFCs. TaO<sub>x</sub>N<sub>y</sub> was chosen for this purpose as the literature has been turning towards metal oxides, nitrides and carbides for this purpose and as our group already had momentum in the area of Ta-based nanomaterials research, especially Ta oxide nanotubes (NTs).

The main discoveries made in this thesis work are:

#### **8.1.1 Physiochemical properties of TaO<sub>x</sub>N<sub>y</sub> NTs in comparison to the precursor Ta<sub>2</sub>O<sub>5</sub> NTs**

Although the photoelectrochemistry of TaO<sub>x</sub>N<sub>y</sub> has attracted attention lately, their other physiochemical properties are less well known. Because the TaO<sub>x</sub>N<sub>y</sub> NTs are produced by anodization of Ta followed by nitriding, they remain attached to the underlying Ta metal, which means there is no necessity for another current collector. It was shown that TaO<sub>x</sub>N<sub>y</sub> NTs up to 4 μm in length and having regularly spaced 25 nm diameter holes along the NT walls are redox active in a range of aqueous solutions [0.5 M H<sub>2</sub>SO<sub>4</sub>, 0.2 M phosphate buffer (PB) and 0.5 M KOH] at < 0.6 V vs. RHE, believed to be related to Ta<sup>4+/5+</sup> redox chemistry with proton

insertion/de-insertion, thus making the redox chemistry pH dependent. At  $> 0.6$  V, the NTs shows only double layer charging and hence are redox inactive. These redox switching properties are also seen in organic solvents. Interestingly, it was found that only a small fraction of the Ta ions present in the NT structure is electrochemically active. The reason for this remains unknown as yet.

TaO<sub>x</sub>N<sub>y</sub> is an n-type semiconductor due to the anion vacancies in the crystal structure, as shown by Mott-Shottky analysis in this work (band gap of 2.26 eV) Further, to the author's knowledge, this is the first time the donor density within TaO<sub>x</sub>N<sub>y</sub> ( $5.7 \times 10^{21}$  cm<sup>-3</sup> at 25 kHz) has been reported, on-par with the donor density for N-doped TiO<sub>2</sub> NTs. This large a donor density is valuable information if this material were to be used in photoelectrochemistry.

The TaO<sub>x</sub>N<sub>y</sub> NTs also show electrochromism, a desired property for sensor applications. The yellow-orange color of the TaO<sub>x</sub>N<sub>y</sub> NTs changes to black-blue at more cathodic potentials and the intensity of the colour is related to the proton concentration in the solution. In neutral phosphate solutions, an intense black-blue colour is observed at ca. -0.4 V vs. RHE, while in 0.5 M H<sub>2</sub>SO<sub>4</sub>, it is seen already at ca. -0.1 V.

### **8.1.2 TaO<sub>x</sub>N<sub>y</sub> NTs (with and without Pt NPs) as ORR and HOR catalysts and as catalyst support materials**

Consistent with the fact that TaO<sub>x</sub>N<sub>y</sub> NTs are not conductive at the potential where the ORR occurs, but have little catalytic ORR activity. At the same time, they are very resistant to corrosion, even when the potential is extended to 1.4 V vs. RHE. Therefore, they were examined primarily as catalyst supports, by the deposition of Pt NPs on their surfaces. Using TaO<sub>x</sub>N<sub>y</sub> as a

catalyst support material could thus be useful for niche applications where the support stability is of utmost importance.

As a proof of concept, experiments were first carried out by depositing Pt NPs on a thin TaO<sub>x</sub>N<sub>y</sub> compact layer (CL), giving the normal Pt electrochemical signature and good ORR activity (61 mV·decade<sup>-1</sup>). Thus, the quality of the TaO<sub>x</sub>N<sub>y</sub>/Pt interface was deemed to be good. However, it was also found that not all of the Pt NPs on the TaO<sub>x</sub>N<sub>y</sub> CL were electrochemically addressable. This observation could be due to the presence of a Magnèli type TaO<sub>x</sub>N<sub>y</sub> phase close to the Pt NPs that are active, although why this phase did not permeate throughout the CL is not clear.

When the Pt NPs/TaO<sub>x</sub>N<sub>y</sub> NTs (one micron) material was examined, the Pt electrochemistry was absent, although reasonable ORR activity was observed. However, several features in the electrochemistry may be indirectly revealing the presence of the Pt NPs, one being the enhanced current in the Pt HUPD region (0.1-0.3 V vs. RHE). Coincidentally, these HUPD peaks appears in the Ta<sup>4+/5+</sup> redox chemistry region and therefore the HUPD peaks may be masked by the Ta redox chemistry. The second indirect evidence of the presence of Pt is the clear ORR activity seen in O<sub>2</sub>-saturated solution, showing the onset of the ORR at 0.8 V vs. RHE and a Tafel slope of 105 mV·decade<sup>-1</sup>. However, this onset potential is still quite low, compared to Pt/C catalysts, and may be due to the low conductivity of TaO<sub>x</sub>N<sub>y</sub> at > 0.8 V or perhaps the porous structure of the TaO<sub>x</sub>N<sub>y</sub> NTs that negatively influences the utilization of the Pt NPs present in the NTs. When shorter NTs were examined (0.3 microns), the Pt HUPD region could be clearly seen, although the ORR activity was hardly different than seen for the 1 micron NTs

(Tafel slope  $105 \text{ mV}\cdot\text{decade}^{-1}$ ). Also, from the scan rate work and using the Randels-Sevcik equation, it can be said that the ORR has taken a  $2e$  pathway at the Pt NPs/ $\text{TaO}_x\text{N}_y$  NT catalyst.

Based on the knowledge obtained regarding the ORR at the Pt NPs/ $\text{TaO}_x\text{N}_y$  NTs materials, revealing the need for good conductivity of the  $\text{TaO}_x\text{N}_y$  support, efforts were made to examine the hydrogen oxidation reaction (HOR). As discussed earlier,  $\text{TaO}_x\text{N}_y$  NTs are redox active and thus conducting at  $< 0.6 \text{ V vs. RHE}$ . However, with Pt NPs present, this switching potential moved to  $0.8 \text{ V vs. RHE}$ . When examined for the HOR activity in  $\text{H}_2$ -saturated  $0.5 \text{ M H}_2\text{SO}_4$  solution, the activity is quite reasonable, although not on par with Pt/C catalysts. One interesting finding in the present work was that HOR current flows through the system even at potentials where  $\text{TaO}_x\text{N}_y$  should not be conductive, perhaps indicating that the  $\text{H}_2$  environment serves to keep some of the Ta sites in the  $+4$  state, even at high potentials, thus providing the needed redox conductivity.

Based on these findings, it can be concluded that the Pt NPs/ $\text{TaO}_x\text{N}_y$  NTs material is a potential candidate as a HOR catalyst, where the  $\text{TaO}_x\text{N}_y$  NTs would serve as the catalyst support layer. On the other hand, the ORR studies suggest that the conductivity of the  $\text{TaO}_x\text{N}_y$  NTs needs to be improved further.

### **8.1.3 $\text{TaO}_x\text{N}_y$ mixed with carbon nanomaterials**

It was determined in this thesis work that limitations in the  $\text{TaO}_x\text{N}_y$  conductivity may be one reason that it is not very active as a catalyst, especially for the ORR. Therefore, efforts were made to alleviate this problem by mixing it with carbon, specifically a colloid imprinted carbon

(CIC) that contained pores large enough to deposit Pt NPs within them, CIC100 (100 nm pores). CIC 100 was synthesized from Mesophase Pitch and 100 nm diameter silica and then treated with Ta ethoxide to anchor the TaO<sub>x</sub> NPS on its surface, presumably via its oxygenated functional groups. This bottom-up method of mixing carbon with alternative catalyst material was then followed by nitriding and Pt deposition. Their corrosion stability was evaluated by using an accelerated durability test involving potentiostatic steps, preceded and followed by CV cycling.

All of the CV electrochemistry appeared to be typical of that of the CIC100, showing the typical broad double layer charging region and the pseudocapacitive peaks of carbon, but no sign of TaO<sub>x</sub>N<sub>y</sub> electrochemistry, perhaps due to an insufficiently good interfacial contact between these two phases. The ADT data showed that the carbon phase corroded in the normal way, and even some doping of the CIC with N did not change the corrosion stability of the CIC material. However, the TaO<sub>x</sub>N<sub>y</sub> NPs did not seem to be attacked, consistent with the earlier results with TaO<sub>x</sub>N<sub>y</sub> alone, and the CVs after the ADT showed improved Pt HUPD signals, rather than a loss, suggesting that they also were not corroded. What was learned from this work is that the TaO<sub>x</sub>N<sub>y</sub> NPs did not influence the corrosion stability of the CICs, even by potentially blocking some of the CIC active sites. While the presence of carbon may have increased the conductivity of the catalyst vs. TaO<sub>x</sub>N<sub>y</sub> alone, as was intended, there was insufficient time left to carry out ORR work with these materials.

One other interesting discovery of this work was the recognition that the cathodic charge passed in the potential step during ADT did not track the real carbon surface area, as had been

expected from previous work with the CIC materials. This is because some sort of passivating layer seems to develop on the carbon surface in the potential steps to 1.4 V. During the negative CV scan to 0 V after the ADT, this layer (oxide-based) is reduced, thus exposing the full new CIC surface area after corrosion. This means that it is difficult to correct the  $i$  vs.  $t$  data during the stepping protocol for the real surface area, with further work needed on this, as indicated in Section 8.2 below.

## 8.2 Suggestions for Future Work

Although this thesis provided a systematic study of an alternative material for PEMFC use, there are still many directions that could be taken, as suggested here.

- Throughout the thesis work,  $\text{TaO}_x\text{N}_y$  was the only form of this compound used so as to keep one variable unchanged. Some other stoichiometries were also prepared by changing the nitrating time, but these results were not included in the thesis as they were not properly characterized. Therefore, further work on other  $\text{TaO}_x\text{N}_y$  stoichiometries, including the fully nitrated  $\text{Ta}_3\text{N}_5$  material, should be studied for their structure and electrochemistry. Also, a method needs to be developed to obtain the pure form of a particular stoichiometry, especially in nanotubular form. These types of investigations would also have an impact on the photoelectrochemical properties of the  $\text{TaO}_x\text{N}_y$  NTs.

- An interesting property observed in the Chapter 4 is the electrochromism of the  $\text{TaO}_x\text{N}_y$  NT material. It is understood that proton concentration and applied potential have an impact on the colour change. However, the nanotubular arrays were not spectroelectrochemically

characterized because of the difficulty of fabrication of the spectroelectrochemical cell for the TaO<sub>x</sub>N<sub>y</sub> NTs. Thus, a study of the electrochromism of TaO<sub>x</sub>N<sub>y</sub> should be carried also, also for sensor applications.

- Four different lengths of TaO<sub>x</sub>N<sub>y</sub> NTs were studied in Chapter 4, and based on the data, it was found that the stable maximum length was after 5 min of anodization time and thus only 2.5 min and 5 min NTs were studied here. However, a more detailed study of NT length in relation to conductivity and the ability to detect the electrochemical signature of Pt NPs deposited on the NT surfaces should be carried out.

- In Chapter 5, one of the lingering questions was the exact location of the Pt NPs on the NTs, although the TEM and SEM images seemed to indicate that the NPs are distributed evenly on the NTs. Depth profiling by XPS would be one of the techniques considered for obtaining this information.

- A proper mechanistic study of the ORR at Pt NPs deposited on the TaO<sub>x</sub>N<sub>y</sub> nanomaterials is warranted.

- In Chapter 6, insufficient time was available to carry out ORR studies of the Pt NPs/TaO<sub>x</sub>N<sub>y</sub> NPs/CIC100 catalyst material, and thus rigorous studies of this kind should still be carried out.

- It is possible that DFT studies could help in understanding why Pt electrochemistry was often not seen, even when the NTs were in a conducting state, with a particular focus on the Pt/TaO<sub>x</sub>N<sub>y</sub> interfacial properties.

- Another persistent question in this work is why anomalies were noticed between the expected and electrochemically observed surface area of the Pt NPs on the surface of TaO<sub>x</sub>N<sub>y</sub> materials.
- RDE work in this thesis was performed only on 1 μm TaO<sub>x</sub>N<sub>y</sub> NTs, but this study should be extended to TaO<sub>x</sub>N<sub>y</sub> compact layers and shorter NTs to identify mass transport effects on the ORR/HOR. However, this was hampered in this work due to technical issues in the fabrication of the RDEs.
- In Chapter 6, a standard potentiostatic stepping experiment was used to evaluate the corrosion stability of the materials under investigation. However, it was difficult to compare the results with those for other materials. The electrochemical surface area (ECSA) obtained from the CV and potentiostatic stepping experiments differed, which complicated the situation further. Future work should therefore focus on better understanding what the real surface area is of these materials during the corrosion testing to allow these comparisons to be made.

## References

1. UNDP *World Energy Assessment: Energy and the Challenge of Sustainability*; 2004 (United Nations, New York).
2. Hansen, J.; Sato, M.; Ruedy, R.; Lo, K.; Lea, D. W.; Medina-Elizade, M., Global Temperature Change. *Proceedings of the National Academy of Sciences of the United States of America* **2006**, *103* (39), 14288-14293.
3. Bockris, J. O. M., *Fuel Cells: Their Electrochemistry*. 1969; p 659 pp.
4. Larminie, J., *Fuel Cells System Explained*. 2000; p 308 pp.
5. O'Hayre, R. P., *Fuel Cell Fundamentals*. 2009; p 546 pp.
6. Xianguo, L., *Principles of Fuel Cells*. 2006; p 572 pp.
7. Vielstich, W.; Yokokawa, H.; Gasteiger, H. A.; Editors, *Handbook of Fuel Cells: Fundamentals Technology and Applications, Volume 6; Advances in Electrocatalysis Materials, Diagnostics and Durability: Part 2*. 2009; p 443 pp.
8. Lamy, C.; Jones, D. J.; Coutanceau, C.; Brault, P.; Martemianov, S.; Bultel, Y., Do Not Forget the Electrochemical Characteristics of the Membrane Electrode Assembly When Designing a Proton Exchange Membrane Fuel Cell Stack. *Electrochimica Acta* **2011**, *56* (28), 10406-10423.
9. Steele, B. C. H.; Heinzel, A., Materials for Fuel-Cell Technologies. *Nature* **2001**, *414*, 345.
10. 2020, E. C. s. H. Fuel Cell Hydrogen Joint Undertaking; Multi Annual Work Plan 2014-2020. [http://ec.europa.eu/research/participants/data/ref/h2020/other/legal/jtis/fch-multi-workplan\\_en.pdf](http://ec.europa.eu/research/participants/data/ref/h2020/other/legal/jtis/fch-multi-workplan_en.pdf).
11. DOE, F. C. T. O. Fuel Cell Technologies Office Multi-Year Research, Development and Demonstration Plan, 2017. [https://www.energy.gov/sites/prod/files/2017/05/f34/fcto\\_myrd fuel\\_cells.pdf](https://www.energy.gov/sites/prod/files/2017/05/f34/fcto_myrd fuel_cells.pdf).
12. Wang, Y.-J.; Wilkinson, D. P.; Zhang, J., Non-Carbon Support Materials for Polymer Electrolyte Membrane Fuel Cell Electrocatalysts. *Chemical Reviews (Washington, DC, United States)* **2011**, *111* (12), 7625-7651.
13. Shao, Y.; Liu, J.; Wang, Y.; Lin, Y., Novel Catalyst Support Materials for Pem Fuel Cells: Current Status and Future Prospects. *J. Mater. Chem.* **2009**, *19* (1), 46-59.
14. Antolini, E.; Gonzalez, E. R., Ceramic Materials as Supports for Low-Temperature Fuel Cell Catalysts. *Solid State Ionics* **2009**, *180* (9-10), 746-763.

15. El-Sayed, H. A.; Birss, V. I., Controlled Interconversion of Nanoarray of Ta Dimples and High Aspect Ratio Ta Oxide Nanotubes. *Nano Letters* **2009**, *9* (4), 1350-1355.
16. El-Sayed, H. A.; Birss, V. I., Controlled Growth and Monitoring of Tantalum Oxide Nanostructures. *Nanoscale* **2010**, *2* (5), 793-798.
17. Horwood, C. A.; El-Sayed, H. A.; Birss, V. I., Precise Electrochemical Prediction of Short Tantalum Oxide Nanotube Length. *Electrochimica Acta* **2014**, *132*, 91-97.
18. Horwood, C. A. Electrochemical Formation and Optimization of Ta-Based Nanomaterials. University of Calgary, 2015.
19. El-Sayed, H.; Singh, S.; Greiner, M. T.; Kruse, P., Formation of Highly Ordered Arrays of Dimples on Tantalum at the Nanoscale. *Nano Letters* **2006**, *6* (12), 2995-2999.
20. El-Sayed, H.; Singh, S.; Kruse, P., Formation of Dimpled Tantalum Surfaces from Electropolishing. *Journal of the Electrochemical Society* **2007**, *154* (12), C728-C732.
21. El-Sayed, H. A.; Birss, V. I., Versatile Fabrication of Self-Assembled Metallic Nanoparticle Arrays. *J. Mater. Chem.* **2011**, *21* (45), 18431-18438.
22. El-Sayed, H. A.; Horwood, C. A.; Owusu-Ansah, E.; Shi, Y. J.; Birss, V. I., Gold Nanoparticle Array Formation on Dimpled Ta Templates Using Pulsed Laser-Induced Thin Film Dewetting. *Physical Chemistry Chemical Physics* **2015**, *17* (16), 11062-11069.
23. El-Sayed, H. A.; Molero, H. M.; Birss, V. I., The Impact of Fabrication Conditions on the Quality of Au Nanoparticle Arrays on Dimpled Ta Templates. *Nanotechnology* **2012**, *23* (43), 435602/1-435602/12.
24. Chaneliere, C.; Autran, J. L.; Devine, R. A. B.; Balland, B., Tantalum Pentoxide (Ta<sub>2</sub>O<sub>5</sub>) Thin Films for Advanced Dielectric Applications. *Materials Science & Engineering, R: Reports* **1998**, *R22* (6), 269-322 pp.
25. Abhayawardhana, A. D.; Birss, V. I., Conductivity Switching of N-Doped Ta Oxide Nanotubular Arrays. *Journal of Physical Chemistry C* **2015**, *119* (24), 13847-13857.
26. Abhayawardhana, A. D.; Birss, V. I., Ta-Based Catalyst Support for Proton Exchange Membrane Fuel Cell Applications. *ECS Transactions* **2015**, *69* (17, Polymer Electrolyte Fuel Cells 15), 1227-1235.
27. DOE, F. C. T. O. Comparison of Fuel Cell Technologies. [https://www.energy.gov/sites/prod/files/2016/06/f32/fcto\\_fuel\\_cells\\_comparison\\_chart\\_apr2016.pdf](https://www.energy.gov/sites/prod/files/2016/06/f32/fcto_fuel_cells_comparison_chart_apr2016.pdf).

28. Garrain, D.; Lechon, Y.; de la Rúa, C., Polymer Electrolyte Membrane Fuel Cells (Pemfc) in Automotive Applications: Environmental Relevance of the Manufacturing Stage. *Smart Grid and Renewable Energy* **2011**, *2* (2), 68-74.
29. Lee, K.; Zhang, J.; Wang, H.; Wilkinson, D. P., Progress in the Synthesis of Carbon Nanotube- and Nanofiber-Supported Pt Electrocatalysts for Pem Fuel Cell Catalysis. *Journal of Applied Electrochemistry* **2006**, *36* (5), 507-522.
30. Gasteiger, H. A.; Kocha, S. S.; Sompalli, B.; Wagner, F. T., Activity Benchmarks and Requirements for Pt, Pt-Alloy, and Non-Pt Oxygen Reduction Catalysts for Pemfcs. *Applied Catalysis B: Environmental* **2005**, *56* (1), 9-35.
31. Dubau, L.; Castanheira, L.; Maillard, F.; Chatenet, M.; Lottin, O.; Maranzana, G.; Dillet, J.; Lamibrac, A.; Perrin, J.-C.; Moukheiber, E.; ElKaddouri, A.; De Moor, G.; Bas, C.; Flandin, L.; Caqué, N., A Review of Pem Fuel Cell Durability: Materials Degradation, Local Heterogeneities of Aging and Possible Mitigation Strategies. *Wiley Interdisciplinary Reviews: Energy and Environment* **2014**, *3* (6), 540-560.
32. Meier, J. C.; Galeano, C.; Katsounaros, I.; Witte, J.; Bongard, H. J.; Topalov, A. A.; Baldizzone, C.; Mezzavilla, S.; Schüth, F.; Mayrhofer, K. J. J., Design Criteria for Stable Pt/C Fuel Cell Catalysts. *Beilstein Journal of Nanotechnology* **2014**, *5*, 44-67.
33. Shinozaki, K.; Morimoto, Y.; Pivovar, B. S.; Kocha, S. S., Re-Examination of the Pt Particle Size Effect on the Oxygen Reduction Reaction for Ultrathin Uniform Pt/C Catalyst Layers without Influence from Nafion. *Electrochimica Acta* **2016**, *213*, 783-790.
34. Shao, M.-H.; Peles, A.; Shoemaker, K., Electrocatalysis on Platinum Nanoparticles: Particle Size Effect on Oxygen Reduction Reaction Activity. *Nano Letters* **2011**, *11* (9), 3714-3719.
35. Kinoshita, K., Particle Size Effects for Oxygen Reduction on Highly Dispersed Platinum in Acid Electrolytes. *Journal of the Electrochemical Society* **1990**, *137* (3), 845-8.
36. DOE Hydrogen and Fuel Cells Program Record 8002. [https://www.hydrogen.energy.gov/pdfs/8002\\_fuel\\_cell\\_system\\_cost.pdf](https://www.hydrogen.energy.gov/pdfs/8002_fuel_cell_system_cost.pdf).
37. DOE Hydrogen and Fuel Cells Program Record 17007. [https://www.hydrogen.energy.gov/pdfs/17007\\_fuel\\_cell\\_system\\_cost\\_2017.pdf](https://www.hydrogen.energy.gov/pdfs/17007_fuel_cell_system_cost_2017.pdf).
38. Debe, M. K., Electrocatalyst Approaches and Challenges for Automotive Fuel Cells. *Nature (London, United Kingdom)* **2012**, *486* (7401), 43-51.
39. Lefevre, M.; Proietti, E.; Jaouen, F.; Dodelet, J.-P., Iron-Based Catalysts with Improved Oxygen Reduction Activity in Polymer Electrolyte Fuel Cells. *Science (Washington, DC, United States)* **2009**, *324* (5923), 71-74.

40. Shui, J.; Chen, C.; Grabstanowicz, L.; Zhao, D.; Liu, D.-J., Highly Efficient Nonprecious Metal Catalyst Prepared with Metal-Organic Framework in a Continuous Carbon Nanofibrous Network. *Proceedings of the National Academy of Sciences of the United States of America* **2015**, *112* (34), 10629-10634.
41. Ohgi, Y.; Ishihara, A.; Matsuzawa, K.; Mitsushima, S.; Ota, K.-i.; Matsumoto, M.; Imai, H., Oxygen Reduction Reaction on Tantalum Oxide-Based Catalysts Prepared from Tac and Tan. *Electrochimica Acta* **2012**, *68*, 192-197.
42. Ota, K.-i.; Ohgi, Y.; Nam, K.-D.; Matsuzawa, K.; Mitsushima, S.; Ishihara, A., Development of Group 4 and 5 Metal Oxide-Based Cathodes for Polymer Electrolyte Fuel Cell. *Journal of Power Sources* **2011**, *196* (12), 5256-5263.
43. Ishihara, A.; Tamura, M.; Ohgi, Y.; Matsumoto, M.; Matsuzawa, K.; Mitsushima, S.; Imai, H.; Ota, K.-i., Emergence of Oxygen Reduction Activity in Partially Oxidized Tantalum Carbonitrides: Roles of Deposited Carbon for Oxygen-Reduction-Reaction-Site Creation and Surface Electron Conduction. *Journal of Physical Chemistry C* **2013**, *117* (37), 18837-18844.
44. Wassner, M.; Eckardt, M.; Gebauer, C.; Bourret, G. R.; Huesing, N.; Behm, R. J., Synthesis and Electrocatalytic Performance of Spherical Core-Shell Tantalum (Oxy)Nitride@Nitrided Carbon Composites in the Oxygen Reduction Reaction. *Electrochimica Acta* **2017**, *227*, 367-381.
45. Pasqualetti, A. M.; Padgett, E.; Kuo, D.-Y.; Muller, D. A.; Lima, F. H. B.; Suntivich, J., Influence of Aliovalent Substitutions on Oxygen Reduction on Tantalum Oxynitrides. *Journal of the Electrochemical Society* **2017**, *164* (6), F645-F650.
46. Ishihara, A.; Doi, S.; Mitsushima, S.; Ota, K.-i., Tantalum (Oxy)Nitrides Prepared Using Reactive Sputtering for New Nonplatinum Cathodes of Polymer Electrolyte Fuel Cell. *Electrochimica Acta* **2008**, *53* (16), 5442-5450.
47. Ishihara, A.; Lee, K.; Doi, S.; Mitsushima, S.; Kamiya, N.; Hara, M.; Domen, K.; Fukuda, K.; Ota, K.-i., Tantalum Oxynitride for a Novel Cathode of Pefc. *Electrochemical and Solid-State Letters* **2005**, *8* (4), A201-A203.
48. Ishihara, A.; Shibata, Y.; Mitsushima, S.; Ota, K., Partially Oxidized Tantalum Carbonitrides as a New Nonplatinum Cathode for Pefc-1. *Journal of the Electrochemical Society* **2008**, *155* (4), B400-B406.
49. Ishihara, A.; Tamura, M.; Matsuzawa, K.; Mitsushima, S.; Ota, K.-i., Tantalum Oxide-Based Compounds as New Non-Noble Cathodes for Polymer Electrolyte Fuel Cell. *Electrochimica Acta* **2010**, *55* (26), 7581-7589.

50. Ishihara, A.; Tamura, M.; Matsuzawa, K.; Mitsushima, S.; Ota, K.-i., Partially Oxidized Tantalum Carbonitride as New Cathodes without Platinum Group Metals for Polymer Electrolyte Fuel Cell. *Journal of Fuel Cell Science and Technology* **2011**, *8* (3), 31005/1-31005/6.
51. Chisaka, M.; Ishihara, A.; Uehara, N.; Matsumoto, M.; Imai, H.; Ota, K., Nano-TaOxny Particles Synthesized from Oxy-Tantalum Phthalocyanine: How to Prepare Precursors to Enhance the Oxygen Reduction Reaction Activity after Ammonia Pyrolysis? *Journal of Materials Chemistry A: Materials for Energy and Sustainability* **2015**, *3* (32), 16414-16418.
52. Imai, H.; Matsumoto, M.; Miyazaki, T.; Fujieda, S.; Ishihara, A.; Tamura, M.; Ota, K.-i., Structural Defects Working as Active Oxygen-Reduction Sites in Partially Oxidized Ta-Carbonitride Core-Shell Particles Probed by Using Surface-Sensitive Conversion-Electron-Yield X-Ray Absorption Spectroscopy. *Applied Physics Letters* **2010**, *96* (19), 191905/1-191905/3.
53. Pourbaix, M. J. N., *Atlas of Electrochemical Equilibriums in Aqueous Solutions. 2nd Ed.* 1974; p 644 pp.
54. Lee, J. B., Elevated Temperature Potential-Ph Diagrams for the Chromium-Water, Titanium-Water, Molybdenum-Water, and Platinum-Water Systems. *Corrosion (Houston)* **1981**, *37* (8), 467-81.
55. Uribe, F. A.; Zawodzinski, T. A., A Study of Polymer Electrolyte Fuel Cell Performance at High Voltages. Dependence on Cathode Catalyst Layer Composition and on Voltage Conditioning. *Electrochimica Acta* **2002**, *47* (22-23), 3799-3806.
56. Paik, C. H.; Saloka, G. S.; Graham, G. W., Influence of Cyclic Operation on Pem Fuel Cell Catalyst Stability. *Electrochemical and Solid-State Letters* **2007**, *10* (2), B39-B42.
57. Wang, X.; Kumar, R.; Myers, D. J., Effect of Voltage on Platinum Dissolution. *Electrochemical and Solid-State Letters* **2006**, *9* (5), A225-A227.
58. Borup, R.; Meyers, J.; Pivovar, B.; Kim, Y. S.; Mukundan, R.; Garland, N.; Myers, D.; Wilson, M.; Garzon, F.; Wood, D.; Zelenay, P.; More, K.; Stroh, K.; Zawodzinski, T.; Boncella, J.; McGrath, J. E.; Inaba, M.; Miyatake, K.; Hori, M.; Ota, K.; Ogumi, Z.; Miyata, S.; Nishikata, A.; Siroma, Z.; Uchimoto, Y.; Yasuda, K.; Kimijima, K.-i.; Iwashita, N., Scientific Aspects of Polymer Electrolyte Fuel Cell Durability and Degradation. *Chemical Reviews (Washington, DC, United States)* **2007**, *107* (10), 3904-3951.
59. More, K. L. Doe Hydrogen Program Annual Progress Report. [https://www.hydrogen.energy.gov/pdfs/progress06/v\\_g\\_3\\_more.pdf](https://www.hydrogen.energy.gov/pdfs/progress06/v_g_3_more.pdf).
60. Kim, J.; Lee, J.; Tak, Y., Relationship between Carbon Corrosion and Positive Electrode Potential in a Proton-Exchange Membrane Fuel Cell During Start/Stop Operation. *Journal of Power Sources* **2009**, *192* (2), 674-678.

61. Chaparro, A. M.; Mueller, N.; Atienza, C.; Daza, L., Study of Electrochemical Instabilities of Pemfc Electrodes in Aqueous Solution by Means of Membrane Inlet Mass Spectrometry. *Journal of Electroanalytical Chemistry* **2006**, *591* (1), 69-73.
62. Oh, H.-S.; Oh, J.-G.; Haam, S.; Arunabha, K.; Roh, B.; Hwang, I.; Kim, H., On-Line Mass Spectrometry Study of Carbon Corrosion in Polymer Electrolyte Membrane Fuel Cells. *Electrochem. Commun.* **2008**, *10* (7), 1048-1051.
63. Shen, Q.; Hou, M.; Liang, D.; Zhou, Z.; Li, X.; Shao, Z.; Yi, B., Study on the Processes of Start-up and Shutdown in Proton Exchange Membrane Fuel Cells. *Journal of Power Sources* **2009**, *189* (2), 1114-1119.
64. Yu, P. T.; Liu, Z.; Makharia, R., Investigation of Carbon Corrosion Behavior and Kinetics in Proton Exchange Membrane Fuel Cell Cathode Electrodes. *Journal of the Electrochemical Society* **2013**, *160* (6), F645-F650.
65. Kongkanand, A.; Zhang, J.; Liu, Z.; Lai, Y.-H.; Sinha, P.; Thompson, E. L.; Makharia, R., Degradation of Pemfc Observed on Nstf Electrodes. *Journal of the Electrochemical Society* **2014**, *161* (6), F744-F753.
66. Gu, W.; Yu, P. T.; Carter, R. N.; Makharia, R.; Gasteiger, H. A., Modeling of Membrane-Electrode-Assembly Degradation in Proton-Exchange-Membrane Fuel Cell - Local H<sub>2</sub> Starvation and Start-Stop Induced Carbon-Support Corrosion. *Modern Aspects of Electrochemistry* **2010**, *49* (Modeling and Diagnostics of Polymer Electrolyte Fuel Cells), 45-87.
67. Kangasniemi, K. H.; Condit, D. A.; Jarvi, T. D., Characterization of Vulcan Electrochemically Oxidized under Simulated Pem Fuel Cell Conditions. *Journal of the Electrochemical Society* **2004**, *151* (4), E125-E132.
68. Rush, B. M.; Reimer, J. A.; Cairns, E. J., Nuclear Magnetic Resonance and Voltammetry Studies of Carbon Monoxide Adsorption and Oxidation on a Carbon-Supported Platinum Fuel Cell Electrocatalyst. *Journal of the Electrochemical Society* **2001**, *148* (2), A137-A148.
69. Willsau, J.; Heitbaum, J., The Influence of Platinum Activation on the Corrosion of Carbon in Gas Diffusion Electrodes - a Dems Study. *Journal of Electroanalytical Chemistry and Interfacial Electrochemistry* **1984**, *161* (1), 93-101.
70. Park, Y.-C.; Kakinuma, K.; Uchida, M.; Uchida, H.; Watanabe, M., Deleterious Effects of Interim Cyclic Voltammetry on Pt/Carbon Black Catalyst Degradation During Start-up/Shutdown Cycling Evaluation. *Electrochimica Acta* **2014**, *123*, 84-92.
71. de Bruijn, F. A.; Dam, V. A. T.; Janssen, G. J. M., Review: Durability and Degradation Issues of Pem Fuel Cell Components. *Fuel Cells (Weinheim, Ger.)* **2008**, *8* (1), 3-22.

72. Lebedeva, N. P.; Koper, M. T. M.; Feliu, J. M.; van Santen, R. A., Role of Crystalline Defects in Electrocatalysis: Mechanism and Kinetics of Co Adlayer Oxidation on Stepped Platinum Electrodes. *Journal of Physical Chemistry B* **2002**, *106* (50), 12938-12947.
73. Sugawara, Y.; Okayasu, T.; Yadav, A. P.; Nishikata, A.; Tsuru, T., Dissolution Mechanism of Platinum in Sulfuric Acid Solution. *Journal of the Electrochemical Society* **2012**, *159* (11), F779-F786.
74. Gallagher, K. G.; Wong, D. T.; Fuller, T. F., The Effect of Transient Potential Exposure on the Electrochemical Oxidation of Carbon Black in Low-Temperature Fuel Cells. *Journal of the Electrochemical Society* **2008**, *155* (5), B488-B493.
75. Banham, D.; Feng, F.; Fuerstenhaupt, T.; Pei, K.; Ye, S.; Birss, V., Effect of Pt-Loaded Carbon Support Nanostructure on Oxygen Reduction Catalysis. *Journal of Power Sources* **2011**, *196* (13), 5438-5445.
76. Ishihara, A.; Ohgi, Y.; Matsuzawa, K.; Mitsushima, S.; Ota, K.-i., Progress in Non-Precious Metal Oxide-Based Cathode for Polymer Electrolyte Fuel Cells. *Electrochimica Acta* **2010**, *55* (27), 8005-8012.
77. Chhina, H.; Campbell, S.; Kesler, O., An Oxidation-Resistant Indium Tin Oxide Catalyst Support for Proton Exchange Membrane Fuel Cells. *Journal of Power Sources* **2006**, *161* (2), 893-900.
78. Zhang, P.; Huang, S.-Y.; Popov, B. N., Mesoporous Tin Oxide as an Oxidation-Resistant Catalyst Support for Proton Exchange Membrane Fuel Cells. *Journal of the Electrochemical Society* **2010**, *157* (8), B1163-B1172.
79. Ioroi, T.; Siroma, Z.; Fujiwara, N.; Yamazaki, S.-i.; Yasuda, K., Sub-Stoichiometric Titanium Oxide-Supported Platinum Electrocatalyst for Polymer Electrolyte Fuel Cells. *Electrochem. Commun.* **2005**, *7* (2), 183-188.
80. Arif, A. F.; Balgis, R.; Ogi, T.; Okuyama, K.; Iskandar, F.; Kinoshita, A.; Nakamura, K., Highly Conductive Nano-Sized Magneli Phases Titanium Oxide (Tiox). *Sci Rep* **2017**, *7* (1), 3646.
81. Kim, D.-S.; Zeid, E. F. A.; Kim, Y.-T., Additive Treatment Effect of Tio<sub>2</sub> as Supports for Pt-Based Electrocatalysts on Oxygen Reduction Reaction Activity. *Electrochimica Acta* **2010**, *55* (11), 3628-3633.
82. Huang, S.-Y.; Ganesan, P.; Popov, B. N., Titania Supported Platinum Catalyst with High Electrocatalytic Activity and Stability for Polymer Electrolyte Membrane Fuel Cell. *Applied Catalysis B: Environmental* **2011**, *102* (1), 71-77.
83. Antolini, E.; Gonzalez, E. R., Tungsten-Based Materials for Fuel Cell Applications. *Applied Catalysis, B: Environmental* **2010**, *96* (3-4), 245-266.

84. Maiyalagan, T.; Viswanathan, B., Catalytic Activity of Platinum/Tungsten Oxide Nanorod Electrodes Towards Electro-Oxidation of Methanol. *Journal of Power Sources* **2008**, *175* (2), 789-793.
85. Tauster, S. J., Strong Metal-Support Interactions. *Accounts of Chemical Research* **1987**, *20* (11), 389-94.
86. Jaksic, J. M.; Labou, D.; Papakonstantinou, G. D.; Siokou, E.; Jaksic, M. M., Novel Spillover Interrelating Reversible Electrocatalysts for Oxygen and Hydrogen Electrode Reactions. *Journal of Physical Chemistry C* **2010**, *114* (43), 18298-18312.
87. Chhina, H.; Campbell, S.; Kesler, O., Thermal and Electrochemical Stability of Tungsten Carbide Catalyst Supports. *Journal of Power Sources* **2007**, *164* (2), 431-440.
88. Chhina, H.; Campbell, S.; Kesler, O., High Surface Area Synthesis, Electrochemical Activity, and Stability of Tungsten Carbide Supported Pt During Oxygen Reduction in Proton Exchange Membrane Fuel Cells. *Journal of Power Sources* **2008**, *179* (1), 50-59.
89. Jeon, M. K.; Daimon, H.; Lee, K. R.; Nakahara, A.; Woo, S. I., Co Tolerant Pt/Wc Methanol Electrooxidation Catalyst. *Electrochem. Commun.* **2007**, *9* (11), 2692-2695.
90. Levy, R. B.; Boudart, M., Platinum-Like Behavior of Tungsten Carbide in Surface Catalysis. *Science* **1973**, *181* (4099), 547-9.
91. Lee, J.-M.; Han, S.-B.; Song, Y.-J.; Kim, J.-Y.; Roh, B.; Hwang, I.; Choi, W.; Park, K.-W., Methanol Electrooxidation of Pt Catalyst on Titanium Nitride Nanostructured Support. *Applied Catalysis, A: General* **2010**, *375* (1), 149-155.
92. Lee, J.-M.; Kim, S.-B.; Lee, Y.-W.; Kim, D.-Y.; Han, S.-B.; Roh, B.; Hwang, I.; Park, K.-W., Core-Shell Nanostructure Electrodes for Improved Electrocatalytic Properties in Methanol Electrooxidation. *Applied Catalysis, B: Environmental* **2012**, *111-112*, 200-207.
93. Musthafa, O. T. M.; Sampath, S., High Performance Platinized Titanium Nitride Catalyst for Methanol Oxidation. *Chemical Communications (Cambridge, United Kingdom)* **2008**, (1), 67-69.
94. Isogai, S.; Ohnishi, R.; Katayama, M.; Kubota, J.; Kim, D. Y.; Noda, S.; Cha, D.; Takanabe, K.; Domen, K., Composite of Tin Nanoparticles and Few-Walled Carbon Nanotubes and Its Application to the Electrocatalytic Oxygen Reduction Reaction. *Chemistry--An Asian Journal* **2012**, *7* (2), 286-289.
95. Kakinuma, K.; Wakasugi, Y.; Chida, M.; Kamino, T.; Uchida, H.; Watanabe, M., Electrochemical Activity and Durability of Platinum Catalysts Supported on Nanometer -Size Titanium Nitride Particles for Polymer Electrolyte Fuel Cells. *Electrochemistry (Tokyo, Japan)* **2011**, *79* (5), 399-403.

96. Avasarala, B.; Haldar, P., Electrochemical Oxidation Behavior of Titanium Nitride Based Electrocatalysts under Pem Fuel Cell Conditions. *Electrochimica Acta* **2010**, *55* (28), 9024-9034.
97. Thotiyl, M. M. O.; Sampath, S., Electrochemical Oxidation of Ethanol in Acid Media on Titanium Nitride Supported Fuel Cell Catalysts. *Electrochimica Acta* **2011**, *56* (10), 3549-3554.
98. Avasarala, B.; Murray, T.; Li, W.; Haldar, P., Titanium Nitride Nanoparticles Based Electrocatalysts for Proton Exchange Membrane Fuel Cells. *J. Mater. Chem.* **2009**, *19* (13), 1803-1805.
99. Ottakam Thotiyl, M. M.; Ravikumar, T.; Sampath, S., Platinum Particles Supported on Titanium Nitride: An Efficient Electrode Material for the Oxidation of Methanol in Alkaline Media. *J. Mater. Chem.* **2010**, *20* (47), 10643-10651.
100. Thotiyl, M. M. O.; Kumar, T. R.; Sampath, S., Pd Supported on Titanium Nitride for Efficient Ethanol Oxidation. *Journal of Physical Chemistry C* **2010**, *114* (41), 17934-17941.
101. Fritz, K. E.; Beaucage, P. A.; Matsuoka, F.; Wiesner, U.; Suntivich, J., Mesoporous Titanium and Niobium Nitrides as Conductive and Stable Electrocatalyst Supports in Acid Environments. *Chemical Communications (Cambridge, United Kingdom)* **2017**, *53* (53), 7250-7253.
102. Oyama, S. T., *The Chemistry of Transitionmetal Carbides and Nitrides*. Blackie Acadimics and professionals: 1996; p 536.
103. Bauer, A.; Hui, R.; Ignaszak, A.; Zhang, J.; Jones, D. J., Application of a Composite Structure of Carbon Nanoparticles and Nb-Tio<sub>2</sub> Nanofibers as Electrocatalyst Support for Pem Fuel Cells. *Journal of Power Sources* **2012**, *210*, 15-20.
104. Kou, R.; Shao, Y.; Mei, D.; Nie, Z.; Wang, D.; Wang, C.; Viswanathan, V. V.; Park, S.; Aksay, I. A.; Lin, Y.; Wang, Y.; Liu, J., Stabilization of Electrocatalytic Metal Nanoparticles at Metal-Metal Oxide-Graphene Triple Junction Points. *Journal of the American Chemical Society* **2011**, *133* (8), 2541-2547.
105. Shanmugam, S.; Gedanken, A., Carbon-Coated Anatase Tio<sub>2</sub> Nanocomposite as a High-Performance Electrocatalyst Support. *Small* **2007**, *3* (7), 1189-1193.
106. Bing, Y.; Neburchilov, V.; Song, C.; Baker, R.; Guest, A.; Ghosh, D.; Ye, S.; Campbell, S.; Zhang, J., Effects of Synthesis Condition on Formation of Desired Crystal Structures of Doped-Tio<sub>2</sub>/Carbon Composite Supports for Orr Electrocatalysts. *Electrochimica Acta* **2012**, *77*, 225-231.
107. Setthapun, W.; Bej, S. K.; Thompson, L. T., Carbide and Nitride Supported Methanol Steam Reforming Catalysts: Parallel Synthesis and High Throughput Screening. *Topics in Catalysis* **2008**, *49* (1-2), 73-80.

108. Tan, X.; Wang, L.; Zahiri, B.; Kohandehghan, A.; Karpuzov, D.; Lotfabad, E. M.; Li, Z.; Eikerling, M. H.; Mitlin, D., Titanium Oxynitride Interlayer to Influence Oxygen Reduction Reaction Activity and Corrosion Stability of Pt and Pt–Ni Alloy. *ChemSusChem* **2014**, *8* (2), 361-376.
109. Cracknell, J. A.; Vincent, K. A.; Ludwig, M.; Lenz, O.; Friedrich, B.; Armstrong, F. A., Enzymatic Oxidation of H<sub>2</sub> in Atmospheric O<sub>2</sub>: The Electrochemistry of Energy Generation from Trace H<sub>2</sub> by Aerobic Microorganisms. *Journal of the American Chemical Society* **2008**, *130* (2), 424-425.
110. Genorio, B.; Strmcnik, D.; Subbaraman, R.; Tripkovic, D.; Karapetrov, G.; Stamenkovic, V. R.; Pejovnik, S.; Markovic, N. M., Selective Catalysts for the Hydrogen Oxidation and Oxygen Reduction Reactions by Patterning of Platinum with Calix[4]Arene Molecules. *Nature Materials* **2010**, *9* (12), 998-1003.
111. Banham, D.; Ye, S.; O'Toole, A.; Lemke, A.; Eisenbraun, E., Unexpected Hydrogen Oxidation Selectivity of Pt/NbTiO<sub>2</sub> Catalysts. *Nano Energy* **2016**, *27*, 157-166.
112. Gasteiger, H. A.; Kocha, S. S.; Sompalli, B.; Wagner, F. T., Activity Benchmarks and Requirements for Pt, Pt-Alloy, and Non-Pt Oxygen Reduction Catalysts for Pemfcs. *Applied Catalysis B: Environmental* **2005**, *56* (1–2), 9-35.
113. Shao, Y.; Kou, R.; Wang, J.; Viswanathan, V. V.; Kwak, J. H.; Liu, J.; Wang, Y.; Lin, Y., The Influence of the Electrochemical Stressing (Potential Step and Potential-Static Holding) on the Degradation of Polymer Electrolyte Membrane Fuel Cell Electrocatalysts. *Journal of Power Sources* **2008**, *185* (1), 280-286.
114. Shao, Y.; Wang, J.; Kou, R.; Engelhard, M.; Liu, J.; Wang, Y.; Lin, Y., The Corrosion of Pem Fuel Cell Catalyst Supports and Its Implications for Developing Durable Catalysts. *Electrochimica Acta* **2009**, *54* (11), 3109-3114.
115. Zhang, J., *Pem Fuel Cell Electrocatalysts and Catalyst Layers* 1ed.; Publisher: 2008; p XXI, 1137.
116. Bard, A. J.; Faulkner, L. R., *Electrochemical Methods: Fundamentals and Applications*. 1982; p 808 pp.
117. Bockris, J. O. M.; Reddy, A. K. N.; Gamboa-Aldeco, M. E.; Editors, *Modern Electrochemistry 2a, Second Edition: Fundamentals of Electrodics*. 2001; p 788 pp.
118. Conway, B. E.; Bockris, J. O. m.; Yeager, E.; Khan, S. U. M.; White, R. E.; Editors, *Comprehensive Treatise of Electrochemistry, Vol. 7: Kinetics and Mechanisms of Electrode Processes*. 1983; p 788 pp.

119. O'Grady, W. E.; Taylor, E. J.; Srinivasan, S., Electroreduction of Oxygen on Reduced Platinum in 85% Phosphoric Acid. *Journal of Electroanalytical Chemistry and Interfacial Electrochemistry* **1982**, *132*, 137-50.
120. Puglia, C.; Nilsson, A.; Hernnaes, B.; Karis, O.; Bennich, P.; Martensson, N., Physisorbed, Chemisorbed and Dissociated O<sub>2</sub> on Pt(111) Studied by Different Core Level Spectroscopy Methods. *Surf. Sci.* **1995**, *342* (1-3), 119-33.
121. Wang, J. X.; Markovic, N. M.; Adzic, R. R., Kinetic Analysis of Oxygen Reduction on Pt(111) in Acid Solutions: Intrinsic Kinetic Parameters and Anion Adsorption Effects. *Journal of Physical Chemistry B* **2004**, *108* (13), 4127-4133.
122. Wang, J. X.; Zhang, J.; Adzic, R. R., Double-Trap Kinetic Equation for the Oxygen Reduction Reaction on Pt(111) in Acidic Media. *J. Phys. Chem. A* **2007**, *111* (49), 12702-12710.
123. Jürgen Garche, C. K. D., Patrick T. Moseley, Zempachi Ogumi, David A. J. Rand, Bruno Scrosati, Encyclopedia of Electrochemical Power Sources.
124. Durst, J.; Simon, C.; Hasche, F.; Gasteiger, H. A., Hydrogen Oxidation and Evolution Reaction Kinetics on Carbon Supported Pt, Ir, Rh, and Pd Electrocatalysts in Acidic Media. *Journal of the Electrochemical Society* **2015**, *162* (1), F190-F203.
125. Ham, D. J.; Lee, J. S., Transition Metal Carbides and Nitrides as Electrode Materials for Low Temperature Fuel Cells. *Energies (Basel, Switzerland)* **2009**, *2* (4), 873-899.
126. Liu, J.; Jiang, L., Electrostatic Self-Assembly of Pt Nanoparticles on Hexagonal Tungsten Oxide as an Active Co-Tolerant Hydrogen Oxidation Electrocatalyst. *International Journal of Hydrogen Energy* **2018**, *43* (18), 8944-8952.
127. Wang, L.; Mahoney, E. G.; Zhao, S.; Yang, B.; Chen, J. G., Low Loadings of Platinum on Transition Metal Carbides for Hydrogen Oxidation and Evolution Reactions in Alkaline Electrolytes. *Chemical Communications (Cambridge, United Kingdom)* **2016**, *52* (18), 3697-3700.
128. Suryamas, A. B.; Anilkumar, G. M.; Sago, S.; Ogi, T.; Okuyama, K., Electrospun Pt/SnO<sub>2</sub> Nanofibers as an Excellent Electrocatalysts for Hydrogen Oxidation Reaction with Orr-Blocking Characteristic. *Catalysis Communications* **2013**, *33*, 11-14.
129. Bockris, J. O. M.; Reddy, A. K. N.; Editors, *Modern Electrochemistry 2b, Second Edition: Electrode in Chemistry, Engineering, Biology and Environmental Science*. 2001; p 542 pp.
130. Young, L., *Anodic Oxide Films*. 1961; p 377 pp.

131. Macagno, V.; Schultze, J. W., The Growth and Properties of Thin Oxide Layers on Tantalum Electrodes. *Journal of Electroanalytical Chemistry and Interfacial Electrochemistry* **1984**, *180* (1-2), 157-70.
132. Vanhumbecq, J. F.; Proost, J., Current Understanding of Ti Anodisation: Functional, Morphological, Chemical and Mechanical Aspects. *Corrosion Reviews* **2009**, *27* (3), 117-204.
133. Paramasivam, I.; Jha, H.; Liu, N.; Schmuki, P., A Review of Photocatalysis Using Self-Organized TiO<sub>2</sub> Nanotubes and Other Ordered Oxide Nanostructures. *Small* **2012**, *8* (20), 3073-3103.
134. Masuda, H.; Fukuda, K., Ordered Metal Nanohole Arrays Made by a Two-Step Replication of Honeycomb Structures of Anodic Alumina. *Science (Washington, D. C.)* **1995**, *268* (5216), 1466-68.
135. O'Sullivan, J. P.; Wood, G. C., Morphology and Mechanism of Formation of Porous Anodic Films on Aluminum. *Proceedings of the Royal Society of London, Series A: Mathematical, Physical and Engineering Sciences* **1970**, *317* (1531), 511-43.
136. Yasuda, K.; Macak, J. M.; Berger, S.; Ghicov, A.; Schmuki, P., Mechanistic Aspects of the Self-Organization Process for Oxide Nanotube Formation on Valve Metals. *Journal of the Electrochemical Society* **2007**, *154* (9), C472-C478.
137. Su, Z.; Hahner, G.; Zhou, W., Investigation of the Pore Formation in Anodic Aluminium Oxide. *J. Mater. Chem.* **2008**, *18* (47), 5787-5795.
138. Su, Z.; Zhou, W., Formation Mechanism of Porous Anodic Aluminium and Titanium Oxides. *Advanced Materials (Weinheim, Germany)* **2008**, *20* (19), 3663-3667.
139. Hebert, K. R.; Albu, S. P.; Paramasivam, I.; Schmuki, P., Morphological Instability Leading to Formation of Porous Anodic Oxide Films. *Nature Materials* **2012**, *11* (2), 162-166.
140. El-Sayed, H. A.; Horwood, C. A.; Abhayawardhana, A. D.; Birss, V. I., New Insights into the Initial Stages of Ta Oxide Nanotube Formation on Polycrystalline Ta Electrodes. *Nanoscale* **2013**, *5* (4), 1494-1498.
141. Wei, W.; Berger, S.; Hauser, C.; Meyer, K.; Yang, M.; Schmuki, P., Transition of TiO<sub>2</sub> Nanotubes to Nanopores for Electrolytes with Very Low Water Contents. *Electrochem. Commun.* **2010**, *12* (9), 1184-1186.
142. Berger, S.; Jakubka, F.; Schmuki, P., Self-Ordered Hexagonal Nanoporous Hafnium Oxide and Transition to Aligned HfO<sub>2</sub> Nanotube Layers. *Electrochemical and Solid-State Letters* **2009**, *12* (7), K45-K48.
143. Berger, S.; Jakubka, F.; Schmuki, P., Formation of Hexagonally Ordered Nanoporous Anodic Zirconia. *Electrochem. Commun.* **2008**, *10* (12), 1916-1919.

144. Tsuchiya, H.; Schmuki, P., Self-Organized High Aspect Ratio Porous Hafnium Oxide Prepared by Electrochemical Anodization. *Electrochem. Commun.* **2005**, 7 (1), 49-52.
145. Tsuchiya, H.; Macak, J. M.; Ghicov, A.; Taveira, L.; Schmuki, P., Self-Organized Porous TiO<sub>2</sub> and ZrO<sub>2</sub> Produced by Anodization. *Corros. Sci.* **2005**, 47 (12), 3324-3335.
146. Tsuchiya, H.; Berger, S.; Macak, J. M.; Ghicov, A.; Schmuki, P., Self-Organized Porous and Tubular Oxide Layers on TiAl Alloys. *Electrochem. Commun.* **2007**, 9 (9), 2397-2402.
147. Berger, S.; Tsuchiya, H.; Schmuki, P., Transition from Nanopores to Nanotubes: Self-Ordered Anodic Oxide Structures on Titanium Aluminides. *Chemistry of Materials* **2008**, 20 (10), 3245-3247.
148. Roy, P.; Berger, S.; Schmuki, P., TiO<sub>2</sub> Nanotubes: Synthesis and Applications. *Angewandte Chemie International Edition* **2011**, 50 (13), 2904-2939.
149. Cavigliasso, G. E.; Esplandiu, M. J.; Macagno, V. A., Influence of the Forming Electrolyte on the Electrical Properties of Tantalum and Niobium Oxide Films: An EIS Comparative Study. *Journal of Applied Electrochemistry* **1998**, 28 (11), 1213-1219.
150. Cabrera-Sierra, R.; Vazquez-Arenas, J.; Cardoso, S.; Luna-Sanchez, R. M.; Trejo, M. A.; Marin-Cruz, J.; Hallen, J. M., Analysis of the Formation of Ta<sub>2</sub>O<sub>5</sub> Passive Films in Acid Media through Mechanistic Modeling. *Electrochimica Acta* **2011**, 56 (23), 8040-8047.
151. Allam, N. K.; Feng, X. J.; Grimes, C. A., Self-Assembled Fabrication of Vertically Oriented Ta<sub>2</sub>O<sub>5</sub> Nanotube Arrays, and Membranes Thereof, by One-Step Tantalum Anodization. *Chemistry of Materials* **2008**, 20 (20), 6477-6481.
152. Barton, J. E.; Stender, C. L.; Li, P.; Odom, T. W., Structural Control of Anodized Tantalum Oxide Nanotubes. *J. Mater. Chem.* **2009**, 19 (28), 4896.
153. Buyukaksoy, A.; Furstenhaupt, T.; Birss, V. I., First-Time Electrical Characterization of Nanotubular ZrO<sub>2</sub> Films for Micro-Solid Oxide Fuel Cell Applications. *Nanoscale* **2015**, 7 (18), 8428-8437.
154. Abhayawardhana, A. D., Unpublished Work. University Of Calgary.
155. Singh, S.; Barden, W. R. T.; Kruse, P., Nanopatterning of Transition Metal Surfaces Via Electrochemical Dimple Array Formation. *ACS Nano* **2008**, 2 (12), 2453-2464.
156. El-Sayed, H. A.; Campbell, H. B.; Birss, V. I., Electrochemical Applications of a Au Nanoparticle Array Fabricated Using Highly Ordered Dimpled Ta Templates. *Electrochimica Acta* **2013**, 112, 845-852.

157. Joo, S. H.; Choi, S. J.; Oh, I.; Kwak, J.; Liu, Z.; Terasaki, O.; Ryoo, R., Ordered Nanoporous Arrays of Carbon Supporting High Dispersions of Platinum Nanoparticles. *Nature (London, United Kingdom)* **2001**, *412* (6843), 169-172.
158. Pei, K.; Banham, D.; Feng, F.; Fuerstenhaupt, T.; Ye, S.; Birss, V., Oxygen Reduction Activity Dependence on the Mesoporous Structure of Imprinted Carbon Supports. *Electrochem. Commun.* **2010**, *12* (11), 1666-1669.
159. Li, Z.; Jaroniec, M., Colloidal Imprinting: A Novel Approach to the Synthesis of Mesoporous Carbons. *Journal of the American Chemical Society* **2001**, *123* (37), 9208-9209.
160. Pinna, N.; Garnweitner, G.; Antonietti, M.; Niederberger, M., Non-Aqueous Synthesis of High-Purity Metal Oxide Nanopowders Using an Ether Elimination Process. *Advanced Materials (Weinheim, Germany)* **2004**, *16* (23-24), 2196-2200.
161. Pinna, N., The "Benzyl Alcohol Route": An Elegant Approach Towards Organic-Inorganic Hybrid Nanomaterials. *J. Mater. Chem.* **2007**, *17* (27), 2769-2774.
162. Pinna, N.; Niederberger, M., Surfactant-Free Nonaqueous Synthesis of Metal Oxide Nanostructures. *Angewandte Chemie, International Edition* **2008**, *47* (29), 5292-5304.
163. Banham, D.; Feng, F.; Burt, J.; Alsayheen, E.; Birss, V., Bimodal, Templated Mesoporous Carbons for Capacitor Applications. *Carbon* **2010**, *48* (4), 1056-1063.
164. Forouzandeh, F.; Li, X.; Banham, D. W.; Feng, F.; Ye, S.; Birss, V., Evaluation of Corrosion Resistance of Ordered Mesoporous Carbons for Use as Fuel Cell Cathode Supports. *Journal of the Electrochemical Society* **2015**, *Under Review*
165. Authors, U. Unknown Title. Unknown URL.
166. Garsany, Y.; Baturina, O. A.; Swider-Lyons, K. E.; Kocha, S. S., Experimental Methods for Quantifying the Activity of Platinum Electrocatalysts for the Oxygen Reduction Reaction. *Analytical Chemistry (Washington, DC, United States)* **2010**, *82* (15), 6321-6328.
167. Laboratory, N. R. E. Best Practices and Benchmark Activities for Orr Measurements by the Rotating Disk Electrode Technique. [https://www.hydrogen.energy.gov/pdfs/review14/fc111\\_kocha\\_2014\\_o.pdf](https://www.hydrogen.energy.gov/pdfs/review14/fc111_kocha_2014_o.pdf).
168. Brochure, Z. S., In *Product Information V 2.3*, ZEISS.
169. Dreele, A. C. L. a. R. B. V. *General Structure Analysis System (Gsas)*; LAUR 86-748; Los Alamos National Laboratory 2000; pp LAUR 86-748.
170. Toby, B. H., ExpGui, a Graphical User Interface for Gsas. *J. Appl. Crystallogr.* **2001**, *34* (2), 210-213.
171. Eppendorf, Eppendorf Research Plus- Technical Specification. In *Eppendorf*, 2013.

172. Fürstenhaupt, T., Personal Communication. 2012.
173. Chun, W.-J.; Ishikawa, A.; Fujisawa, H.; Takata, T.; Kondo, J. N.; Hara, M.; Kawai, M.; Matsumoto, Y.; Domen, K., Conduction and Valence Band Positions of Ta<sub>2</sub>O<sub>5</sub>, Taon, and Ta<sub>3</sub>N<sub>5</sub> by Ups and Electrochemical Methods. *Journal of Physical Chemistry B* **2003**, *107* (8), 1798-1803.
174. Hany A. El-Sayed, C. A. H., Anusha D. Abhayawardhana and Viola I. Birss New Insights into the Initial Stages of Ta Oxide Nanotube Formation on Polycrystalline Ta Electrodes. *Nanoscale* **2013**.
175. Macak, J. M.; Tsuchiya, H.; Taveira, L.; Aldabergerova, S.; Schmuki, P., Smooth Anodic TiO<sub>2</sub> Nanotubes. *Angewandte Chemie, International Edition* **2005**, *44* (45), 7463-7465.
176. Lee, W.-J.; Smyrl, W. H., Zirconium Oxide Nanotubes Synthesized Via Direct Electrochemical Anodization. *Electrochemical and Solid-State Letters* **2005**, *8* (3), B7-B9.
177. Qiu, X.; Howe, J. Y.; Cardoso, M. B.; Polat, O.; Heller, W. T.; Paranthaman, M. P., Size Control of Highly Ordered HfO<sub>2</sub> Nanotube Arrays and a Possible Growth Mechanism. *Nanotechnology* **2009**, *20* (45), 455601/1-455601/9.
178. Kang, S. H.; Kim, J.-Y.; Kim, H. S.; Sung, Y.-E., Formation and Mechanistic Study of Self-Ordered TiO<sub>2</sub> Nanotubes on Ti Substrate. *Journal of Industrial and Engineering Chemistry (Amsterdam, Netherlands)* **2008**, *14* (1), 52-59.
179. Valota, A.; LeClere, D. J.; Skeldon, P.; Curioni, M.; Hashimoto, T.; Berger, S.; Kunze, J.; Schmuki, P.; Thompson, G. E., Influence of Water Content on Nanotubular Anodic Titania Formed in Fluoride/Glycerol Electrolytes. *Electrochimica Acta* **2009**, *54* (18), 4321-4327.
180. Lu, D.; Hitoki, G.; Katou, E.; Kondo, J. N.; Hara, M.; Domen, K., Porous Single-Crystalline Taon and Ta<sub>3</sub>N<sub>5</sub> Particles. *Chemistry of Materials* **2004**, *16* (9), 1603-1605.
181. Choi, D.; Kumta, P. N., Synthesis and Characterization of Nanostructured Niobium and Molybdenum Nitrides by a Two-Step Transition Metal Halide Approach. *Journal of the American Ceramic Society* **2011**, *94* (8), 2371-2378.
182. Reisman, A.; Holtzberg, F.; Berkenblit, M.; Berry, M., Reactions of the Group Vb Pentoxides with Alkali Oxides and Carbonates. Iii. Thermal and X-Ray Phase Diagrams of the System K<sub>2</sub>O and K<sub>2</sub>CO<sub>3</sub> with Ta<sub>2</sub>O<sub>5</sub>. *Journal of the American Chemical Society* **1956**, *78*, 4514-20.
183. Orhan, E.; Tessier, F.; Marchand, R., Synthesis and Energetics of Yellow Taon. *Solid State Sciences* **2002**, *4* (8), 1071-1076.

184. Henderson, S. J.; Hector, A. L., Structural and Compositional Variations in Ta<sub>3</sub>N<sub>5</sub> Produced by High-Temperature Ammonolysis of Tantalum Oxide. *Journal of Solid State Chemistry* **2006**, *179* (11), 3518-3524.
185. Banerjee, S.; Mohapatra, S. K.; Misra, M., Synthesis of Taon Nanotube Arrays by Sonoelectrochemical Anodization Followed by Nitridation: A Novel Catalyst for Photoelectrochemical Hydrogen Generation from Water. *Chemical Communications (Cambridge, United Kingdom)* **2009**, (46), 7137-7139.
186. Feng, X.; LaTempa, T. J.; Basham, J. I.; Mor, G. K.; Varghese, O. K.; Grimes, C. A., Ta<sub>3</sub>N<sub>5</sub> Nanotube Arrays for Visible Light Water Photoelectrolysis. *Nano Letters* **2010**, *10* (3), 948-952.
187. Kerrec, O.; Devilliers, D.; Groult, H.; Chemla, M., Dielectric Properties of Anodic Oxide Films on Tantalum. *Electrochimica Acta* **1995**, *40* (6), 719-24.
188. Di Paola, A.; Di Quarto, F.; Sunseri, C., Electrochromism in Anodically Formed Tungsten Oxide Films. *Journal of the Electrochemical Society* **1978**, *125* (8), 1344-7.
189. Kavan, L.; Kratochvilova, K.; Graetzel, M., Study of Nanocrystalline Tio<sub>2</sub> (Anatase) Electrode in the Accumulation Regime. *Journal of Electroanalytical Chemistry* **1995**, *394* (1-2), 93-102.
190. Lyons, M. E. G.; Brandon, M. P., The Oxygen Evolution Reaction on Passive Oxide Covered Transition Metal Electrodes in Alkaline Solution Part Ii - Cobalt. *International Journal of Electrochemical Science* **2008**, *3* (12), 1425-1462.
191. Hui, Y.; Webster, R. D., Absorption of Water into Organic Solvents Used for Electrochemistry under Conventional Operating Conditions. *Analytical Chemistry (Washington, DC, United States)* **2011**, *83* (3), 976-981.
192. Conway, B. E., *Electrochemical Supercapacitors: Scientific Fundermentals and Technological Applications*. New York, 1999; p 230-232.
193. Armytage, D.; Fender, B. E. F., Anion Ordering in Tantalum Oxynitride. Powder Neutron-Diffraction Investigation. *Acta Crystallographica, Section B: Structural Crystallography and Crystal Chemistry* **1974**, *30* (3), 809-12.
194. Munoz, A. G.; Chen, Q.; Schmuki, P., Interfacial Properties of Self-Organized Tio<sub>2</sub> Nanotubes Studied by Impedance Spectroscopy. *Journal of Solid State Electrochemistry* **2006**, *11* (8), 1077-1084.
195. De Levie, R., Electrochemical Response of Porous and Rough Electrodes. *Adv. Electrochem. Electrochem. Eng.* **1967**, *6*, 329-97.

196. De Levie, R., Porous Electrodes in Electrolyte Solutions. Iv. *Electrochimica Acta* **1964**, 9, 1231-45.
197. Lasia, A., Impedance of Porous Electrodes. *Journal of Electroanalytical Chemistry* **1995**, 397 (1-2), 27-33.
198. Mantia, F.; Habazaki, H.; Santamaria, M.; Quarto, F., A Critical Assessment of the Mott-Schottky Analysis for the Characterisation of Passive Film-Electrolyte Junctions. *Russian Journal of Electrochemistry* **2010**, 46 (11), 1306-1322.
199. Tewg, J.-Y.; Kuo, Y.; Lu, J.; Schueler, B. W., Influence of a 5 Å Tantalum Nitride Interface Layer on Dielectric Properties of Zirconium-Doped Tantalum Oxide High-K Films. *Journal of the Electrochemical Society* **2005**, 152 (8), G617-G622.
200. Deb, S. K., Opportunities and Challenges in Science and Technology of  $\text{WO}_3$  for Electrochromic and Related Applications. *Solar Energy Materials & Solar Cells* **2008**, 92 (2), 245-258.
201. Granqvist, C. G., Electrochromic Tungsten Oxide Films: Review of Progress 1993-1998. *Solar Energy Materials & Solar Cells* **2000**, 60 (3), 201-262.
202. Runnerstrom, E. L.; Llordes, A.; Lounis, S. D.; Milliron, D. J., Nanostructured Electrochromic Smart Windows: Traditional Materials and NIR-Selective Plasmonic Nanocrystals. *Chemical Communications (Cambridge, United Kingdom)* **2014**, 50 (73), 10555-10572.
203. zum Felde, U.; Haase, M.; Weller, H., Electrochromism of Highly Doped Nanocrystalline  $\text{SnO}_2:\text{Sb}$ . *Journal of Physical Chemistry B* **2000**, 104 (40), 9388-9395.
204. Zhen, C.; Chen, R.; Wang, L.; Liu, G.; Cheng, H.-M., Tantalum (Oxy)Nitride Based Photoanodes for Solar-Driven Water Oxidation. *Journal of Materials Chemistry A: Materials for Energy and Sustainability* **2016**, 4 (8), 2783-2800.
205. Myers, D. *Polymer Electrolyte Fuel Cell Electrocatalysis*; Argon National Laboratory: DOE, Washington, D.C., February 19, 2009, 2009.
206. Chisaka, M.; Yamamoto, Y.; Itagaki, N.; Hattori, Y., Active Site Formation for Oxygen Reduction Reaction on Carbon-Support-Free Titanium Oxynitride with Boosted Activity in Acidic Media. *ACS Appl. Energy Mater.* **2018**, 1 (1), 211-219.
207. Seifitokaldani, A.; Savadogo, O., Electrochemically Stable Titanium Oxy-Nitride Support for Platinum Electro-Catalyst for Pem Fuel Cell Applications. *Electrochimica Acta* **2015**, 167, 237-245.
208. Seifitokaldani, A.; Oishi, K.; Perrier, M.; Savadogo, O., Electrochemical and Physicochemical Properties of Titanium Oxy-Nitride Electrocatalyst Prepared by Sol-Gel

Methods for the Oxygen Reduction Reaction Purposes. *Journal of Solid State Electrochemistry* **2015**, *19* (10), 3097-3109.

209. Chisaka, M.; Suzuki, Y.; Iijima, T.; Ishihara, Y.; Inada, R.; Sakurai, Y., Active Sites for Oxygen Reduction Reaction and the Reaction Mechanism in Carbon-Supported Hafnium Oxynitride. *ECS Electrochemistry Letters* **2012**, *1* (1), F4-F8.

210. Chisaka, M.; Sasaki, H.; Muramoto, H., Monoclinic Hafnium Oxynitride Supported on Reduced Graphene Oxide to Catalyse the Oxygen Reduction Reaction in Acidic Media. *Physical Chemistry Chemical Physics* **2014**, *16* (38), 20415-20419.

211. Chisaka, M.; Iijima, T.; Yaguchi, T.; Sakurai, Y., Carbon-Supported Hafnium Oxynitride as Cathode Catalyst for Polymer Electrolyte Membrane Fuel Cells. *Electrochimica Acta* **2011**, *56* (12), 4581-4588.

212. Chisaka, M.; Suzuki, Y.; Iijima, T.; Sakurai, Y., Effect of Synthesis Route on Oxygen Reduction Reaction Activity of Carbon-Supported Hafnium Oxynitride in Acid Media. *Journal of Physical Chemistry C* **2011**, *115* (42), 20610-20617.

213. Shinozaki, K.; Morimoto, Y.; Pivovar, B. S.; Kocha, S. S., Re-Examination of the Pt Particle Size Effect on the Oxygen Reduction Reaction for Ultrathin Uniform Pt/C Catalyst Layers without Influence from Nafion. *Electrochimica Acta* **2016**, *213*, 783-790.

214. Paramasivam, I.; Macak, J. M.; Schmuki, P., Photocatalytic Activity of TiO<sub>2</sub> Nanotube Layers Loaded with Ag and Au Nanoparticles. *Electrochem. Commun.* **2008**, *10* (1), 71-75.

215. Badam, R.; Vedarajan, R.; Okaya, K.; Matsutani, K.; Matsumi, N., Sacrificial Reducing Agent Free Photo-Generation of Platinum Nano Particle over Carbon/TiO<sub>2</sub> for Highly Efficient Oxygen Reduction Reaction. *Sci. Rep.* **2016**, *6*, 37006.

216. Losiewicz, B.; Jurczakowski, R.; Lasia, A., Kinetics of Hydrogen Underpotential Deposition at Polycrystalline Platinum in Acidic Solutions. *Electrochimica Acta* **2012**, *80*, 292-301.

217. Trasatti, S.; Petrii, O. A., Real Surface Area Measurements in Electrochemistry. *Pure and Applied Chemistry* **1991**, *63* (5), 711-34.

218. Migas, D. B.; Shaposhnikov, V. L.; Rodin, V. N.; Borisenko, V. E., Tungsten Oxides. I. Effects of Oxygen Vacancies and Doping on Electronic and Optical Properties of Different Phases of Wo<sub>3</sub>. *Journal of Applied Physics* **2010**, *108* (9), 093713/1-093713/7.

219. Sasaki, K.; Zhang, L.; Adzic, R. R., Niobium Oxide-Supported Platinum Ultra-Low Amount Electrocatalysts for Oxygen Reduction. *Physical Chemistry Chemical Physics* **2008**, *10* (1), 159-167.

220. Kocha, S. S.; Shinozaki, K.; Zack, J. W.; Myers, D. J.; Kariuki, N. N.; Nowicki, T.; Stamenkovic, V.; Kang, Y.; Li, D.; Papageorgopoulos, D., Best Practices and Testing Protocols for Benchmarking Orr Activities of Fuel Cell Electrocatalysts Using Rotating Disk Electrode. *Electrocatalysis* **2017**, *8* (4), 366-374.
221. Shinozaki, K.; Zack, J. W.; Richards, R. M.; Pivovar, B. S.; Kocha, S. S., Oxygen Reduction Reaction Measurements on Platinum Electrocatalysts Utilizing Rotating Disk Electrode Technique. *Journal of the Electrochemical Society* **2015**, *162* (10), F1144-F1158.
222. Wakabayashi, N.; Takeichi, M.; Itagaki, M.; Uchida, H.; Watanabe, M., Temperature-Dependence of Oxygen Reduction Activity at a Platinum Electrode in an Acidic Electrolyte Solution Investigated with a Channel Flow Double Electrode. *Journal of Electroanalytical Chemistry* **2005**, *574* (2), 339-346.
223. Norskov, J. K.; Rossmeisl, J.; Logadottir, A.; Lindqvist, L.; Kitchin, J. R.; Bligaard, T.; Jonsson, H., Origin of the Overpotential for Oxygen Reduction at a Fuel-Cell Cathode. *Journal of Physical Chemistry B* **2004**, *108* (46), 17886-17892.
224. Zhdanov, V. P.; Kasemo, B., Kinetics of Electrochemical O<sub>2</sub> Reduction on Pt. *Electrochemistry Communications* **2006**, *8* (7), 1132-1136.
225. Damjanovic, A.; Dey, A.; Bockris, J. O. M., Kinetics of Oxygen Evolution and Dissolution on Platinum Electrodes. *Electrochimica Acta* **1966**, *11* (7), 791-814.
226. Sepa, D. B.; Vojnovic, M. V.; Damjanovic, A., Reaction Intermediates as a Controlling Factor in the Kinetics and Mechanism of Oxygen Reduction at Platinum Electrodes. *Electrochimica Acta* **1981**, *26* (6), 781-93.
227. Ishikawa, A.; Takata, T.; Kondo, J. N.; Hara, M.; Domen, K., Electrochemical Behavior of Thin Ta<sub>3</sub>n<sub>5</sub> Semiconductor Film. *Journal of Physical Chemistry B* **2004**, *108* (30), 11049-11053.
228. Watanabe, E.; Ushiyama, H.; Yamashita, K., Theoretical Studies on the Mechanism of Oxygen Reduction Reaction on Clean and O-Substituted Ta<sub>3</sub>n<sub>5</sub>(100) Surfaces. *Catal. Sci. Technol.* **2015**, *5* (5), 2769-2776.
229. Ohnishi, R.; Takanabe, K.; Katayama, M.; Kubota, J.; Domen, K., Nano-Nitride Cathode Catalysts of Ti, Ta, and Nb for Polymer Electrolyte Fuel Cells: Temperature-Programmed Desorption Investigation of Molecularly Adsorbed Oxygen at Low Temperature. *Journal of Physical Chemistry C* **2013**, *117* (1), 496-502.
230. Hsieh, B.-J.; Tsai, M.-C.; Pan, C.-J.; Su, W.-N.; Rick, J.; Lee, J.-F.; Yang, Y.-W.; Hwang, B.-J., Platinum Loaded on Dual-Doped TiO<sub>2</sub> as an Active and Durable Oxygen Reduction Reaction Catalyst. *NPG Asia Mater.* **2017**, *9* (7), e403.

231. Savych, I.; Subianto, S.; Nabil, Y.; Cavaliere, S.; Jones, D.; Roziere, J., Negligible Degradation Upon in Situ Voltage Cycling of a Pemfc Using an Electrospun Niobium-Doped Tin Oxide Supported Pt Cathode. *Physical Chemistry Chemical Physics* **2015**, *17* (26), 16970-16976.
232. Viswanathan, V.; Pickrahn, K. L.; Luntz, A. C.; Bent, S. F.; Noerskov, J. K., Nanoscale Limitations in Metal Oxide Electrocatalysts for Oxygen Evolution. *Nano Letters* **2014**, *14* (10), 5853-5857.
233. Trotochaud, L.; Young, S. L.; Ranney, J. K.; Boettcher, S. W., Nickel-Iron Oxyhydroxide Oxygen-Evolution Electrocatalysts: The Role of Intentional and Incidental Iron Incorporation. *Journal of the American Chemical Society* **2014**, *136* (18), 6744-6753.
234. MacDonald, J. J.; Conway, B. E., The Role of Surface Films in the Kinetics of Oxygen Evolution at Pd + Au Alloy Electrodes. *Proc. Roy. Soc. (London)* **1962**, *Ser. A* *269*, 419-40.
235. Bjoernbom, P., Modeling of a Double-Layered Ptfе-Bonded Oxygen Electrode. *Electrochimica Acta* **1987**, *32* (1), 115-9.
236. Banham, D. W.; Soderberg, J. N.; Birss, V. I., Pt/Carbon Catalyst Layer Microstructural Effects on Measured and Predicted Tafel Slopes for the Oxygen Reduction Reaction. *Journal of Physical Chemistry C* **2009**, *113* (23), 10103-10111.
237. Banham, D.; Feng, F.; Furstenhaupt, T.; Pei, K.; Ye, S.; Birss, V., Novel Mesoporous Carbon Supports for Pemfc Catalysts. *Catalysts* **2015**, *5* (3), 1046-1067.
238. Wang, J. X.; Uribe, F. A.; Springer, T. E.; Zhang, J.; Adzic, R. R., Intrinsic Kinetic Equation for Oxygen Reduction Reaction in Acidic Media: The Double Tafel Slope and Fuel Cell Applications. *Faraday Discussions* **2008**, *140* (Electrocatalysis--Theory and Experiment at the Interface), 347-362.
239. Research, P. <https://www.pineresearch.com/shop/rotators/cpr-main/>.
240. Garsany, Y.; Singer, I. L.; Swider-Lyons, K. E., Impact of Film Drying Procedures on Rde Characterization of Pt/Vc Electrocatalysts. *Journal of Electroanalytical Chemistry* **2011**, *662* (2), 396-406.
241. Neufeld, O.; Toroker, M. C., Novel High-Throughput Screening Approach for Functional Metal/Oxide Interfaces. *J. Chem. Theory Comput.* **2016**, *12* (4), 1572-1582.
242. Banham, D. W. H. Design and Optimization of Nanoporous Carbon for Electrochemical Applications. 2012.
243. Yu, X.; Ye, S., Recent Advances in Activity and Durability Enhancement of Pt/C Catalytic Cathode in Pemfc. *Journal of Power Sources* **2007**, *172* (1), 145-154.

244. Huang, S.-Y.; Ganesan, P.; Park, S.; Popov, B. N., Development of a Titanium Dioxide-Supported Platinum Catalyst with Ultrahigh Stability for Polymer Electrolyte Membrane Fuel Cell Applications. *Journal of the American Chemical Society* **2009**, *131* (39), 13898-13899.
245. Wang, D.; Subban, C. V.; Wang, H.; Rus, E.; Di Salvo, F. J.; Abruna, H. D., Highly Stable and Co-Tolerant Pt/Ti<sub>0.7</sub>W<sub>0.3</sub>O<sub>2</sub> Electrocatalyst for Proton-Exchange Membrane Fuel Cells. *Journal of the American Chemical Society* **2010**, *132* (30), 10218-10220.
246. Jimenez-Morales, I.; Cavaliere, S.; Jones, D.; Roziere, J., Strong Metal-Support Interaction Improves Activity and Stability of Pt Electrocatalysts on Doped Metal Oxides. *Physical Chemistry Chemical Physics* **2018**, *20* (13), 8765-8772.
247. Cavaliere, S.; Jimenez-Morales, I.; Ercolano, G.; Savych, I.; Jones, D.; Roziere, J., Highly Stable Pemfc Electrodes Based on Electrospun Antimony-Doped SnO<sub>2</sub>. *ChemElectroChem* **2015**, *2* (12), 1966-1973.
248. Bauer, A.; Song, C.; Ignaszak, A.; Hui, R.; Zhang, J.; Chevallier, L.; Jones, D.; Roziere, J., Improved Stability of Mesoporous Carbon Fuel Cell Catalyst Support through Incorporation of TiO<sub>2</sub>. *Electrochimica Acta* **2010**, *55* (28), 8365-8370.
249. Forouzandeh, F.; Li, X.; Banham, D. W.; Feng, F.; Ye, S.; Birss, V., Evaluation of the Corrosion Resistance of Carbons for Use as Pem Fuel Cell Cathode Supports. *Journal of the Electrochemical Society* **2015**, *162* (12), F1333-F1341.
250. Speder, J.; Zana, A.; Spanos, I.; Kirkensgaard, J. J. K.; Mortensen, K.; Hanzlik, M.; Arenz, M., Comparative Degradation Study of Carbon Supported Proton Exchange Membrane Fuel Cell Electrocatalysts - the Influence of the Platinum to Carbon Ratio on the Degradation Rate. *Journal of Power Sources* **2014**, *261*, 14-22.
251. Rabis, A.; Rodriguez, P.; Schmidt, T. J., Electrocatalysis for Polymer Electrolyte Fuel Cells: Recent Achievements and Future Challenges. *ACS Catalysis* **2012**, *2* (5), 864-890.
252. Chan, K.-Y.; Ding, J.; Ren, J.; Cheng, S.; Tsang, K. Y., Supported Mixed Metal Nanoparticles as Electrocatalysts in Low Temperature Fuel Cells. *J. Mater. Chem.* **2004**, *14* (4), 505-516.
253. Banham, D.; Feng, F.; Pei, K.; Ye, S.; Birss, V., Effect of Carbon Support Nanostructure on the Oxygen Reduction Activity of Pt/C Catalysts. *Journal of Materials Chemistry A: Materials for Energy and Sustainability* **2013**, *1* (8), 2812-2820.
254. Banham, D.; Feng, F.; Fuerstenhaupt, T.; Ye, S.; Birss, V., First Time Investigation of Pt Nanocatalysts Deposited inside Carbon Mesopores of Controlled Length and Diameter. *J. Mater. Chem.* **2012**, *22* (15), 7164-7171.

255. Li, X.; Banham, D.; Feng, F.; Forouzandeh, F.; Ye, S.; Kwok, D. Y.; Birss, V., Wettability of Colloid-Imprinted Carbons by Contact Angle Kinetics and Water Vapor Sorption Measurements. *Carbon* **2015**, *87*, 44-60.
256. Li, X.; Forouzandeh, F.; Furstenhaupt, T.; Banham, D.; Feng, F.; Ye, S.; Kwok, D. Y.; Birss, V., New Insights into the Surface Properties of Hard-Templated Ordered Mesoporous Carbons. *Carbon* **2018**, *127*, 707-717.
257. Li, X.; Forouzandeh, F.; Kakanat, A. J.; Feng, F.; Banham, D. W. H.; Ye, S.; Kwok, D. Y.; Birss, V., Surface Characteristics of Microporous and Mesoporous Carbons Functionalized with Pentafluorophenyl Groups. *ACS Appl. Mater. Interfaces* **2018**, *10* (2), 2130-2142.
258. Xiaoan, L. Understanding and Controlling Wettability of Carbon Powders for Pem Fuel Cell Applications. University of Calgary, 2015.
259. Zhao, Q.; Wang, X.; Liu, J.; Wang, H.; Zhang, Y.; Gao, J.; Lu, Q.; Zhou, H., Design and Synthesis of Three-Dimensional Hierarchical Ordered Porous Carbons for Supercapacitors. *Electrochimica Acta* **2015**, *154*, 110-118.
260. Niederberger, M.; Garnweitner, G., Organic Reaction Pathways in the Nonaqueous Synthesis of Metal Oxide Nanoparticles. *Chemistry - A European Journal* **2006**, *12* (28), 7282-7302.
261. Shafeeyan, M. S.; Daud, W. M. A. W.; Houshmand, A.; Shamiri, A., A Review on Surface Modification of Activated Carbon for Carbon Dioxide Adsorption. *J. Anal. Appl. Pyrolysis* **2010**, *89* (2), 143-151.
262. Wang, H.; Maiyalagan, T.; Wang, X., Review on Recent Progress in Nitrogen-Doped Graphene: Synthesis, Characterization, and Its Potential Applications. *ACS Catalysis* **2012**, *2* (5), 781-794.
263. Chen, Y.; Wang, J.; Liu, H.; Banis, M. N.; Li, R.; Sun, X.; Sham, T.-K.; Ye, S.; Knights, S., Nitrogen Doping Effects on Carbon Nanotubes and the Origin of the Enhanced Electrocatalytic Activity of Supported Pt for Proton-Exchange Membrane Fuel Cells. *Journal of Physical Chemistry C* **2011**, *115* (9), 3769-3776.
264. Shao, Y.; Sui, J.; Yin, G.; Gao, Y., Nitrogen-Doped Carbon Nanostructures and Their Composites as Catalytic Materials for Proton Exchange Membrane Fuel Cell. *Applied Catalysis, B: Environmental* **2008**, *79* (1), 89-99.
265. Stephenson, N. C.; Roth, R. S., Structural Systematics in the Binary System Tantalum Pentoxide-Tungsten Trioxide. V. Structure of the Low Temperature Form of Tantalum Oxide L-Ta<sub>2</sub>O<sub>5</sub>. *Acta Crystallographica, Section B: Structural Crystallography and Crystal Chemistry* **1971**, *27* (Pt. 5), 1037-44.

266. Bleda-Martinez, M. J.; Lozano-Castello, D.; Morallon, E.; Cazorla-Amoros, D.; Linares-Solano, A., Chemical and Electrochemical Characterization of Porous Carbon Materials. *Carbon* **2006**, *44* (13), 2642-2651.
267. Forouzandeh, F. Enhancing the Durability of the Cathode Layer (Pt/C) in Pem Fuel Cells. University of Calgary, 2017.
268. Knotter, D. M., Etching Mechanism of Vitreous Silicon Dioxide in Hf-Based Solutions. *Journal of the American Chemical Society* **2000**, *122* (18), 4345-4351.
269. Dieckmann, G. R.; Langer, S. H., Selective Electrogenative Oxidation of Benzyl Alcohol with Platinum-Graphite Packed-Bed Anodes. *Journal of Applied Electrochemistry* **1997**, *27* (1), 1-8.
270. Forouzandeh, F.; Li, X.; Banham, D. W.; Feng, F.; Kakanat, A. J.; Ye, S.; Birss, V., Improving the Corrosion Resistance of Proton Exchange Membrane Fuel Cell Carbon Supports by Pentafluorophenyl Surface Functionalization. *Journal of Power Sources* **2018**, *378*, 732-741.
271. Forouzandeh, F.; Li, X.; Banham, D. W.; Feng, F.; Ye, S.; Birss, V., Understanding the Corrosion Resistance of Meso- and Micro-Porous Carbons for Application in Pem Fuel Cells. *Journal of the Electrochemical Society* **2018**, *165* (6), F3230-F3240.
272. Forouzandeh, F. U. W.
273. Hara, M.; Hitoki, G.; Takata, T.; Kondo, J. N.; Kobayashi, H.; Domen, K., Taon and Ta<sub>3</sub>n<sub>5</sub> as New Visible Light Driven Photocatalysts. *Catalysis Today* **2003**, *78* (1-4), 555-560.
274. Higashi, M.; Domen, K.; Abe, R., Fabrication of Efficient Taon and Ta<sub>3</sub>n<sub>5</sub> Photoanodes for Water Splitting under Visible Light Irradiation. *Energy & Environmental Science* **2011**, *4* (10), 4138-4147.
275. Higashi, M.; Domen, K.; Abe, R., Highly Stable Water Splitting on Oxynitride Taon Photoanode System under Visible Light Irradiation. *Journal of the American Chemical Society* **2012**, *134* (16), 6968-6971.
276. Nakamura, R.; Tanaka, T.; Nakato, Y., Oxygen Photoevolution on a Tantalum Oxynitride Photocatalyst under Visible-Light Irradiation: How Does Water Photooxidation Proceed on a Metal-Oxynitride Surface? *Journal of Physical Chemistry B* **2005**, *109* (18), 8920-8927.
277. Kim, E. S.; Nishimura, N.; Magesh, G.; Kim, J. Y.; Jang, J.-W.; Jun, H.; Kubota, J.; Domen, K.; Lee, J. S., Fabrication of Cafe<sub>2</sub>o<sub>4</sub>/Taon Heterojunction Photoanode for Photoelectrochemical Water Oxidation. *Journal of the American Chemical Society* **2013**, *135* (14), 5375-5383.
278. Gao, Q.; Giordano, C.; Antonietti, M., Controlled Synthesis of Tantalum Oxynitride and Nitride Nanoparticles. *Small* **2011**, *7* (23), 3334-40.

279. Toon, G. [https://mark4sun.jpl.nasa.gov/report/UT\\_seminar\\_Solar\\_Spectrum\\_Toon.pdf](https://mark4sun.jpl.nasa.gov/report/UT_seminar_Solar_Spectrum_Toon.pdf).
280. Abghoui, Y.; Skulason, E., Hydrogen Evolution Reaction Catalyzed by Transition-Metal Nitrides. *Journal of Physical Chemistry C* **2017**, *121* (43), 24036-24045.
281. Chen, J. G., Carbide and Nitride Overlayers on Early Transition Metal Surfaces: Preparation, Characterization, and Reactivities. *Chemical Reviews (Washington, D. C.)* **1996**, *96* (4), 1477-1498.
282. Kitchin, J. R.; Norskov, J. K.; Barteau, M. A.; Chen, J. G., Trends in the Chemical Properties of Early Transition Metal Carbide Surfaces: A Density Functional Study. *Catalysis Today* **2005**, *105* (1), 66-73.
283. Hara, Y.; Minami, N.; Itagaki, H., Synthesis and Characterization of High-Surface Area Tungsten Carbides and Application to Electrocatalytic Hydrogen Oxidation. *Applied Catalysis, A: General* **2007**, *323*, 86-93.
284. Hassan, A.; Paganin, V. A.; Ticianelli, E. A., Pt Modified Tungsten Carbide as Anode Electrocatalyst for Hydrogen Oxidation in Proton Exchange Membrane Fuel Cell: Co Tolerance and Stability. *Applied Catalysis, B: Environmental* **2015**, *165*, 611-619.
285. DOE, F. C. T. O. *Hydrogen Fuel Quality Specifications for Polymer Electrolyte Fuel Cells in Road Vehicles*; Fuel Cell Technology Office, 2016.
286. Shukla, A. K.; Ravikumar, M. K.; Arico, A. S.; Candiano, G.; Antonucci, V.; Giordano, N.; Hamnett, A., Methanol Electrooxidation on Carbon-Supported Pt-Wo<sub>3</sub>-X Electrodes in Sulfuric Acid Electrolyte. *Journal of Applied Electrochemistry* **1995**, *25* (6), 528-32.
287. Prins, R., Hydrogen Spillover. Facts and Fiction. *Chemical Reviews (Washington, DC, United States)* **2012**, *112* (5), 2714-2738.
288. Karim, W.; Spreafico, C.; Kleibert, A.; Gobrecht, J.; VandeVondele, J.; Ekinici, Y.; van Bokhoven, J. A., Catalyst Support Effects on Hydrogen Spillover. *Nature* **2017**, *541* (7635), 68-71.
289. Sheng, W.; Gasteiger, H. A.; Shao-Horn, Y., Hydrogen Oxidation and Evolution Reaction Kinetics on Platinum: Acid Vs Alkaline Electrolytes. *Journal of the Electrochemical Society* **2010**, *157* (11), B1529-B1536.
290. Maruyama, J.; Inaba, M.; Katakura, K.; Ogumi, Z.; Takehara, Z.-i., Influence of Nafion® Film on the Kinetics of Anodic Hydrogen Oxidation. *Journal of Electroanalytical Chemistry* **1998**, *447* (1), 201-209.
291. Markovic, N. M.; Grgur, B. N.; Ross, P. N., Temperature-Dependent Hydrogen Electrochemistry on Platinum Low-Index Single-Crystal Surfaces in Acid Solutions. *Journal of Physical Chemistry B* **1997**, *101* (27), 5405-5413.

292. Wang, J. X.; Brankovic, S. R.; Zhu, Y.; Hanson, J. C.; Adzic, R. R., Kinetic Characterization of Pt Fuel Cell Anode Catalysts Made by Spontaneous Pt Deposition on Ru Nanoparticles. *Journal of the Electrochemical Society* **2003**, *150* (8), A1108-A1117.
293. Chen, S.; Kucernak, A., Electrocatalysis under Conditions of High Mass Transport: Investigation of Hydrogen Oxidation on Single Submicron Pt Particles Supported on Carbon. *Journal of Physical Chemistry B* **2004**, *108* (37), 13984-13994.
294. Vogel, W.; Lundquist, L.; Ross, P.; Stonehart, P., Reaction Pathways and Poisons—II: The Rate Controlling Step for Electrochemical Oxidation of Hydrogen on Pt in Acid and Poisoning of the Reaction by Co. *Electrochimica Acta* **1975**, *20* (1), 79-93.
295. Neyerlin, K. C.; Gu, W.; Jorne, J.; Gasteiger, H. A., Study of the Exchange Current Density for the Hydrogen Oxidation and Evolution Reactions. *Journal of the Electrochemical Society* **2007**, *154* (7), B631-B635.

## Appendix

### Copy right permission

7/16/2018

Rightslink® by Copyright Clearance Center



# RightsLink®

[Home](#)
[Create Account](#)
[Help](#)

**ACS Publications**  
Most Trusted. Most Cited. Most Read.
**Title:** Conductivity Switching of N-Doped Ta Oxide Nanotubular Arrays

**Author:** Anusha D. Abhayawardhana, Viola I. Birss

**Publication:** The Journal of Physical Chemistry C

**Publisher:** American Chemical Society

**Date:** Jun 1, 2015

Copyright © 2015, American Chemical Society

#### LOGIN

If you're a [copyright.com](#) user, you can login to RightsLink using your [copyright.com](#) credentials.

Already a [RightsLink user](#) or want to [learn more?](#)

#### PERMISSION/LICENSE IS GRANTED FOR YOUR ORDER AT NO CHARGE

This type of permission/license, instead of the standard Terms & Conditions, is sent to you because no fee is being charged for your order. Please note the following:

- Permission is granted for your request in both print and electronic formats, and translations.
- If figures and/or tables were requested, they may be adapted or used in part.
- Please print this page for your records and send a copy of it to your publisher/graduate school.
- Appropriate credit for the requested material should be given as follows: "Reprinted (adapted) with permission from (COMPLETE REFERENCE CITATION). Copyright (YEAR) American Chemical Society." Insert appropriate information in place of the capitalized words.
- One-time permission is granted only for the use specified in your request. No additional uses are granted (such as derivative works or other editions). For any other uses, please submit a new request.

[BACK](#)
[CLOSE WINDOW](#)

Copyright © 2018 [Copyright Clearance Center, Inc.](#) All Rights Reserved. [Privacy statement](#). [Terms and Conditions](#). Comments? We would like to hear from you. E-mail us at [customer@copyright.com](mailto:customer@copyright.com)

**SPRINGER NATURE LICENSE  
TERMS AND CONDITIONS**

Aug 14, 2018

This Agreement between Ms. Anusha Abhayawardhana ("You") and Springer Nature ("Springer Nature") consists of your license details and the terms and conditions provided by Springer Nature and Copyright Clearance Center.

License Number	4407441113960
License date	Aug 14, 2018
Licensed Content Publisher	Springer Nature
Licensed Content Publication	Nature
Licensed Content Title	Materials for fuel-cell technologies
Licensed Content Author	Brian C. H. Steele, Angelika Heinzl
Licensed Content Date	Nov 15, 2001
Licensed Content Volume	414
Licensed Content Issue	6861
Type of Use	Thesis/Dissertation
Requestor type	academic/university or research institute
Format	print and electronic
Portion	figures/tables/illustrations
Number of figures/tables/illustrations	1
Will you be translating?	no
Circulation/distribution	<501
Author of this Springer Nature content	no
Title	Ta based materials for Fuel Cells
Instructor name	V.I. Birss
Institution name	University of Calgary
Expected presentation date	Sep 2018
Portions	Figure 1: Summary of fuel-cell types

**ELSEVIER LICENSE  
TERMS AND CONDITIONS**

Aug 14, 2018

This Agreement between Ms. Anusha Abhayawardhana ("You") and Elsevier ("Elsevier") consists of your license details and the terms and conditions provided by Elsevier and Copyright Clearance Center.

License Number	4407471453641
License date	Aug 14, 2018
Licensed Content Publisher	Elsevier
Licensed Content Publication	Applied Catalysis B: Environmental
Licensed Content Title	Probing the structure, the composition and the ORR activity of Pt <sub>3</sub> Co/C nanocrystallites during a 3422h PEMFC ageing test
Licensed Content Author	Laetitia Dubau, Miguel Lopez-Haro, Luis Castanheira, Julien Durst, Marian Chatenet, Pascale Bayle-Guillemaud, Laure Guétaz, Nicolas Caqué, Elisabeth Rossinot, Frédéric Maillard
Licensed Content Date	October–November 2013
Licensed Content Volume	142
Licensed Content Issue	n/a
Licensed Content Pages	8
Start Page	801
End Page	808
Type of Use	reuse in a thesis/dissertation
Intended publisher of new work	other
Portion	figures/tables/illustrations
Number of figures/tables/illustrations	1
Format	both print and electronic
Are you the author of this Elsevier article?	No
Will you be translating?	No
Original figure numbers	Figure 1
Title of your thesis/dissertation	Ta based materials for Fuel Cells
Publisher of new work	University of Calgary
Author of new work	V.I. Birss
Expected completion date	Sep 2018
Estimated size (number of pages)	1

**ELSEVIER LICENSE  
TERMS AND CONDITIONS**

Aug 14, 2018

This Agreement between Ms. Anusha Abhayawardhana ("You") and Elsevier ("Elsevier") consists of your license details and the terms and conditions provided by Elsevier and Copyright Clearance Center.

License Number	4407471161829
License date	Aug 14, 2018
Licensed Content Publisher	Elsevier
Licensed Content Publication	Applied Catalysis B: Environmental
Licensed Content Title	Probing the structure, the composition and the ORR activity of Pt <sub>3</sub> Co/C nanocrystallites during a 3422h PEMFC ageing test
Licensed Content Author	Laetitia Dubau, Miguel Lopez-Haro, Luis Castanheira, Julien Durst, Marian Chatenet, Pascale Bayle-Guillemaud, Laure Guétaz, Nicolas Caqué, Elisabeth Rossinot, Frédéric Maillard
Licensed Content Date	October–November 2013
Licensed Content Volume	142
Licensed Content Issue	n/a
Licensed Content Pages	8
Start Page	801
End Page	808
Type of Use	reuse in a thesis/dissertation
Intended publisher of new work	other
Portion	figures/tables/illustrations
Number of figures/tables/illustrations	1
Format	both print and electronic
Are you the author of this Elsevier article?	No
Will you be translating?	No
Original figure numbers	Figure 2
Title of your thesis/dissertation	Ta based materials for Fuel Cells
Publisher of new work	University of Calgary
Author of new work	V.I. Birss
Expected completion date	Sep 2018
Estimated size (number of pages)	1

**JOHN WILEY AND SONS LICENSE  
TERMS AND CONDITIONS**

Aug 14, 2018

---

This Agreement between Ms. Anusha Abhayawardhana ("You") and John Wiley and Sons ("John Wiley and Sons") consists of your license details and the terms and conditions provided by John Wiley and Sons and Copyright Clearance Center.

License Number	4407480780281
License date	Aug 14, 2018
Licensed Content Publisher	John Wiley and Sons
Licensed Content Publication	WILEY INTERDISCIPLINARY REVIEWS: ENERGY AND ENVIRONMENT
Licensed Content Title	A review of PEM fuel cell durability: materials degradation, local heterogeneities of aging and possible mitigation strategies
Licensed Content Author	Laetitia Dubau, Luis Castanheira, Frédéric Maillard, et al
Licensed Content Date	Mar 5, 2014
Licensed Content Volume	3
Licensed Content Issue	6
Licensed Content Pages	21
Type of use	Dissertation/Thesis
Requestor type	University/Academic
Format	Print and electronic
Portion	Figure/table
Number of figures/tables	2
Original Wiley figure/table number(s)	Figure 6 Figure 9
Will you be translating?	No
Title of your thesis / dissertation	Ta based materials for Fuel Cells
Expected completion date	Sep 2018
Expected size (number of pages)	1

**SPRINGER NATURE LICENSE  
TERMS AND CONDITIONS**

Aug 14, 2018

This Agreement between Ms. Anusha Abhayawardhana ("You") and Springer Nature ("Springer Nature") consists of your license details and the terms and conditions provided by Springer Nature and Copyright Clearance Center.

License Number	4407510141436
License date	Aug 14, 2018
Licensed Content Publisher	Springer Nature
Licensed Content Publication	Springer eBook
Licensed Content Title	Modeling of Membrane-Electrode-Assembly Degradation in Proton-Exchange-Membrane Fuel Cells – Local H <sub>2</sub> Starvation and Start –Stop Induced Carbon-Support Corrosion
Licensed Content Author	Wenbin Gu, Paul T. Yu, Robert N. Carter et al
Licensed Content Date	Jan 1, 2009
Type of Use	Thesis/Dissertation
Requestor type	academic/university or research institute
Format	print and electronic
Portion	figures/tables/illustrations
Number of figures/tables/illustrations	1
Will you be translating?	no
Circulation/distribution	<501
Author of this Springer Nature content	no
Title	Ta based materials for Fuel Cells
Instructor name	V.I. Birss
Institution name	University of Calgary
Expected presentation date	Sep 2018
Portions	Figure 1